MEASUREMENTS AND MODELING OF TURBULENT CONSUMPTION SPEEDS OF SYNGAS FUEL BLENDS

A Dissertation
Presented to
The Academic Faculty

by

Prabhakar Venkateswaran

In Partial Fulfillment
of the Requirements for the Degree
Doctor of Philosophy in the
School of Aerospace Engineering

Georgia Institute of Technology
May 2013

MEASUREMENTS AND MODELING OF TURBULENT CONSUMPTION SPEEDS OF SYNGAS FUEL BLENDS

Approved by:

Dr. Tim Lieuwen, Advisor
School of Aerospace Engineering
Georgia Institute of Technology

Dr. Jerry Seitzman
School of Aerospace Engineering
Georgia Institute of Technology

Dr. Suresh Menon
School of Aerospace Engineering
Georgia Institute of Technology

Dr. Caroline Genzale
School of Mechanical Engineering
Georgia Institute of Technology

Dr. Robert Cheng
Combustion Technologies Group
Lawrence Berkeley National Laboratory

Date Approved: Febuary 8th, 2013

To my beloved parents

Acknowledgements

It is quite challenging to concisely express my heartfelt gratitude towards the numerous individuals who have made this dissertation a possibility. However, you only get to write a PhD dissertation once, so I will dispense with all notions of brevity and really stretch this out.

I would be remiss if I did not open by thanking my parents. I struggle to come up with the words to express my gratitude for their unwavering support and encouragement. My two sisters, Kanmani and Narmada have also been a source of much laughter and positive thoughts, which was instrumental in helping me work through the difficult times.

None of this work would have been possible without the stellar mentorship of Tim Lieuwen. I am extremely grateful for Tim's guidance and encouragement in all aspects of graduate school life, research and otherwise. Tim's work ethic and commitment to excellence in research have been a model to me, and I am deeply thankful for the unique opportunity he extended to me five and a half years ago. I hope our association will continue for many years to come. In addition, I will miss the annual trips to Tim's cabin, where his blend of hospitality and fearlessness as we bushwhacked through the mountain trails in North Georgia made for many happy memories. Except of course for the time when the poison ivy made its presence felt.

Many thanks to Jerry Seitzman, who was essentially a co-advisor during my time at Georgia Tech. Jerry instilled in me the value of constantly asking questions, which is

the engine behind good research. In addition, his passion and commitment to teaching is something I hope to emulate in my own future career.

I am grateful to Professor Genzale, Professor Menon and Dr. Cheng for agreeing to serve on my dissertation committee. Their insightful comments and critiques have improved this manuscript immeasurably.

I also want to thank Dr. Jagoda and Daurette Joseph for being incredibly helpful in all aspects of my graduate education.

It is often said that we stand on the shoulder of giants, which could not be truer at the combustion lab. I have derived much inspiration from former colleagues and friends, Santosh Hemchandra, Shreekrishna, Sai Kumar Thumuluru, Karthik Periagaram, Jack Crawford and Jacqueline O'Connor. You all have been wonderful role models and left very big shoes to fill. In addition, many of you have continued to lend me an ear for which I am very grateful.

Andrew Marshall has been a true partner in crime in this endeavor. More than a colleague, Andrew has become one of my closest friends. Much of this work would not have been possible without his patient and meticulous efforts, and I have often relied on his level-headedness to mitigate some of my more inane (research and non-research) ideas. His fingerprints can be found all over this manuscript. I am especially thankful to Andrew for introducing me to the beautiful (and often agonizing) sport of cycling. Those long hours spent on the Comet will be dearly missed.

Special thanks must go out to Chris Foley for being a wonderful friend, colleague and fellow connoisseur of good food. Our four year friendship culminated in Chris acquiring the additional title of “room-mate extraordinaire” (even if it was only for a few weeks). I am looking forward to our future communications and encounters which will no doubt feature Chris’ unique brand of manic humor and recipe exchanges. I would also be remiss if I did not thank Chris for introducing me to the nuances of a good cup of coffee and for re-igniting my love for volleyball.

Michael Malanoski’s hyper-literalisms and constant reality checks are something I will simultaneously miss and not miss. It is a real quandary. His effort to rally the troops for weekly volleyball was a clinic in leadership and your influence is evident in the new generation of volley-ballers.

My graduate school experience was punctuated by many hallmark events. The first example was the trip to Vancouver for Turbo Expo 2011. Ben Emerson was a tremendous roommate on this trip, and Jackie deserves a special commendation for tolerating us during that week. Actually, I think Jackie deserves a commendation for tolerating many of us during the whole time we were together at the Combustion Lab. However, I did want to use this opportunity to thank Ben for being a wonderful colleague and a source for criminally understated but hilarious anecdotes.

The Princeton Summer Schools were also memorable events, for which Matt Quinlan played no small part. I think all of us younger folk can take a lesson from Matt on how to maintain a zest for life even in your advanced age.

I want to thank Alberto Amato for sharing many of his deep insights, which had a notable impact on much of this work. In addition, his unparalleled knowledge of Chemkin was instrumental in making some of the trickier cases converge. However, I will steadfastly stay on course to not refer to Alberto as “The Converger” as much as he may try to change my mind.

I also want to acknowledge Ben Wilde for willingly sharing an office with me for the better part of a year. I will miss many of our discussions about science, sports and everything in between.

A big thank you to the rest of the Combustion Lab crew for many stimulating discussions and laughs. The list, in no particular order: Bobby Noble, David Scarborough, Brad Ochs, Arun Radhakrishnan, Yash Kochar, Sampath Adusumili, Brandon Sforzo, Nick Magina, Luke Humphrey, Michael Aguilar, Vishal Acharya, Dong-hyuk Shin, Gina Magnotti, Ben Knox, Ianko Chterev, Nishant Jain and Ryan Sullivan.

The opportunity to mentor and work with the many undergraduate students has been a memorable aspect of my graduate experience. Much of this work would not have been possible without their help. Special thanks go to Ramon Romero, Edouard Bahous, Andrew Irby and Juan Camilo Pedroza.

I also want to wish Julia all the best as she takes over the turbulent flame speed work. She has been a great colleague, and it has been a pleasure working with her during the ‘transition phase’.

A big thank you to my friends outside of the combustion lab, for helping me keep things in perspective. Anirudh Mathur has been my closest friend for sixteen years, and it has been a pleasure to grow up together and share our successes with each other over all these years. Attending his wedding in Goa is an experience I will not forget. A big perk of Atlanta has been the opportunity to see Sagar Patel often. I have greatly enjoyed our late night chats at Fellini’s and the Thanksgiving and Christmas holidays spent together watching football and terrible early 90s movies. Laura Quinlan and Hillary Marshall have also been a constant source of mirth that I will miss. Alex Pace has been, and continues to be, my go-to source for popular culture references of all kinds. I also admire his commitment to keeping ‘Friday’ a viral video, and I am especially appreciative to him for introducing me to Critical Mass.

Finally, Kavitha has been a model for patience and a constant source of encouragement and positivity. You had a very tangible role in the success of this work, and for that, I thank you deeply.

Table of Contents

Chapter 4 Analysis of Flame Speed Data 103

Chapter 5 Characteristics of the Turbulent Flame Brush 152

Chapter 6 Conclusions and Recommendations for Future Work 192

List of Tables

List of Figures

List of Symbols and Abbreviations

A	Flame area
A_T	Instantaneous turbulent flame area
c	Progress variable
c_Y	Progress variable based on species mass fraction
c_θ	Progress variable based on temperature
D	Burner diameter
Da	Damköhler number
g	Flame front slope
G	Level-set
Ka	Karlovitz number
κ	Stretch rate
κ_{ext}	Extinction strain rate
Le	Lewis number
l_{int}	Integral length scale
l_L	Lagrangian length scale
l_M	Markstein length
$\vec{n}$	Unit normal
Ma	Markstein number
$\dot{q}$	Heat release rate
Re_B	Bulk Reynolds number
Re_λ	Taylor scale Reynolds number
s	Distance along <c> = 0.5 contour
S_L	Laminar flame speed
$S_{L,0}$	Un-stretched laminar flame speed
$S_{L,max}$	Maximum stretched laminar flame speed
$S_{L,D,max}$	Maximum stretched laminar flame speed based on displacement definition
$S_{L,HR,max}$	Maximum stretched laminar flame speed based on heat release consumption
S_T	Turbulent flame speed
$S_{T,GC}$	Global turbulent consumption speed
$S_{T,GD}$	Global turbulent displacement speed
$S_{T,LC}$	Local turbulent consumption speed
$S_{T,LD}$	Local turbulent displacement speed
T	Temperature
T_b	Temperature of burnt gases
T_u	Temperature of unburnt gases
t_F	Flame development time

U_0	Mean axial velocity
u'	Axial fluctuating velocity
u'_{rms}	Root mean square turbulence fluctuations
$\vec{v}_t$	Component of flow velocity tangential to flame surface
$\vec{v}_F$	Flame velocity in the laboratory reference frame
v'	Radial fluctuating velocity
w'	Azimuthal fluctuating velocity
Y	Mass fraction
Ze	Zeldovich number

γ	Density ratio,
δ_F	Laminar flame thickness
δ_{FBT}	Flame brush thickness
μ	Mean
ω	Frequency
$\dot{\omega}$	Reaction rate
ϕ	Equivalence ratio
ρ_b	Burnt gas density
ρ_u	Fresh gas density
σ	Standard deviation
τ_{flow}	Flow time scale
τ_{int}	Integral time scale
τ_L	Lagrangian time scale
τ_λ	Taylor time scale
$\tau_{S_{L,\max}}$	Chemical time scale defined as $\tau_{S_{L,\max}} = \frac{\delta_F\big|_{S_{L,\max}}}{S_{L,\max}}$
χ	Ratio of pilot mass flow rate to main flow rate

Summary

Increasingly stringent emission requirements and dwindling petroleum reserves have generated interest in expanding the role of synthesis gas (syngas) fuels in power generation applications. Syngas fuels are the product of gasifying organic-based feedstock such as coal and biomass and are composed of mainly H_2 and CO. However, the use of syngas fuels in lean premixed gas turbine systems has been limited in part because the behavior of turbulent flames in these mixtures at practical gas turbine operating conditions are not well understood. This thesis presents an investigation of the influence of fuel composition and pressure on the turbulent consumption speed, $S_{T,GC}$, and the turbulent flame brush thickness, δ_{FBT}, for these mixtures. $S_{T,GC}$ and δ_{FBT} are global parameters which represent the average rate of conversion of reactants to products and the average heat release distribution of the turbulent flame respectively.

A comprehensive database of turbulent consumption speed measurements obtained at pressures up to 20 atm and H_2/CO ratios of 30/70 to 90/10 by volume is presented. There are two key findings from this database. First, mixtures of different H_2/CO ratios but with the same un-stretched laminar flame speeds, $S_{L,0}$, exposed to the same turbulence intensities u'_{rms}, have different turbulent consumption speeds. Second, higher pressures augment the turbulent consumption speed when $S_{L,0}$ is held constant across pressures and H_2/CO ratios.

These observations are attributed to the mixture stretch sensitivities, which are incorporated into a physics-based model for the turbulent consumption speed using quasi-steady leading points concepts. The derived scaling law closely resembles Damköhler's classical turbulent flame speed scaling, except that the maximum stretched laminar flame speed, $S_{L,max}$, arises as the normalizing parameter. Scaling the $S_{T,GC}$ data by $S_{L,max}$ shows good collapse of the data at fixed pressures, but systematic differences between data taken at different pressures are observed. These differences are attributed to non-quasi-steady chemistry effects, which are quantified with a Damköhler number defined as the ratio of the chemical time scale associated with $S_{L,max}$ and a fluid mechanic time scale. The observed scatter in the normalized turbulent consumption speed data correlates very well with this Damköhler number, suggesting that $S_{T,GC}$ can be parameterized by $u'_{rms}/S_{L,\max}$ and the leading point Damköhler number.

Finally, a systematic investigation of the influence of pressure and fuel composition on the flame brush thickness is presented. The flame brush thickness is shown to be independent of the H_2/CO ratio if $S_{L,0}$ is held constant across the mixtures. However, increasing the equivalence ratio for lean mixtures at a constant H_2/CO ratio, results in a thicker flame brush. Increasing the pressure is shown to augment the flame brush thickness, a result which has not been previously reported in the literature. Classical correlations based on turbulent diffusion concepts collapse the flame brush thickness data obtained at fixed u'_{rms}/U_0 and pressure reasonably well, but systematic differences exist between the data at different u'_{rms}/U_0 and pressures.

Chapter 1
Introduction

1.1 Background and motivation

The chemical energy derived from the combustion of fossil fuels supplies roughly 85% of the world's total energy needs [1]. However, the increasingly stringent emission requirements, dwindling petroleum reserves, rising petroleum prices and threatening energy security issues have raised interest in expanding the range of fuels that can be used for practical applications. In particular, there has been renewed focus on coal because of its relative abundance compared to oil. However, despite the fact that half the energy required for electricity is derived from coal [2], current emission regulations demand a different approach, since burning coal in the solid phase in a clean manner is difficult.

Synthesis gas, or syngas, which is the product of gasifying organic or carbon-containing matter, has garnered significant interest [3]. Syngas production is not restricted to coal; other feedstocks include petroleum coke, residual oil and biomass. The primary constituents of syngas are H_2 and CO along with trace quantities of other species such as N_2, and CH_4 [3]. In addition, syngas fuels typically have high hydrogen contents making them attractive from a carbon-based emissions standpoint, and they are also amenable to use in conjunction with CO_2 sequestration technologies.

However, the strong dependence of syngas composition on the feedstock and gasification process has limited its applicability. In power generation gas turbine applications, this fuel composition variability can have significant effects on key combustor operational issues such as the flame's propensity to flashback or blow-off, the thermal loadings on the fuel nozzle and combustor liner, and the susceptibility to combustion dynamics [4].

The turbulent flame speed, S_T, which can be thought of as the average rate of propagation of a turbulent flame, is an important parameter that has a leading order influence on these operational metrics [4]. For example, the turbulent flame speed has a direct impact on the flame length and its spatial distribution in the combustor. This, in turn, affects the thermal loading distribution on the combustor liners, fuel nozzles and other hardware. Furthermore, the flame's proclivity to flashback is directly a function of how rapidly the flame propagates into the reactants, which is dependent on the turbulent flame speed. In addition, the turbulent flame speed has an important influence on combustion instability limits through its influence on the flame shape and length [5]. For example, measurements from Figura *et al.*[6] have clearly shown how combustion instability boundaries are influenced by changes in flame location due to changes in H_2 content of the fuel or mixture stoichiometry.

More fundamentally, the turbulent flame speed is also a key parameter in some models for the average reaction rate in RANS simulations and the subgrid-scale reaction rate in LES simulations [7]. One class of models that are utilized are the so-called 'flame speed closure' models [7]. In order to apply these models, the turbulent flame is considered as an ensemble of laminar flames that have been wrinkled and convected by the turbulence [8]. The average reaction rate and subgrid-scale terms are then related to the local average mass burning rate or the average rate of propagation, which are essentially different interpretations for the local turbulent flame speed. These issues have necessitated a better fundamental understanding of the turbulent flame speed and the development of rigorous models that capture the key physics.

The subsequent sections of this chapter focus on reviewing the relevant theoretical background, providing an overview of the literature pertinent to this work, and concluding with the scope and organization of this thesis.

1.2 Theoretical background

1.2.1 Premixed turbulent combustion

To gain an appreciation for the factors influencing the turbulent flame propagation, one has to delve into the field of turbulent combustion which is a vast field of study dedicated to understanding the interaction between the combustion process and the turbulent flow field. The reader is referred to the texts by Peters [9] and Veynante and Poinsot [7] to appreciate the rich array of physics that arise in this field of study. Salient concepts that are pertinent to turbulent flame propagation in premixed systems are reviewed in this section.

Premixed turbulent combustion is characterized by the interaction of the flame and turbulent flow over a wide range of length and time scales. Depending on the different relative length and time scales, the combustion characteristics can vary from burning in thin regions known as ‘flamelets’ to more distributed modes of burning akin to well-stirred reactors. These different regimes were first presented by Borghi in terms of the turbulence intensity, $u'_{rms}/S_{L,0}$ and the ratio of the integral length scale to the flame thickness, l_{int}/δ_F [10]. A slightly modified version of this diagram known as the Peters-Borghi diagram [11] is given in Figure 1.

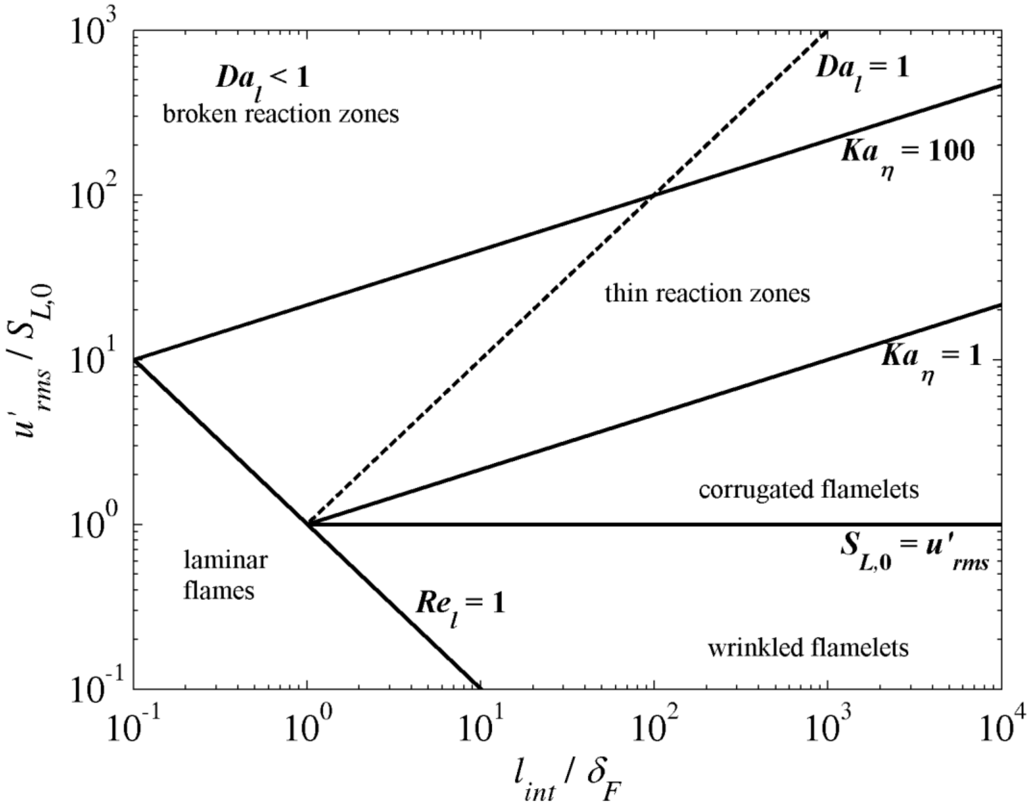

Figure 1:Borghi-Peters diagram.

In this work, the primary regions of interest are the ‘wrinkled flamelets’, ‘corrugated flamelets’ and ‘thin reaction zone’, which are characterized by high Damköhler numbers signifying that the chemical time scale is short with respect to the large turbulent time scales. A consequence of this is that the flame maintains a thin laminar premixed flame structure. We are also interested in the regions where the Reynolds's numbers are also high, indicating turbulent flows.

In the region labeled as 'wrinkled flamelets', all the turbulent length scales are larger than the laminar flame thickness. As a result, the turbulence serves to wrinkle the flame front, while preserving the characteristics of a quasi-steady premixed laminar flame. Furthermore, since $u'_{rms}/S_{L,0} < 1$, the turbulence only weakly perturbs the flame and not enough to produce flame-flame interactions [7].

The 'corrugated flamelets' regime shares many of the same characteristics of the 'wrinkled flamelets' regime, except the larger $u'_{rms}/S_{L,0}$ suggest that turbulent motions can cause flame-flame interactions leading to formation of pockets of fresh and burnt gases [7].

Finally, in the 'thin reaction zones' region, the turbulent Kolmogorov eddy is smaller than the thickness of the preheat zone allowing it to enter the preheat zone and alter the diffusive processes while preserving the laminar structure of the reaction zone. This has been speculated to lead to flame thickening, although this is yet to have been experimentally demonstrated conclusively [12]. Furthermore, the high strain rates associated with this regime can also lead to localized extinction events [7].

As discussed earlier, in these flamelet regimes, the turbulent flame can be described as an ensemble of laminar flamelets [8]. Because these flamelets are wrinkled and convected by the turbulence, they occupy a finite volume of space, known as the turbulent flame brush, which is depicted in Figure 2 for a Bunsen configuration.

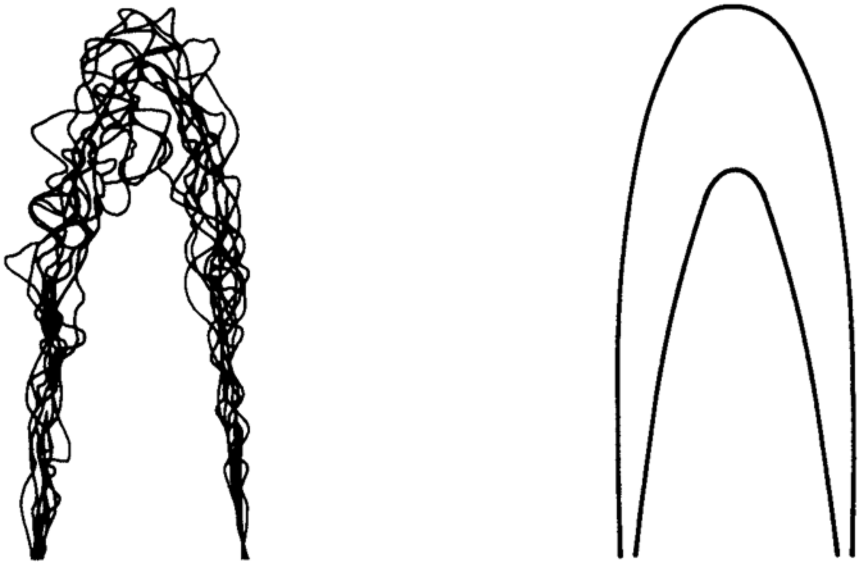
(a) (b)

Figure 2: Depiction of the (a) ensemble of laminar flamelets and (b) the turbulent flame brush in a Bunsen configuration. Figure adapted from Ref. [13].

A useful concept in analyzing turbulent premixed systems is the progress variable. The progress variable is often defined for a specific species *F*, c_Y or for temperature, c_θ, as follows:

$$c_Y = \frac{Y_F}{Y_{F,u}} \tag{1.1}$$

$$c_\theta = \frac{T - T_u}{T_b - T_u} \tag{1.2}$$

In Eq. (1.1) and Eq. (1.2), *Y* and *T* indicate mass fraction and temperature respectively, while the subscripts '*u*' and '*b*' indicate unburnt and burnt quantities respectively. The utility of the progress variable arises when analyzing systems under the simplifications of infinitely-fast chemistry, adiabatic and unity Lewis number. For such a case, when Eq. (1.1) and (1.2) are substituted into the species and energy equations, respectively, the resulting non-dimensional equations are essentially identical. From a computation perspective, this reduces the number of equations to be solved by one, and the non-dimensional temperature and species are related by:

$$c_Y + c_\theta = 1 \tag{1.3}$$

In practical systems, these simplifications are rather restrictive and the relation between the normalized temperature and mass fraction most likely will not hold. However, the progress variable is a still a useful quantity in turbulent flames, as the ensemble average progress variable, $\langle c \rangle$, can be regarded as the cumulative distribution function for the flame location. The $\langle c \rangle$ field can then be used to determine various properties of the turbulent flame.

One such global parameter characterizing the premixed turbulent flame is the turbulent flame speed, S_T. As described above, the turbulent flame speed has important applications for evaluating operational metrics for combustion devices as well for computational closure and sub-grid scale models. However, the precise definition of the turbulent flame speed is hindered by a few factors.

First, like the laminar flame speed, the calculation of a turbulent flame speed also relies on the prescription of a reference area. However, as depicted in Figure 2, the turbulent flame brush thickness is significantly larger than the laminar flame thickness, and so there no obvious area on which to base the calculation of the turbulent flame speed. As a result, reference areas were calculated or extracted in an inconsistent manner, leading to large reported scatter in the data [12].

Second, as discussed in recent reviews [12, 14], the turbulent flame speed depends not only on the fuel-air mixture, the operating conditions and the turbulent flow field; it also depends on the experimental configuration in which the measurements are carried out. As discussed by Driscoll [12], this arises due to the fact that each configuration imposes its own unique boundary condition, and the flame wrinkling at a point is due to the local turbulence as well as the wrinkle generated by the upstream stabilization process. This non-local effect was termed as the 'memory effect' [15].

To address these issues and to bring consistency to how the turbulent flame speed is quantified, recent reviews [12, 14] and the International Workshop on Premixed Flames [16] noted that there are actually multiple useful definitions for S_T that are relevant for different combustion issues (e.g., flashback versus heat release per volume). Furthermore, they also recommended that comparisons be made only between identically defined flame speeds; consumption speeds should not be compared against displacement speeds.

These turbulent flame speed definitions are as follows:

Global turbulent consumption speed, $S_{T,GC}$: This definition of the turbulent flame speed considers the total average rate of conversion of reactants to products. A derivation for an expression of the global consumption speed, which closely follows

Damköhler's derivation for the turbulent flame speed for large-scale turbulence [17], is provided below.

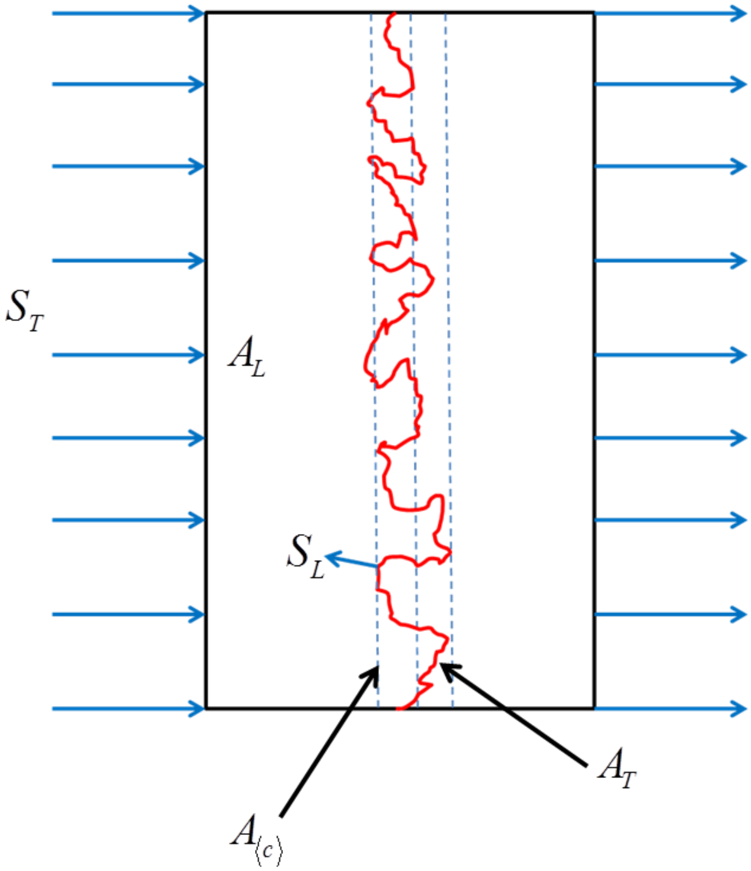

Figure 3: Illustration used to derive an expression for the turbulent consumption speed.

In Figure 3, the instantaneous flame has been indicated by the wrinkled convoluted red line, whose area is A_T, and it is assumed that the flame is everywhere propagating at the local laminar flame speed, S_L. Reactants enter the control volume, indicated by the black lines, through an area given by A_L. The dotted lines indicate representative progress variable surfaces of area $A_{<c>}$, which in this configuration are all the same since the flame is statistically one-dimensional. Assuming that the flame is statistically stationary, the continuity equation can be used to equate the mass flow rate entering the control volume and the ensemble average rate of conversion of reactants to products:

$$\dot{m}_R = \rho_R S_{T,GC} A_L = \left\langle \rho_R S_L A_T \right\rangle \tag{1.4}$$

It is worthwhile to point out that if S_L is assumed to be constant over the flame surface and Eq. (1.4) is re-arranged to give:

$$\frac{S_{T,GC}}{S_L} = \frac{A_T}{A_L} \tag{1.5}$$

then it is clear that the reason that the turbulent flame speed is larger than the laminar flame speed is because of the larger area of the turbulent flame. Damköhler then assumed that the interaction between the wrinkled flame front and the turbulent flow field is purely kinematic and approximated the area ratio as [17]:

$$\frac{A_T}{A_L} \sim \frac{u'_{rms}}{S_L} \tag{1.6}$$

This expression is quite remarkable since many future expressions for the turbulent flame speed were also found to be a function of u'_{rms}/S_L .

In practical systems, the reactant mass flow rate and density are known, and Eq. (1.4) can be expressed as:

$$S_{T,GC} = \frac{\dot{m}_R}{\rho_R A_{\langle c \rangle}} \tag{1.7}$$

Note that in Eq. (1.7), A_L has been replaced by $A_{<c>}$, which is the area of the progress variable surface of choice. Since the turbulent flame brush in Figure 3 is statistically one-dimensional, the average progress variable surfaces are all parallel, and as a result, have the same areas. On the other hand, for Bunsen flames such as the one shown in Figure 2, it is apparent that the choice of the progress variable surface will influence the calculated value of $S_{T,GC}$. For consistency, Driscoll [12] recommends that the $<c>$ = 0.5 surface is utilized in Eq. (1.7).

From the development of Eq.(1.4), it is clear that in order to use this definition, all the reactants must pass through the flame brush. As a result, $S_{T,GC}$ is typically defined for such configurations, called envelope flames, of which Bunsen flames are an example [12, 16] .

Local turbulent consumption speed, $S_{T,LC}$: The local consumption speed is defined by Eq. (1.8) and is indicative of the local average rate of conversion from reactants to products.

$$S_{T,LC} = S_{L,0} I_0 \int_{-\infty}^{\infty} \Sigma d\eta \tag{1.8}$$

In Eq. (1.8), I_0, Σ and η are the stretch factor, flame surface density and the co-ordinate normal to the designated progress variable respectively. The stretch factor, I_0, is the ratio of the mean flamelet consumption speed and the un-stretched laminar flame speed [18]. The flame surface density is the flame area per unit volume, and is an indicator of how convoluted the flame front is. Higher flame surface densities are associated with more wrinkled flame fronts, and higher average local reaction rates [7]. Clearly, this integral is a function of the integration path, η, through the turbulent flame brush. Several authors suggest that it be performed in a direction normal to the flame brush [12], which is itself generally a function of reaction progress variable.

Like the global consumption speed, Driscoll also recommends that <*c*> = 0.5 is utilized to define the normal [12].

This definition of the turbulent flame speed is of interest because it accounts for local variations in the consumption speed, which are of use in combustion codes that utilize the local consumption speed to model the local average reaction rate.

Local turbulent displacement, $S_{T,LD}$: the local turbulent displacement speed, is defined as the average speed at which the turbulent flame locally propagates into the reactants, and can be expressed as:

$$S_{T,LD} = (\vec{v}_F - \vec{v}) \cdot \vec{n} \tag{1.9}$$

where $\vec{v}_F$, $\vec{v}$ and $\vec{n}$ are the flame velocity in a fixed co-ordinate system, the reactant flow velocity and the normal to the reference flame surface. The reactant flow velocity and normal are typically defined at the leading edge of the flame brush [12].

It is instructive to discuss in a little more detail the difference between the turbulent displacement and consumption speeds. More details may be found in [19, 20]. Similar to laminar flames, the consumption speed and displacement speed yield identical values when the flame and flow are statistically one-dimensional. To illustrate this consider the equations of mass (Eq. (1.10)) and species (Eq. (1.11)) conservation for a steady-state, one-dimensional laminar flame under the assumptions of adiabaticity and Fickian diffusion:

$$\frac{d}{dx}(\rho u) = 0 \rightarrow \rho u = \text{constant} = \rho_1 u_1 = \rho_1 S_{L,0} \tag{1.10}$$

$$\rho S_{L,0} \frac{dY_F}{dx} = \frac{d}{dx}\left(\rho D \frac{dY_F}{dx} \right) + \dot{\omega}_F \tag{1.11}$$

If Eq. (1.11) is integrated from -∞ to ∞, and recognizing that the diffusive terms go to zero at the boundaries due to vanishing gradients, the resulting expression is:

$$\rho S_{L,0} \left(Y_{F,\infty} - Y_{F,-\infty} \right) = \int_{-\infty}^{\infty} \dot{\omega}_F \, dx \tag{1.12}$$

The term on the left-hand side is associated with the convective mass flux of reactants into the flame, and so $S_{L,0}$ can be thought of as the displacement speed. The right-hand side represents the conversion of reactants to products, which can be thought of as the consumption speed. In this one-dimensional, steady-state formulation, it is clear that the displacement and consumption speeds yield identical values. A similar analysis with time-averaged equations can be performed to show the equality between turbulent displacement and consumption speed.

However, in the presence of flow divergence, these two definitions yield different results. To illustrate consider Figure 4, which depicts a control volume ABCD in a turbulent flame brush and consider the turbulent consumption and displacement speeds with respect to the <c> = 0 contour.

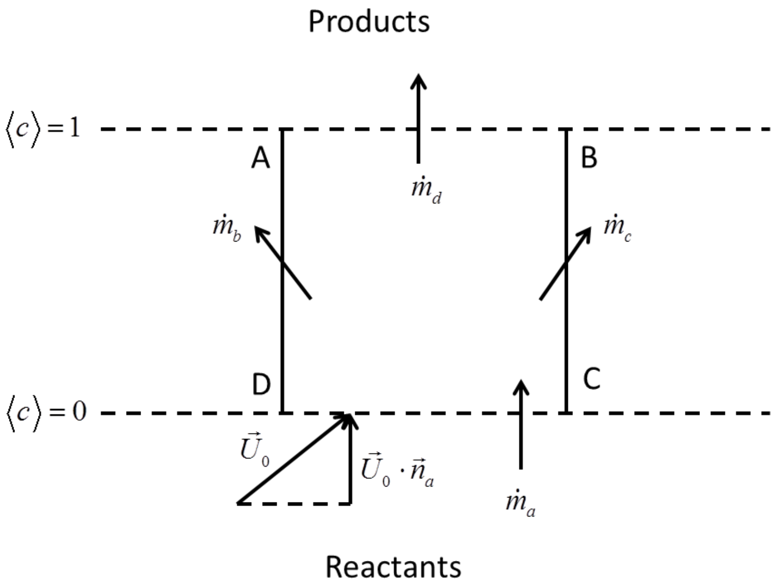

Figure 4: Illustration of a control volume in a turbulent flame brush following Ref. [19].

We can also define the time-averaged reactant flow rates into each surface of the control volume as $\dot{m}_a$, $\dot{m}_b$, $\dot{m}_c$, and $\dot{m}_d$. Assuming that all the reactants are converted to products, $\dot{m}_d = 0$, the following mass balance can be written for the control volume ABCD:

$$\dot{m}_a + \dot{m}_b + \dot{m}_c = -\iiint_{CV} \overline{\dot{\omega}}_{\text{reactants}} dV \tag{1.13}$$

where $-\iiint_{CV} \overline{\dot{\omega}}_{\text{reactants}} dV$ is the average rate of conversion of reactants to products. Noting that this term is the definition for the turbulent consumption speed, we can write:

$$-\iiint_{CV} \overline{\dot{\omega}}_{\text{reactants}} dV = \rho_u A_a S_{T,LC} \tag{1.14}$$

where A_a denotes the surface area of the front edge of the control volume defined as the $<c> = 0$ contour. The mass flow rate of reactants entering the control volume through surface a is given by:

$$\dot{m}_a = \rho_u \vec{U}_0 \cdot \vec{n}_a A_a = \rho_u S_{T,LD} A_a \tag{1.15}$$

where the interpretation of the displacement speed as the average speed at which reactants enter the flame brush has been used. Substituting Eq. (1.14) and (1.15) into Eq. (1.13) yields:

$$S_{T,LC} - S_{T,LD} = \frac{\dot{m}_b + \dot{m}_c}{\rho_u A_a} \tag{1.16}$$

which reveals that the consumption and displacement speeds differ because of time-averaged mass flux through the sides of the control volume. As a result, for these configurations, the turbulent displacement speed is greater than the consumption speed, as shown in Figure 5.

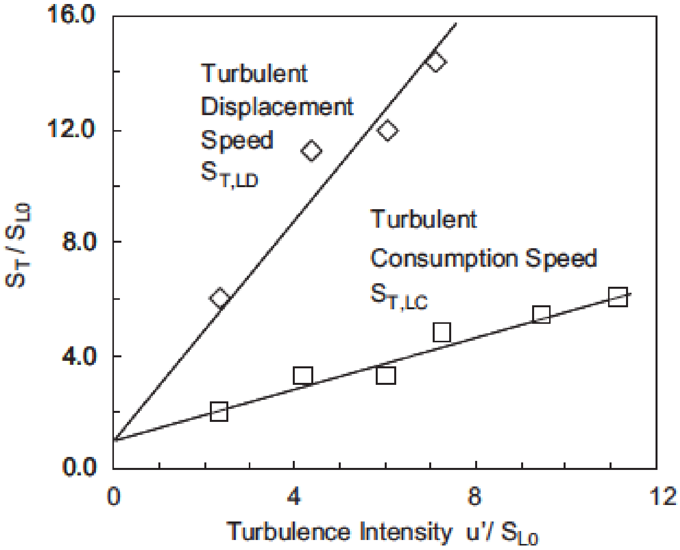

Figure 5: Variation of normalized $S_{T,LD}$ and $S_{T,LC}$ with $u'/S_{L,0}$ in a low swirl burner for a $\phi = 0.9$, CH_4/air flame in a low swirl burner. Figure adapted from Ref. [21].

1.2.2 Stretch physics

An important aspect of premixed turbulent combustion is the role of the mixture stretch sensitivity. The reader is referred to the review paper by Sung and Law [22] and textbooks by Law [1] and Williams [23] for a thorough coverage of stretch physics. Once again, only the concepts relevant to this work will be covered here.

The first level of idealization of the laminar, premixed flame is one where the flame and flow are one-dimensional and steady. This is known as the un-stretched laminar flame, and the associated burning rate is called the un-stretched laminar flame speed, $S_{L,0}$. However, when deviations from this one-dimensional idealization occur in the form of flow non-uniformity, flame curvature and flame motion, the flame is said to be stretched. Williams called the degree of this non-uniformity the stretch rate, κ, and defined it to be the Lagrangian derivative of the flame area [23]:

$$\kappa = \frac{1}{A}\frac{DA}{Dt} \tag{1.17}$$

Through the use of vector geometry and assuming the flame is an infinitely thin interface [24, 25], an expression for stretch in terms of the flow field, $\vec{v}$, and flame motion, $\vec{v}_F$ was derived as:

$$\kappa = \nabla_t \cdot \vec{v}_t + \left(\vec{v}_F \cdot \vec{n}\right)\left(\nabla \cdot \vec{n}\right) \tag{1.18}$$

The first term in Eq. (1.18) is known as hydrodynamic strain and signifies the effect of tangential gradients in the tangential components of the flow velocity, which are indicated by the subscript '*t*'. The second term is the stretch due to the combination of flame curvature and flame motion. Although Eq. (1.17) and (1.18) provide a mathematical description of stretch, Figure 6 can be used to present a more physical understanding.

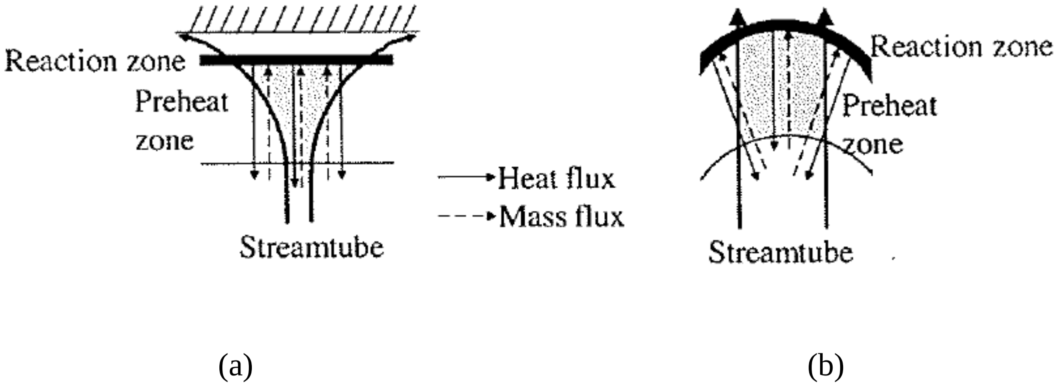

(a) (b)

Figure 6: Illustrations depicting influence of (a) hydrodynamic strain and (b) flame curvature. Figure adapted from Ref. [19].

Figure 6(a) depicts a flame in a divergent flow field, which can be realized in the laboratory by stagnating a premixed reactant stream against a wall. Figure 6(b) depicts a curved flame in a uniform flow field which is often seen at a Bunsen tip. In both cases, convective transport, depicted by streamlines, and the diffusive transport of heat and mass are clearly indicated. On the other hand, recall that for the one-dimensional, un-stretched laminar flame, the convection and diffusion occur in parallel directions. As a result, the physical manifestations of stretch, which are described below, are a result of the misalignment between the convective and diffusive directions.

First consider the situation depicted in Figure 6(a) where a flat flame is subjected to only hydrodynamic strain. A control volume can be drawn as shown, where the sides are bound by streamlines across which diffusive transfer can occur but not convective transfer. Since the flame is a source of heat and a sink for reactants, heat diffuses normal to the flame out of the control volume, while reactants diffuse into the control volume towards the flame from exterior streamtubes. The relative importance of these two processes can be assessed by considering the Lewis number defined as $Le = \alpha_{mix} / D_{def}$, where α_{mix} is the mixture thermal diffusivity and D_{def} is the mass diffusivity of the deficient species. If $Le = 1$, the effects of mass and thermal diffusion are balanced, and the control volume is adiabatic and the flame temperature will equal the adiabatic flame temperature corresponding to the mixture global equivalence ratio. For $Le < 1$ mixtures, the mass diffusivity dominates over the heat diffusion, and the overall effect is for the flame temperature to increase above the adiabatic flame temperature, which results in an increase of the burning velocity. On the other hand, for $Le > 1$, the heat loss by thermal diffusion dominates the rise in the concentration of the deficient reactant which causes the flame temperature and flame speed to decrease.

These effects are known as non-unity Lewis number effects. Another diffusion-based phenomenon associated with stretch known as preferential diffusion, occurs when the reactant constituents have large variations in mass diffusivities [1]. To illustrate, consider Figure 6(a) for a lean H_2/air mixture. Both H_2 and air will diffuse into the control volume, but since H_2 is lighter than air, it will diffuse faster. As a result, this causes the local equivalence ratio to increase towards stoichiometric resulting in a higher flame temperature and flame speed. For a rich H_2/air mixture, similar arguments can be made to show that the local equivalence ratio will become even richer resulting in a lower flame temperature and flame speed. Similar lines of reasoning can also be employed for C_3H_8/air flames, which experience opposite effects since C_3H_8 is now heavier than air.

Now consider the second configuration depicted in Figure 6(b). As before, consider a control volume bound by the flame tip and the vertical streamlines. It is assumed that the flame does not cause any streamline divergence, which is generally not the case, but the simplification is useful to elucidate the key physics. It is also important to keep in mind that this configuration does not reflect the stretch arising from the second term on the left-hand side of Eq. (1.18) since the curved tip is not moving; it is a different manifestation of the first term on the left-hand side of Eq. (1.18).

For the non-unity Lewis number effects in this configuration, first consider a $Le < 1$ mixture. Since diffusion occurs in the direction of the maximum gradient, which is normal to the flame front, heat is ‘focused’ into the control volume, while reactants are ‘de-focused’ from the control volume as they diffuse outwards towards the flame. Since $Le < 1$, the loss of the deficient reactant from the control volume will dominate over the heat gain, and the local flame temperature and flame speed will decrease. This reasoning can be extended to $Le > 1$ mixtures to show that the local flame temperature and flame speed will increase.

To illustrate preferential diffusion effects, consider a lean H_2/air mixture. Since H_2 will diffuse faster than the air, the equivalence ratio in the control volume will decrease causing the flame temperature and flame speed to decrease. Once again similar arguments can be used to describe what happens for rich H_2/air mixtures. Using similar arguments, the effects for rich H_2/air and for C_3H_8/air mixtures can also be described.

The effects of stretch were investigated more quantitatively by Matalon and Matkowsky [26], who performed a two-scale asymptotic analysis for an irreversible, one-step reaction, and found the following linear relation in the limit for weak stretch:

$$S_L = S_{L,0} - l_M \kappa \tag{1.19}$$

where l_M is the is the Markstein length, which can take on both positive and negative values. As a result, a negative Markstein length mixture, such as lean H_2/air, exposed to positive stretch, as in Figure 6(a), will experience an augmentation in the local burning velocity.

Equation (1.19) can be non-dimensionalized using the un-stretched laminar flame speed, $S_{L,0}$, and the associated flame thickness, $\delta_{F,0}$ to obtain:

$$\frac{S_L}{S_{L,0}} = 1 - MaKa \tag{1.20}$$

where *Ma* is the Markstein number defined as l_M / δ_F and *Ka* is the Karlovitz number defined as $\delta_F \kappa / S_{L,0}$. The limit of weak stretch can be expressed more precisely as $Ka \ll 1$. In the same work, the following relation for the Markstein number, defined as the ratio of the Markstein length to the flame thickness, l_M / δ_F, was also derived:

$$Ma = \frac{1}{\gamma - 1}\left[\gamma \ln \gamma + \frac{Ze}{2}\left(1 - \frac{1}{Le}\right)\int_0^{\gamma - 1} \frac{\ln(1 + x)}{x} dx\right] \text{cx} \tag{1.21}$$

Equation (1.21) shows that the Markstein length, which is a quantitative measure of a mixture's stretch sensitivity, is a thermo-chemical property of the mixture that depends on the gas expansion ratio, γ, the Lewis number, and the Zeldovich number, *Ze*, which can be thought of as the non-dimensional activation energy. An interesting feature of Eq. (1.19) is that in the limit of weak stretch, the stretched flame speed depends only the total stretch, and not on the type of stretch.

However, as the stretch rate is increased, the linear relation between stretch and flame speed expressed in Eq. (1.19) ceases to hold and the flame responds differently to curvature and hydrodynamic strain [27], as shown in Figure 7.

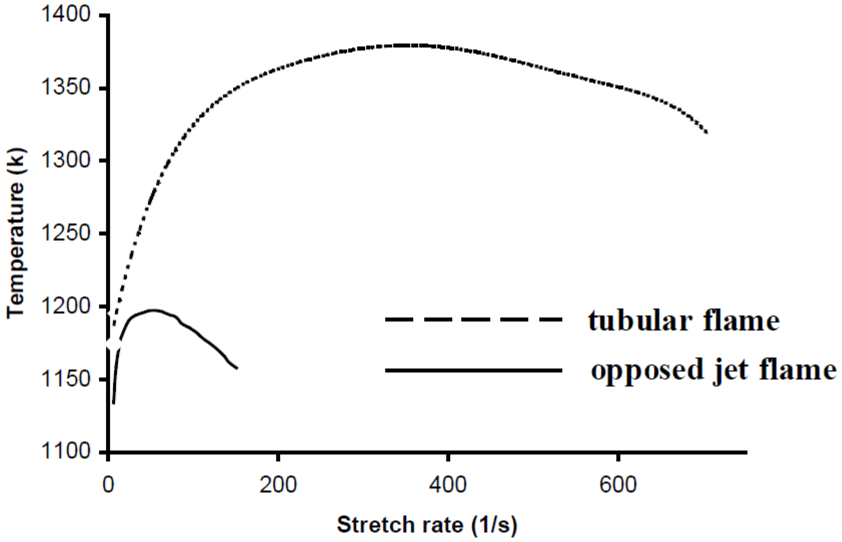

Figure 7: Variation of computed flame temperature with stretch rate for a ϕ = 0.175 H_2/air flame in a tubular and opposed jet geometry. Figure adapted from Ref. [27].

In addition, consider Figure 6(a) again. As the stretch rate (or nozzle exit velocity) is increased, there is a larger variation of mass flux through the flame due to the increased flow divergence, which as discussed above, results in different values of the burning velocity depending on the flame speed definition considered. This in turn results in different values of the Markstein lengths defined using displacement and consumption speeds. Furthermore, the residence time through the flame also decreases owing to the larger velocities. These effects result in the flame being able to withstand a certain maximum stretch rate, κ_{ext}, before extinguishing, as shown in Figure 8. However, following on from the discussions above, the extinction mechanisms vary with the mixture and configuration. For instance, for a $Le < 1$ mixture in a divergent flowfield as in Figure 6(a), as the stretch rate is increased, the flame speed also increases as discussed before, but the flame gets pushed closer towards the stagnation plane. As the flame gets closer to the stagnation plane, its movement becomes more restrained and the resulting short residence times and the inability of the reaction rate to consume reactants in this time, causes the flame to extinguish. However, in the case of a $Le > 1$ mixture, the extinction mechanism is the reduction of flame temperature in the control volume due to the diffusional processes, and not incomplete reactions.

Unfortunately, these high stretch effects cannot be described with simple expressions such as Eq. (1.19). But the availability of computational software such as OPPDIF [28] in the CHEMKIN package, which simulates a configuration similar to that in Figure 6(a), can be used to determine the total stretch response while utilizing detailed chemical kinetics and transport models. Furthermore, in reality, both non-unity Lewis number and preferential diffusion effects occur simultaneously, and so software of this kind is very useful in capturing many of the key physics. Figure 8 is an example of an OPPDIF calculation, where two $\phi = 0.5$ H_2/air mixtures at STP (1 atm and 300 K) are stagnated against each other, and twin premixed flames are stabilized in the divergent flow field on opposite sides of the stagnation plane. The nozzle velocities are increased simultaneously to maintain a symmetric configuration until the flame extinguishes at the extinction strain rate, κ_{ext}, as shown. The linear response in the low stretch region is indicated as a dashed line along with the Markstein length, l_M, which, according to Eq. (1.19), is the slope.

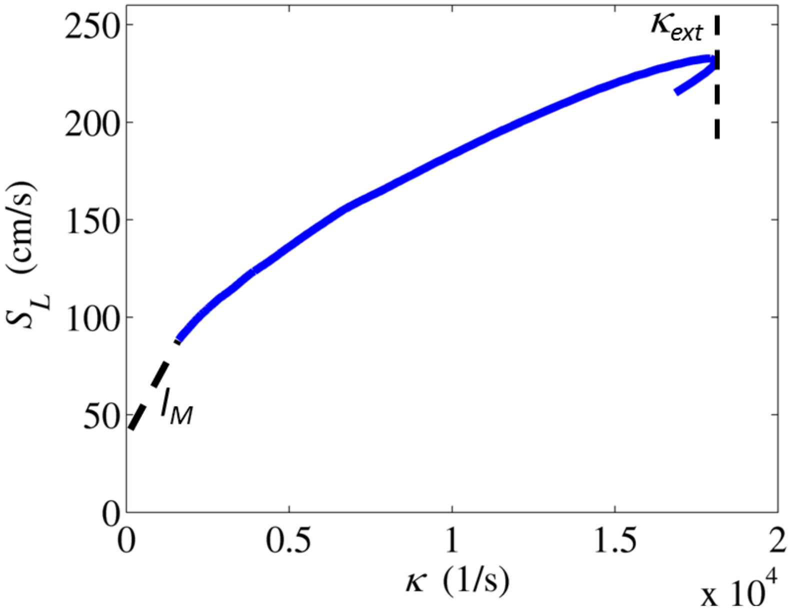

Figure 8: Typical stretch sensitivity calculation for a $\phi = 0.5$ H_2/air flame at STP in the symmetric opposed flow configuration simulated in OPPDIF.

In addition, lean H_2/air mixtures are strongly stretch sensitive due to the highly diffusive nature of H_2. This is particularly evident from Figure 8, which shows that the stretched burning velocities can be far in excess of the un-stretched value (by as much as a factor of 5). In fact, introducing even small quantities of H_2 to mixtures can significantly alter the stretch sensitivity of mixtures [29], and this is an important consideration for syngas fuels.

One additional point to consider under the general topic of stretch is the impact of unsteady stretch effects. Up until now, most of the discussion has focused on steady-state stretch effects. However, turbulence is a highly unsteady phenomenon, and consequently, the flame experiences unsteady stretch. Work to understand this effect has been performed by many authors who have simulated the counter-flow configuration with periodic flows [30, 31]. One such example is shown in Figure 9 from the work of Im and Chen [31]. In this work, a $\phi = 0.4$ H_2/air mixture was stagnating against burned products and stretch sensitivity calculations were performed for periodic mean flows of various frequencies.

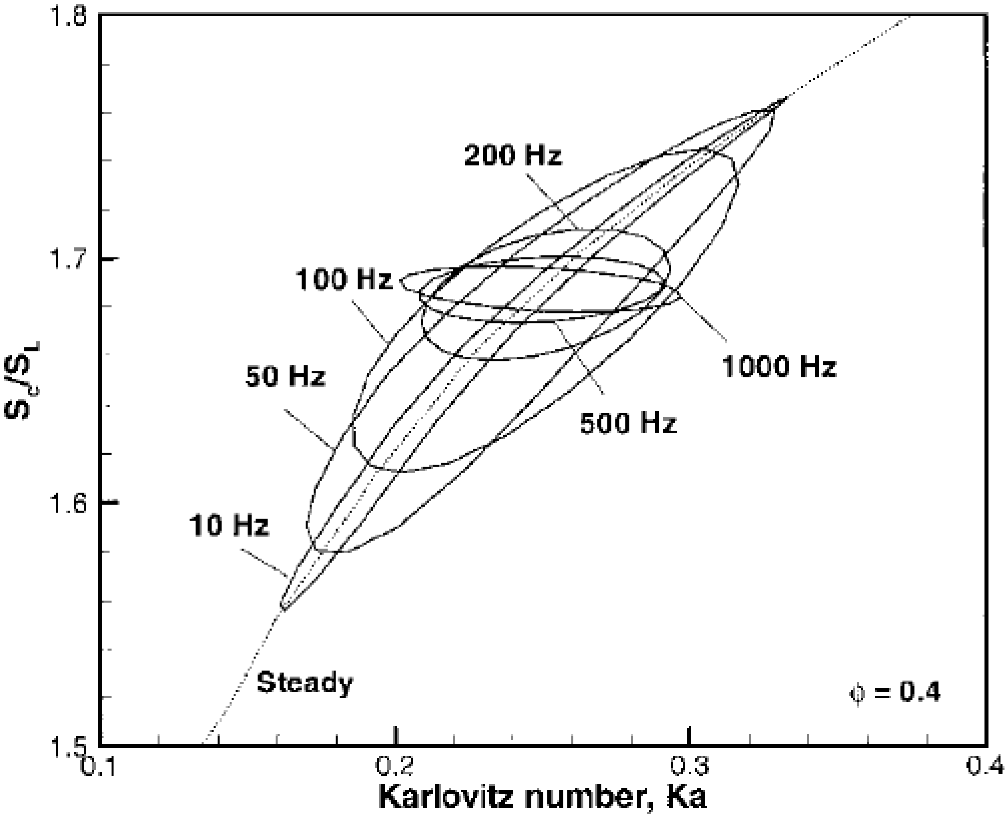

Figure 9: Stretch sensitivity calculations of a premixed $\phi = 0.4$ H_2/air mixture stagnating against burned products for periodic mean flows of various frequencies [31].

Figure 9 plots the results of this calculation. Note that at low frequencies, the flame behaves much like the steady-state case. However, as the frequency of oscillation is increased, the flame's stretch response or Markstein length decreases, due to the inability of the diffusive processes to keep up with the time-varying strain rate. In fact it is evident that at a frequency of 1000 Hz, the flame is essentially insensitive to the stretch rate. This has important implications for turbulent combustion since it raises questions as to which turbulent eddies actually affect the flame front.

In conclusion, the importance of stretch in turbulent premixed flames can be appreciated, particularly in the flamelet regimes, and this has been corroborated by computational [32, 33] and experimental studies [34, 35].This point is expounded further in Sec. 1.4 and will be a major theme of this thesis.

1.3 Flame brush thickness

The turbulent flame brush indicates the spatial region over which the instantaneous turbulent flame fronts are located [12], which can be related to the time averaged heat release distribution normal to the flame, which is an important parameter when designing combustion systems. In addition, like the turbulent flame speed, it is proposed that combustion codes can be assessed by their ability to predict realistic values for δ_{FBT} [12, 36].

Since the flame brush is a time-averaged quantity, the average progress variable distribution through the flame brush can also be extracted, which can serve as an input for turbulent combustion modeling. In Ref. [36], Lipatnikov and Chomiak show that the average progress variable profiles through the flame brush follow a self-similar profile when the distance through the flame brush is normalized by the local flame brush thickness. In other words,

$$\langle c \rangle = \langle c \rangle(\xi) \tag{1.22}$$

where ξ is given by:

$$\xi = \frac{x_{<c>=0.5} - x}{\delta_{FBT}} \tag{1.23}$$

The normalization given in Eq. (1.23) was demonstrated to collapse the average progress variable profiles obtained from various experimental configurations (Bunsen, rod-stabilized), for primarily hydrocarbon-air mixtures, by measuring various scalar quantities such as temperature, species concentrations and density. The collapsed data was seen to follow a complimentary error function profile, as shown in Figure 10.

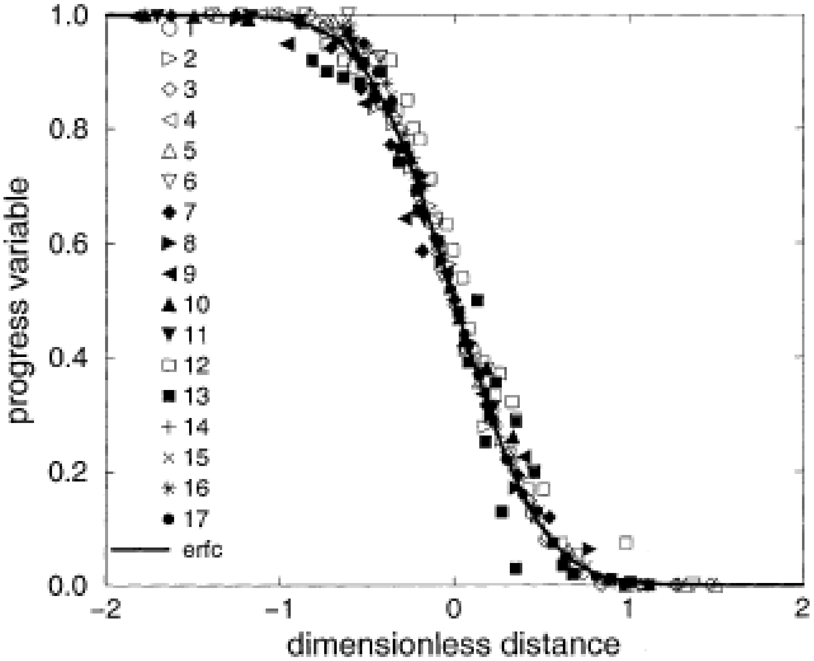

Figure 10: Variation of the average progress variable through the flame brush. The dimensional distance is defined in Eq. (1.23). Figure reproduced from Ref. [36].

It is also proposed in Ref.[36], that the self-similar property of the average progress variable distribution may offer potential to simplify the Favre-averaged progress variable equation, given in Eq.(1.24), to a one-dimensional problem which may be more tractable to analytical treatment.

$$\frac{\partial}{\partial t}\left(\bar{\rho}\tilde{c}\right)+\frac{\partial}{\partial x_j}\left(\bar{\rho}\tilde{u}_j\tilde{c}\right)=-\frac{\partial}{\partial x_j}\left(\overline{\rho u_j'' c'''}\right)+\bar{\rho}\tilde{W} \tag{1.24}$$

A common model for the flame brush thickness is given by Eq. (1.25), which was derived in the limit of large $u'_{rms}/S_{L,0}$, where it can be assumed that flame elements are convected by fluid particles in an isotropic turbulent field [37]. The flame brush thickness is then derived from the dispersion of these fluid particles

$$\delta_{FBT}^2=2u'_{rms}l_L t_F\left\{1-\frac{\tau_L}{t_F}\left[1-\exp\left(-\frac{t_F}{\tau_L}\right)\right]\right\} \tag{1.25}$$

The flame brush thickness is related to the Lagrangian length scale, l_L, and time scale, τ_L and u'_{rms} as well as a flame development time, t_F. In spherically expanding flames, t_F is the time taken for the point of interest to propagate from ignition. In Bunsen flames, t_F is the time taken to convect from the burner exit to the point of interest on the flame brush. Limit expressions for Eq. (1.25) show that for short flame development times, the flame brush thickness is proportional to the flame development time, while for longer development times the flame brush thickness scales as a square root of the development time [38].

$$\delta_{FBT}=\begin{cases} u'_{rms}t_F & t_F \ll \tau_L \\ \sqrt{2u'_{rms}l_L t_F} & t_F \gg \tau_L \end{cases} \tag{1.26}$$

The key point in Eq. (1.25) is that the turbulent flame brush thickness is primarily controlled by large-scale turbulent diffusion processes. Since the flame is treated as a passive scalar in the development of Eq. (1.25), it is not surprising that characteristics of the flame, such as heat release and flame propagation, are not present in Eq. (1.25). However, it is interesting to note that data reported in the literature follow the scaling given by Eq. (1.25) quite well. These data were acquired in fairly simple geometries and it has been suggested that Eq. (1.25) may not hold in more complex flow fields where the inhomogeneity of the turbulence field and factors such as heat release could become more prominent [12].

Similar to the turbulent flame speed, the flame brush thickness is also a definition dependent quantity. For instance, some workers have defined the flame brush thickness to be the distance between two average progress variable contours along the normal to the <c> = 0.5 average progress variable contour [39, 40]. There are other works that have utilized a definition given by Eq. (1.27), which is analogous to the way the laminar flame thickness is often defined [41]. The gradient is calculated along the normal to the local <*c*> = 0.5 contour.

$$\delta_{FBT} = \max\left(\frac{d\left\langle c\right\rangle}{dx}\right)^{-1} \tag{1.27}$$

However, the data compiled in Figure 10 consists of thicknesses calculated using Eq. (1.27) as well as by calculating the distance between the <*c*>= 0.1 and 0.9 surfaces. As a result, it appears that the self-similar profile is obtained regardless of the approach used to calculate the flame brush thickness.

Finally, we note that the flame brush thickness is controlled by two processes; wrinkling of the instantaneous flame front, and flame movement/flapping. Thumuluru noted that the flame brush thickness could increase via both mechanisms as shown in Figure 11 [42].

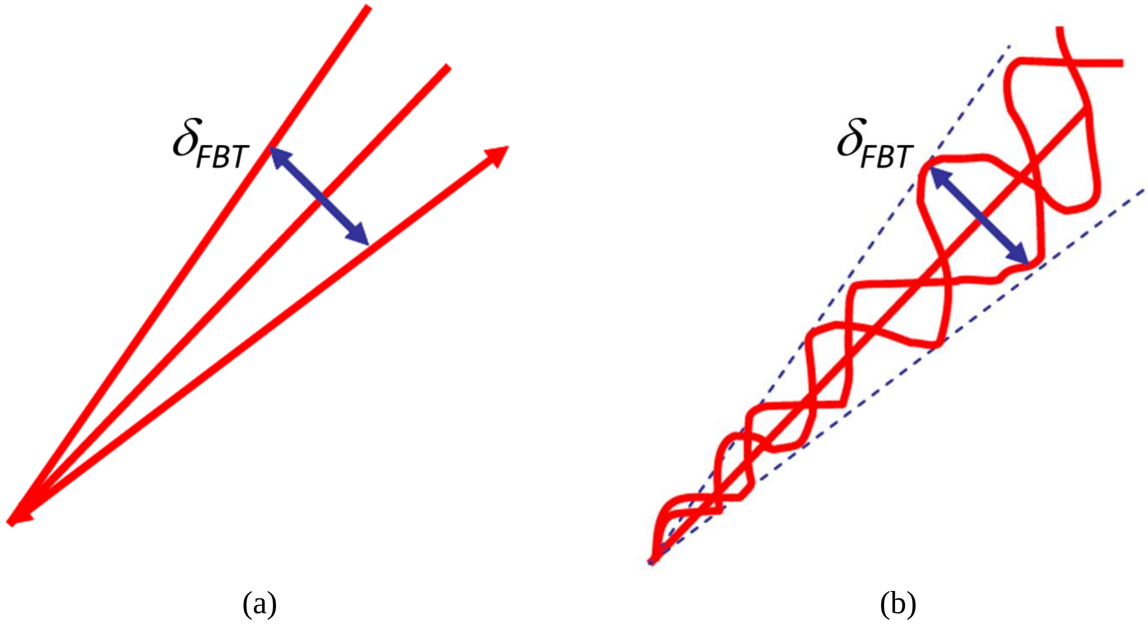

Figure 11: Effect of (a) flame flapping and (b) flame front wrinkling on the turbulent flame brush thickness. Figure adapted from Ref.[42].

1.4 Literature review

The practical significance of the turbulent flame speed has motivated its measurement for many years and the reader is referred to the recent reviews by Lipatnikov and Chomiak [36, 43] and Driscoll [12] for a compilation of the of S_T databases reported in the literature.

As discussed earlier, these reviews reveal that S_T, like the laminar flame speed, S_L, is a function of the fuel composition, equivalence ratio, reactant temperature, and pressure. However, it also has additional dependencies such as the burner geometry and properties of the flow such as the mean flow velocity [44], turbulent length scale [45-47], and turbulence intensity [36]. An example turbulent flame speed data set is shown in Figure 12. This dataset, obtained by Kobayashi *et al.*[48], for a ϕ = 0.9, CH_4/air Bunsen flame at a variety of pressures, exhibits fairly classical features for the turbulent flame speed.

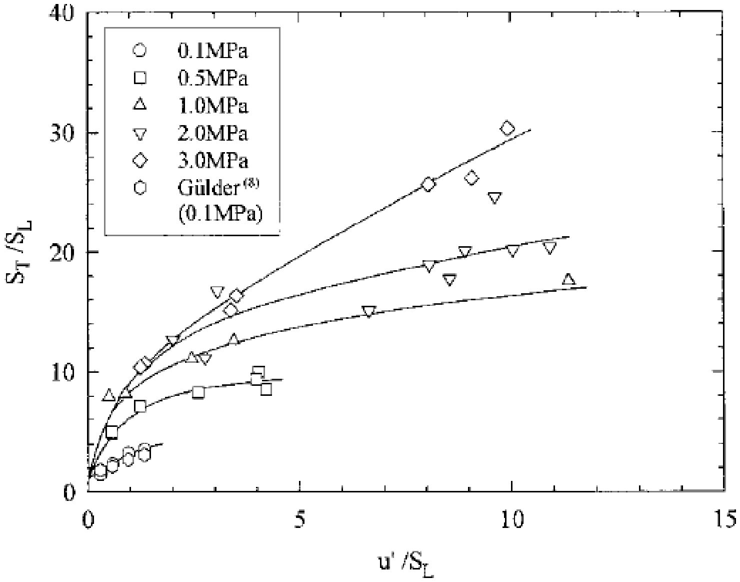

Figure 12: Variation of normalized turbulent consumption speed with the normalized turbulence intensity for a ϕ = 0.9, CH_4/air Bunsen flame [48].

Focusing on a given pressure case, the normalized turbulent flame speed initially increases with the turbulent intensity, until a certain a point where the response starts to saturate. This is termed as the 'bending effect', which has been attributed to the loss of flame area through flamelet merging and quenching [7].

There are numerous data sets that can be found in the literature that exhibit similar features. However, upon inspection, two limitations are evident. Firstly, following the earlier discussion, there are limited S_T data that investigate the influence of fuel composition variability on S_T in the context of H_2/CO mixtures. Secondly, there are even fewer data sets that investigate the influence of pressure on S_T. The remainder of this section provides an overview of the literature pertinent to these two points.

Figure 13 is a set of measurements obtained by Kido *et al*. [34] that clearly illustrate the influence of fuel composition variability.

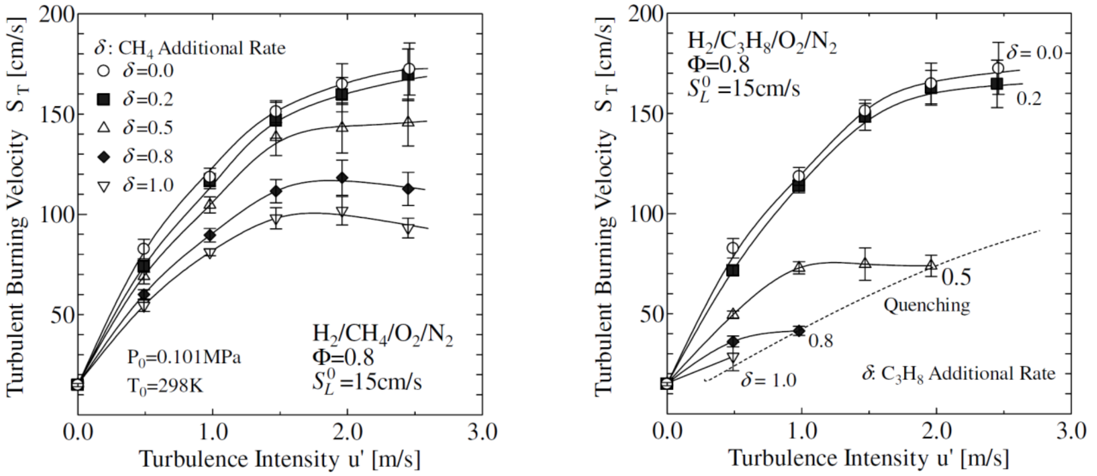

(a) (b)

Figure 13: S_T as a function of the turbulent intensity for a) $CH_4/H_2/O_2/N_2$ and b) $C_3H_8/H_2/O_2/N_2$ mixtures. $S_{L,0}$ was kept constant across the different mixtures by varying the O_2/N_2 ratio [34].

S_T data is shown for H_2/CH_4 and H_2/C_3H_8 mixtures where, by adjusting the dilution and stoichiometries of the different fuel blends, they obtained different mixtures with the same un-stretched laminar flame speed, $S_{L,0}$. Their data clearly show that these mixtures have substantially different turbulent flame speeds, with the high H_2 mixtures having an order of magnitude larger S_T value than the propane mixture. Thus, two different fuel mixtures can have appreciably different turbulent flame speeds, despite having the same un-stretched laminar flame speed, turbulence intensity and burner configuration.

These fuels effects are believed to be associated with the stretch sensitivity of the reactant mixture which leads to significant variation in the flame speed along the turbulent flame front. In particular, the high mass diffusivity of H_2 makes the flame front particularly susceptible to stretch.

However, since these stretch effects are molecular diffusion processes, there has been some speculation as to whether these effects will persist at higher turbulent intensities, where turbulent diffusion can dominate. Other authors conjectured that at these higher turbulence intensities, the primary mechanism through which the turbulent flame speed increased with turbulence intensity was through flame area increase [17, 49]. However, if at high turbulent intensities the instantaneous flame front retains the laminar flamelet structure, which is critically dependent on molecular diffusion processes, then there is good reason to believe that these stretch effects will exert non-negligible effects [8].

However, as discussed earlier, limited data are available for H_2/CO fuel mixtures; a few examples are from Daniele *et al.*[50] and Karpov and Severin [51]. Second, much of the turbulent flame speed data where strong stretch effects may be present have been obtained at turbulence intensities, $u'_{rms}/S_{L,0}$, often less than 20 [35, 52-56]. Obtaining such data at high turbulence intensities is of fundamental interest to explore the relative roles and interactions between turbulent stretching of the flame front and its stretch sensitivity, in particular whether stretch effects change with turbulence intensity. The above studies suggest that fuel effects persist at higher turbulence intensities, but further data are needed to validate this point.

The second area of interest in this work is to investigate the influence of pressure on the turbulent flame speed particularly in the context of these fuel effects There are limited data of this kind in the literature and the results are not well understood as reported influences of pressure on the flame speeds are not in agreement [36]. Kobayashi *et al.*[48] reported turbulent consumption speed measurements of $\phi = 0.9$ CH_4/air mixtures and showed that $s_{T,GC}/s_{L,0}$ increased with pressure due to decreases in $S_{L,0}$, but that $S_{T,GC}$ itself was independent of pressure. Kitagawa *et al.*[52] reported similar measurements on turbulent flame speeds of H_2/air mixtures at pressures from 1-5 atm; i.e., that $s_T/s_{L,0}$ was primarily sensitive to pressure through influences on $S_{L,0}$. However, the influence on S_T is unclear. Daniele *et al.*[50] reported $S_{T,GC}$ measurements of H_2/CO mixtures for pressures of 1-20 atm at 623 K. They found that $s_{T,GC}/s_{L,0}$ increased with pressure at each given H_2/CO ratio and $u'_{rms}/s_{L,0}$ value.

There are very few reduced-order models that capture the essential physics that govern the turbulent flame propagation, which is partly due to the difficulties associated with defining the turbulent flame speed. As a result most formulas for the turbulent flame speed are empirical fits where the turbulent flame is a function of the un-stretched laminar flame speed and other typical turbulence quantities such as the turbulence intensity, and the turbulent length scale. Empirical relations involving the product of the Karlovitz number and the Lewis number to capture stretch effects were also investigated by Bradley [57] for a dataset of over a 1000 measurements. However, these data sets were obtained on a variety of different experimental configurations, and the flame speeds were not quantified in a consistent manner. As a result, there was no real reason to expect all the data to correlate very well. More recently, Dinkelacker *et al.*[58] modeled the average reaction rate term rate arising in the averaged progress variable equation by relating it to the local flame area ratio, which, from Eq. (1.5), the ratio of the local turbulent consumption speed to the laminar burning velocity. The area ratio was modeled using traditional turbulence quantities and an effective Lewis number to account for the varying mass diffusivities of the reactant mixture of CH_4 and H_2. Kido *et al.*[34] suggested that the turbulent flame speed in negative Markstein length fuel blends may be controlled by positively curved points where the local burning velocities are enhanced by preferential diffusion effects. They then attempted to correlate the turbulent flame speeds across different fuels by utilizing mixtures properties at an adjusted equivalence ratio, equal to the actual value plus some $\Delta\phi$, where $\Delta\phi$ presumably accounts for the average modification of the stoichiometry at the positively curved points due to differential diffusion of fuel and oxidizer. This model bears similarities to the concept of leading points, which are loosely defined as positively curved points on the turbulent flame front that propagate out furthest into the reactants in spatial regions where turbulent eddies induce low approach flow velocities. It has been hypothesized that the dynamics of these leading points control the overall turbulent flame propagation [43]. These leading points concepts are discussed further in Chapter 4 and form the basis of the scaling law developed to correlate the turbulent flame speed data.

The final part of this work will analyze the sensitivities of the turbulent flame brush thickness to pressure and fuel composition. Much of the work summarized in Ref. [36] has focused primarily on the self-similar nature of the progress variable distribution through the flame brush and the evolution of the flame brush thickness with the downstream distance. Furthermore, most of the data have been obtained in V-shaped flame configurations [36, 59]. Studies that have investigated the influence of fuel composition are very limited with the conclusion that the flame brush thickness is largely unaffected by the fuel composition, although the fuel compositions considered have been mainly hydrocarbon/air mixtures [36]. However, we are not aware of any studies that systematically analyze the influence of pressure and mixture composition on the flame brush thickness.

1.5 Scope and organization of thesis

To summarize the previous section, it is quite apparent that although the turbulent flame speed has been a subject of study for many years, there are still a number of unresolved issues. Firstly, there are limited studies that measure the turbulence flame speeds of H_2/CO mixtures and assess the importance of the previously mentioned fuel effects for these mixtures particularly at high turbulence intensities. Second, there are even fewer studies that investigate these issues at elevated pressure conditions. Third, there is a need for a robust reduced-order model for the turbulent flame speed that looks to capture these key physics using a first-principles approach. Finally, the sensitivities of the flame brush thickness to pressure and fuel composition is not well characterized. This thesis seeks to answer some of these questions and work is organized as follows.

Chapter 2 gives a detailed description of the experimental facility along with results of the velocity characterization studies performed to quantify the turbulent flow field. Chapter 3 outlines all the $S_{T,GC}$ measurements made throughout the course of this work. The chapter also has a compilation of other turbulent flame speed data of interest found in the literature. Chapter 4 discusses the development of the leading points scaling law and its application to correlate turbulent flame speed data obtained in this work as well those found in the literature. The chapter also includes an in-depth discussion of the stretch sensitivity calculations that provide the key inputs into the scaling law. Chapter 5 focuses on the experimental characterization of the flame brush thickness. The chapter includes a detailed description by which the flame brush thicknesses are determined from the flame images. The chapter then discusses the various sensitivities of the flame brush thickness. The chapter concludes with some comparisons to models for the flame brush thickness and a discussion of the self-similar nature of the progress variable distribution through the flame brush. Finally, Chapter 6 summarizes the main findings from this work, and provides a list of recommendations for future work.

Chapter 2
Experimental Methods

2.1 Experimental facility

This thesis focuses on measurements of $S_{T,GC}$ using a turbulent Bunsen flame, an $S_{T,GC}$ measurement approach recommended by Gouldin and Cheng [16]. This configuration was used because of the wide variety of available data in similar geometries for benchmarking and comparisons, such as the extensive data sets from Kobayashi's group [48, 60-62].

A schematic of the system is shown in Figure 14. The burner is a smoothly contoured nozzle with high contraction ratio to inhibit boundary layer growth and to achieve a top hat exit velocity profile. Measurements were taken using burners with 12 and 20 mm exit diameters. An annular sintered plate is placed around the burner outlet to hold a premixed, methane-air pilot flame, needed to stabilize the main flame at the higher flow velocities used in this study. The total mass flow rate of the pilot does not exceed 5% of the main flow rate to ensure minimal impact of the pilot on the main flame.

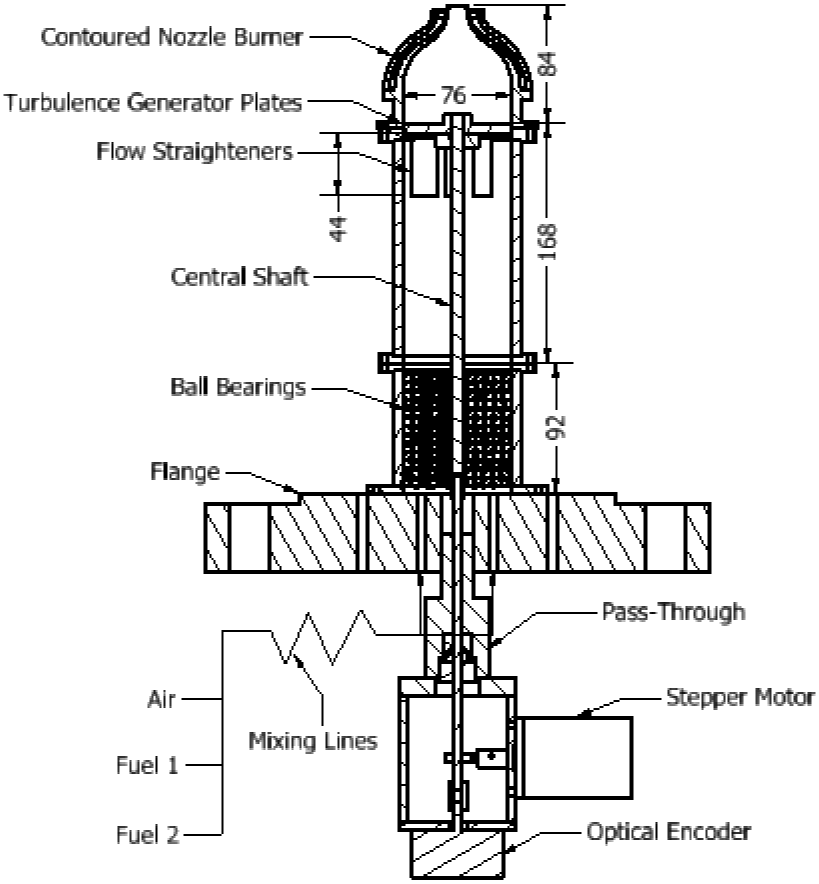

Figure 14: Schematic of the burner facility. Dimensions in mm.

The results of experiments conducted to verify the minimal influence of the pilot flame on $S_{T,GC}$ are shown in Figure 15. Experiments were carried out for two H_2/CO fuel mixtures of 50/50 and 70/30 at equivalence ratios of 0.68 and 0.63 respectively at a mean flow velocity of 50 m/s. The pilot flow composition was held fixed at $\phi = 0.9$ for a CH_4/air mixture, and experiments were carried out at 5 atm and 300 K reactant and pilot temperatures. The parameter, χ, is the ratio of the total pilot flow to the total main flow given by Eq. (2.1). Details on how $S_{T,GC}$ is calculated is described in Chapter 3.

$$\chi = \frac{\dot{m}_{pilot}}{\dot{m}_{main}} \tag{2.1}$$

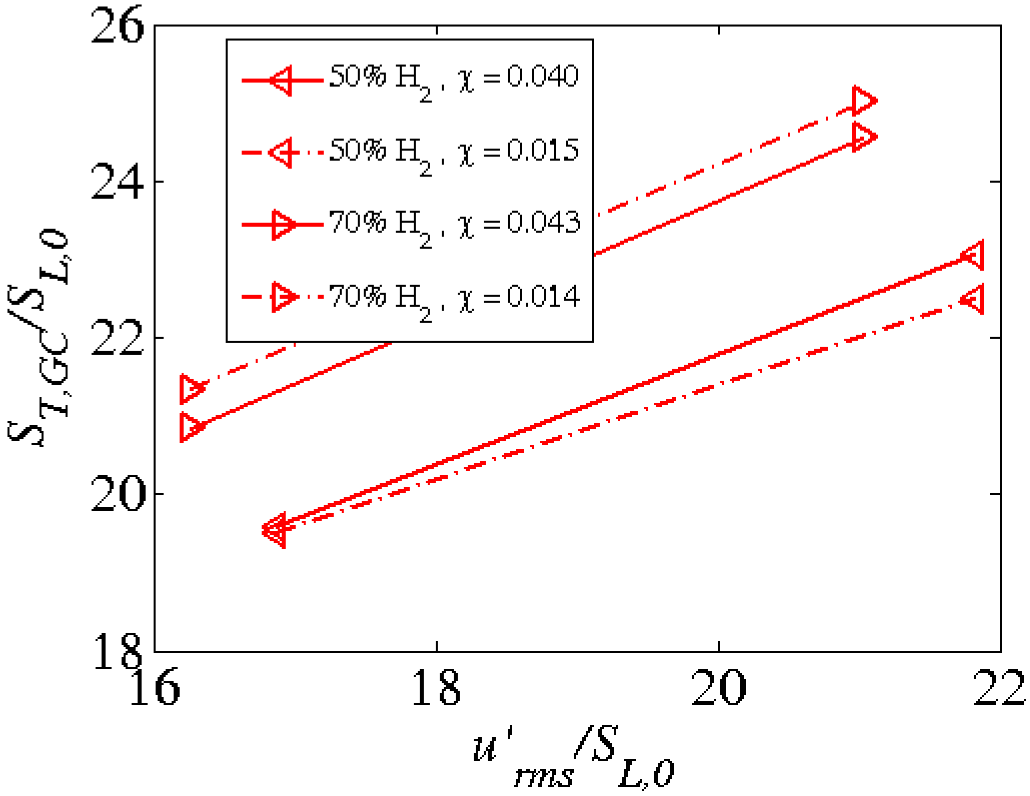

Figure 15: Influence of the pilot flow rate on $S_{T,GC}$ for two H_2/CO ratios at mean flow velocity, reactant and pilot flow temperatures and pressure of 50 m/s, 300 K and 5 atm respectively.

From Figure 15 $S_{T,GC}$ is observed to change by about 2.5% when χ is increased from about 1.5% to 4%, while the experimental uncertainty in the $S_{T,GC}$ at these conditions is about 0.40 %, as shown in Appendix A. Although this suggests that the pilot flow rate has some influence on the turbulent flame speed, the dependence is still very weak. During all experiments, pilot mass flow rates were generally maintained below 1.5% of the main flow rate.

The fuels for the main flame and the gases for the pilot flame are supplied from tanks. Their flows are metered using sonic orifices and controlled by varying the upstream gas pressure using air-loaded pressure regulators. The downstream pressure of the air-loaded pressure regulators is controlled using ER-3000 pressure controllers. Calibration of the sonic orifices was performed using a Ritter drum-meter calibrator with an accuracy of ± 0.2%.

The airflow for the main flame is delivered from blow down tanks that store compressed air from the main facility compressors. The main airflow rate is metered using sub-critical orifices by measuring the upstream pressure and temperature and the differential pressure across the orifice. The airflow is then choked before being mixed with the fuel 2 m ahead of the burner. Upon entering the main burner assembly, the flow passes through a layer of ball bearings to minimize “jetting” effects from the smaller diameter reactant feed lines. The flow system is depicted in Figure 16.

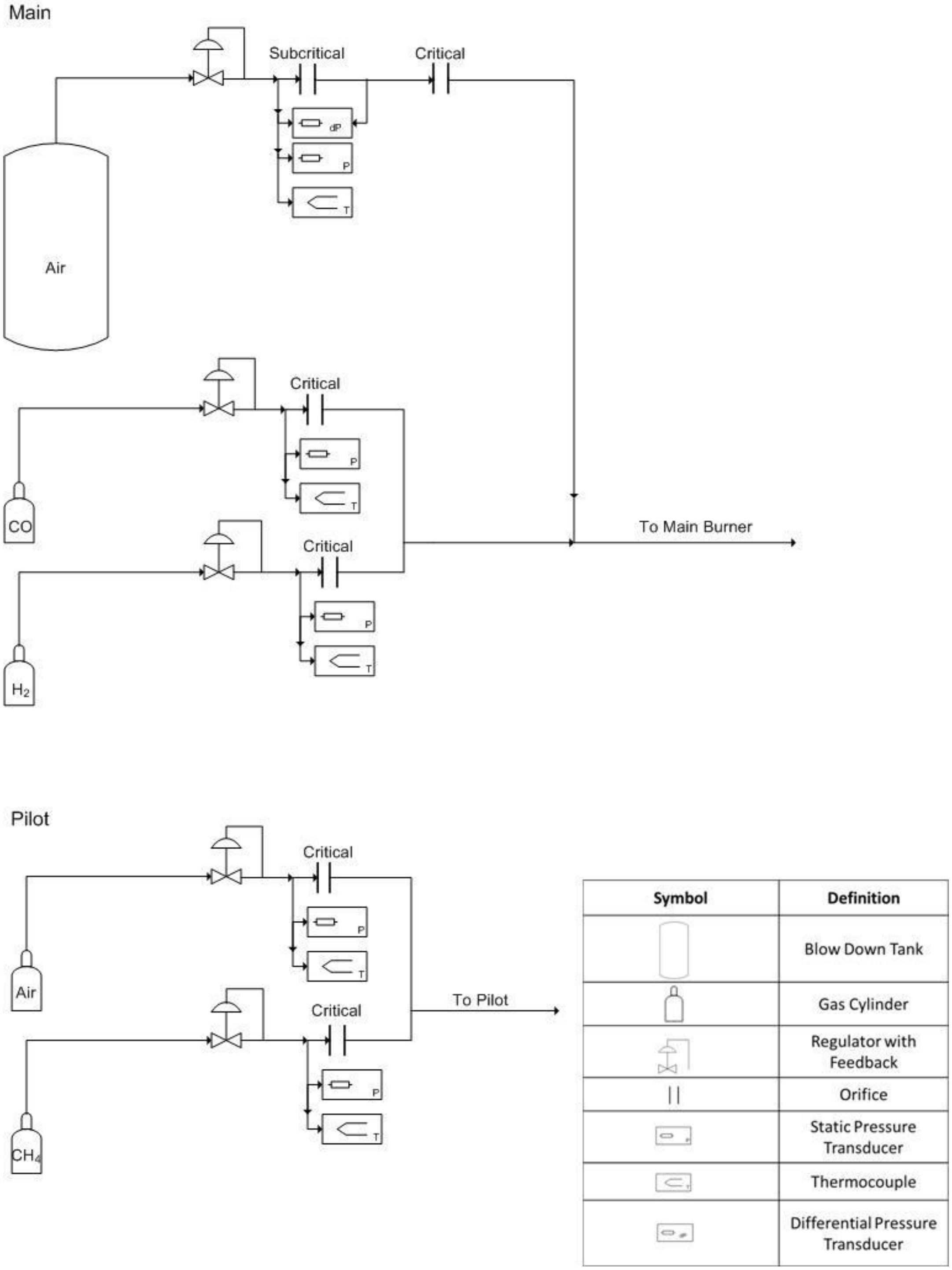

Figure 16: Flow diagrams for the main and pilot flows.

The flow then passes through the turbulence generator plates, shown in Figure 17. The turbulence generating plates are secured 84 mm upstream of the burner exit, as shown in Figure 14. Both plates have an identical annular slot pattern milled in them so the turbulence intensity can be varied by rotating the top plate, resulting in a change in the blockage ratio, depicted in Figure 17. This design is motivated by the systems developed by Videto and Santavicca [63] and Bédat and Cheng [64]. The main flow passes through these slots, generating vortical structures that then impinge on the inclined wall of the converging section of the nozzle, breaking down into finer scale turbulence.

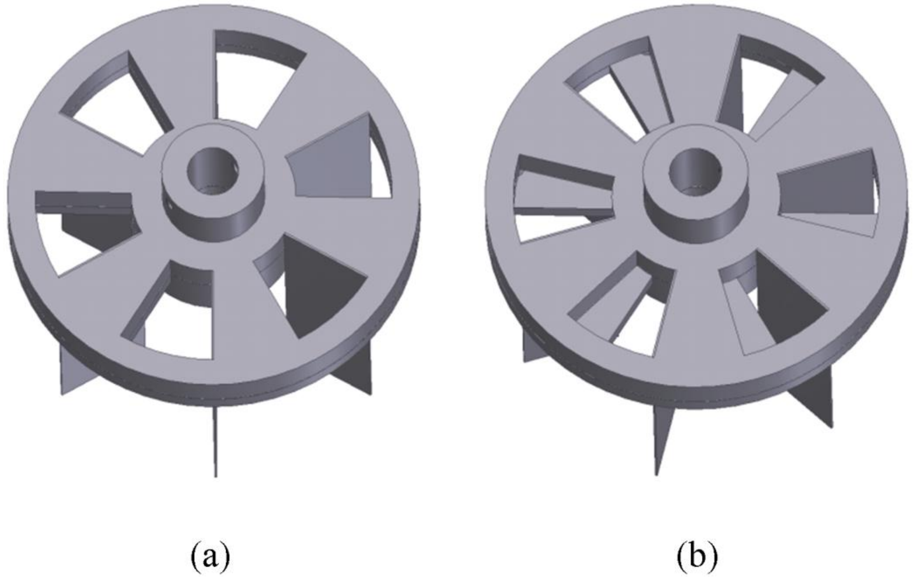

Figure 17: Schematic of the turbulence generating plate at the (a) fully open and (b) partially closed configuration.

At very high blockage ratios, the mixture passes through the slots at an angle, leading to swirl in the flow, as shown in Figure 18(a). This effect was reduced somewhat by the addition of straighteners shown in Figure 18(b). We used the criterion that the swirl velocity remains less than 20% of the mean axial flow velocity, which limited the maximum usable blockage ratio to 93% for all flame speed experiments.

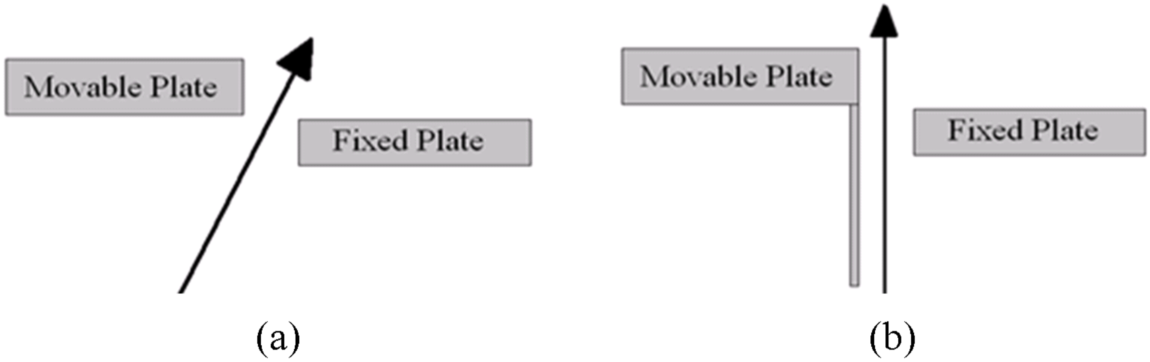

Figure 18: Flow characteristics (a) without and (b) with flow straighteners.

After passing through the turbulence generator plates, the flow impinges on the walls of the contoured nozzle. This is an important design element, as nozzles with too large of a diameter, or blockage plates with too small a diameter of the open area, allow the large scale structure generated at the blockage plate to exit the nozzle without impinging upon the walls of the contoured nozzle. Since we are aiming to achieve homogeneous turbulence with no narrowband spectral features, this is undesirable. As such, the inner diameter of the radial slots was set to 30 mm, 1.5 times larger than our largest nozzle diameter. Measurements and characterization studies were conducted under isothermal flow conditions with burner diameters of 12 and 20 mm to achieve different ranges of length scales and assess their influence on the turbulent flame properties. Details of these studies are outlined in the following section.

The turbulence generator is a unique aspect of this experimental facility and substantial effort was invested to meet key goals that were derived from shortcomings of turbulence generators used in other studies. The criteria set forth in designing the turbulence generator were to (1) have the ability to vary the turbulence intensity without changing out plates or changing mean flow velocity, (2) access a wide range of turbulence intensities, (3) have uniform exit mean and turbulent quantities, (4) be able to operate at high air temperatures and pressures, (5) be remotely operable, and (6) have very thin boundary layers to prevent flashback of high flame speed fuels, such as high H_2 mixtures. The need for remote operability and continuously variable turbulence intensity was motivated by the need to access a range of turbulence intensities in high pressure situations without having to shut down and cool the experiment to replace blockage plates. Furthermore, due to the influence of the mean flow velocity on the turbulent flame speed, we wanted the ability to change the turbulence intensity independently of the mean flow velocity.

The turbulence generator system consists of a 3 mm thick bottom plate that is secured to the plenum and a 6 mm thick top plate attached to a central shaft, as shown in Figure 14. This central shaft passes through the flange as shown in Figure 14. A significant amount of work was put into the design of the pass-through assembly in order to ensure that the system would not leak at high pressures. The system was designed so that increased chamber pressure would induce a force imbalance on the pass-through components (hemispherical nut and outer seal), thereby effectively enhancing their ability to seal. This pass-through has been leak tested at pressures up to 10 atm. Outside the flange, the central shaft is coupled to a DC stepper motor through a 50:1 worm and worm gear. This system has been tested to successfully rotate the turbulence plates at inlet temperatures up to 600 K and pressures up to 20 atm. In addition, the worm and worm gear were chosen for the low amount of backlash inherent in their design. The plate's angular position is measured with an optical encoder, attached to the other end of the central shaft, to an accuracy of ±0.1° [65]. The range of blockage ratios possible with this setup is 69-97%, corresponding to angular slot openings from 30°-2°. The 30° angular slot opening corresponds to the fully open position, where the two plates are aligned. It will be shown later that the turbulence intensity increases monotonically with increasing blockage ratio.

The burner is placed inside a pressure vessel with four orthogonal quartz windows each providing viewing areas of 7" x 2" as shown in Figure 19. During high-pressure experiments, only two quartz windows are used while the other windows are replaced by high-carbon steel blanks, one of which is used to pass through the ignition system. The ignition system consists of a 1/4" diameter stainless steel tube and a 1/8" diameter copper rod that run parallel to each other 2.5" apart into the pressure vessel through the window blank. The stainless steel tube is connected to a hydrogen tank with two inline 'normally-closed' solenoid valves, while the copper rod is connected to a high-voltage transformer. The solenoid valves and the transformer are on the same circuit operated by a switch. When the switch is activated, a spark is generated between the copper rod and stainless steel tube, igniting the flowing hydrogen, which subsequently ignites the pilot flame.

A cold co-flow, which is choked upstream of the pressure vessel, enters the vessel through two ports at the bottom. The co-flow serves to keep the walls of the pressure vessel cool as well as to pressurize the vessel. Like the main burner flow, the co-flow also passes through a layer of ball bearings to minimize "jetting" effects from the smaller diameter feed lines. The chamber pressure is then varied by opening and closing a remotely operable exhaust valve.

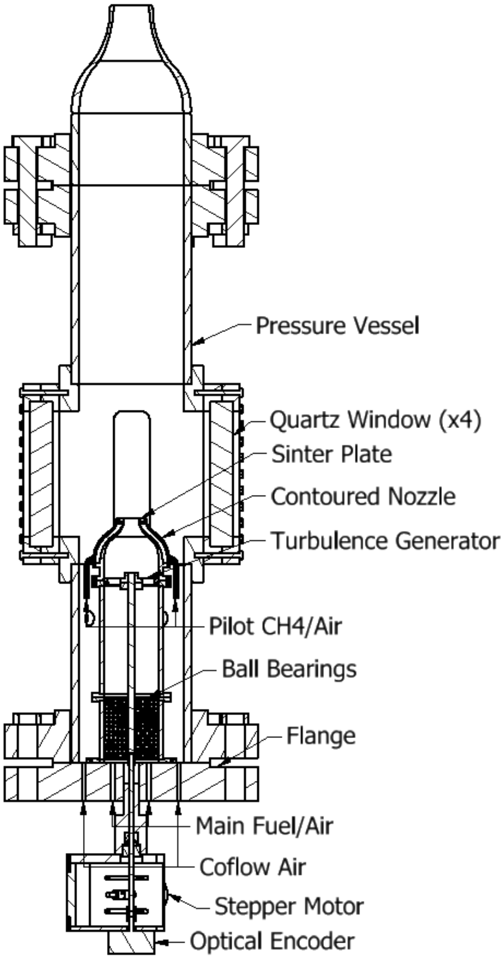

Figure 19: Schematic of high pressure facility.

2.2 Flow field characterization

This section gives an overview of the velocity characterization studies that were conducted. Complete details may be found in Ref. [65].

The flow-field was characterized using 3-component Laser Doppler Velocimetry (LDV). The air flow was seeded using 5 µm alumina (Al_2O_3) particles and the flow field velocity at the burner exit was mapped using a TSI 3-component LDV system mounted on a computer-controlled, three-axis traverse to enable axial and radial scanning across the burner exit along three orthogonal directions. The LDV system comprised of a 5 W argon ion laser with an FBL-3 multicolor beam generator. Two fiber optic transceiver probes were mounted 90º apart and operated in backward-scatter mode. The signal from the transceiver probe was connected to a PDM 1000-3 three-channel photodetector module and the output was processed by an FSA 3500-3 signal processor to record three components of velocity in non-coincidence mode. The typical number of realizations used to generate the quoted velocity statistics we about 10,000 counts on the axial channel and over 1000 on the radial and azimuthal channels.

Velocity characterization studies were done under cold-flow conditions for both burners of 12 and 20 mm diameters. The seeding was achieved by having a separate flow of air, supplied by bottles and metered using the critical orifice configuration described earlier, pass through a seeder before being connected into the main airflow line just upstream of the burner.

Figure 20 provides a bird's eye view of how the two transceiver probes, arranged at right angles, are positioned relative to the burner exit of the 12 mm diameter burner. Also indicated are the co-ordinate system and the locations at which measurements were made. Measurements were made along two lines indicated by 'Traverse 1' and 'Traverse 2' that were aligned with the Y-axis and the X-axis to check verify that the velocity fields were axisymmetric. As an additional check, attempts were also made to align 'Traverse X' and 'Traverse Y' over the top of an open and closed portion of the turbulence generator respectively. The measurements were taken 2 mm above the burner exit to ensure that the burner did not interfere with the laser beam path.

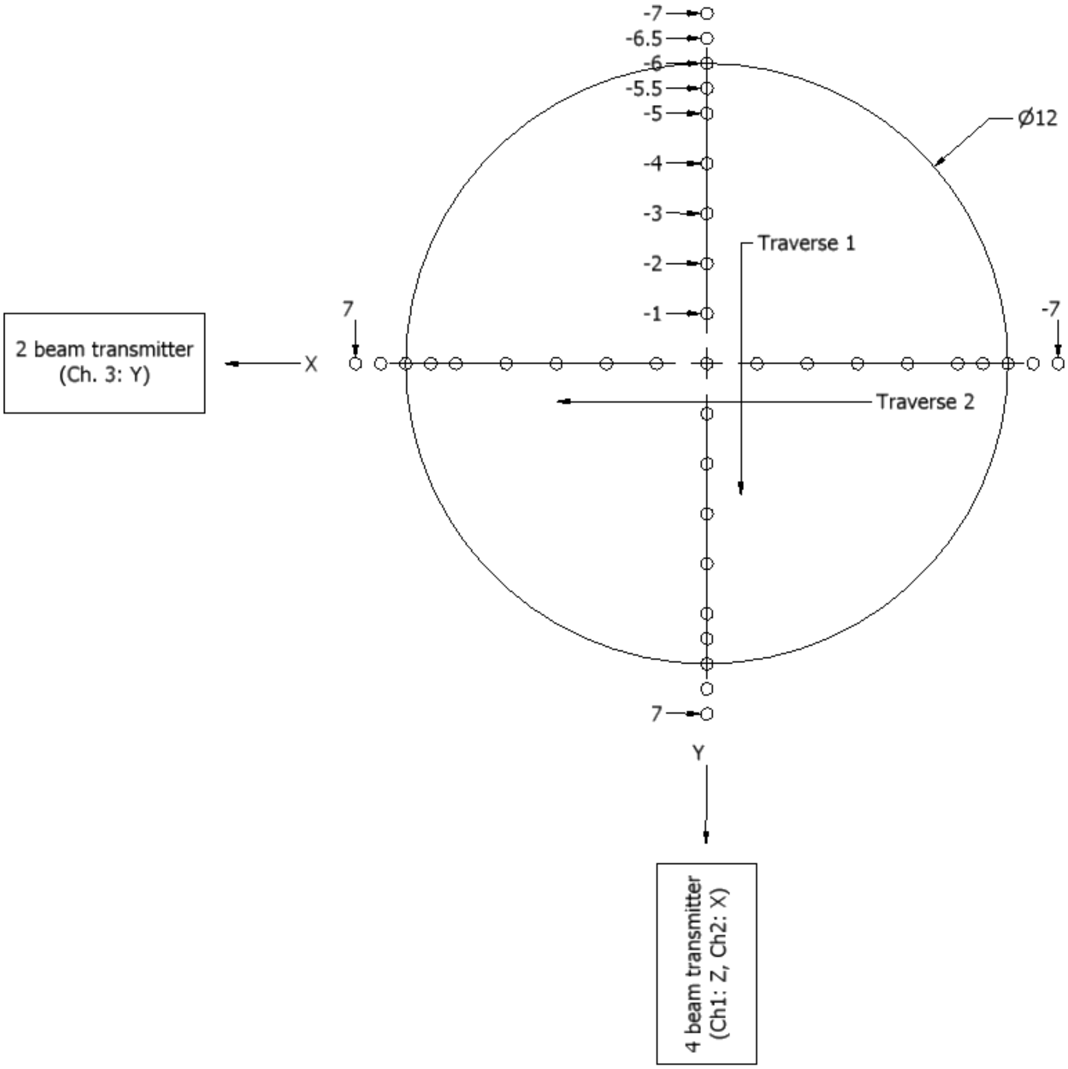

Figure 20: Birds'eye view of the setup used to perform the velocity characterization studies along with the locations of where velocity measurements were made.

The studies were done for the 12 and 20 mm diameter burners over a wide range of mean flow velocities, pressures and temperatures ranging from 4-50 m/s, 1–20 atm, and 300–525 K respectively. This corresponds to a bulk Reynolds number (

$\mathrm{Re}_B = U_0 D / \upsilon$) range of 5040 - 253,000 and by varying the blockage ratios, a turbulent Reynolds number ($\mathrm{Re}_t = u'_{rms} l / \upsilon$) range of about 213-8200 was also obtained. The turbulence intensities quoted below, u'_{rms} , are based upon the total turbulence intensity using all three velocity components; i.e., $u'_{rms} = \sqrt{\overline{u'^2} + \overline{v'^2} + \overline{w'^2}}$. As such, some care should be taken when comparing with other data in the literature, such as when measurements are obtained with hot wire anemometers that capture two velocity components.

Figure 21 through Figure 23 plot representative profiles of the mean and fluctuating axial, radial and azimuthal velocities as a function of the radial location. The data presented are for the 20 mm diameter burner for a mean flow velocity of 50 m/s at STP (300 K and 1 atm) at three different blockage ratios.

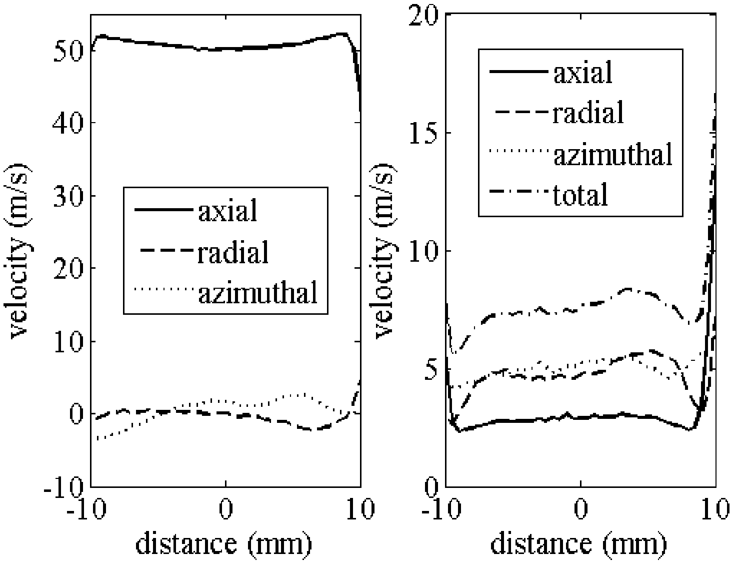

(a) (b)

Figure 21: Plots of (a) mean axial, radial and azimuthal velocities and (b) fluctuating axial, radial, and azimuthal and total fluctuating velocities as a function of radial distance from the center of the burner for U_0 = 50 m/s at a blockage ratio of 69%.

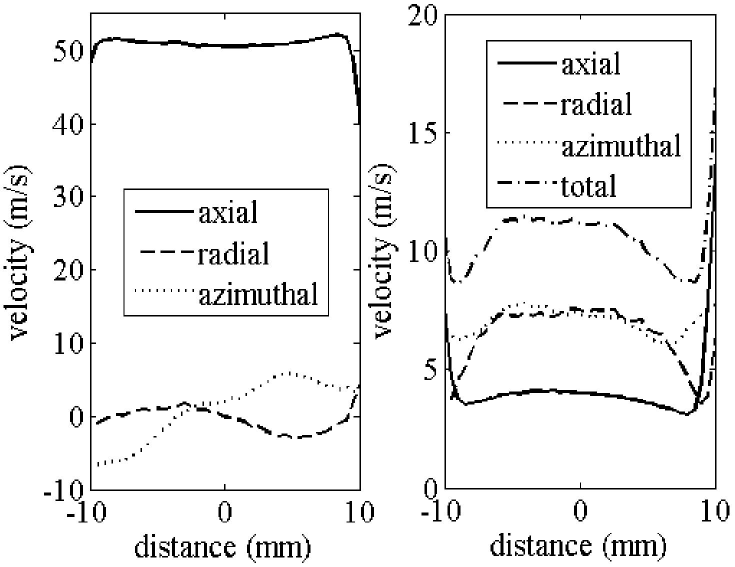

(a) (b)

Figure 22: Plots of (a) mean axial, radial and azimuthal velocities and (b) fluctuating axial, radial, and azimuthal and total fluctuating velocities as a function of radial distance from the center of the burner for U_0 = 50 m/s at a blockage ratio of 81%.

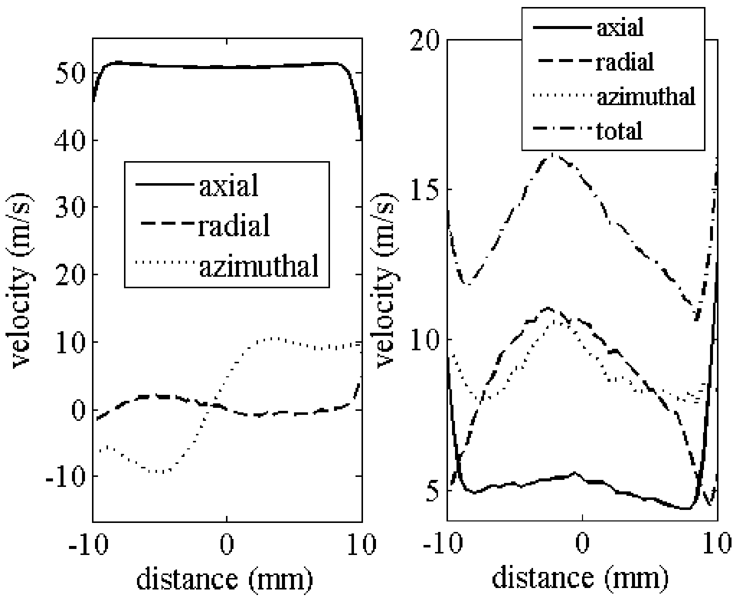

(a) (b)

Figure 23: Plots of (a) mean axial, radial and azimuthal velocities and (b) fluctuating axial, radial, and azimuthal and total fluctuating velocities as a function of radial distance from the center of the burner for U_0 = 50 m/s at a blockage ratio of 93%.

The data show a well-defined top-hat mean axial velocity, along with low radial velocity. The mean azimuthal velocity increases with increasing blockage ratio, as discussed earlier. It should be noted that the time averaged mean and fluctuating velocity profiles are flat, except in the boundary layer, and that as the blockage ratio is increased from 69% in Figure 21 to 93% in Figure 23 the turbulence intensity monotonically increases.

These figures also show that the turbulent fluctuations in the axial direction, ~3-5 m/s, are about half of the fluctuations in the transverse directions, ~6-12 m/s. This is due to the well understood phenomenon of turbulent flow dynamics through a contraction [66, 67]. Essentially, the vortex tubes that are aligned with the main axis of the burner are elongated as the flow accelerates through the contraction, increasing their vorticity and increasing the transverse velocity fluctuations (v', w'). In addition, the vortex tubes aligned perpendicular to the main axis are contracted, reducing their vorticity and decreasing the axial velocity fluctuations (u'). This is different from the results reported by Videto and Santavicca [63], who reported nearly isotropic turbulence. It is common to use a contraction after a turbulence generator (i.e. grid, perforated plate, etc.) to improve the isotropy of the turbulence [68], because the resulting flow turbulence is strongest in the axial direction. The contraction causes vortex stretching which equilibrates the three components. However, this is generally a weak contraction; an area contraction ratio of 1.27 and 2.6 were used in the studies of Comte-Bellot [68] and Videto and Santavicca [63], respectively. Our area contraction ratios are 40 and 14 for nozzle diameters of 12 and 20 mm, respectively. These high area contraction ratios produce radially uniform velocity profiles as shown above, as well as flashback-resistant burners, but also lead to this anisotropy in turbulence intensity.

Figure 24 and Figure 25 summarize the performance of the turbulence generator, by plotting the dependence of the centerline turbulence intensity, u'_{rms}/U_0, upon blockage ratio for the 12 mm and 20 mm diameter burners respectively over a wide range of operating conditions. For both burners the turbulence intensity monotonically increases with blockage ratio. Turbulence intensities obtained with the 12 mm burner are lower than that obtained with the 20 mm burner at the same blockage ratio. This occurs because, at a fixed nozzle exit velocity, the flow velocity through the blockage plate gaps is lower for the smaller burner.

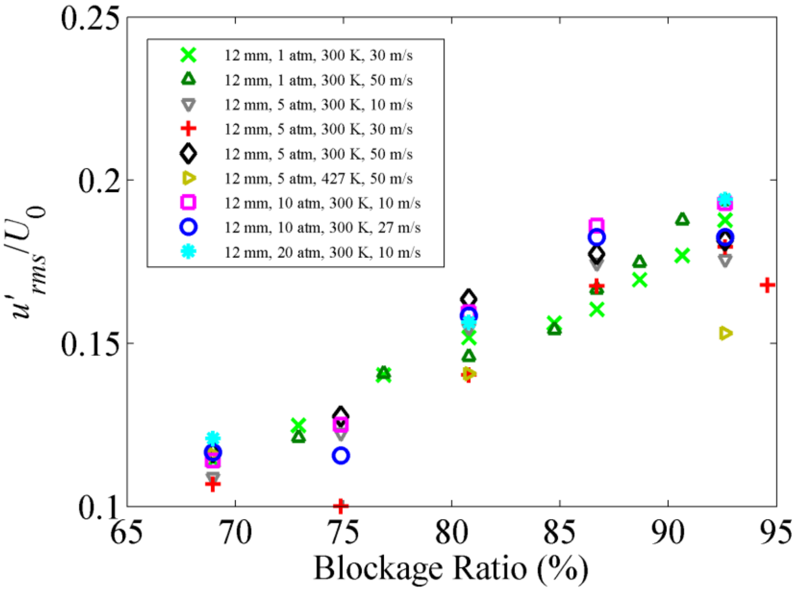

Figure 24: Dependence of burner centerline total turbulence intensity (i.e. summed over all 3 fluctuating velocity components) upon blockage ratio for the 12 mm diameter burner for the conditions shown.

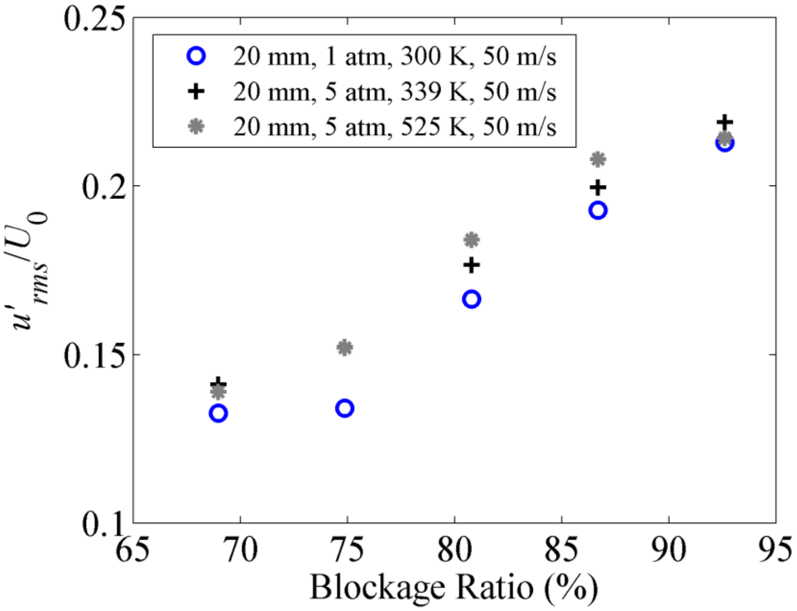

Figure 25: Dependence of burner centerline total turbulence intensity (i.e. summed over all 3 fluctuating velocity components) upon blockage ratio for the 20 mm diameter burner for the conditions shown.

An important question for configurations such as used here, where the turbulence intensity varies radially and axially, and where there is strong shear generated turbulence, is the appropriate turbulence intensity that should be used to characterize u'_{rms}. While we do not weigh in on this question here, we do note that the centerline turbulence intensity scales well with that at other locations. To illustrate, Figure 26 presents a comparison between the shear (or, more precisely, u'_{rms} at r = 10 mm) and centerline turbulence intensities for the 20 mm burner at STP. Note the one-to-one correspondence between the two, with u'_{rms} (r = 10 mm) = 0.87 u'_{rms} (r = 0 mm) + 6.9U_0.

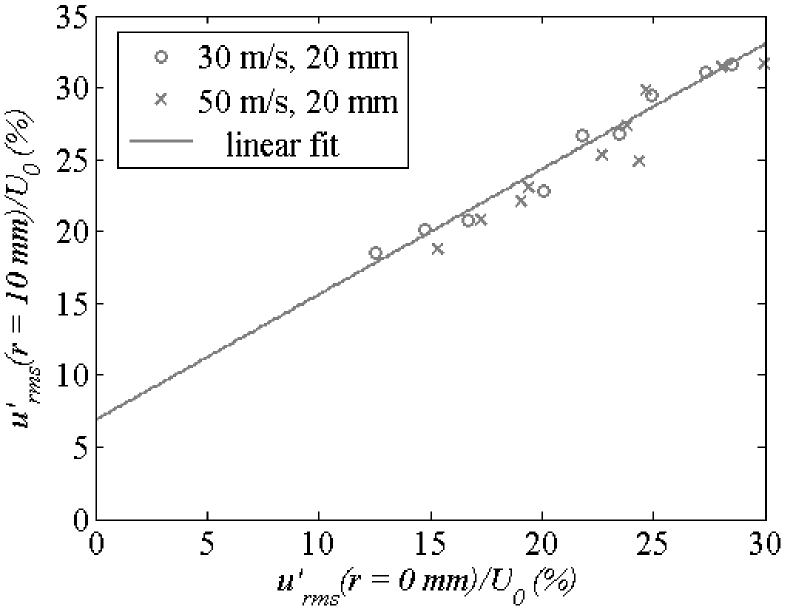

Figure 26: Comparison of turbulence intensity in the shear layer to turbulence intensity along the nozzle centerline.

Integral time scales, t_{int}, were determined from autocorrelations of the centerline LDV velocity data. Complete details of the algorithms used to extract the autocorrelations from the unevenly sampled LDV data can be found in Ref. [65]. The integral time scale was calculated from the autocorrelation using the relationship [37]:

$$\tau_{\text{int}} = \int_0^\infty \rho(\tau)\, d\tau \tag{2.2}$$

where τ is the time delay. Because of the high uncertainties associated with the autocorrelation at large time lags (because of its low value), an exponential expression of the form $\rho(\tau) = ae^{-b\tau} + (1-a)e^{-c\tau}$ was fit to the autocorrelation function and used to evaluate this integral, so that t_{int} is given by Eq.(2.3),

$$\tau_{\text{int}} = \frac{a}{b} + \frac{1-a}{c} \tag{2.3}$$

These integral time scales were converted to integral length scales, l_{int}, using the relation $l_{\text{int}} = U_0 \tau_{\text{int}}$, as per Taylors' hypothesis [37]. Figure 27 summarizes the calculated l_{int}/D values at mean flow velocities of 4, 30, and 50 m/s at various blockage ratios for the 20 mm diameter burner at STP. The data indicate that l_{int}/D is nearly constant at 30 and 50 m/s, and changes slightly with blockage ratio. These data show that turbulence length scales are not varying with blockage gap width and therefore, that the associated variations in turbulence intensity are at essentially constant integral length scale. The t_{int} values in the 4 m/s case are substantially higher in value and do indicate a somewhat higher sensitivity to blockage ratio. It is assumed that this reflects a different characteristic of the turbulence generator system at the much lower Reynolds numbers these data were obtained.

These calculations were performed for the velocity measurements obtained at STP. Integral length scales were assumed to be invariant with pressure since the large scales typically scale with the dimensions of the configuration.

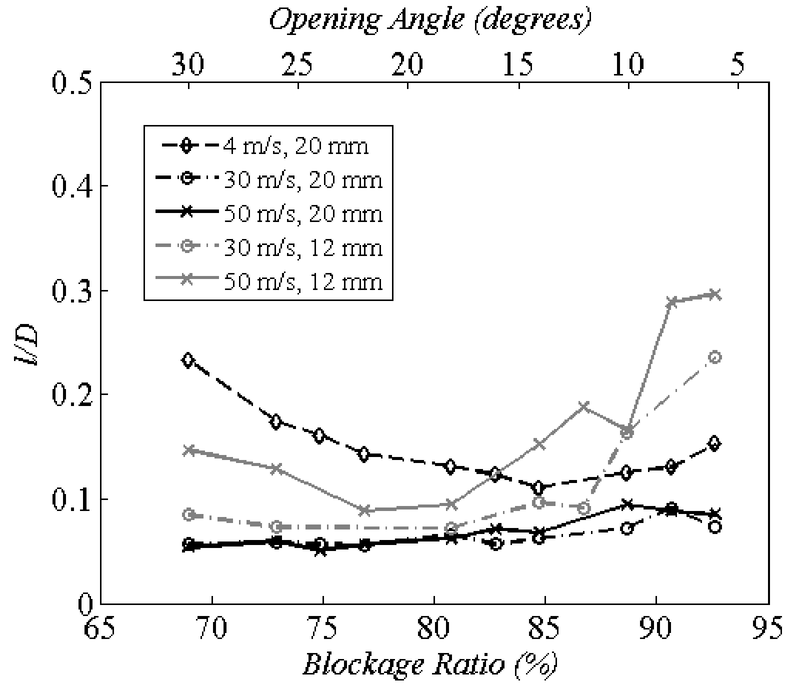

Figure 27: Comparison of characteristic longitudinal length scale, *l* (normalized by burner diameter) as a function of blockage ratio for the two burner diameters over a range of mean flow velocities

2.3 Flame imaging

The chemiluminescence from the turbulent flames were captured with either a 512 x 512 pixel resolution or 1024 x 256 pixel resolution camera depending on the aspect ratio of the flame. The cameras used were Princeton Instruments 16-bit intensified charge-coupled devices (ICCD). The two cameras are also equipped with different intensifiers; the 512 x 512 camera (PI-MAX 512) comes equipped with a Gen III HB filmless intensifier, while the 1024 x 256 (PI-MAX 1024) comes equipped with a Gen II intensifier. For the high hydrogen content flames, a 105 mm, f/4.5, UV camera lens was used since this lens is sensitive in the visible and ultraviolet regions (~220-650 nm) and, hence, is capable of capturing both OH* and CO_2*. This is important since the OH* chemiluminescence associated with hydrogen flames emits in the UV range. For the pure methane flames, lenses of varying focal lengths were utilized along with a CH* filter. The CH* filter was bandpass filter with a center wavelength of 430±2nm with a FWHM of 10±2nm (Newport 20BPF10-430) to capture the primary CH* emission at 431nm.

Chapter 3
Turbulent Flame Speed Data

3.1 Georgia Tech $S_{T,GC}$ database

This section of the chapter describes the database of turbulent consumption speed, $S_{T,GC}$, measurements that have been acquired in the course of this study. In this thesis, this database of measurements will be referred to as the 'Georgia Tech database'.

A detailed description on the image processing methodology that is used to extract $S_{T,GC}$ from the chemiluminescence images is also included.

3.1.1 Experimental conditions

Measurements of $S_{T,GC}$ have been obtained at pressures of 1-20 atm as a function of $u'_{rms}/S_{L,0}$ using the 12 and 20 mm diameter Bunsen burners for a reactant temperature of 300 K. Data were acquired at mean flow velocities of 4-50 m/s and H_2/CO ratios ranging from 30/70-90/10 by volume.

Two sets of experiments were conducted. In the first set, data were obtained where the mixture $S_{L,0}$ was kept nominally constant at 34 cm/s by adjusting the equivalence ratio at each H_2/CO ratio. These experiments were conducted at 1 atm with the 20 mm diameter burner and up to 10 atm for the 12 mm diameter burner. Additionally, a CH_4/air data set at 1 atm was obtained at the same $S_{L,0}$ using the 20 mm diameter burner. Table 1 summarizes the experimental conditions and plotting legend employed for the constant $S_{L,0}$ data set.

In the second of experiments, data was obtained for mixtures with constant H_2/CO ratio but different equivalence ratios, which results in the $S_{L,0}$ varying across the mixtures. These data were obtained using the 20 mm diameter burner. Table 2 summarizes the experimental conditions and plotting legends employed for these data

Estimates of $S_{L,0}$ were determined using the PREMIX module [69] in CHEMKIN with the Davis H_2/CO mechanism for H_2/CO mixtures [70] and GRI 3.0 for the CH_4/air [71].

Table 1: Experimental conditions and plotting legend for constant $S_{L,0}$ data set obtained using the 12 and 20 mm diameter burners. Pressure data are represented by filled symbols, and the fill color is indicted by the cell color for ϕ in the leftmost column.

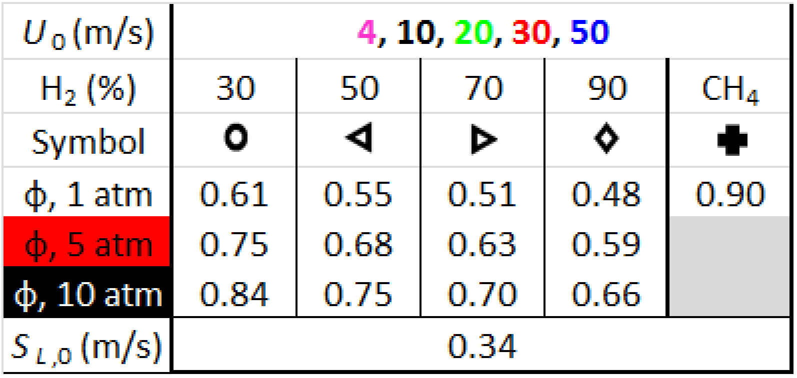

U_0 (m/s)	4, 10, 20, 30, 50				
H_2 (%)	30	50	70	90	CH_4
Symbol	○	◁	▷	◇	✚
ϕ, 1 atm	0.61	0.55	0.51	0.48	0.90
ϕ, 5 atm	0.75	0.68	0.63	0.59	
ϕ, 10 atm	0.84	0.75	0.70	0.66	
$S_{L,0}$ (m/s)	0.34				

Table 2: Experimental conditions and plotting legend for ϕ sweep data set obtained using the 20 mm diameter burner. Pressure data are represented by filled symbols, and the fill color is indicted by the cell color for ϕ in the leftmost column.

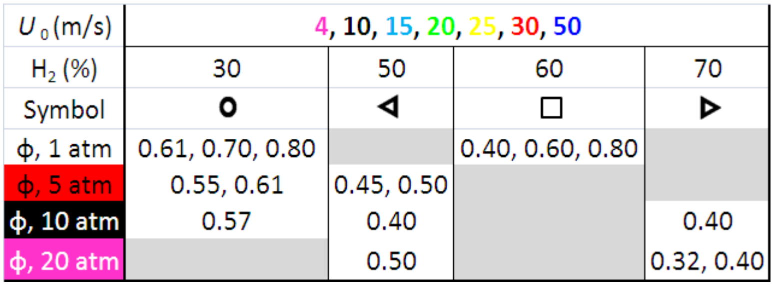

U_0 (m/s)	4, 10, 15, 20, 25, 30, 50			
H_2 (%)	30	50	60	70
Symbol	○	◁	□	▷
ϕ, 1 atm	0.61, 0.70, 0.80		0.40, 0.60, 0.80	
ϕ, 5 atm	0.55, 0.61	0.45, 0.50		
ϕ, 10 atm	0.57	0.40		0.40
ϕ, 20 atm		0.50		0.32, 0.40

Figure 28 summarizes where the measured data are located on a Borghi-Peters diagram [10, 11] for the 12 and 20 mm data. The Karlovitz number in this figure is defined as:

$$Ka_\eta = \frac{\left(u'_{rms}/S_{L,0}\right)^{3/2}}{\left(l_{\mathrm{int}}/\delta_F\right)^{1/2}} \tag{3.1}$$

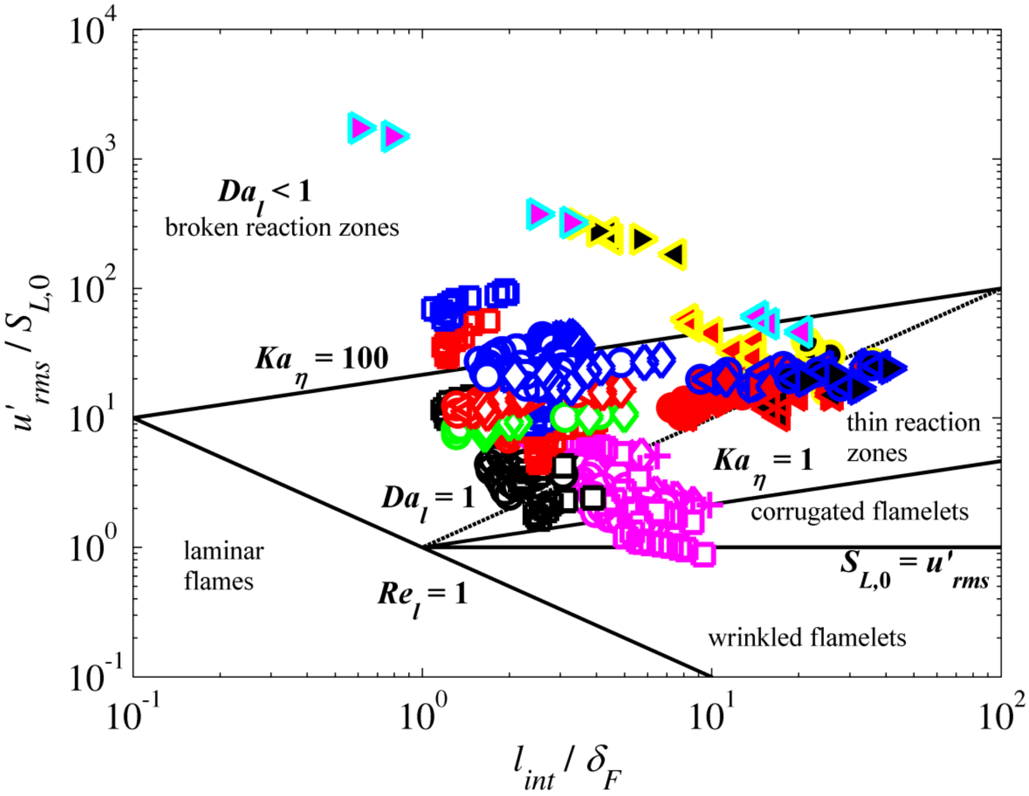

Figure 28: Location of all the data reported in this study (12 and 20 mm) on the Borghi-Peters diagram.

Note from Figure 28, the wide range of $u'_{rms}/S_{L,0}$ values that have been obtained in this study. However, the values of $u'_{rms}/S_{L,0}$, particularly those that correspond to the data lying in the broken reaction zones, need to be regarded with some suspicion. As stated above, $S_{L,0}$ values are estimated using the PREMIX module in CHEMKIN, and the key input in these calculations are the kinetic mechanisms. It is important to recognize that the conditions explored in this study are often outside the conditions for which the mechanism has been optimized. For instance, the Davis mechanism [70], which was used to estimate $S_{L,0}$ for the H_2/CO mixtures, has been optimized by using flame speed data targets obtained at primarily 1 atm. A few $S_{L,0}$ targets at 15 atm were also used for primarily rich H_2/air mixtures. The lack of flame speed targets at higher pressures for lean hydrogen containing mixtures is due to the fact that these flames typically exhibit cellular structures rendering the determination of $S_{L,0}$ impossible [1]. In order to examine the uncertainties introduced by the chemical mechanisms, Figure 29 plots the $S_{L,0}$ estimated using various kinetic mechanisms as a function of the H_2 content for the constant $S_{L,0}$ studies. In addition to the mechanisms described earlier, calculations were also carried out using a C1 mechanism, details of which can be found in Ref. [72].

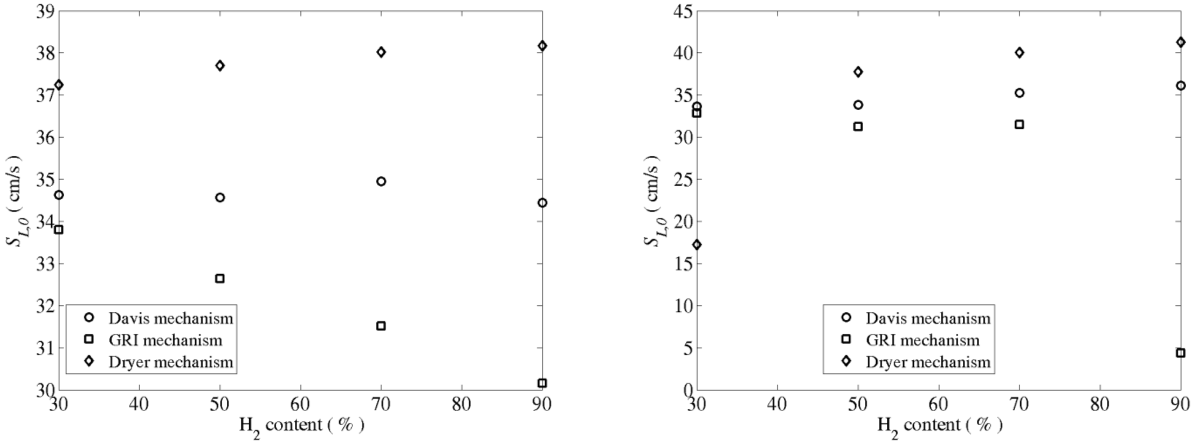

(a) (b)

Figure 29: Comparison of estimates of $S_{L,0}$ using various mechanisms for mixtures studied in the constant $S_{L,0}$ experiments. Calculations are shown for pressures of (a) 1 and (b) 10 atm.

From Figure 29 it is evident that, depending on the mixture and the pressure, different mechanisms can produce different estimates for $S_{L,0}$. In particular, the GRI mechanism under-predicts the flame speed at a given equivalence ratio relative to the Davis mechanism, and that the degree of under-prediction increases with H_2 content and pressure. To further illustrate this point, results of similar calculations performed for the lean mixtures at 20 atm given in Table 2, are shown in Table 3. These conditions are well outside the conditions at which the mechanisms have been validated and optimized for, and this is evident from the results in Table 3. Differences as much 66% between $S_{L,0}$ values calculated using different mechanisms are evident, revealing the limitations of current state-of-the-art chemical kinetic mechanisms at these high pressure conditions.

Table 3: Comparison of $S_{L,0}$ estimated with various mechanisms for mixtures investigated at 20 atm. $S_{L,0}$ values in cm/s.

H_2/CO	50/50	70/30	
ϕ	0.5	0.32	0.4
Davis	4.41	0.136	0.628
GRI	3.33	0.184	0.774
C1	5.53	0.15	0.857

3.1.2 Image analysis

$S_{T,GC}$ was calculated using Eq. (1.7), for which the average flame area is the key input. This section outlines the methodology used to determine the average area. As described in Chapter 2, the integrated line-of-sight flame chemiluminescence was imaged using an ICCD camera. Images of the flame were obtained over 5 seconds and time-averaged; see Figure 30(a). These averaged images are nearly symmetric about the centerline. The left and right halves were then averaged and filtered with a 2-D median filter with a 3 x 3 kernel size. Note that other potential Bunsen flame $S_{T,GC}$ measurement approaches include Mie scattering [48, 73] or OH-PLIF [74] measurements for flame characterization. The resulting progress variable contours (described below) are equivalent for the two methods, assuming that the OH-PLIF or Mie interface surface is equivalent to the chemiluminescence flamelet surface [75, 76]. This line-of-sight approach was used here, however, because the OH-PLIF or Mie scattering technique does not capture flame surface density in the out-of-plane direction and, as such, significantly underestimates it [77]. The spatial distribution of heat release is fully captured by a line-of-sight measurement. This question is discussed in more detail in the final section of this chapter.

To estimate the time-averaged flame brush location from the line-of-sight images, a three-point Abel deconvolution scheme was used [78]; see Figure 30(b). The axial distribution of the centerline intensity is then fit to a Gaussian curve, from which the location of the maximum intensity is identified; see Figure 30(c). This point is associated with the most probable location of the flame, and defined as the $<c> = 0.5$ progress variable contour. The estimated uncertainty in identifying this point is 1-2%. The other progress variables were then defined by the following relation:

$$\langle c \rangle = \frac{1}{2}\left[1 + erf\left(\frac{x_{\langle c \rangle} - \mu}{\sigma\sqrt{2}}\right)\right] \tag{3.2}$$

Straight lines are then drawn from this point to the two flame anchoring points and rotated about the line of symmetry to generate a cone. The $<c> = 0.5$ surface is drawn in Figure 30(b). This method was used to aid in comparing the results of this study with other data in the literature where a similar method was used to determine the flame area (e.g., the "angle method") [48, 73, 79].

In Sec. 3.1.3, the influence of calculating the mean flame area by revolving the $<c> = 0.5$ contour around the axis of symmetry is also discussed. The methodology employed to determine the $<c> = 0.5$ contour is described in detail in Sec. 5.2.

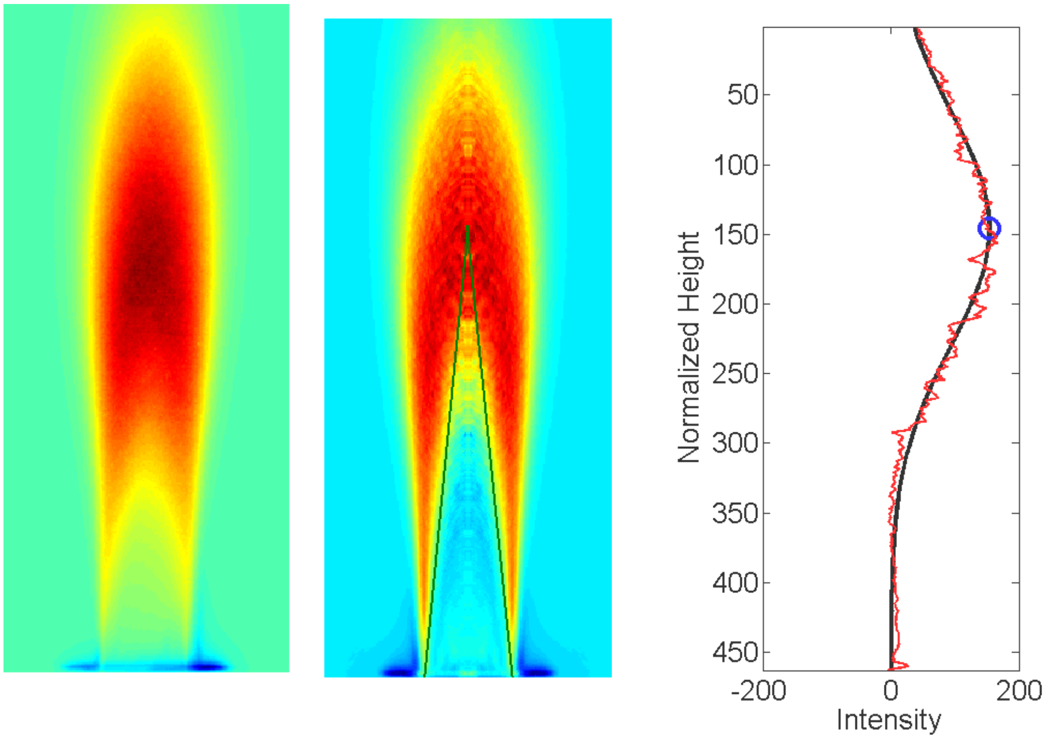

(a) (b) (c)

Figure 30: Example images from each image processing step (a) time averaged raw image (b) Abel-transformed flame along with the cone referenced to <c> = 0.5 and (c) centerline intensity with the point of maximum intensity corresponding to <c> = 0.5 marked with a blue circle.

As noted earlier, $S_{T,GC}$ is a function of the progress variable, $<c>$, used to define $\overline{A}_{<c>}$. Figure 31 plots the dependence of $S_{T,GC}$ upon the progress variable contour, $<c>$, at several H_2/CO ratios, in order to enable comparison of the data in this paper to reported $S_{T,GC}$ data using other progress variable values. As expected, $S_{T,GC}$ decreases with increasing <*c*> value. This graph also shows that the different H_2/CO ratio flames have similar dependence upon <*c*> contour. It also shows that the highest H_2 mixture (90/10 mixture), has the least sensitivity to <*c*>, suggesting that the flame brush thickness is decreasing with increased H_2 content along the centerline. More plots of this kind are given in Appendix C to facilitate conversion between turbulent flame speed measurements based on different progress variable contours.

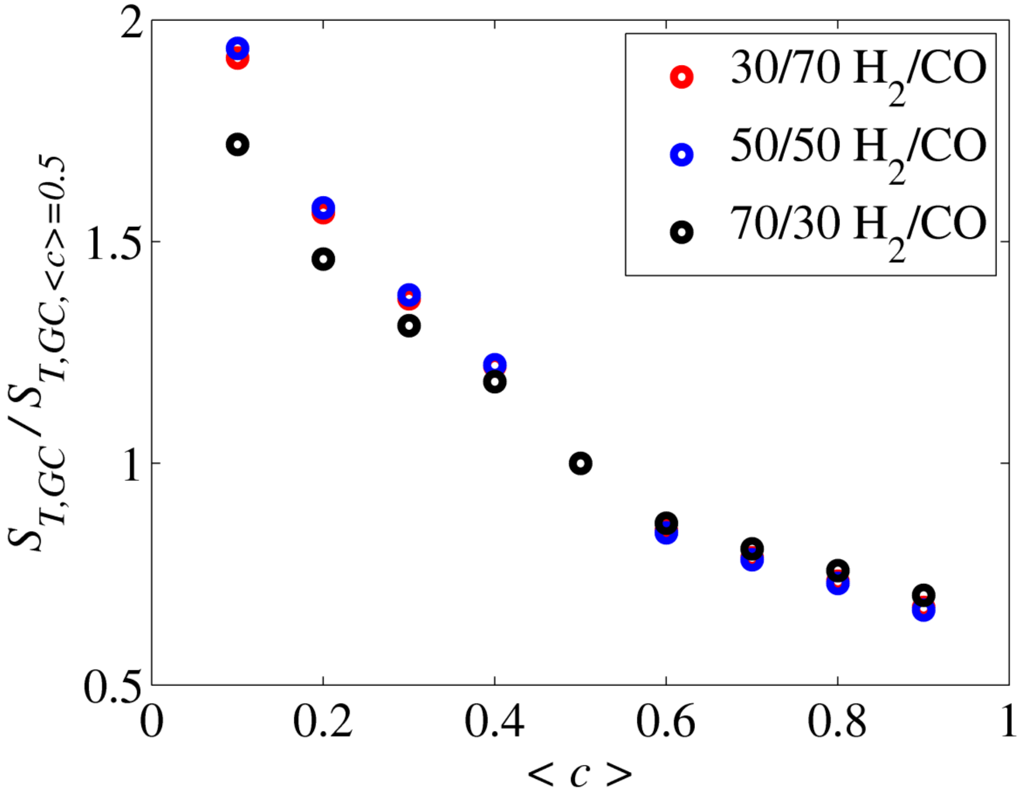

Figure 31: Dependence of $S_{T,GC}$ value calculated using different progress variables normalized by $S_{T,GC}$ calculated using <c> = 0.5 as a function of the progress variable for different H_2/CO ratios. Data are from measurements at 30m/s, $u'_{rms}/S_{L,0} = 10.5$, $S_{L,0}$ = 0.34 m/s, and 5 atm acquired with the 12 mm burner.

3.1.3 H_2/CO sweeps at constant $S_{L,0}$

This section presents data for various H_2/CO ratios at nominally constant $S_{L,0}$. These data were obtained using the 12 and 20 mm burner diameters, and the investigated mixture compositions are given in Table 1. Data were obtained using the 12 mm diameter burner at pressures ranging from 1 to 10 atm at mean flow velocities of 20, 30 and 50 m/s. Data with the 20 mm diameter burner were obtained at atmospheric pressure for mean flow velocities of 4, 10, 30 and 50 m/s. H_2/CO ratios ranging from 30/70 to 90/10 by volume were investigated in both burners. One set of CH_4/air data at $\phi = 0.9$ was also obtained using the 20 mm diameter burner at 1 atm for mean flow velocities of 4, 10 and 30 m/s.

Figure 32 plots the 20 mm burner diameter data acquired at 1 atm. As expected, $S_{T,GC}$ increases monotonically with turbulence intensity for a given fuel composition. The data also clearly indicate the presence of the 'fuel effects' discussed in Chapter 1. In other words, different H_2/CO blends at constant $S_{L,0}$ and u'_{rms} have different turbulent flame speeds. For example, at U_0=30 m/s and $u'_{rms}/S_{L,0} = 25$, $S_{T,GC}/S_{L,0}$ has a value of 8 for CH_4, of 14 for the 30/70 H_2/CO mix and 22 for the 90/10 H_2/CO mix. Moreover, the data indicate that these 'fuel effects' persist even at very high turbulence intensities. Note also the significant similarities between each fixed mean flow velocity group as fuel composition is varied. It appears that the same curve is shifted vertically to higher $S_{T,GC}$ values as H_2 fraction is increased.

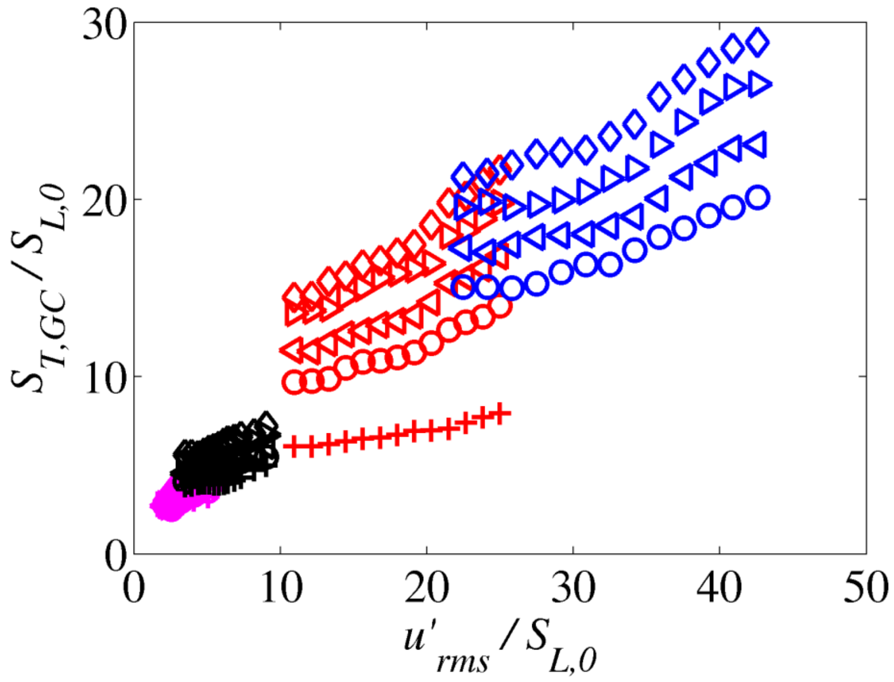

Figure 32: $S_{T,GC}$ as a function of u'_{rms} normalized by $S_{L,0}$ for the constant $S_{L,0}$ studies using the 20 mm diameter burner (See Table 1 for the legend).

Although not the primary focus of this study, the mean flow dependencies at a given fuel composition are worthy of mention. First, these data clearly show the well-known dependence of $S_{T,GC}$ upon U_0, a fact highlighted in other studies [12, 44]. Each velocity result appears to lie on a separate curve, which is roughly parallel to the other velocity results, but does not intersect it at the same turbulence intensity. For example, $S_{T,GC}/S_{L,0}$ differs by 100% at U_0 = 10 and 30m/s, for the 90% H_2 mixture at $u'_{rms}/S_{L,0}$ = 10. As a second example, $S_{T,GC}/S_{L,0}$ differs by 36% between the U_0 = 4 and 10 m/s cases, at $u'_{rms}/S_{L,0}$ = 5 for the 90% H_2 mixture. This mean flow dependence is less obvious between the U_0 = 30 and 50 m/s cases, presumably because the fractional variation in U_0 is smaller here than in the other cases.

Note from Figure 32 that $S_{T,GC}$ data was not acquired for the CH_4/air mixture at U_0 = 50 m/s. This was because significant flame tip opening was observed at this condition. Tip opening results in the leakage of reactants making the application of Eq. (1.7) to determine $S_{T,GC}$ dubious since this equation can only be applied to envelope flames where all the reactants pass through the flame brush and are converted to products. Although there may be some tip opening in the H_2/CO mixtures as well, it was not apparent and probably occurs to a much smaller degree.

The data for the 12 mm burner at various H_2/CO ratios at nominally constant $S_{L,0}$ are presented in Figure 33.

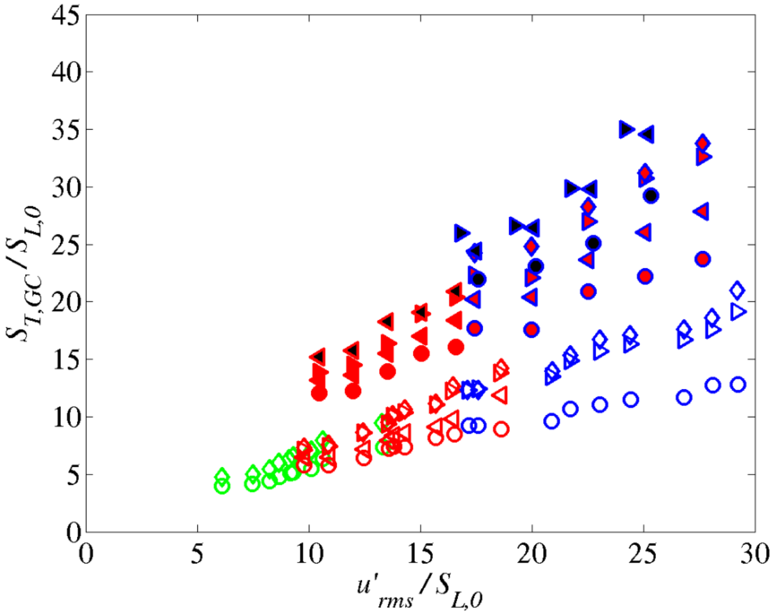

Figure 33: $S_{T,GC}$ as a function of u'_{rms} normalized by $S_{L,0}$ for the constant $S_{L,0}$ studies using the 12 mm diameter burner (See Table 1 for the legend).

A few interesting observations can be made from Figure 33. First, note that larger average consumption speeds are seen with the larger burner diameter, at a given fuel composition, turbulence intensity, mean flow velocity and pressure. These differences are about 50% for 50 m/s and 60% for 30 m/s. This shows the well-known length scale sensitivity of the turbulent flame speed [36]. Second, the fuel effects observed with the 20 mm data is also seen here, but at all pressures. Third, increasing pressure leads to increased turbulent flame speed, i.e., at constant $S_{L,0}$ and u'_{rms}, $S_{T,GC}$ increases with pressure. This increase is quantified in Figure 34, which plots the ratio of $S_{T,GC}/S_{L,0}$ at 5 and 10 atm to 1 atm for each mixture and mean flow velocity as a function of turbulence intensity. This ratio has values of about 1.8-2.1 and 2.2-2.5 at 5 and 10 atm, respectively. Note that this is not an $S_{L,0}$ effect, as $S_{L,0}$ is kept fixed at 34 cm/s.

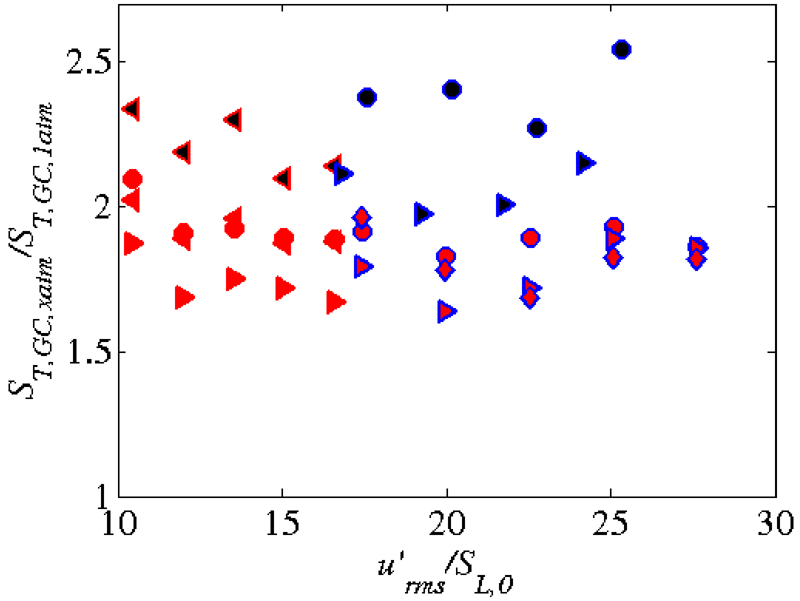

Figure 34: Ratio of $S_{T,GC}$ at 5 and 10 atm to 1 atm across the range of turbulence intensities investigated.

It is worth making a few comments at this point on how the observed fuel and pressure effects are affected when the alternative definitions of the average flame area are used. Recall that in all the data presented so far, the average flame area is calculated as the surface area of a cone formed by revolving the triangle whose vertices are the <c> = 0.5 point along the centerline and the flame anchoring points, about the axis of symmetry (see Sec. 3.1.2). This definition was used to be consistent with how average flame areas for Bunsen flames were typically calculated in the literature [48]. However, it is of interest to investigate how alternative definitions of the flame area affect the observed trends. For instance, in Appendix C it is shown that basing the surface area on increasing values of the progress variable results in smaller values of $S_{T,GC}$. However, the qualitative trends are not altered.

An alternate definition of the average flame area to consider is the surface area obtained when the $<c>$ = 0.5 contour, determined at every point along the flame brush, is rotated about its axis. Daniele *et al*. [50] calculate the average flame based on the <c> = 0.05 contour using this approach. The methodology employed to determine the <c> = 0.5 point at each location along the flame brush is described in detail in Sec. 5.2.

Figure 35 re-plots some of the data from Figure 33 using the new definition of the average flame area. Qualitatively, the fuel and pressure sensitivities observed in Figure 33 are also observed here. The magnitude of $S_{T,GC}$ is smaller, which is expected since the new area definition produces larger values for the flame area than that cone definitions used up to this point. Figure 36, which plots the same ratio of turbulent consumption speeds as in Figure 34, shows that when the new area definition is used the pressure augments $S_{T,GC}$ to a greater degree than when the cone definition is used. However, compared to Figure 34, note that the 5 atm and 10 atm are grouped closer together in

Figure 36. Computing the flame area using a cone is a measure of the height of the flame and the results in Figure 33 suggest that the flame gets shorter with pressure for a given set of conditions. On the other hand, the results in Figure 36 suggest that flame brush is becoming less cone-like and more bulbous, which counteracts the reduction in flame area due to the shortening.

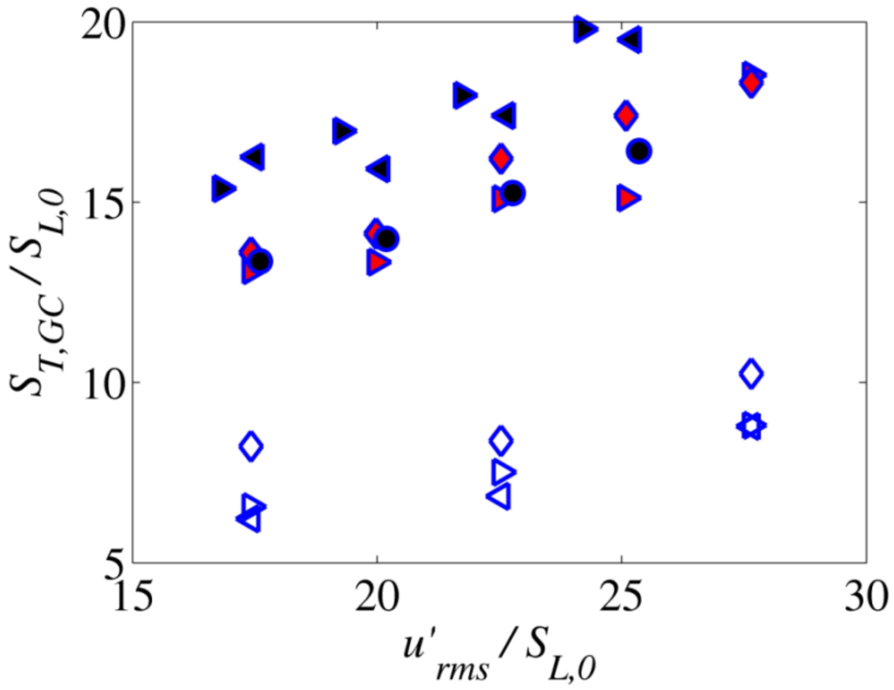

Figure 35: $S_{T,GC}$ as a function of u'_{rms} normalized by $S_{L,0}$ for the constant $S_{L,0}$ studies using the 12 mm diameter burner (See Table 1 for the legend). Flame area calculated by revolving <c>=0.5 contour about axis of symmetry.

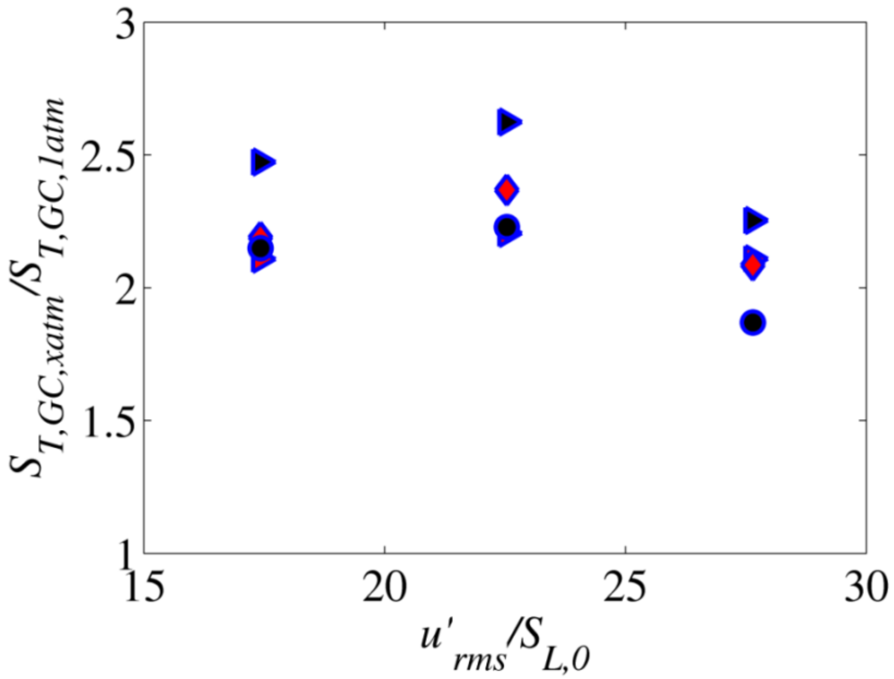

Figure 36: Ratio of $S_{T,GC}$ at 5 and 10 atm to 1 atm across the range of turbulence intensities investigated. Flame area calculated by revolving <c>=0.5 contour about axis of symmetry.

Although not a focus of this work, it is important acknowledge the importance of density ratio, ρ_u/ρ_b, effects on the turbulent flame speed [80-82]. For the constant $S_{L,0}$ studies, the density ratio varies with both H_2 content and pressure since the equivalence ratio is adjusted in order to maintain the $S_{L,0}$ at 34 cm/s. The influence of these parametric variations on the density ratio is presented in Figure 37.

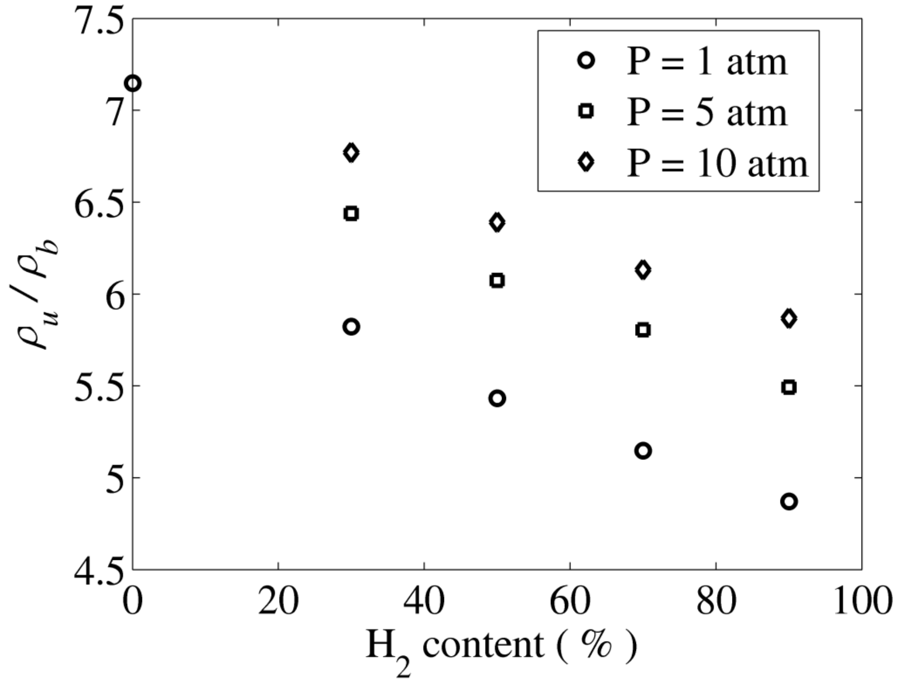

Figure 37: Variation of gas expansion ratio with H_2 content at different pressures for the constant $S_{L,0}$ studies

Note from Figure 37 that the density ratio decreases with H_2 content at fixed pressure and increases with pressure at a fixed H_2 content. These trends can be explained using the following arguments. At a fixed pressure, increasing the H_2 content necessitates a reduction in the equivalence ratio to maintain a constant $S_{L,0}$, which reduces the flame temperature and hence reduces the density ratio. Although the increasing H_2 content causes the reactant density to decrease, the density ratio is primarily influenced by the decreasing flame temperature. Similarly, increasing the pressure at fixed H_2 content necessitates increasing the equivalence to maintain constant $S_{L,0}$. As a result, the flame temperature increases causing the density ratio to increase.

Work by Peters *et al.* [80] and Aldredge and Williams [81] showed that the turbulent flame speed increases with gas density ratio, which was attributed to the enhancement of the D-L instability leading to higher flame areas. However, Peters *et al.* [80] also showed that increasing $u'_{rms}/S_{L,0}$ decreased the influence of the gas expansion ratio, which was a point that was emphasized in a recent review by Lipatnikov and Chomiak [82]. Returning to the data obtained in this work, since the density ratio decreases with increasing H_2/CO ratio, it seems that the observed fuel effects may actually be counteracted by the suppressive influence of the diminishing density ratio. On the other hand, the pressure effects observed in Figure 33 may be partly due to the increasing density ratio with pressure. However, these points need further investigation since these density ratio effects may not be important in this work due to the high turbulence intensities, $u'_{rms}/S_{L,0}$.

While on the topic of flow-flame interaction, the review article by Lipatnikov and Chomiak [82] also discussed the modification of the turbulent flow field upstream of the flame suggesting that greater care needs to be exercised in selecting the appropriate turbulence intensities which interact with the flame. An additional point to consider is the evolution of the turbulence field downstream of the burner exit. In this work the turbulence field is characterized by the total turbulence intensity at the centerline of the burner exit. However, as shown in Sec. 2.2, the turbulence field at the burner exit is anisotropic owing to the large burner contraction ratio. Re-distribution of energies between the fluctuations in the different directions may occur in the region downstream of the burner exit which may cause the turbulence to become more isotropic. However, further work is needed to characterize this downstream evolution of the initially anisotropic turbulent field. Using planar imaging techniques, important insights can be gained into the precise nature of the turbulent field that is actually interacting with the flame.

3.1.4 Equivalence ratio sweeps at constant H_2 content

In order to determine the effect of varying $S_{L,0}$ at fixed H_2 fractions, equivalence ratio sweeps were also performed at fixed H_2 contents using the 20 mm burner diameter. These measurements were acquired for pressures ranging from 1 to 20 atm and the details of the mixtures and the plot legend for this data are provided in Table 2.

Due to the wide range in $u'_{rms}/S_{L,0}$ obtained in these experiments, the 1 atm data is plotted separately in Figure 38 and Figure 39, while Figure 40 and Figure 41 plot all the data together. It is important to note that $S_{L,0}$ is not constant for these data, as it was in the prior section.

Figure 38 and Figure 39 shows the results for a 30% H_2 mixture at $\phi = 0.61$, 0.7, 0.8 and a 60% H_2 mixture at $\phi = 0.4$, 0.6, 0.8, respectively, for mean flow velocities of 4, 10, 30, and 50 m/s and pressure of 1 atm. Figure 40and Figure 41 plot all the equivalence ratio sweep data obtained in this study, which includes data at pressures up to 20 atm, on a linear and log-log plot respectively.

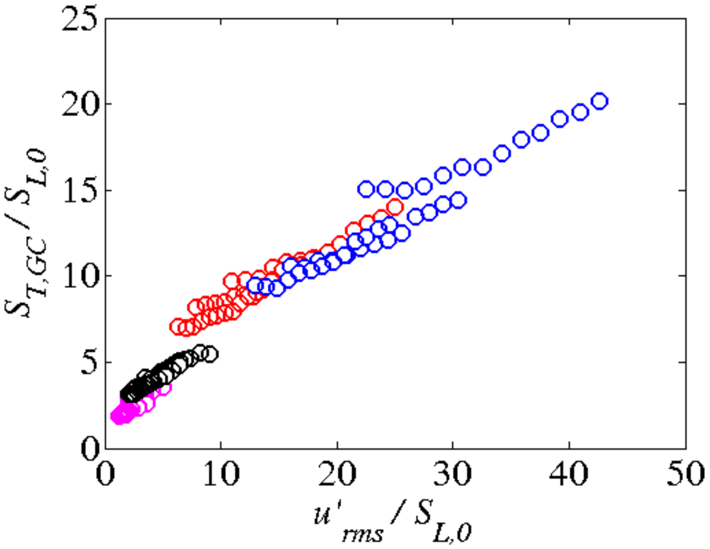

Figure 38: $S_{T,GC}$ as a function of u'_{rms} normalized by $S_{L,0}$ for the phi sweep studies for the H_2 = 30% mixture using the 20 mm diameter burner (See Table 2 for the legend).

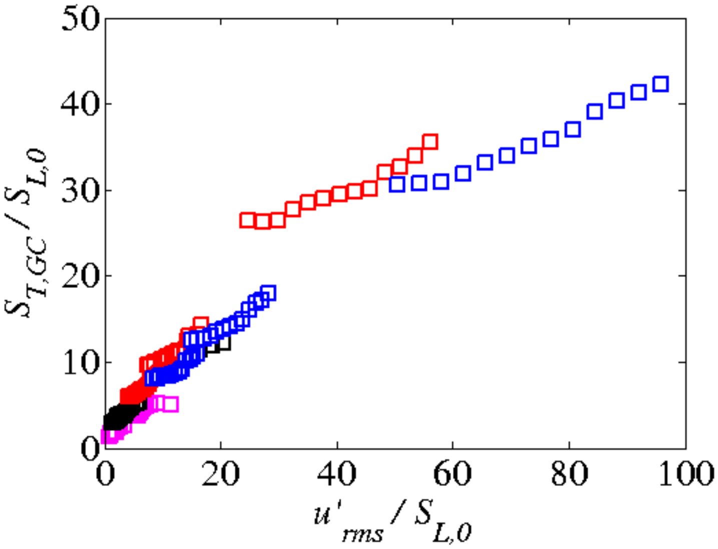

Figure 39: $S_{T,GC}$ as a function of u'_{rms} normalized by $S_{L,0}$ for the phi sweep studies for the H_2 = 60% mixture using the 20 mm diameter burner (See Table 2 for the legend).

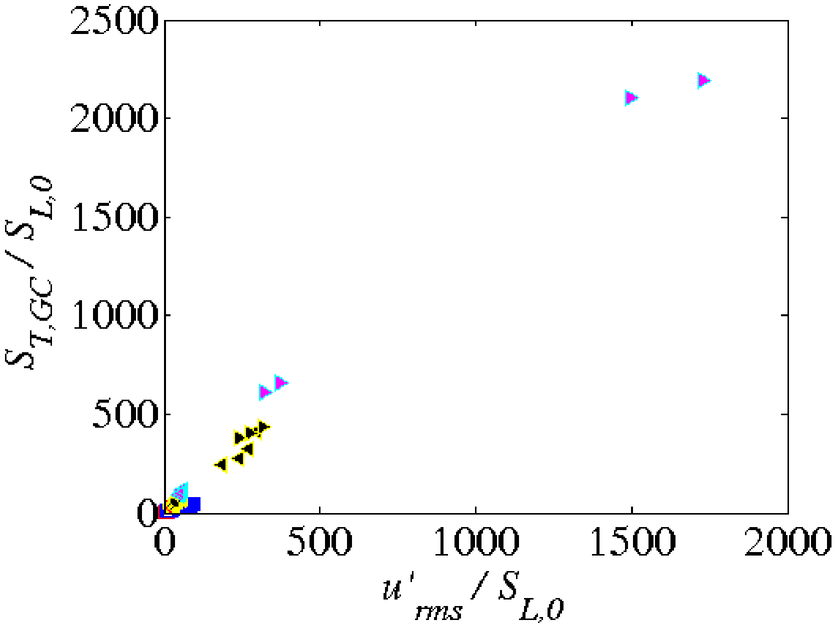

Figure 40: Linear plot of $S_{T,GC}$ as function of u'_{rms} normalized by $S_{L,0}$ at various mean flow velocities, H_2/CO ratios, and pressures for the 20 mm diameter burner (See Table 1 and Table 2 for the legend).

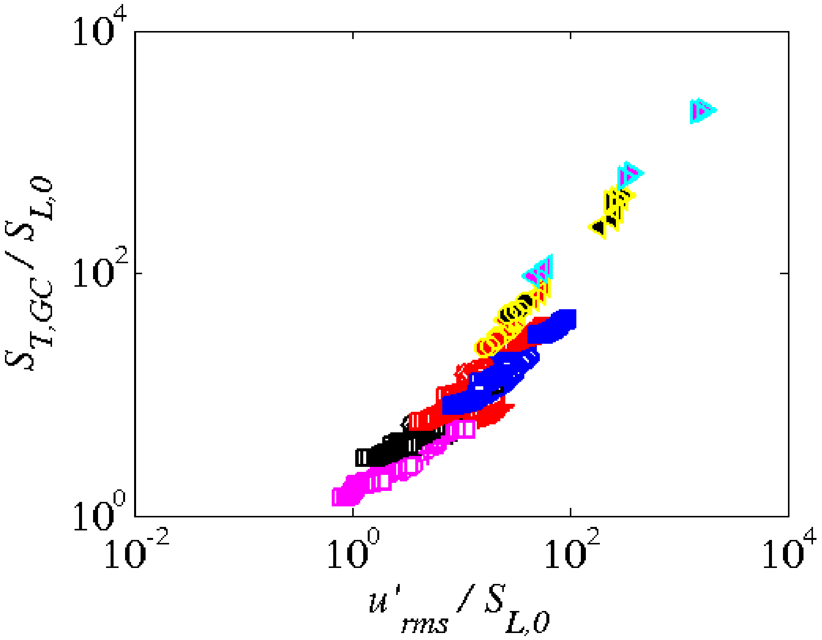

Figure 41: Log-log plot of $S_{T,GC}$ as function of u'_{rms} normalized by $S_{L,0}$ at various mean flow velocities, H_2/CO ratios, and pressures for the 20 mm diameter burner (See Table 1 and Table 2 for the legend).

Note from Figure 40 and Figure 41 that data have been acquired at $u'_{rms}/S_{L,0}$ up to almost 2000, which is some of the highest reported normalized turbulence intensities at which S_T data have been acquired. The reasons for these large values and the caution with which they should be regarded with have been discussed extensively in Sec. 3.1.1.

3.2 S_T databases from the literature

In this section of the chapter, other turbulent flame speed databases from the literature that investigate fuel and pressure effects are described. Noting the definition dependence of S_T, the data sets are grouped according to the specific configurations used to make the measurements. These data are presented to facilitate the discussion in the following chapter, which focuses on the development of a reduced order model for S_T.

3.2.1 PSI Database

This section presents the turbulent flame speed database acquired by Daniele *et al.* [50] at the Paul Scherrer Institute (PSI). This database of measurements will be referred to as the ‘PSI database’ in this thesis.

The PSI $S_{T,GC}$ database was acquired for H_2/CO mixtures of 33/67, 50/50 and 67/33 at a reactant temperature of 623 K and pressures ranging from 1 – 20 atm at a mean flow velocity of 40 m/s. The experimental configuration, shown in Figure 42, consists of a straight tube of 25 mm diameter that exits into a dump geometry. The sudden expansion produces corner recirculation zones that stabilize the main jet flame. The flames were imaged using OH-PLIF, from which the instantaneous flame edges are extracted and then summed to generate the turbulent flame brush. $S_{T,GC}$ was then calculated using Eq. (1.7), where a flame area based on $\langle c \rangle = 0.05$ is used.

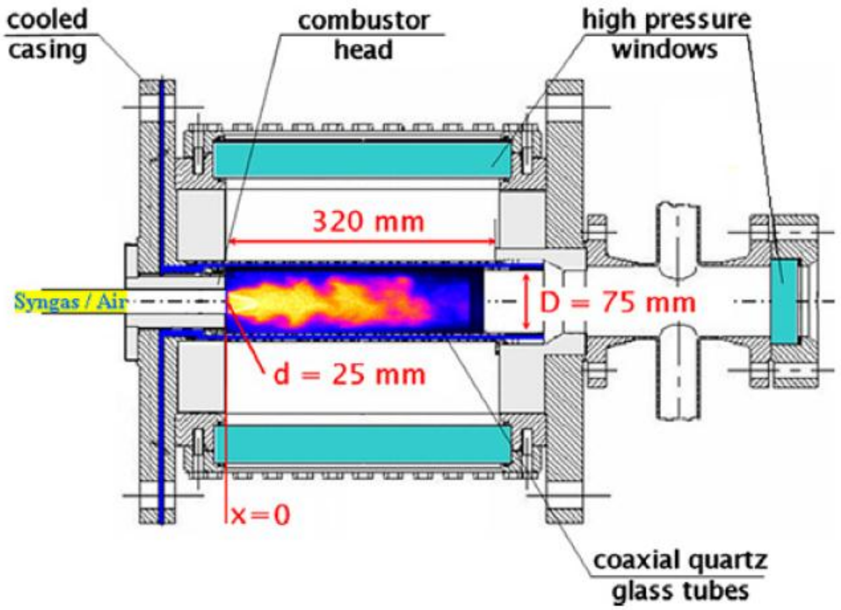

Figure 42: Experimental configuration used to acquire the PSI $S_{T,GC}$ database. Figure adapted from Ref. [50].

Table 4 summarizes the mixtures and pressures over which the data have been acquired. The legend used to plot this database is also incorporated into this table. Figure 43 also plots the location of these data on the Borghi-Peters diagram.

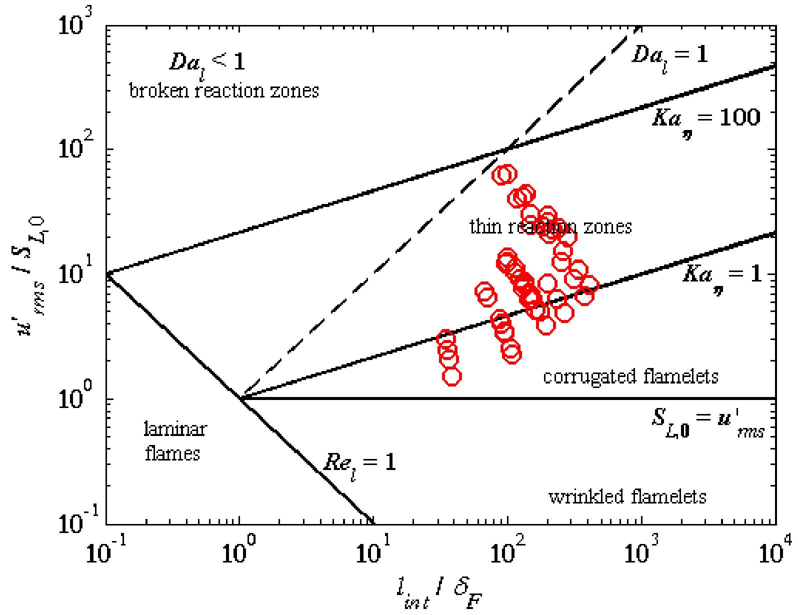

Figure 43: Location of the PSI database on the Borghi-Peters diagram.

Table 4: Mixture and pressures for which $S_{T,GC}$ data have been acquired in the PSI database. Plotting legend is also included. Text colors for H_2/CO ratios indicate symbol colors.

P (bar)	1	2.5	5			7.5	12.5	15	17.5	20
Symbol	x	o	□			◇	◁	▷	△	+
H_2/CO	50/50	50/50	33/67	50/50	67/33	50/50	50/50	50/50	50/50	50/50
ϕ	0.41	0.33	0.33	0.33	0.33	0.33	0.33	0.33	0.31	0.32
	0.38	0.38	0.38	0.36	0.32	0.38	0.38	0.36	0.33	0.33
	0.44	0.42	0.41	0.38	0.30	0.42	0.42	0.38	0.35	0.36
	0.53	0.50	0.45	0.42		0.45	0.45	0.41	0.36	0.37
		0.32	0.32	0.45				0.45		0.38
		0.39		0.38				0.32		
		0.42		0.38				0.35		
		0.48		0.34						

Figure 44 plots the data reported in Ref.[50] with one modification. Originally, the turbulence intensity used to correlate the $S_{T,GC}$ data was determined at the intersection of the flame centerline and the $<c>$ = 0.05 progress variable. The Georgia Tech data is plotted using the turbulence intensity measured at the center of the burner exit. To maintain consistency, the PSI data is re-plotted here using the turbulence intensity at the center of the burner exit. In their work, since the turbulence generating device and the mean flow velocity of 40 m/s were unchanged across all conditions, the turbulence intensity, u'_{rms}, at the burner exit is assumed to be the same, at 2.8 m/s, across all conditions. As a result, the observed variation in $u'_{rms}/S_{L,0}$ is due to the changing $S_{L,0}$.

In addition, the PSI $S_{T,GC}$ data is calculated using $<c>=0.05$, while the Georgia Tech results were determined at $<c>=0.5$. To facilitate comparisons between the Georgia Tech and PSI datasets in the following chapter, the Georgia Tech data is adjusted to the <c> = 0.05 progress variable using a correction factor derived from Figure 31 .

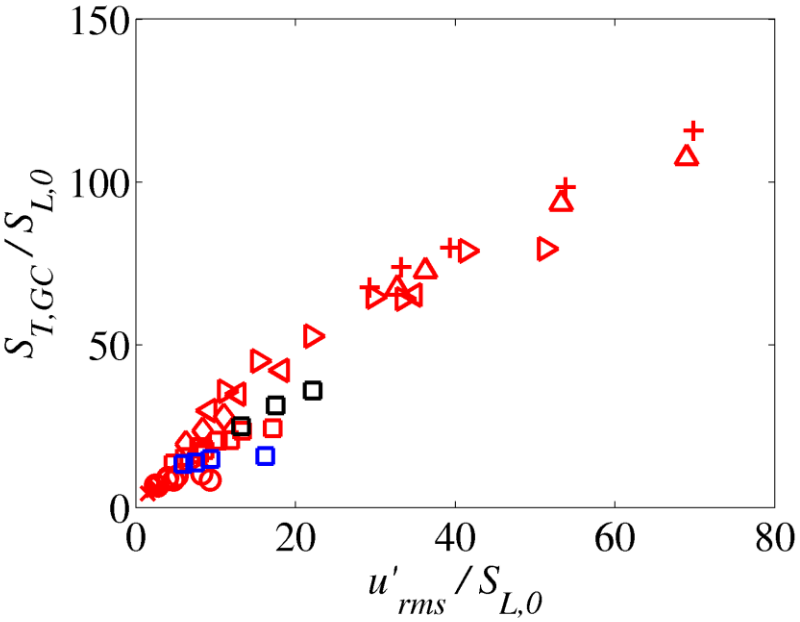

Figure 44: $S_{T,GC}$ as a function of u'_{rms} all normalized by $S_{L,0}$ for the PSI data (see Table 4 for the legend).

Some interesting points can be noted from Figure 44. For a fixed H_2/CO ratio and equivalence ratio, $S_{T,GC}$ seems to increase with pressure at fixed u'_{rms}, shown more explicitly in Figure 45. This is interesting for a few reasons. Firstly, this observation runs contrary to the findings in Ref. [48] that the pressure did not affect the turbulent flame speed for CH_4/air mixtures at fixed equivalence ratios. Secondly, $S_{L,0}$ is also decreasing with pressure suggesting that the increase in $S_{T,GC}$ may be affected more by the Darrieus-Landau instability, particularly at high pressures, that may generate flame area. Also, as expected, for a fixed H_2/CO ratio, $S_{T,GC}$ increases with the mixture equivalence ratio, since the local burning velocity along the turbulent flame front would be higher.

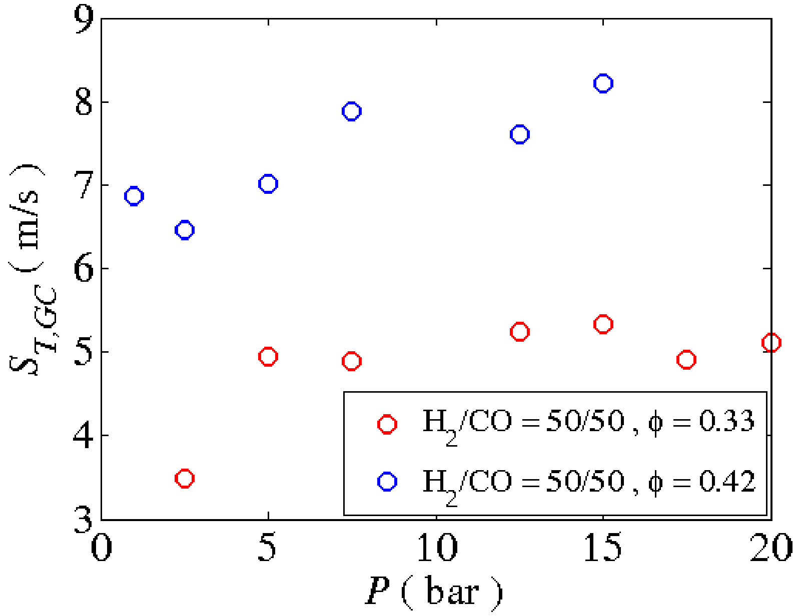

Figure 45: $S_{T,GC}$ as a function of pressure at a constant H_2/CO ratio and equivalence ratio.

3.2.2 Spherical bomb flame speed database

The database of spherical bomb experiments that are analyzed in this work is comprised of data reported in Ref. [34, 52, 83]. Although there are many other spherical bomb studies reported in the literature [84-86], these data sets have been selected since they investigate fuel and coupled fuel and pressure effects.

These measurements were acquired in a spherical bomb configuration, shown in Figure 46, for centrally ignited, expanding flames. The combustion chamber used is a nearly spherical vessel with an equivalent inner diameter of about 100 mm. The chamber has four windows for optical access, and two perforated plates on the remaining sides of the vessel. Behind each perforated plate there is a fan used to mix the gases and generate nearly isotropic turbulence in the central region of the combustion chamber. The turbulence intensity and turbulent length scales are characterized using hot-wire anemometry and then related to the fan shaft rotational speed.

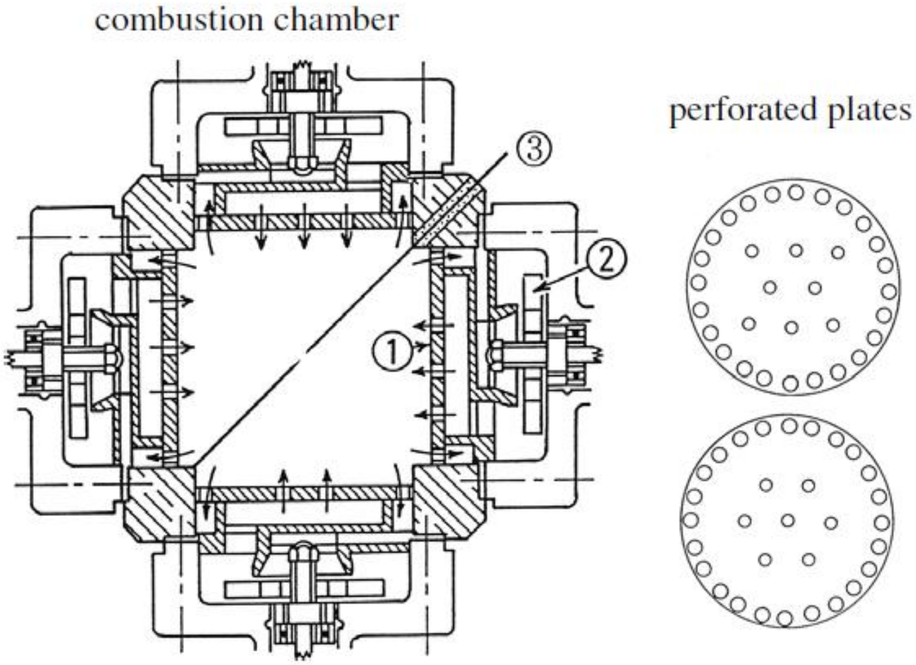

Figure 46: Spherical bomb facility utilized in Ref. [34, 83]. Features indicated in figure include (1) the perforated turbulence generating plates, (2) the fan and (3) the ignition plug.

S_T was determined from the temporal change in the pressure as the flame ball expanded outwards. The relation between the time rate of change of pressure and the flame speed is derived by relating the rate of reactant mass depletion to the rate of product generation, suggesting that these are measurements of $S_{T,GC}$. Figure 47 plots the location of these data on a Borghi-Peters diagram.

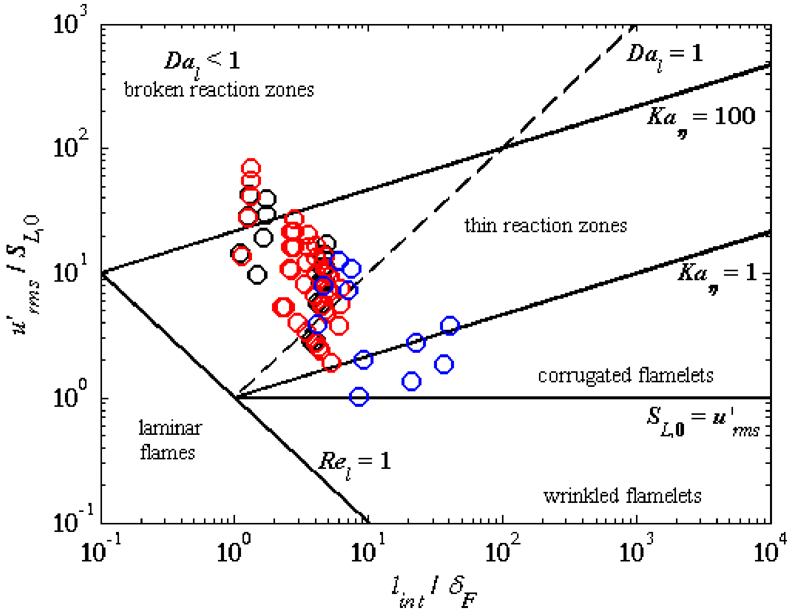

Figure 47: Location of the spherical bomb database on the Borghi-Peters diagram.

The $S_{T,GC}$ data reported in Ref. [83], which is obtained for $H_2/O_2/N_2$ and $CH_4/O_2/N_2$ mixtures for equivalence ratios, $\phi = 0.7$, 0.9 and 0.98, is reproduced in Figure 48 and Figure 49, with one important modification. The authors of the original work state that all the mixtures had the same $S_{L,0}$ of 15 cm/s, which was achieved by varying the O_2/N_2 ratio. However, the O_2/N_2 ratio necessary to maintain this constant $S_{L,0}$ was determined experimentally also using the spherical bomb technique As a result, when $S_{L,0}$ for these mixtures was computed using PREMIX, the results did not match those quoted in Ref. [83], as is evident from Table 5. The discrepancies are particularly severe for the $H_2/O_2/N_2$ cases. As a result, for consistency, the $S_{L,0}$ values used to normalize the data in Figure 49 are those obtained from PREMIX.

Table 5: Computed values of $S_{L,0}$ for the mixtures investigated in Ref. [83].

Fuel	ϕ	Computed $S_{L,0}$ (cm/s)
H_2	0.70	3.4
	0.90	5.1
CH_4	0.70	17.4
	0.90	17.4
	0.98	17.0

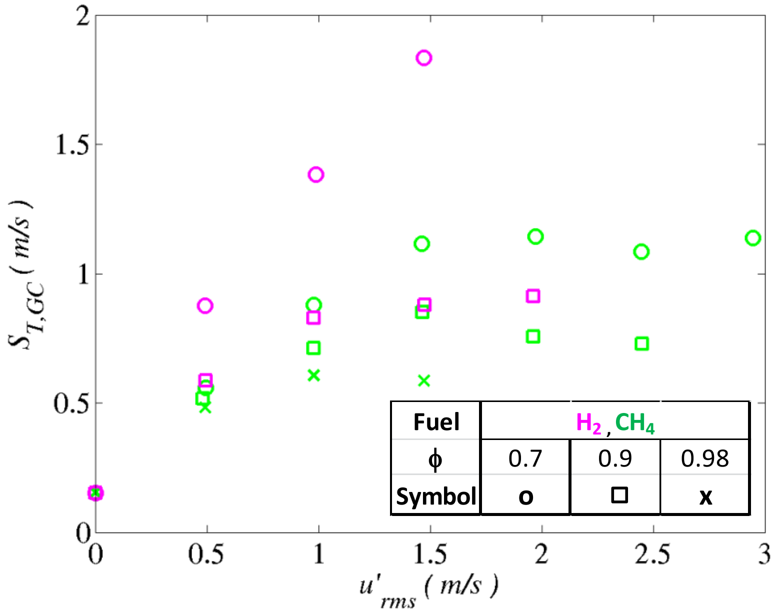

Figure 48: $S_{T,GC}$ as a function of u'_{rms} for the data reported in Ref. [83].

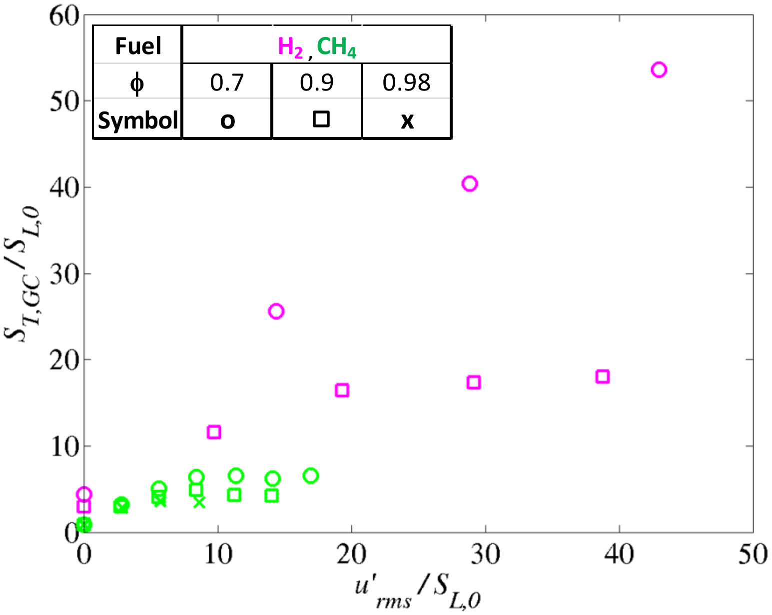

Figure 49: $S_{T,GC}$ as a function of u'_{rms} all normalized by $S_{L,0}$ for the data reported in Ref. [83].

Figure 51and Figure 52 plot the data reported in Ref. [34]. This work extended the studies in Ref. [83] to multicomponent fuels. The $S_{T,GC}$ data reproduced here were acquired for various CH_4/H_2 mixtures at a fixed equivalence ratio of 0.8. Data were obtained where the mixture $S_{L,0}$ was held constant at 15 and 25 cm/s by adjusting the N_2/O_2 ratio.

However, as above, the mixture compositions necessary to maintain this constant $S_{L,0}$ was determined experimentally. Figure 50 presents the computed $S_{L,0}$ for these mixtures and it is evident that these values differ appreciably from the quoted values, particularly at the higher H_2 content.

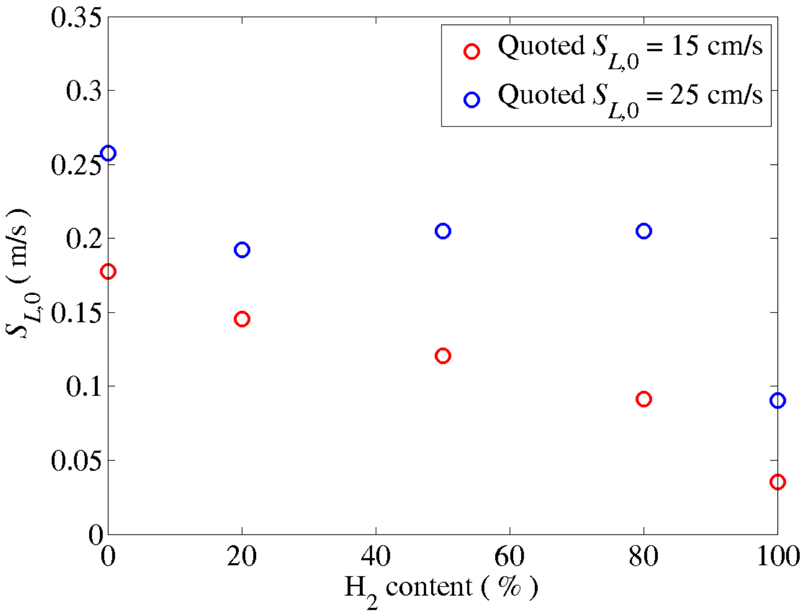

Figure 50: Calculated $S_{L,0}$ as a function of H_2 content for the two quoted $S_{L,0}$ in Ref. [34].

The conclusions drawn from the data in Ref. [34, 83] were quite similar; mixtures could have substantially different turbulent flame speeds even if they have the same un-stretched laminar flame speed and are exposed to the same turbulence intensity. However, this conclusion needs re-visiting in light of the results from Table 5 and Figure 50 as it appears that the un-stretched laminar flame speed is not constant across the different mixtures. For instance, Figure 51 plots the raw un-normalized data from Ref. [34]. It is observed that for a fixed turbulence intensity, as the H_2 content in the fuel increases, $S_{T,GC}$ also increases. But from Figure 50, as the H_2 content is increased, the mixture $S_{L,0}$ is decreasing. So it is unclear what is causing the rise in $S_{T,GC}$ with H_2 content, especially since the role of the N_2 diluent is also uncertain.

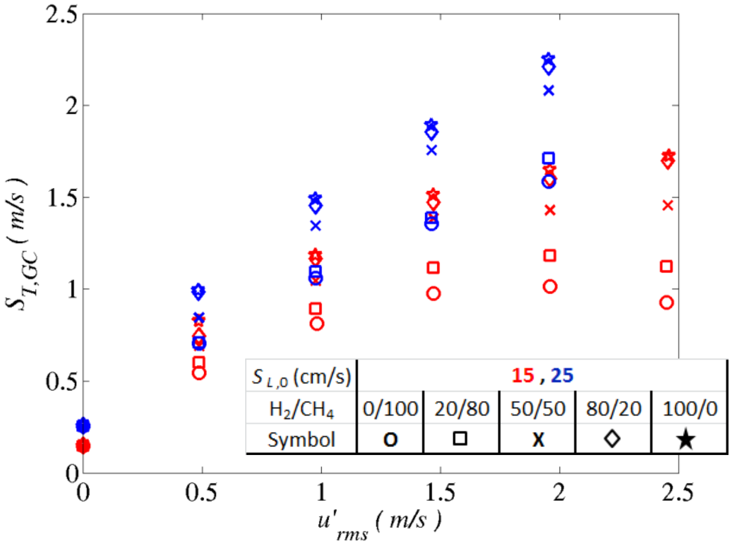

Figure 51: $S_{T,GC}$ as a function of u'_{rms} for the data reported in Ref.[34].

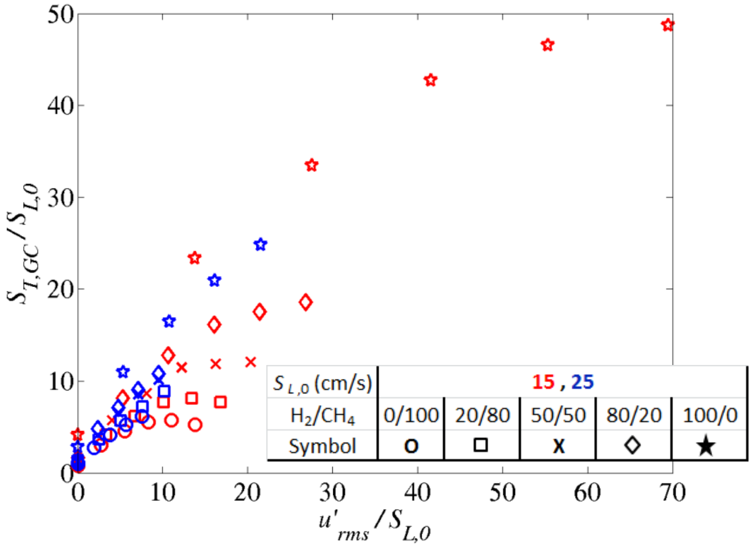

Figure 52: $S_{T,GC}$ as a function of u'_{rms} normalized by $S_{L,0}$ for the data reported in Ref. [34].

The final spherical bomb data set presented is by Kitagawa *et al.* [52]. The data was acquired in a different, but similar, experimental facility to that depicted in Figure 46. The combustion vessel is comprised of three 265 mm diameter cylinders, which intersect orthogonally to produce a volume corresponding to a 40.6 cm diameter spherical chamber. Two fans are mounted on the top and bottom of the vessel to mix the gases and generate isotropic turbulence in the central region. Once the desired mixture is injected and mixed in the vessel it is centrally ignited.

The flame propagation is visualized using Schlieren photography, and S_T is determined from the time rate change of the average flame radius. At a given instant, the average flame radius is derived by calculating a circle which has an equivalent area to the experimentally observed flame.

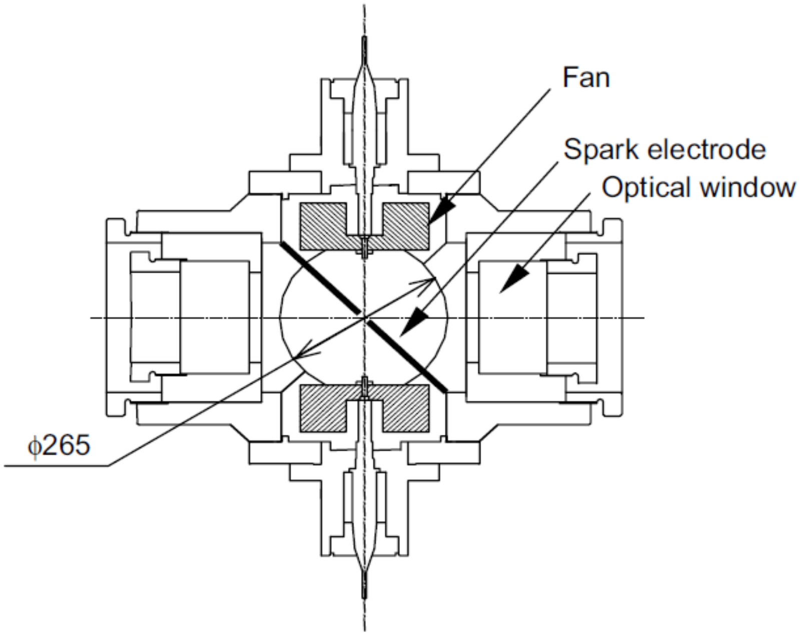

Figure 53: Schematic of experimental facility used to measure S_T in Ref. [52].

Data were acquired for pure H_2/air mixtures at ϕ = 0.4, 0.6 , 0.8 and 1.0 and pressures of 1, 2.5 and 5 atm. Figure 54 and Figure 55 plot these data on a linear and log plot respectively.

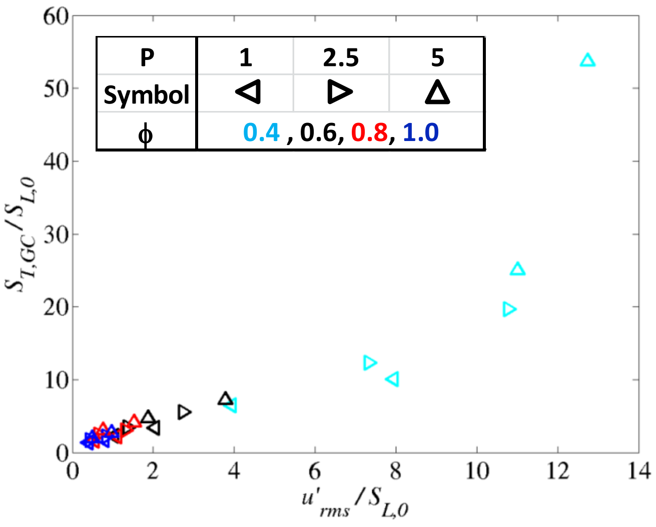

Figure 54: Linear plot of $S_{T,GC}$ as a function of u'_{rms} normalized by $S_{L,0}$ for the data reported in Ref. [52].

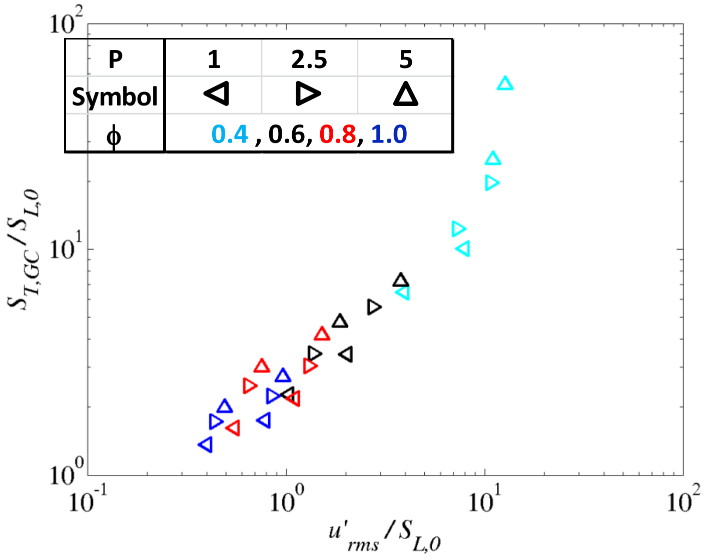

Figure 55: Log plot of $S_{T,GC}$ as a function of u'_{rms} normalized by $S_{L,0}$ for the data reported in Ref. [52].

Note that for a given equivalence ratio, $S_{T,GC}/S_{L,0}$ increases with pressure. However, similar to the PSI database, this is most likely due to $S_{L,0}$ decreasing with pressure at a fixed equivalence ratio. Figure 56 plots the un-normalized data, and the dependence of $S_{T,GC}$ on pressure appears to depend on the mixture equivalence ratio. As a result, it is difficult to make arrive at any conclusions regarding the influence of pressure.

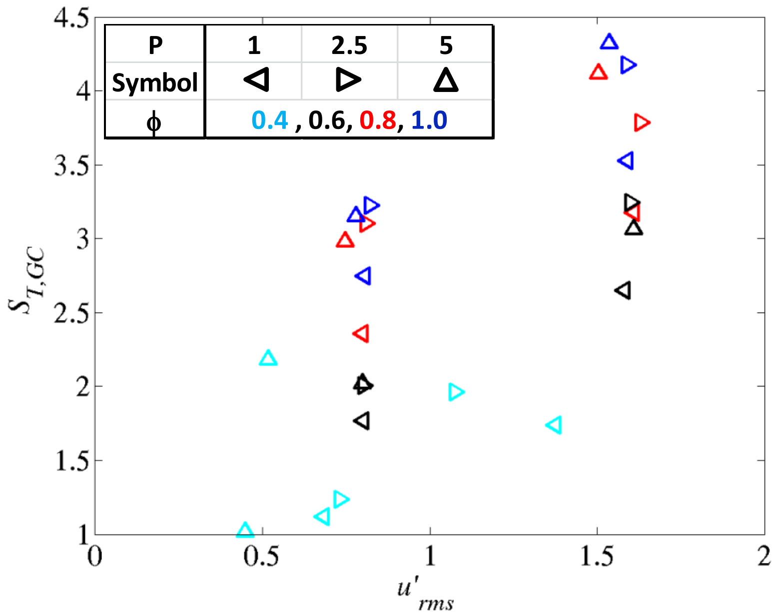

Figure 56: Plot of $S_{T,GC}$ as a function of u'_{rms} for the data reported in Ref. [52].

Finally, Figure 57 plots the entire spherical bomb data together. This is done mainly to facilitate the discussion on flame speed modeling in the following chapter.

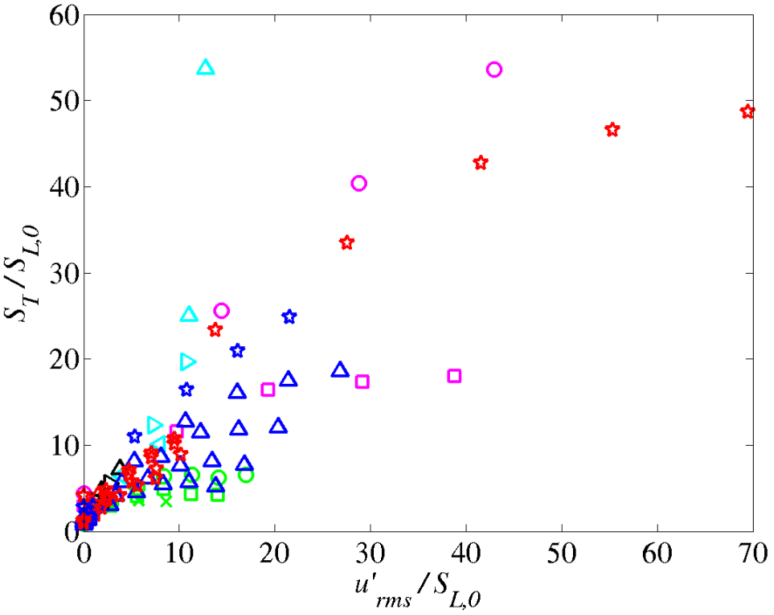

Figure 57: $S_{T,GC}$ as a function of u'_{rms} normalized by $S_{L,0}$ for the entire spherical bomb database. Legend has been carried over from the individual datasets.

3.2.3 Low swirl burner database

This section reviews the measurements of local turbulent displacement speed, $S_{T,LD}$, reported in Ref. [87-89]. These data were acquired using the low-swirl burner (LSB) at the Lawrence Berkeley National Laboratories (LBNL) and for the purposes of this thesis, will be referred to as the ‘Low swirl burner database’. The LSB is a recommended configuration in which to quantify the turbulent local displacement speed, $S_{T,LD}$ [16].

A schematic of the LSB is given in Figure 58. The burner consists of a swirler section of length L_S = 2.8 cm, and an outer radius of R_i = 3.17 cm, and sixteen curved vanes, of vane angle 42° at the exit, attached to the outer surface of the center-channel of radius R_c = 2 cm. The ratio of the distance from the swirler to the burner exit to the swirler diameter, $L_i/(2R_i)$, is about 1.5. The open center-channel allows a portion of the reactant flow to remain un-swirled and this non-swirling flow inhibits flow recirculation and promotes formation of a divergent flowfield, which is a key feature of the flame stabilization mechanism. This divergent flowfield results in an axially decaying flow field along the centerline of the burner, and the flame stabilizes where the turbulent flame speed matches the local axial mean flow velocity. Furthermore, along the centerline the turbulent flame brush is statistically one-dimensional and $S_{T,LD}$ can be determined from measuring the mean axial flow velocity just upstream of the turbulent flame brush.

In the data reproduced here, the velocity field was characterized using PIV, and $S_{T,LD}$ is defined at the point where the centerline mean flow velocity deviates from its initial linear decay [90].

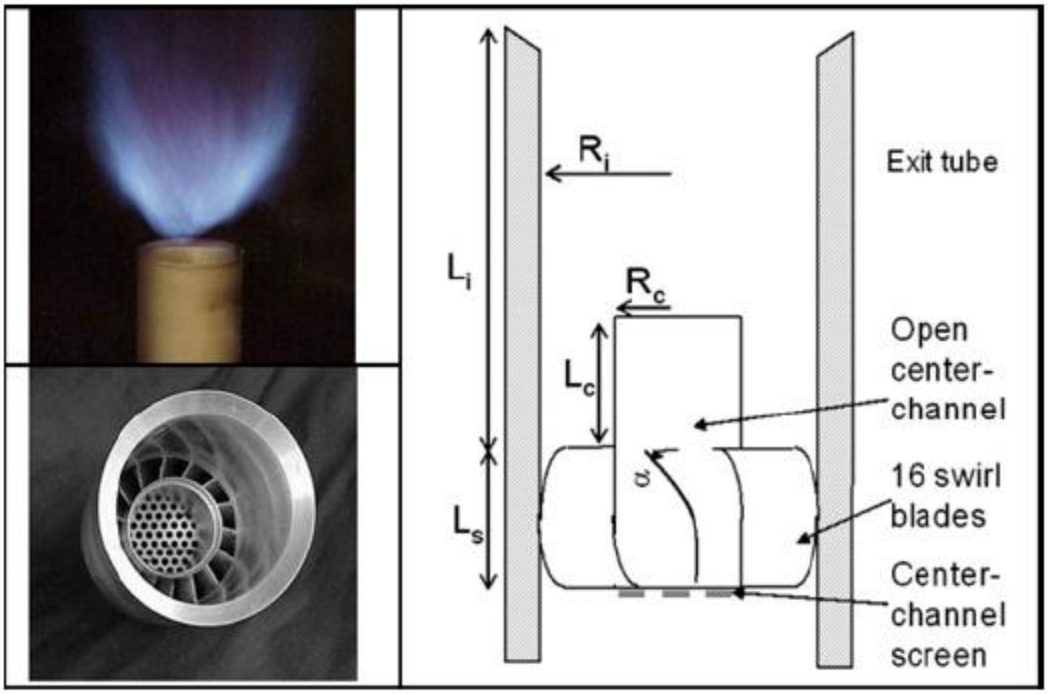

Figure 58: Schematic and photograph of the low-swirl burner. Figure adapted from Ref.[90].

Measurements of $S_{T,LD}$ were obtained at 1 atm and 300 K for a variety of mixtures which are outlined in Table 6. The legend used to plot the data is also incorporated into Table 6. Turbulence is generated by a grid in the center-channel through which the non-swirling flow passes. The turbulence intensity for a given mixture is then varied by changing the mean flow velocity. The location of the data on the Borghi-Peters diagram is shown in Figure 59.

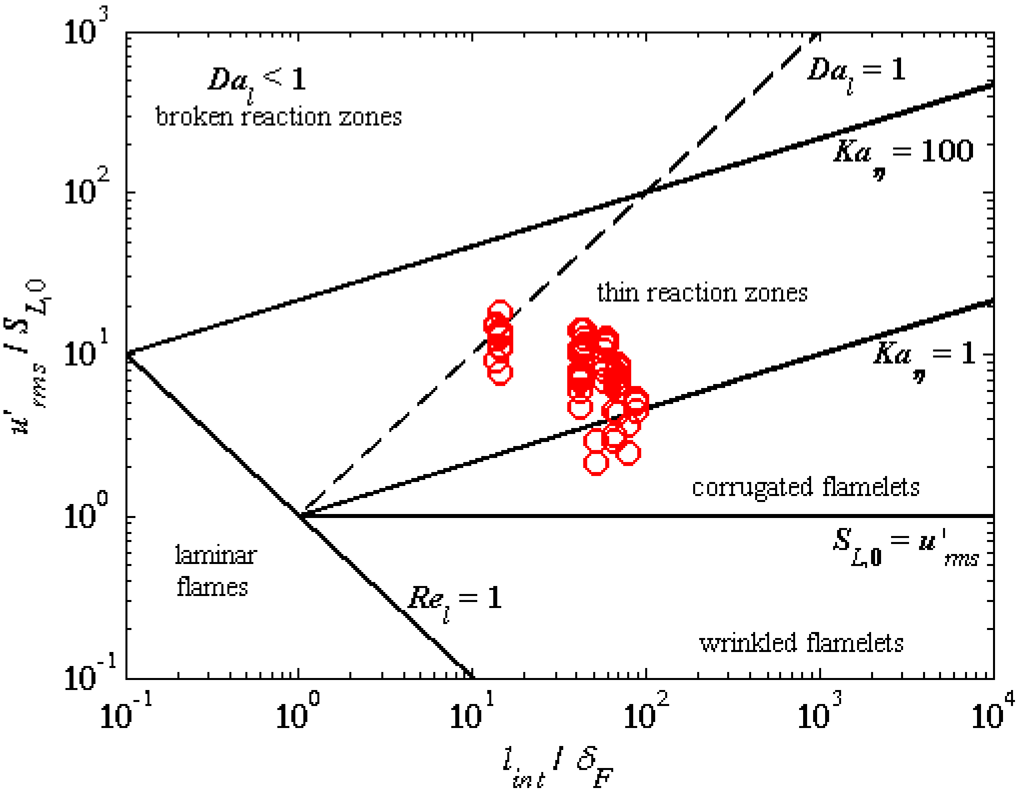

Figure 59: Location of the low swirl burner database on the Borghi-Peters diagram.

Table 6: Mixtures investigated in the low swirl burner database, along with the plot symbols utilized.

Fuel	CH_4/CO_2 = 50/50	CH_4/H_2 = 50/50	CH_4/H_2 = 60/40	$H_2/CO/CH_4$ = 20/40/40
Symbol	+	X	◁	◇
ϕ	0.83	0.65	0.65	0.58

Fuel	$H_2/CO/CO_2$ = 30/30/40	H_2/CO = 60/40	H_2/N_2 = 75/25	H_2	CH_4/N_2 = 60/40
Symbol	★	✡	○	△	□
ϕ	0.55 0.64	0.45	0.31 0.37	0.30 0.35 0.38	0.76

Figure 60 plots $S_{T,LD}$ as a function of u'_{rms} all normalized by $S_{L,0}$. Although this work investigates a broad range of fuels, it is difficult to make conclusions about fuel effects in this data since a variety of parameters are being changed simultaneously. However, a few conclusions were derived from this work. Firstly, the ‘bending effect’ that has been observed in other data, such as the one presented in Figure 12, does not appear to be present here. Secondly, it was shown that $S_{T,GC}/S_{L,0}$ could be correlated linearly with $u'_{rms}/S_{L,0}$, with the slope of the fit for the H_2 blends being higher than that for the CH_4 blends.

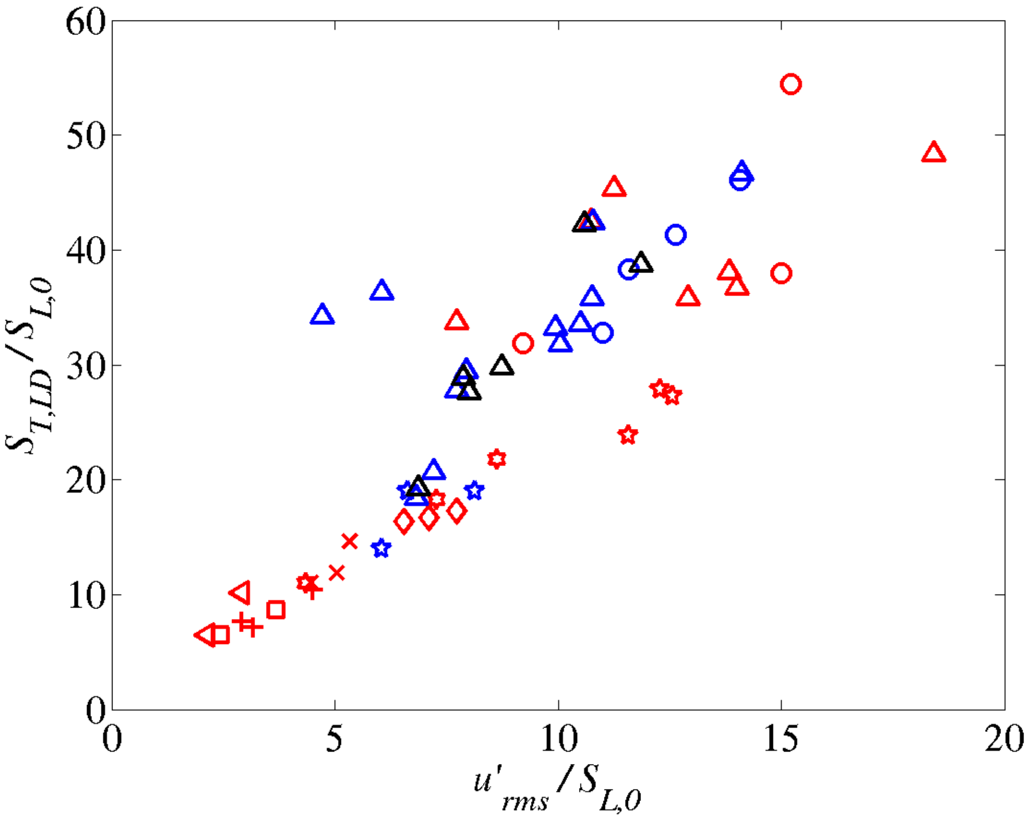

Figure 60: $S_{T,GC}$ as a function of u'_{rms} normalized by $S_{L,0}$ for the data reported in Ref. [87-89] (See Table 6 for legend).

3.3 Discussion of uncertainties in the progress variable field

This section delves deeper into the impact of the flame imaging technique on the observed trends, an issue alluded to in Sec. 3.1.2. In particular, we focus on the constant $S_{L,0}$ studies where we noted the presence of the fuel effects, which has been one of the focus areas of this thesis.

There is a possibility that the progress variable field based on the chemiluminescence measurements can be biased due to the fuel composition. To explain this point more fully, consider Figure 61, which is a notional plot of the pdfs of heat release rate and [OH*] through the flame brush. If the ‘true’ flame brush is assumed to be captured by the heat release, then a variation of the offset, Δx, with fuel composition is of interest. This is an important consideration since there could then be a situation where although the location of maximum [OH*] is moving closer to the burner (shorter flame) with increasing H_2 content, the location of maximum of heat release may not vary as much, suggesting that the observed fuel effects might not be strictly physical but a manifestation of the measurement technique employed.

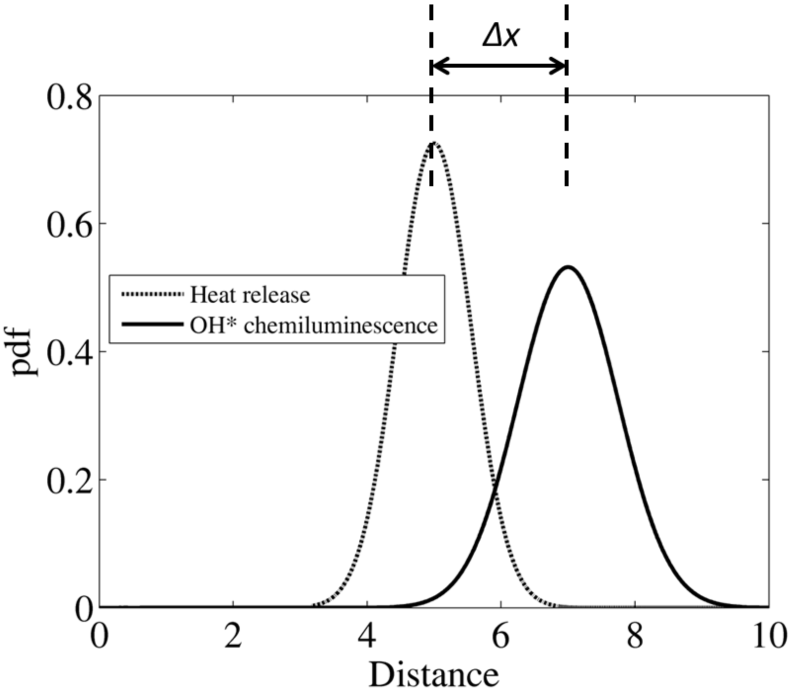

Figure 61: Notional plot of the pdf of heat release and [OH*] through a flame brush.

Recognizing that the heat release may not be properly characterized by the chemiluminescence measurements, Lauer *et al.* [91] derived a correction factor which converted the chemiluminescence measurements to heat release rates for CH_4/air flames. The correction factor was derived from an energy balance which related the local heat release to the local mass flow rate and temperature. The temperature was estimated from the local equivalence ratio, determined from the ratio of [OH*] and [CH*], while the local mass flow rate was determined from the local velocity obtained from PIV measurements.

To investigate this relationship between the heat release rate and chemiluminescence further, the first step is to recognize that the integrated OH* chemiluminescence and integrated heat release are stretch sensitive properties, as shown in Figure 62 and Figure 63, respectively. These results were derived from simulating a symmetric opposed-flow configuration in Chemkin's OPPDIF package. In this configuration twin flames are stabilized on either side of the resulting stagnation plane, and are subjected to only tangential strain. Complete details of these calculations are provided in Chapter 4.

Figure 62 plots the normalized integrated OH* chemiluminescence, defined by Eq. (3.3), through the flame for the mixtures studies in the constant $S_{L,0}$ studies at 1 and 10 atm. Figure 63, plots the normalized integrated heat release, defined by Eq. (3.4), through the flame for same mixtures and conditions.

$$\left[OH*\right] Ratio = \frac{\int_{0}^{L} \left[OH*\right] dx}{\int_{-\infty}^{\infty} \left[OH*\right]_{0} dx} \tag{3.3}$$

$$HR\ Ratio = \frac{\int_{0}^{L} \dot{q}\, dx}{\int_{-\infty}^{\infty} \dot{q}_{0}\, dx} \tag{3.4}$$

In Eq. (3.3) and (3.4), $[OH^*]_0$ and $\dot{q}_0$ correspond to the un-stretched values of [OH*] and heat release rates. The domain of integration for the stretched flames is from the burner exit to the stagnation plane, *L*. The calculation of [OH*] follows the work by Nori [92].

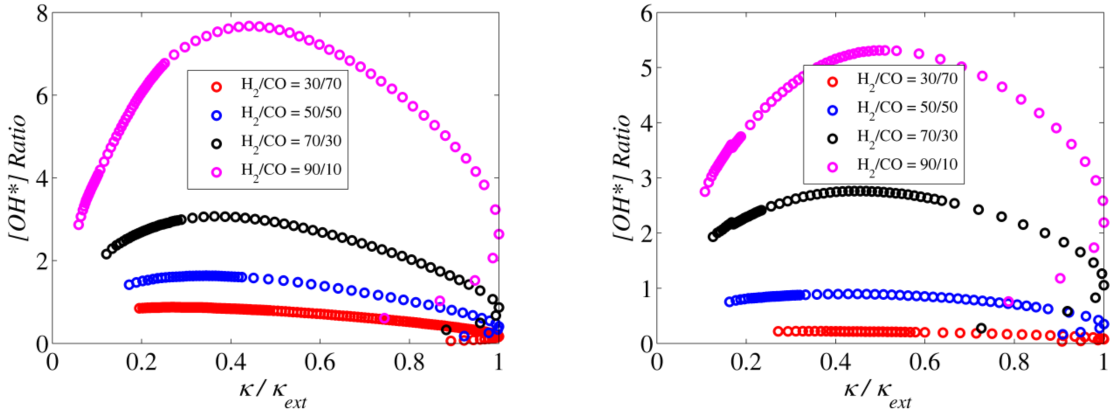

(a) (b)

Figure 62: Variation of the normalized integrated OH* chemiluminescence as a function of the normalized strain rate for the constant $S_{L,0}$ studies at (a) 1 atm and (b) 10 atm.

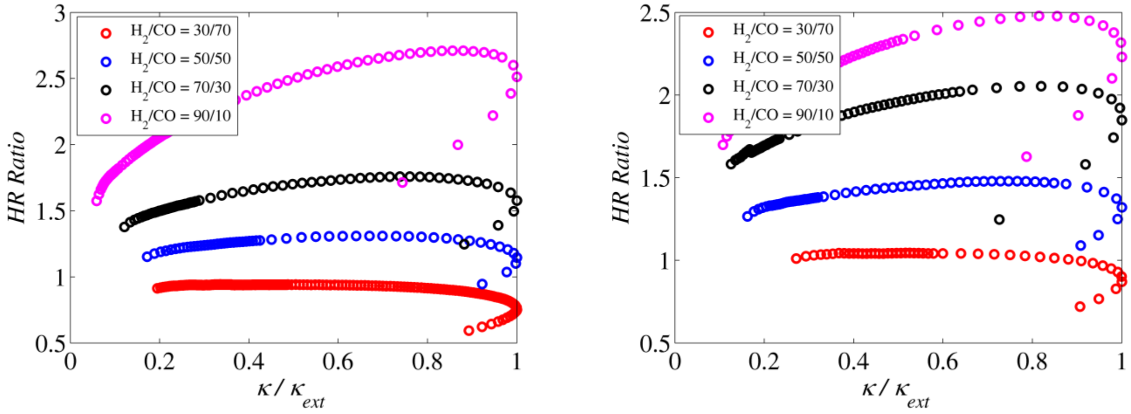

(a) (b)

Figure 63: Variation of the normalized integrated heat release rate as a function of the normalized strain rate for the constant $S_{L,0}$ studies at (a) 1 atm and (b) 10 atm.

The average heat release rate and [OH*] at a point in the flame brush, *x*, can be calculated from Eq. (1) and Eq. (2) respectively:

$$\langle \dot{q} \rangle (x) = \int_{-\infty}^{\infty} \dot{q}(\kappa)\, p(\kappa | x) d\kappa \tag{3.5}$$

$$\langle [OH^*] \rangle (x) = \int_{-\infty}^{\infty} [OH^*](\kappa)\, p(\kappa | x) d\kappa \tag{3.6}$$

The key input required to determine the $\langle \dot{q} \rangle (x)$ and $\langle [OH^*] \rangle (x)$ is the stretch rate pdf conditioned on the location in the flame brush, $p(\kappa | x)$. This quantity needs to be considered carefully in the analysis. Recall from Eq. (1.18), that the stretch rate has two contributors; tangential strain rate and stretch due to flame curvature and motion. In the study by Lauer *et al.*[91], only the tangential strain rate was considered because the tangential stretch response of flames can be calculated using commercial software such as Chemkin's OPPDIF module. The tangential strain rate pdf was also assumed to be constant through the flame brush. From Eq. (3.5) and (3.6), it is straightforward to see that the progress variable fields for the heat release and chemiluminescence will be identical if the curvature pdf does not vary through the turbulent flame brush, i.e., $p(\kappa | x) = p(\kappa)$.

However, Day *et al.*[93] demonstrated that the curvature pdfs conditioned on the progress variable do vary through the flame brush for a CH_4/air mixture. The variation can be expected to be more pronounced for lean H_2/CO mixtures since they are more stretch sensitive than CH_4/air mixtures. However, to our knowledge there are no works that explore the variation in the conditioned pdfs of strain rate or curvature-induced-stretch through the flame brush for varying fuel mixture compositions. As a result, it is difficult to make the assessment of how the progress variable fields between the heat release and chemiluminescence field vary with fuel composition.

The problem can be simplified considerably if the heat release and chemiluminescence rate can be shown to be proportional. If this is the case, then the progress variables from the two measurements are identical, even if the stretch rate pdf varies through the flame brush. To investigate this point, Figure 64 plots the relationship between the heat release ratio (Eq.(3.3)) and the chemiluminescence ratio (Eq.(3.4)) at 1 and 10 atm. The point corresponding to the extinction strain rate is indicated by the large circle.

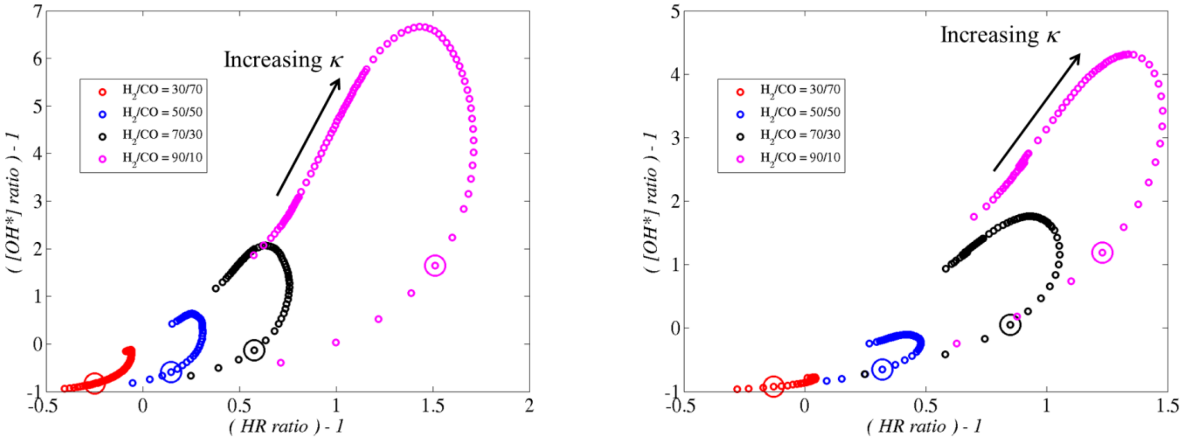

(a) (b)

Figure 64: Ratio of the normalized OH* chemiluminescence to the normalized heat release rate as a function of normalized strain rate for variation H_2/CO mixtures at constant $S_{L,0}$ at (a) 1 and (b) 10 atm.

Note from Figure 64 that there is a range of strain rates, below the extinction strain rate, over which the heat release rate and the chemiluminescence are linearly related. However, it is also apparent that the nonlinearity sets in well before the extinction strain rate. As a result, if the strain rates experienced by the flame are primarily in the linear range, then the progress variables would not be expected to be biased by fuel composition.

Although further work is needed to determine the stretch rates experienced by the flame front at different locations within the turbulent flame brush, for the purposes of this work, it is assumed that any biases present are not sufficient to counteract the observed fuel effects.

Chapter 4
Analysis of Flame Speed Data

4.1 Introduction

This chapter focuses on the development of a physics-based model for the turbulent flame speed using quasi-steady-state leading points concepts. The observed fuel effects trends in the turbulent flame speed have been attributed to the mixture stretch sensitivity, which can be incorporated into the leading points framework.

This chapter starts with a discussion of the stretch sensitivity of the mixtures studied in the experimental portion of this work. Particular attention is paid to the dependence of the high stretch rate characteristics on fuel composition and pressure variations.

The next part of the chapter focuses on the development of the model using leading points concepts. The resulting model closely resembles Damköhler's classical expression for the turbulent flame speed except the normalizing parameter that arises from the analysis is $S_{L,max}$. This scaling law is then applied to the different databases presented in Chapter 3.

The chapter concludes with an exploration of the possible causes for the observed scatter in the normalized data, with particular emphasis on chemical non-quasi-steady effects.

4.2 Stretch sensitivity calculations

4.2.1 Preliminaries

As discussed in Chapter 1, a flame is said to be stretched if neither the flame nor the flow are one-dimensional. This can occur if there are flow gradients tangential to the flame front, and/or flame curvature, and flame motion. These effects result in the misalignment of the convective and diffusive processes that alter the local flame temperature, and consequently, burning velocity.

Commercial software such as CHEMKIN's OPPDIF [28] package allow for the calculation of a flame's steady-state stretch response. The OPPDIF module can simulate the three configurations shown in Figure 65.

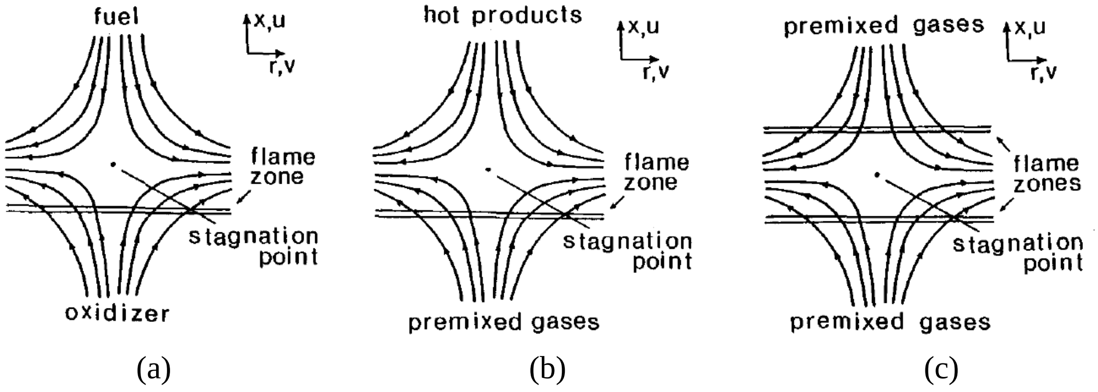

(a) (b) (c)

Figure 65: Illustrations of the different configurations that can be simulated using the OPPDIF module. Figure adapted from Ref. [94].

In this particular work, the axisymmetric version of the configuration depicted in Figure 65(c) is simulated with a nozzle separation of 20 mm. The governing equations of mass, species and energy conservation are simplified by assuming that the radial velocity, *v*, varies linearly in the radial direction, *r*, which leads to a simplification that all other fluid properties are only a function of the axial co-ordinate, *x* [95]. The resulting one-dimensional model then represents the variations in the flow properties along the centerline stagnation streamline.

Stretch sensitivity calculations are performed for all the mixtures investigated in Chapter 3, which includes the Georgia Tech database and the other databases extracted from the literature. For each mixture and condition, the calculations are done in two parts. For the low to intermediate strain rates, the OPPDIF module is utilized. From these calculations the Markstein length, l_M, of the mixture could be extracted, as shown in Figure 66. However, at the higher strain rates, particularly at conditions nearing extinction, numerical difficulties are encountered since the Jacobian becomes singular. The OPPDIF module is not well-suited to determine the stretch response in this region, and the Extinction Simulator is utilized instead, which solves the problem using a numerical approach known as the arc-length continuation [28]. The extinction simulations are initialized with the results of the OPPDIF calculations. Similar to the $S_{L,0}$ calculations presented in Sec. 3.1.1, stretch sensitivity calculations for the H2/CO mixtures were performed using the Davis mechanism [70], while the GRI mechanism [71] was used for the CH_4/air mixtures.

4.2.2 Characteristics of $S_{L,max}$

In this section we review the stretch characteristics of the flames investigated in this work. In particular, for reasons to be discussed below, we focus on the high stretch rate characteristics, namely the maximum stretched laminar flame speed, $S_{L,max}$, which is indicated in Figure 66.

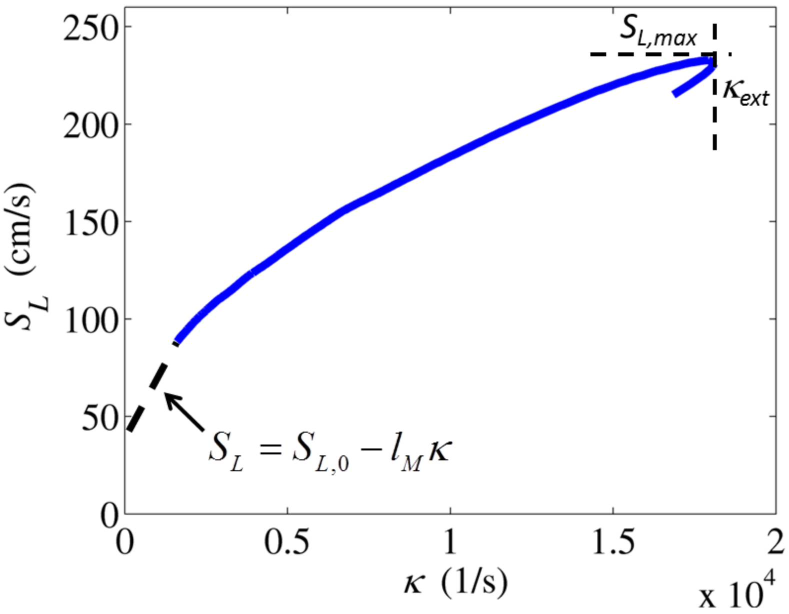

Figure 66: illustration of the high and low characteristics of a negative Markstein fuel blend. Calculation performed for a ϕ=0.5, H_2/air mixture at STP.

It is instructive to remind ourselves that the laminar flame speed can be defined using a consumption or displacement speed. When the flame is un-stretched, both definitions yield identical values. However, when the flame is stretched, these definitions can yield different values, as illustrated with an example calculation in Figure 67. The calculation is performed for a ϕ = 0.55, 50/50 H_2/CO mixture at STP. The displacement flame speed, $S_{L,D}$, is defined as the minimum velocity just ahead of the reaction zone, as suggested by Wu and Law [96]. The consumption flame speed can be based on a species (SC) or heat release consumption (HR) rates given by Eq.(4.1) and (4.2) respectively [97]. For illustrative purposes, the species consumption rate in Figure 67 is based on H_2.

$$S_{L,SC} = \frac{\int_{-\infty}^{\infty} \dot{\omega}_{H_2} dx}{\rho_u \left(Y_{H_2,\infty} - Y_{H_2,-\infty} \right)} \tag{4.1}$$

$$S_{L,HR} = \frac{\int_{-\infty}^{\infty} \dot{q} dx}{\rho_u \left(h_{sens,\infty} - h_{sens,-\infty} \right)} \tag{4.2}$$

It is apparent from Figure 67 that Markstein lengths based on different laminar flame speed definitions can also vary.

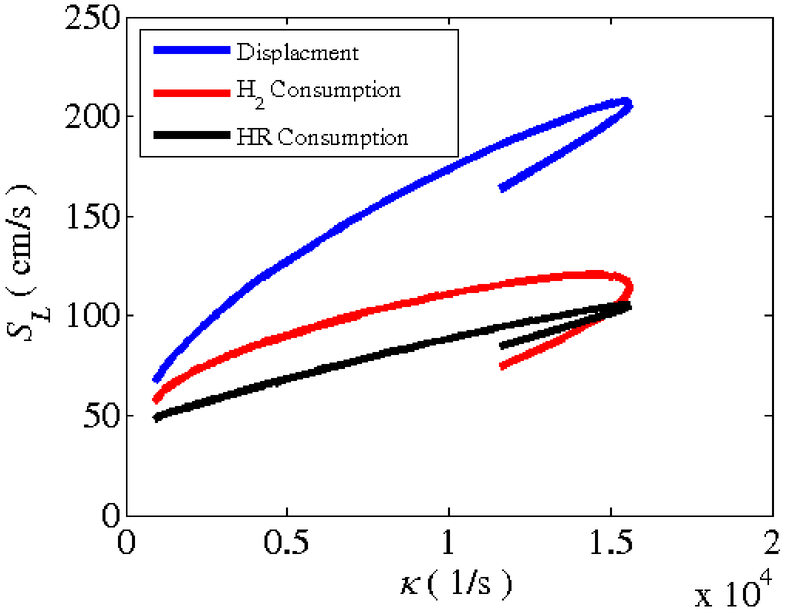

Figure 67: Differences in stretched flame characteristics depending on the laminar flame speed definition used. Calculation is for a 50/50 H_2/CO mixture at ϕ=0.55 at STP.

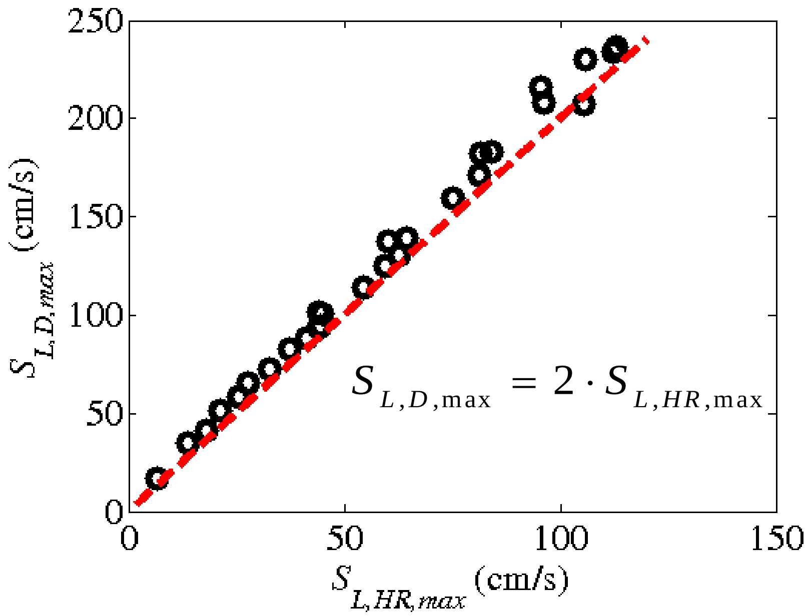

Figure 68: Relationship between $S_{L,max}$ based on displacement speed definition and thermal consumption for all mixtures studied in this work. Also shown for reference in red is a line of slope 2.

Figure 68 plots the relationship between $S_{L,max}$ derived from a displacement speed definition and a heat release consumption based definition for all the mixtures in the Georgia Tech database at pressures up to 10 atm. It is interesting to note that $S_{L,max}$ based on the displacement speed definition appears to be consistently double the $S_{L,max}$ based on the heat release consumption definition.

For comparison, Figure 69 plots the relationship between $S_{L,max}$ derived from a displacement speed definition and the species consumption speed based on H_2 and CO, given by Eq.(4.1), for all the mixtures in the Georgia Tech database at pressures up to 10 atm.

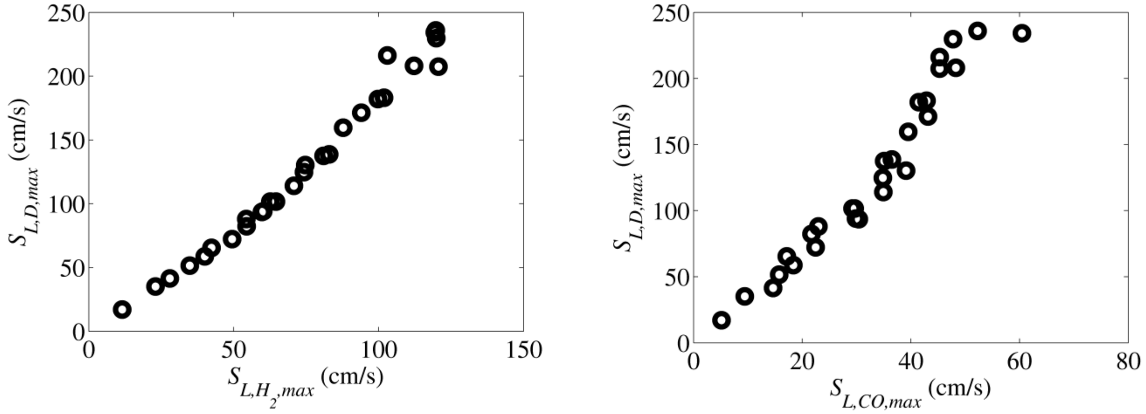

(a) (b)

Figure 69: Relationship between $S_{L,max}$ based on displacement speed definition and species consumption speed based on (a) H_2 and (b) CO, for all mixtures studied in this work.

We focus on the relationship between the displacement speed and heat release consumption speed for a few important reasons. First, the model for the turbulent flame speed, which will be developed in the subsequent sections of this chapter, is based on kinematic arguments for the instantaneous turbulent flame front for which a displacement speed is a natural choice to describe the flame front propagation. However, when we looked to extend the model to other data in the literature, certain issues arose. In particular, the PSI database is acquired at highly preheated conditions and for these conditions there is no minimum in the velocity profile at high stretch rates, making the displacement speed definition more arbitrary. As a result, for those data, the laminar flame speed based on the heat release consumption is utilized in the model. In addition, to facilitate comparisons, the heat release consumption speed definition is also used when scaling the Georgia Tech database.

Second, since multicomponent fuel mixtures are a focus of this study, it is not apparent which species is most appropriate to base a species consumption speed on. This is not an issue with the heat release consumption speed since all species are considered in its calculation.

Third, there are some mixtures where the Markstein length based on the species consumption speed is positive, in which case $S_{L,max}$ takes on the value of $S_{L,0}$ and not a value that lies closer to the value corresponding to the extinction strain rate. An example is shown in Figure 70, where the flame speed based on the CO consumption shows a positive Markstein length behavior, while the other definitions show a negative Markstein length behavior.

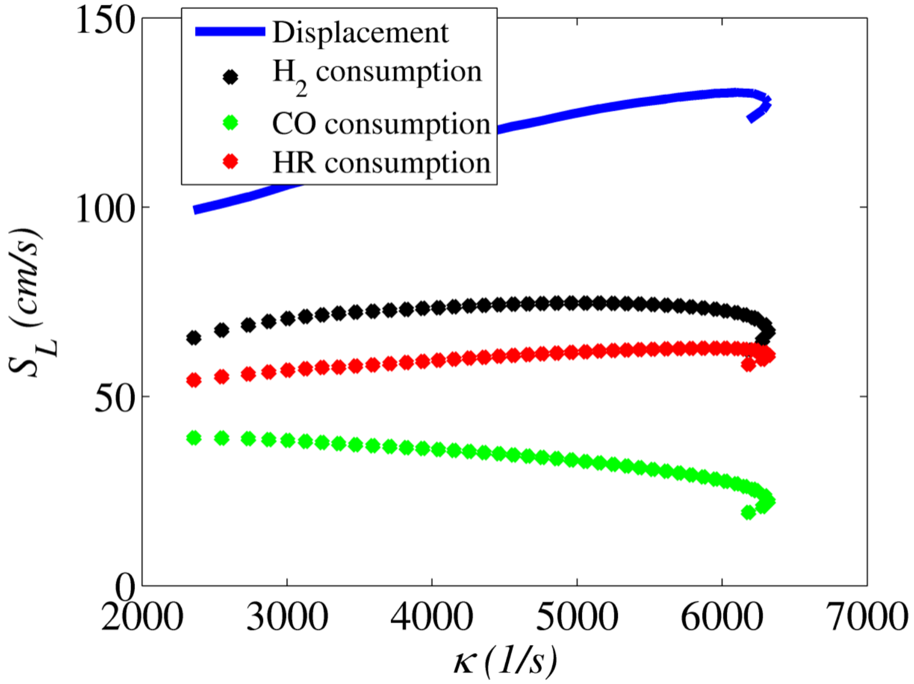

Figure 70: Dependence of stretch response of a ϕ = 0.80 30/70 H_2/CO mixture at 1 atm on the definition of the laminar flame speed.

The rest of this section focuses on the influence of fuel composition and pressure on the $S_{L,max}$ of H_2/CO mixtures. Figure 71 plots the stretch response of various H_2/CO mixtures whose equivalence ratios have been adjusted to maintain a constant $S_{L,0}$ of 34 cm/s at 1 atm and 300 K.

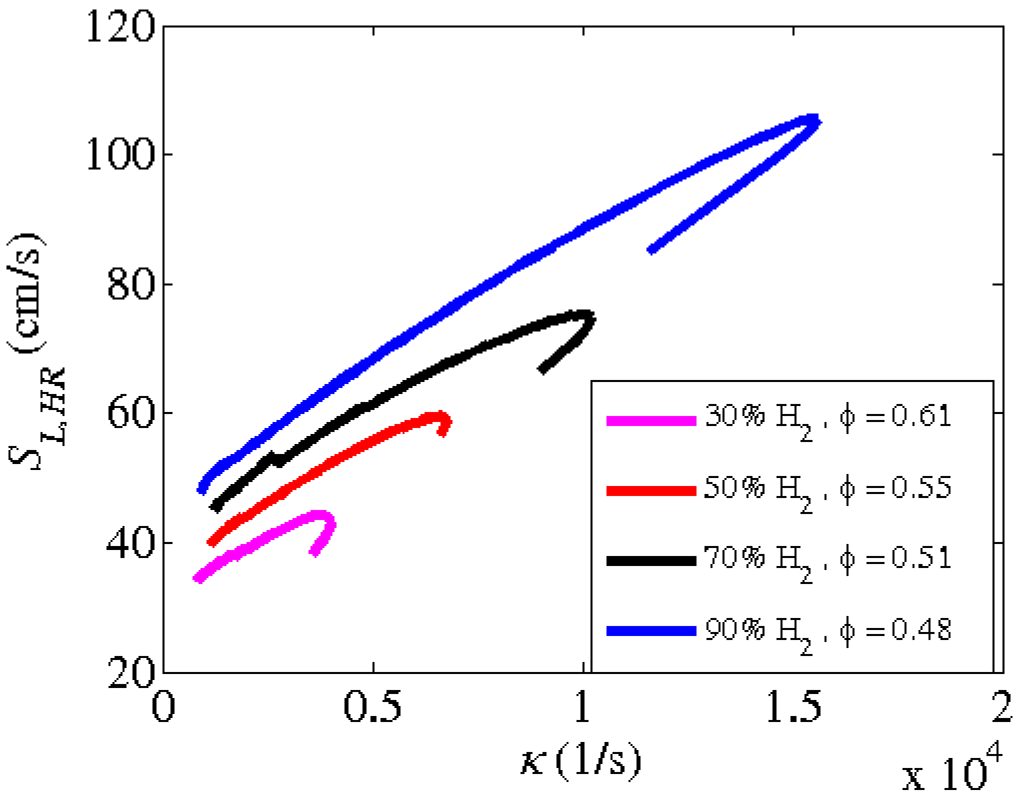

Figure 71: Stretch sensitivity of various H_2/CO mixtures all having the same $S_{L,0}$ at 1 atm and 300 K.

Note from Figure 71 that all the mixtures converge towards the same $S_{L,0}$ at $\kappa = 0$. However, all the mixtures have different Markstein lengths and extinction strain rates. More specifically, as the H_2 content in the fuel is increased while maintaining the mixture $S_{L,0}$, the absolute value of the Markstein length increases, suggesting that mixture is more stretch sensitive. In addition, $S_{L,max}$ and κ_{ext} for the mixture also increases monotonically with hydrogen content.

Some further insight into fuel compositional effects can be gained from Figure 72, which plots the stretch sensitivity of various mixtures of constant H_2/CO ratio, but different equivalence ratios.

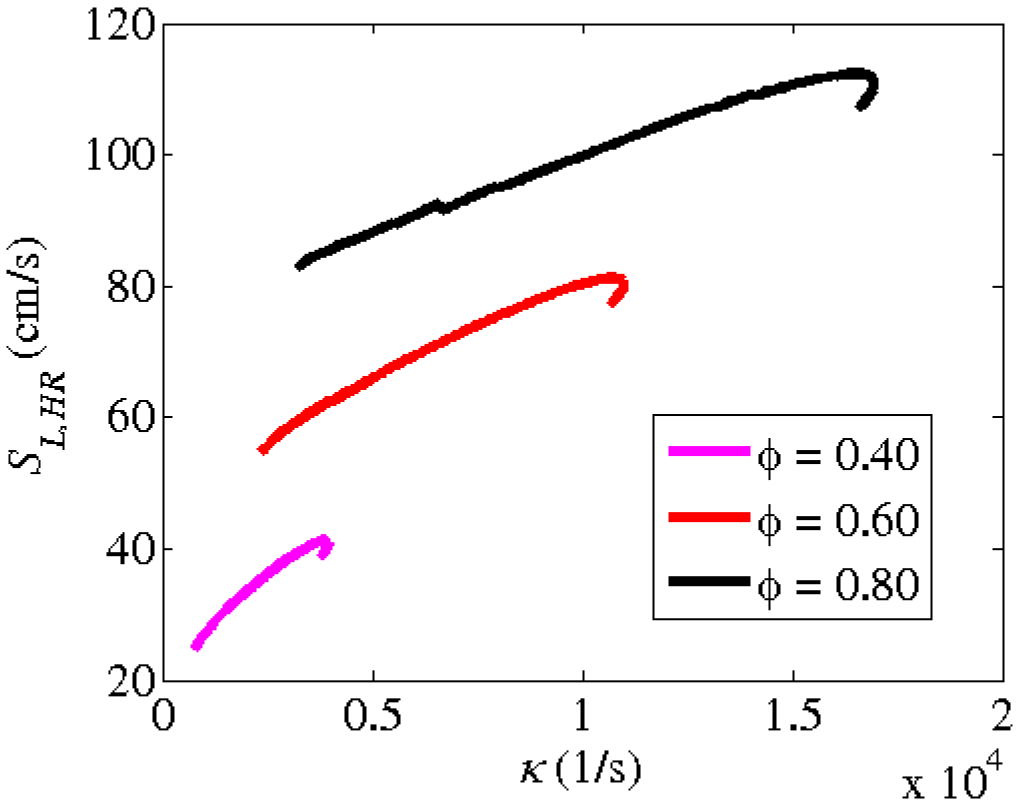

Figure 72: Stretch sensitivity of H_2/CO = 60/40 mixtures of different equivalence ratios at 1 atm and 300 K.

Note from Figure 72 that the leaner the mixture, the larger the magnitude of the mixture Markstein length. This is consistent with theory and experimental findings that report increasing $|l_M|$ as a H_2/air mixture is made leaner [1]. However, $S_{L,max}$ and κ_{ext} decrease with equivalence ratio since the flame temperatures, and consequently, the burning intensity are decreasing with the equivalence ratio.

Figure 73 plots the stretch response of 50/50 H_2/CO mixtures for different pressures. The mixture $S_{L,0}$ of these mixtures is held constant by adjusting the equivalence ratio at each pressure.

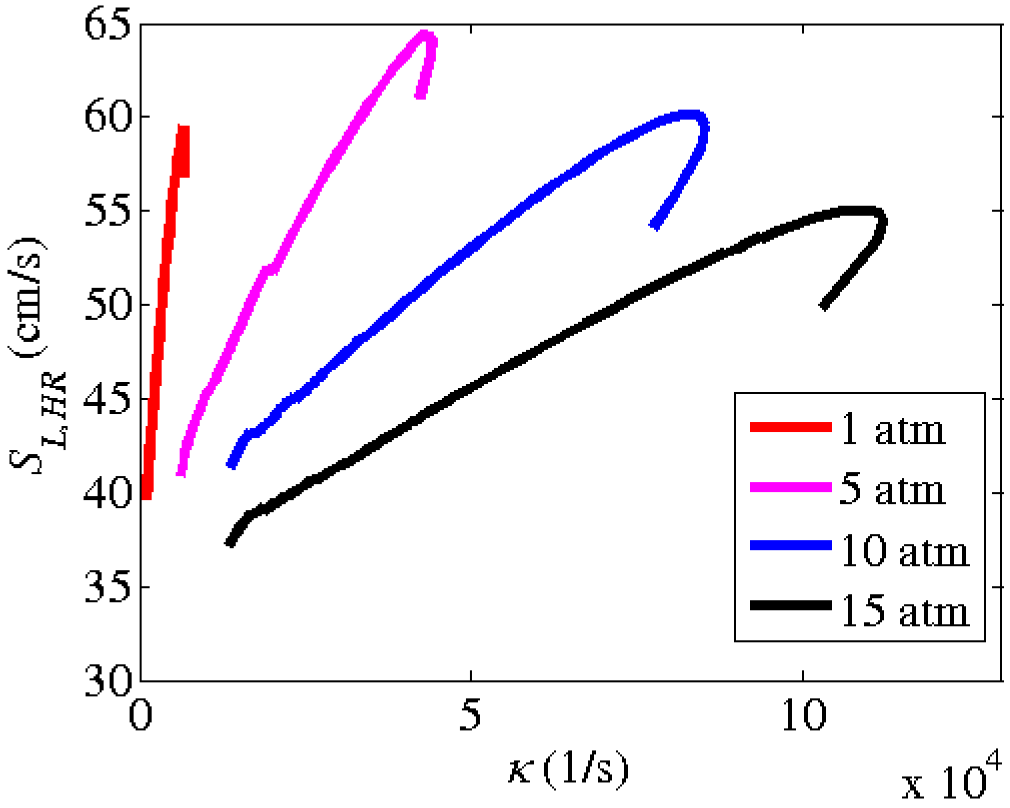

Figure 73: Stretch sensitivity of H_2/CO = 50/50 mixtures at constant $S_{L,0}$ across different pressures.

Note from Figure 73 that the extinction stretch rate and the Markstein length scale with the pressure. In other words, if the pressure is increased by a factor of 5, the extinction stretch rate and Markstein length increase and decrease by a factor of approximately 5, respectively. This can be explained by the thinning of the flame with pressure. These two effects compensate so that $S_{L,max}$ is relatively insensitive to pressure, as illustrated in Figure 74. In fact, above 5 atm $S_{L,max}$ remains almost constant and actually decreases beyond about 12.5 atm.

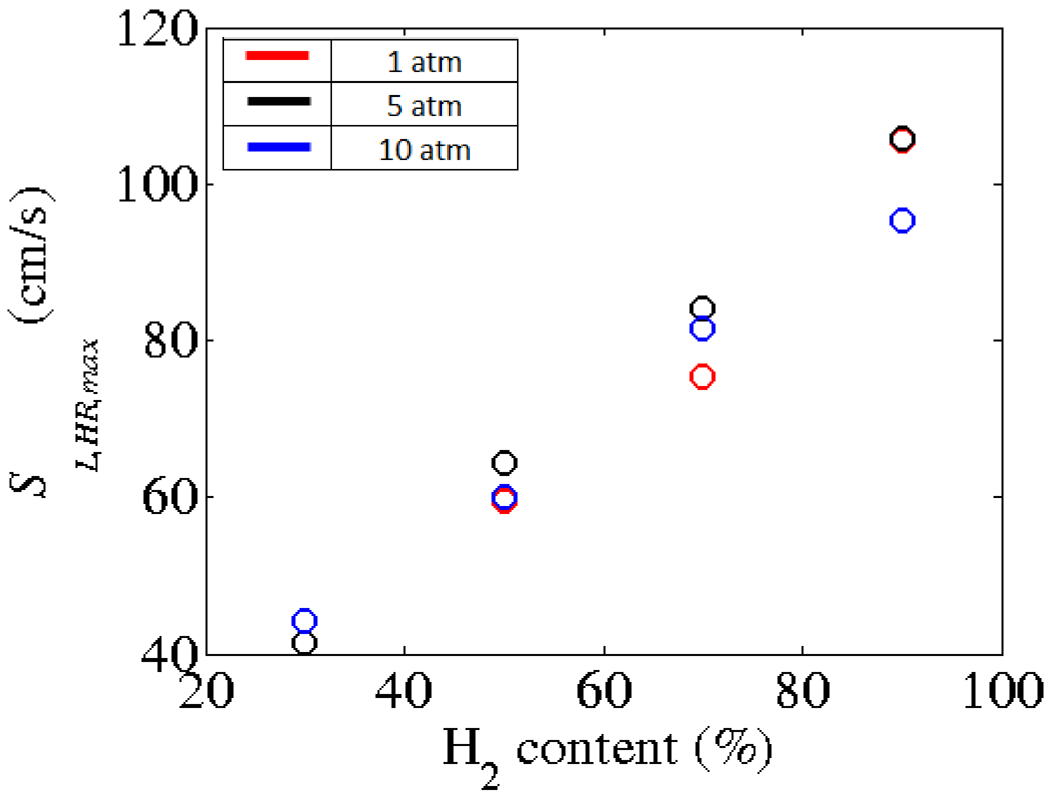

Figure 74: Variation of $S_{L,max}$ based on heat release consumption as a function of H_2 content at different pressures for the constant $S_{L,0}$ studies.

The differences in the low and high stretch rate behavior, highlighted in Figure 73, have important implications for turbulent flame speed modeling. This point will be explored in greater detail in the subsequent section which will focus on capturing coupled fuel and pressure effects on the turbulent flame speed.

4.3 Leading Points Concepts

The observed trends in the $S_{T,GC}$ data obtained in this work are consistent with prior studies showing that stretch sensitivity of the reactants has an important impact on the turbulent flame speed [12, 43]. This point is shown in Figure 75, which plots the dependence of these data upon calculated Markstein length of the reactants at two different turbulence intensities for the constant $S_{L,0}$ studies obtained at STP with the 20 mm diameter burner. The point located at l_M = -0.02 for $u'_{rms}/S_{L,0} = 20$ corresponds to the methane-air mixture at ϕ = 0.9. Note the monotonically increasing value of $S_{T,GC}$ with $|l_M|$. The difference in flame speeds between low and high H_2 flames for the H_2/CO blends and the CH_4/air and H_2/CO/air flames is significant, being as large as two and three, respectively.

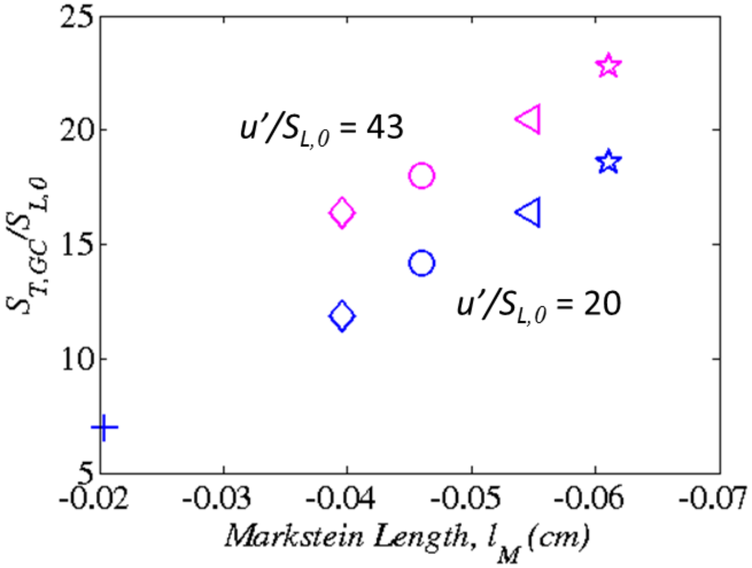

Figure 75: Dependence of $S_{T,GC}/S_{L,0}$ upon Markstein length, l_M, for $u'_{rms}/S_{L,0}$ = 20 and 43 at $S_{L,0}$ = 0.34 m/s.

To incorporate this effect, some workers have included stretch sensitivity characteristics into correlations by using the mixture Markstein length [35, 84, 85]. These approaches capture some aspects of the fuel composition sensitivity of S_T, as measurements typically show increased turbulent flame speeds with increasing stretch sensitivity [12, 35, 53]. However, a Markstein length scaling does not capture coupled fuel composition and pressure effects, as increasing pressure decreases Markstein lengths by thinning the flame, as seen in Figure 73. Different measurements, which have been presented in Chapter 3, show that pressure both increases and has no effect on turbulent burning velocities [48, 50]; a Markstein length scaling argument would predict that increasing pressure, and thereby decreasing Markstein lengths, should decrease turbulent burning velocities for negative Markstein length mixtures.

As a first step in our efforts to develop a model, it is useful to review a common approach for scaling turbulent flame speeds using the consumption based definition [12]:

$$S_T = \frac{\left\langle S_L A_T \right\rangle}{A_{<c>}} \tag{4.3}$$

or, by introducing the stretch factor, $I_0 = S_L/S_{L,0}$ [7, 98]:

$$S_T = \frac{S_{L,0} \left\langle I_0 A_T \right\rangle}{A_{<c>}} \tag{4.4}$$

For stretch insensitive flames, the I_0 factor equals unity, leading to the classical S_T scaling described by Damköhler [17]. For stretch sensitive flames, one is left with the function $<I_0 A_T>$, which requires understanding the correlation between local flame speed and flame area. Assuming that these functions are uncorrelated, i.e., that $<I_0 A_T> =$

$<I_0><A_T>$leads to the erroneous prediction that the mixture's stretch sensitivity should not influence S_T [99]. This prediction follows from measurements and computations which show that the flame curvature PDF is roughly symmetric about $\kappa = 0$ [32, 100-102], implying that regions of enhanced and diminished local consumption rate should roughly cancel and, thus, that $<I_0>\approx 1$. Hydrodynamic strain, which is not symmetric about $\kappa = 0$ [32, 49, 102] does introduce a non-unity $<I_0>$ value, but it seems unlikely that this effect is significant enough to explain the appreciable fuel effects reported here and in the literature.

However, it can easily be seen that assuming uncorrelated A_T and I_0 passes over key physics; in particular, there are implicit I_0 effects in the $<A_T>$ term because the local flame speed and area are highly correlated. For example, as illustrated in Figure 76, if the positively curved leading point of the flame has a higher local flame speed, it will propagate at a faster speed into the unburned reactants, increasing flame area accordingly. In the same way, the slower, negatively curved trailing point of the flame will lag backwards, also increasing flame area.

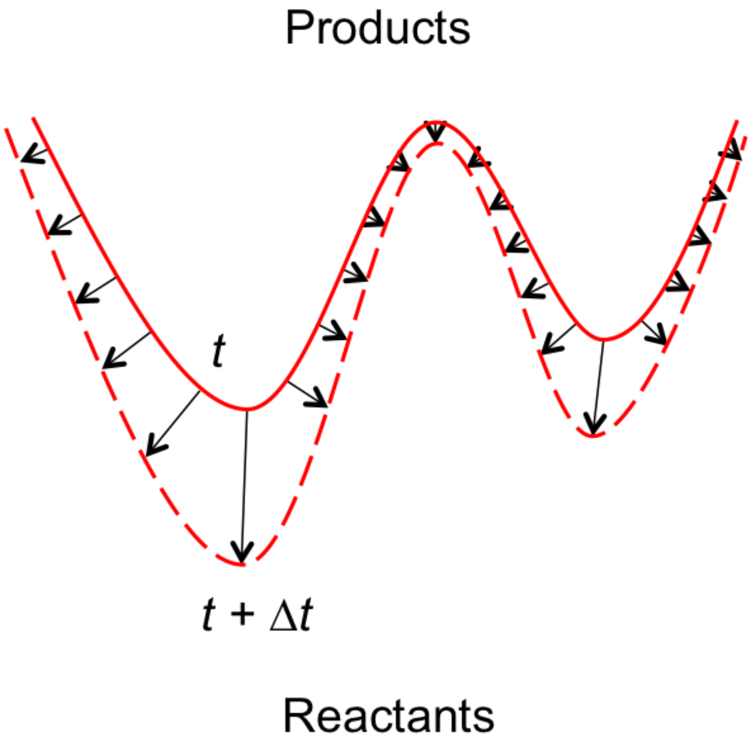

Figure 76: Illustration of the correlation between the local flame speed and flame area.

Given the implicit presence of the I_0 term in the $<A_T>$ term, modeling approaches based upon leading points concepts [43, 47, 103] may be more useful for explicitly bringing out stretch sensitivity effects. The leading points are roughly defined as the necessarily positively curved points on the turbulent flame front that propagate farthest into the reactants, as illustrated in Figure 77. Leading points have origins in the Kolmogorov-Petrovski-Piskunov (KPP) theory, which relates the turbulent flame speed of a statistically 1D flame residing in a prescribed statistically stationary turbulent flow field to the average reaction rate at the leading edge of the flame brush [7, 104]. As a result, some authors have hypothesized that the dynamics of these points controls the overall propagation velocity of the turbulent flame [43, 103]. Thus, fuel/air mixtures with negative Markstein numbers will have enhanced laminar flame speeds at the positively curved leading points, resulting in larger displacement speeds.

This basic leading points argument can be readily understood from the simple model problem of a flat flame propagating into a spatially varying iso-density velocity field with zero mean flow velocity, as depicted in Figure 78.

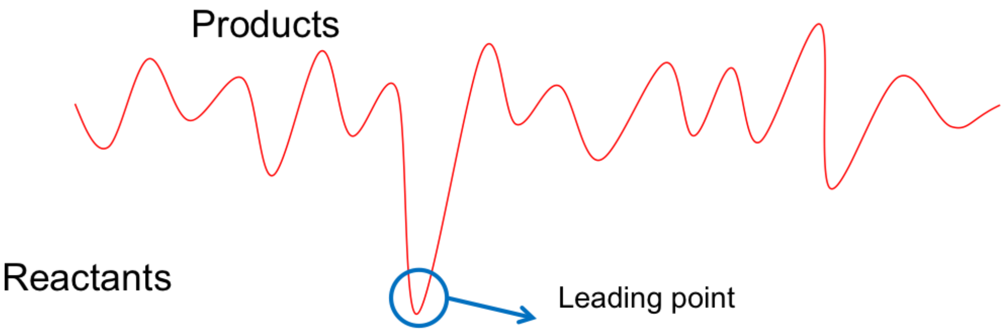

Figure 77: Illustration of leading points.

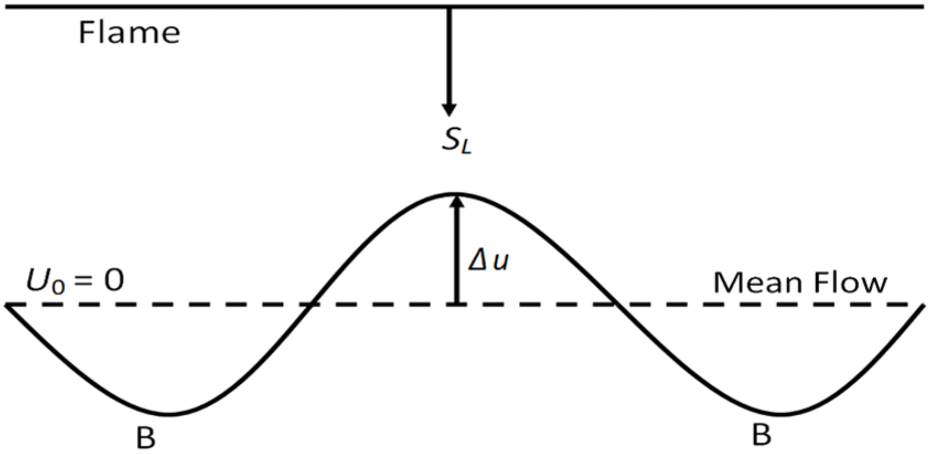

Figure 78: Illustration of a simple model problem of a flat flame propagating into a spatially varying mean flow.

If S_L is assumed to remain constant, then it is seen that the portion of the flame at the lowest approach flow velocity point propagates out the fastest. In the lab-fixed coordinate system, the flame at Point B moves at a speed of $S_L + (\Delta u)_{LP}$, where the subscript "*LP*" denotes the leading point. Moreover, it was shown by a front tracking computation performed by Shin [105], that after an initial transient, the entire front reaches a stationary shape and propagation speed with the value $S_L + (\Delta u)_{LP}$ as shown in Figure 79. As such, the overall displacement speed is controlled by the leading points of the flame that propagate into the lowest velocity regions ahead of the flame. Note also that the flame area would increase as well, but this is an *effect* of the higher displacement speed, not the *cause*.

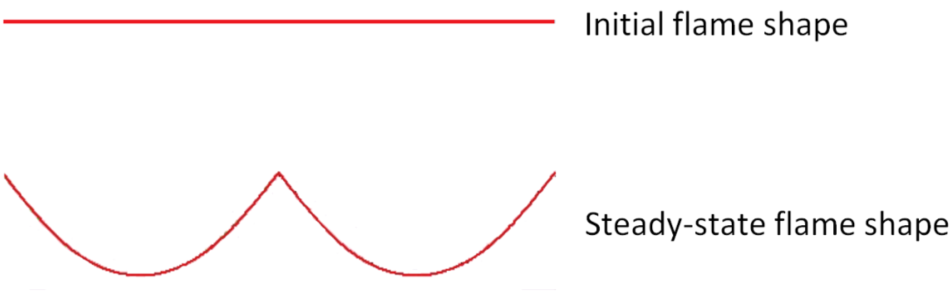

Figure 79: Figure depicting the initial and final flame shapes for the model problem.

In reality, the positively curved leading point of the flame will have an altered flame speed, $(S_L)_{LP} = S_{L,0} + (S'_L)_{LP}$, where $(S'_L)_{LP}$ is the modification of the un-stretched laminar flame speed at the leading point, because of the mixture's nonzero Markstein length. If the mixture has a negative Markstein number, then the flame speed at this point will further increase, causing an increase in curvature, further increasing the local flame speed. This is, in essence, a restatement of the fact that such negative Markstein length mixtures are thermo-diffusively unstable [1]. As a result, the above expression can be modified to take into account the flame speed augmentation:

$$S_D = S_{L,0} + (S'_L)_{LP} + (\Delta u)_{LP} \tag{4.5}$$

The key difference to note from this scaling approach relative to Eq. (4.4) is that this focuses on a local flame characteristic – namely the positively curved leading point – as opposed to some global average, $<I_0A>$, which obscures the stretch effect.

The key problem lies in scaling $(S'_L)_{LP}$. If the positively curved leading point is weakly stretched, then $(S'_L)_{LP} \sim l_M\kappa_{LP}$. This switches the problem to scaling the strain statistics conditioned on the leading point of the flame, κ_{LP}, an important fundamental problem in turbulent combustion; see Lipatnikov and Chomiak [43] for discussion. However, the properties of negative Markstein number fuels can be utilized to place a bound on $(S_L)_{LP}$. Since the investigated mixtures are thermo-diffusively unstable, the $\kappa = 0$, $S_L = S_{L,0}$ point is 'repelling' points in flame strain rate space. In other words, any perturbation of a flat flame will grow, causing an increase in curvature of the positively curved leading edge of the flame. This increase in curvature causes a further increase in flame speed and, therefore, a further increase in curvature, as shown in Figure 80. In fact, as will be shown more rigorously in the subsequent discussion, S_L=$S_{L,max}$ is a steady-state 'attracting' point for a positively curved wrinkle. Moreover, the flame speed at the leading point, $(S_L)_{LP}$ is bounded by the $S_{L,max}$ value; i.e., $S_{L,max} > (S_L)_{LP} > S_{L,0}$. For example, this leads to the following inequality for the 30% H_2 blend: 95 cm/s > $(S_L)_{LP}$> 34 cm/s.

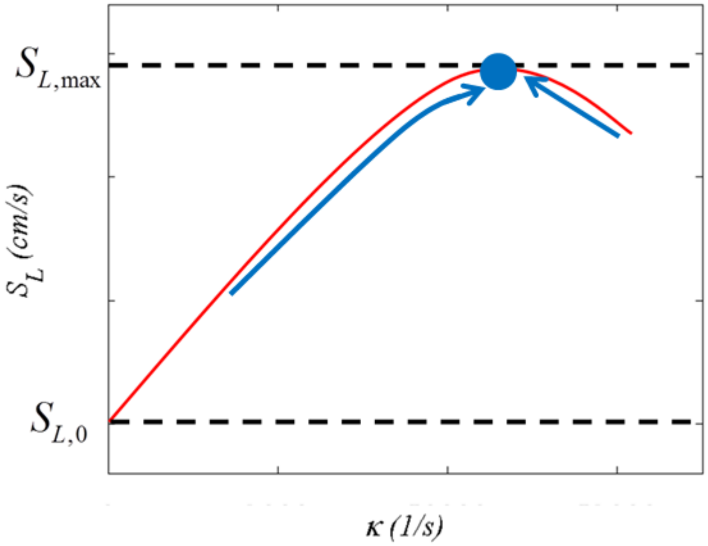

Figure 80: Illustration to depict $S_{L,max}$ as an attractor for negative Markstein length fuel/air mixtures.

Substituting $S_{L,max}$ in for $(S_L)_{LP}$ and writing $(\Delta u)_{LP}$ as u'_{LP} ,leads to the following:

$$\frac{S_D}{S_{L,\max}} \leq 1 + \frac{u'_{LP}}{S_{L,\max}} \tag{4.6}$$

Note that this is similar to Damköhler's classical result [17] where S_L has been replaced by $S_{L,max}$ and *u'* by u'_{LP} .

This point was made heuristically above, but it can also be shown formally by considering the level set equation describing the flame's spatio-temporal dynamics [23] given by Eq. (4.7). The analysis presented below follows the work of Shin in Ref. [106]

$$\frac{\partial G}{\partial t} + \vec{u} \cdot \vec{\nabla} G = S_L \left| \vec{\nabla} G \right| \tag{4.7}$$

This is a suitable model for the flame's dynamics, as Figure 28 shows that the data falls primarily in the corrugated flamelets and thin reaction zone regimes. This equation can be treated analytically in the low turbulence intensity limit, where the flame position is a single-valued function of some coordinate $G = y - \xi(x,t)$, as shown in Figure 81.

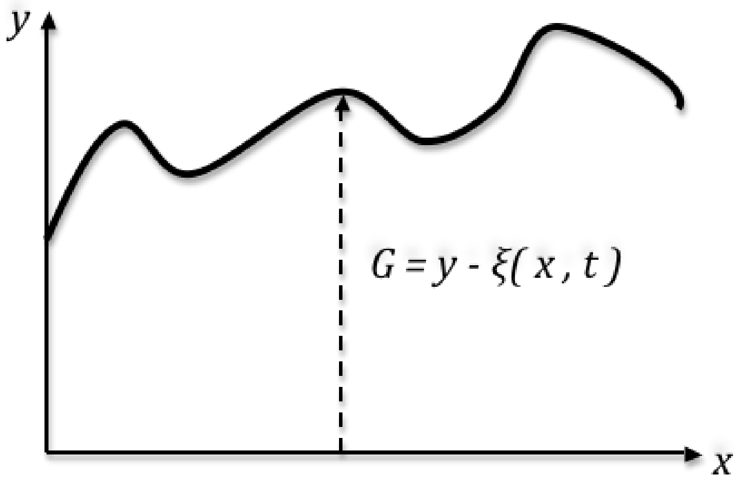

Figure 81: Coordinate system defining the instantaneous flame location, $\xi(x,t)$.

Writing the stretch sensitive flame speed as $S_L = S_{L,0}[1 + f(\kappa)]$, we obtain:

$$-\frac{\partial \xi}{\partial t} - U\frac{\partial \xi}{\partial x} + V = S_{L,0}\left[1 + f(\kappa)\right]\left[1 + \left(\frac{\partial \xi}{\partial x}\right)^2\right]^{1/2} \tag{4.8}$$

Differentiating this expression with respect to x, and substituting $g = \partial\xi/\partial x$:

$$-\frac{\partial g}{\partial t} - \frac{\partial}{\partial x}(Ug) + \frac{\partial V}{\partial x} = S_{L,0}\left(1 + g^2\right)^{1/2}\frac{\partial f}{\partial \kappa}\frac{\partial \kappa}{\partial x} + S_{L,0}\left[1 + f(\kappa)\right]\frac{g}{\left(1 + g^2\right)^{1/2}}\frac{\partial g}{\partial x} \tag{4.9}$$

A necessary condition for leading points, located at the points, x_{LP}, is that $g(x_{LP}, t) = 0$ and $\partial g(x_{LP}, t)/\partial x < 0$. We can determine the asymptotic tendencies of these leading points in a quiescent medium by taking the steady-state limit of this equation by setting

$\partial g/\partial t = 0$ and $U = V = 0$. Furthermore, by explicitly writing the curvature induced strain, κ, as $\frac{\partial g/\partial x}{\left(1+g^2\right)^{3/2}}$, we can re-write Eq.(4.9) as:

$$\begin{aligned} 0 = S_{L,0}\left(1+g_{ss}^2\right)^{1/2}\frac{\partial f}{\partial \kappa}\left[\frac{\partial^2 g_{ss}}{\partial x^2}\left(1+g_{ss}^2\right)^{-3/2} - 3g_{ss}\left(1+g_{ss}^2\right)^{-5/2}\left(\frac{\partial g_{ss}}{\partial x}\right)^2\right] \\ + S_{L,0}\left[1+f\left(\kappa\right)\right]\frac{g_{ss}}{\left(1+g_{ss}^2\right)^{1/2}}\frac{\partial g_{ss}}{\partial x} \end{aligned} \tag{4.10}$$

Setting $g_{ss} = 0$ shows that the following necessary condition is satisfied at the leading point:

$$\frac{\partial f}{\partial \kappa}\frac{\partial^2 g_{ss}}{\partial x^2} = 0 \tag{4.11}$$

Equation (4.11) shows that the steady-state leading points must occur where $\partial f/\partial \kappa = 0$, which coincides with the location of $S_L = S_{L,max}$. Physical arguments can also be used to show that this is a stable attracting point if $\partial^2 f/\partial^2 \kappa < 0$, and that $\partial g/\partial x < 0$ at this $\partial f/\partial \kappa = 0$ point.

The above analysis clearly shows that equating $(S_L)_{LP}$ with $S_{L,max}$ is appropriate in the "quasi-steady" limit of slow turbulent fluctuations. In reality, the leading points continuously evolve in time, as the character of the turbulent fluctuations change, causing points to move and the leading points at a given instant approximately corresponding to the points of local minimum in velocity.

4.4 $S_{L,max}$ correlation

4.4.1 Georgia Tech database

Figure 82 plots the 12 mm diameter burner data normalized by $S_{L,max}$. Note that the 1, 5 and 10 atm data sets collapse quite well individually, but that there are systematic differences between them.

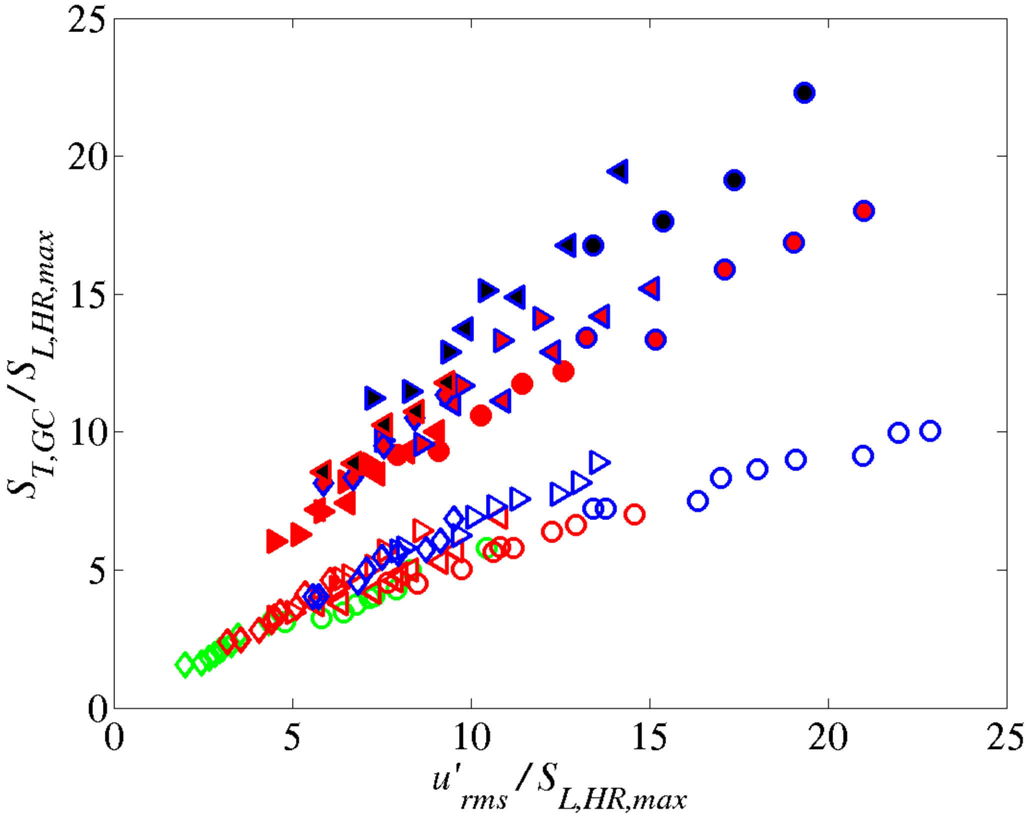

Figure 82: $S_{T,GC}$ as function of u'_{rms} normalized by $S_{L,max}$ at various mean flow velocities, H_2/CO ratios and pressures using the 12 mm diameter burner (See Table 1 for the legend).

Figure 83 plots the result of normalizing all the 20 mm diameter burner data acquired at 1 atm by $S_{L,max}$. This data has the interesting behavior that all the data at 1 atm collapses very well except for the 30 m/s CH_4/air case. Figure 83 has also been reproduced here because it is difficult to see this collapse in Figure 84, which plots the entire $S_{L,max}$ normalized 20 mm diameter burner data set.

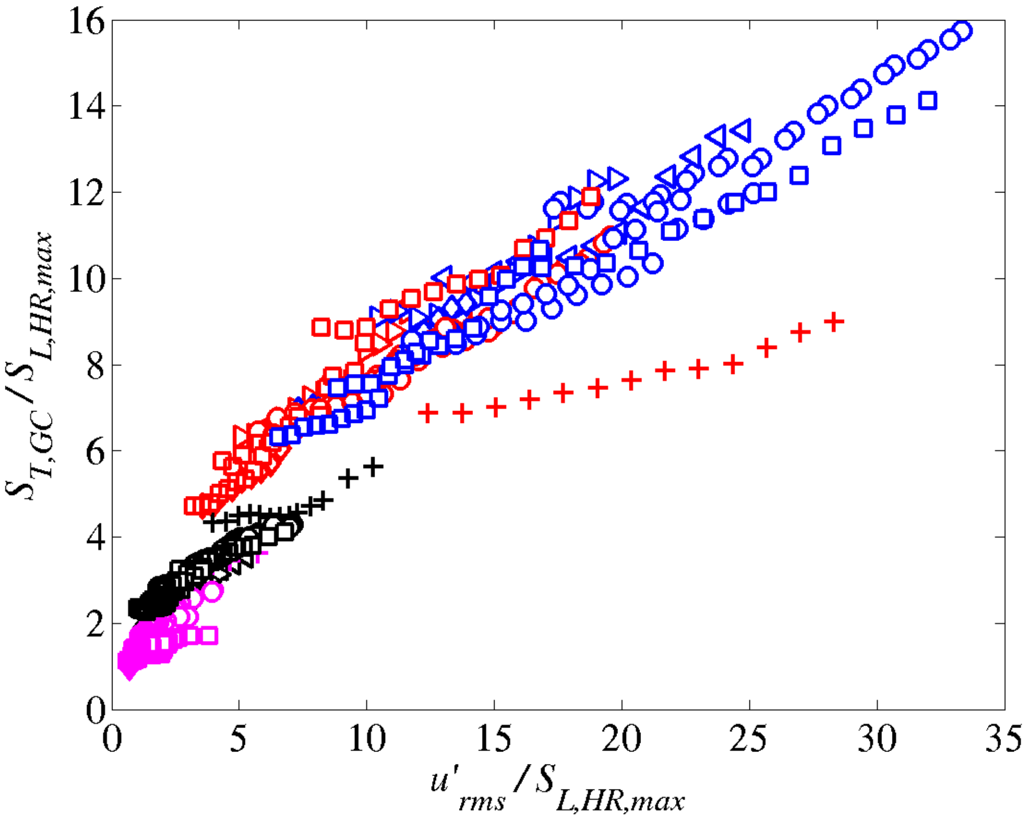

Figure 83: $S_{T,GC}$ as function of u'_{rms} normalized by $S_{L,\mathrm{max}}$ for all the data obtained using the 20mm diameter burner at 1 atm (See Table 1 and Table 2 for the legend).

From Figure 84, we can make similar observations regarding the data of a given pressure collapsing reasonably well, but not collapsing across pressures. However, this trend is not as clear-cut as in Figure 82, because of the broad range in $S_{L,0}$ and $S_{L,max}$ present in this data set.

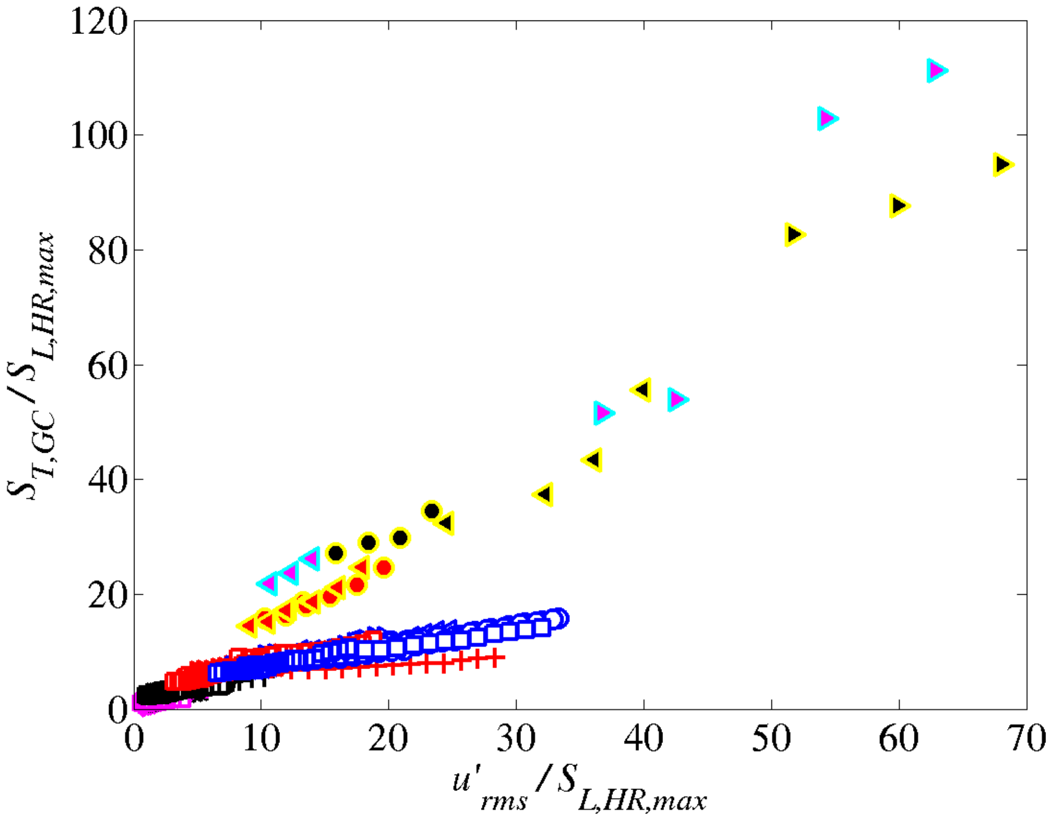

Figure 84: $S_{T,GC}$ as function of u'_{rms} normalized by $S_{L,max}$ for all the data obtained using the 20mm diameter burner at 1 atm (See Table 1 and Table 2 for the legend).

To summarize, the scaling law given by Eq.(4.6) successfully collapses the $S_{T,GC}$ across H_2/CO ratios and equivalence ratios for a given pressure. However, the scaling is unable to collapse the 30 m/s CH_4/air data nor data taken at different pressures.

4.4.2 PSI database

Figure 85 plots the results of normalizing the PSI data in Figure 44 by $S_{L,max}$ based on the heat release consumption definition. It is clear that the data does not appear to collapse as well as the Georgia Tech 12 mm or the 1 atm 20 mm data.

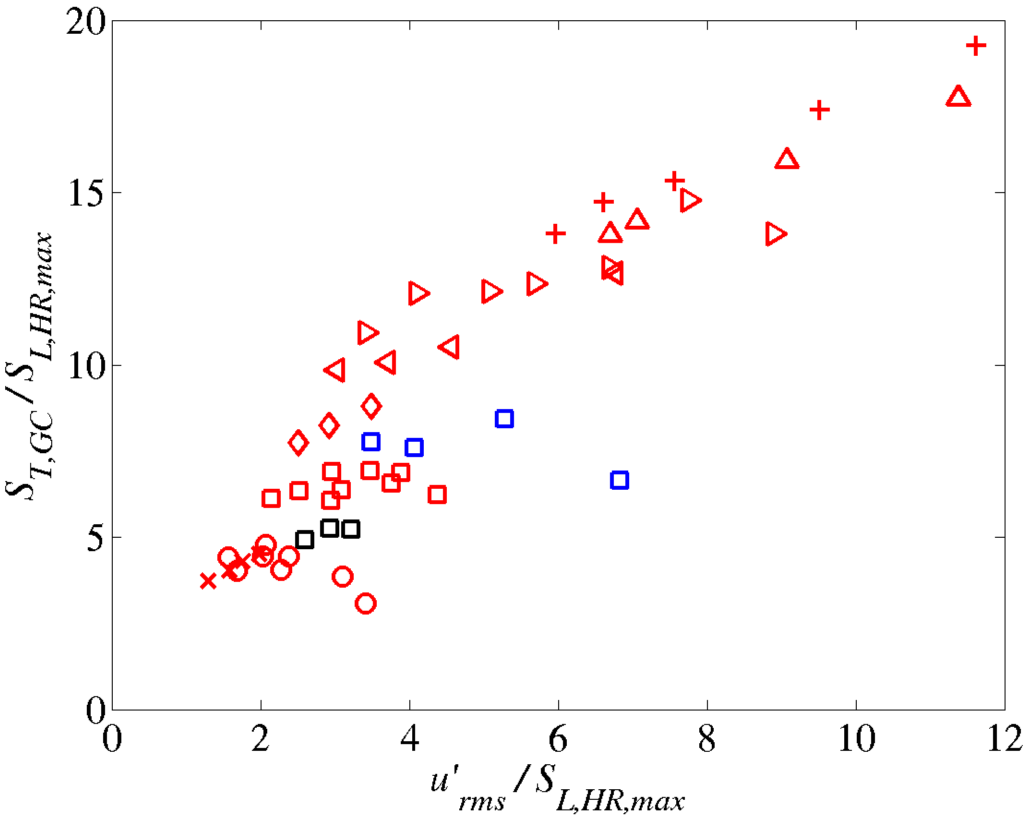

Figure 85: $S_{T,GC}$ as a function of u'_{rms} all normalized by $S_{L,max}$ for the data presented in Figure 44. (See Table 4 for legend).

However, it is not completely surprising that this data does not appear to collapse very well. This data is similar to the Georgia Tech 20 mm data, since it spans a wide range of pressures and mixtures resulting in a wide range of $S_{L,0}$ and $S_{L,max}$. Potential sources for the scatter in the normalized data will be investigated in the subsequent sections.

4.4.3 Spherical bomb flame speed database

In this section we present the results of normalizing the spherical bomb data by $S_{L,max}$. For these data, the displacement speed definition of the laminar flame speed is utilized. Since three sets of data were presented in Sec. 3.2.2, the results of normalizing each data set is shown separately first, before collating them into a single plot.

Figure 86 plots the results of normalizing the data from Kido *et al.*[83], presented in Figure 49, by $S_{L,max}$. Comparing to Figure 49, it appears that the $S_{L,max}$ normalization has managed to collapse the data reasonably well, except for the $\phi = 0.7$ $H_2/O_2/N_2$ data.

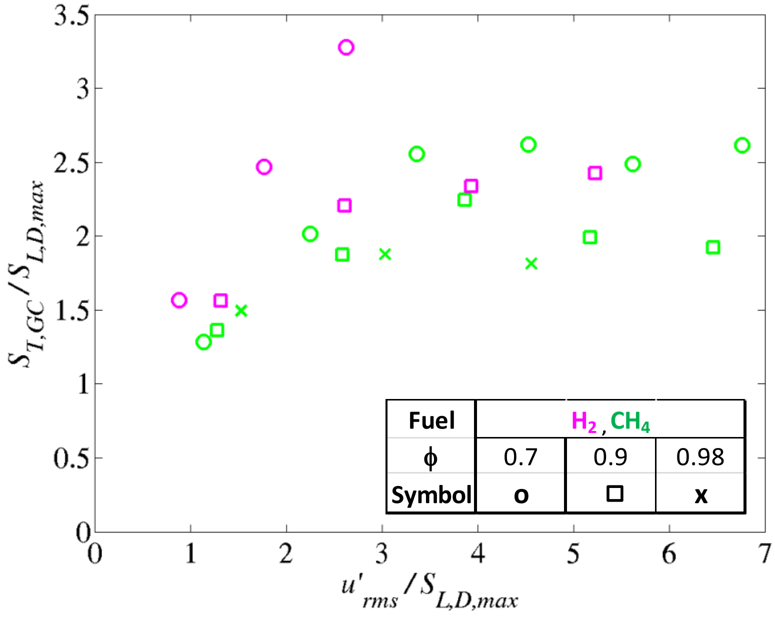

Figure 86: $S_{T,GC}$ as a function of u'_{rms} normalized by $S_{L,max}$ for the data reported in Ref. [19].

Figure 87 plots the results of normalizing the data from Nakahara *et al.* [34], presented in Figure 52, by $S_{L,max}$. Comparing to Figure 52, the data collapses quite well at low $u'_{rms}/S_{L,D,\max}$, while exhibiting more scatter at the higher $u'_{rms}/S_{L,D,\max}$.

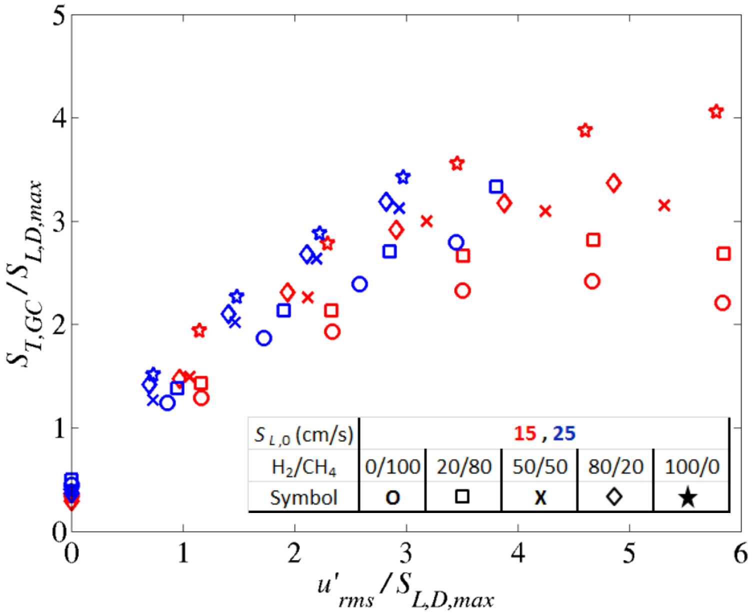

Figure 87: $S_{T,GC}$ as a function of u'_{rms} normalized by $S_{L,max}$ for the data reported in Ref. [34].

Figure 88 plots the results of normalizing the data from Kitagawa *et al.* [52], presented in Figure 54, by $S_{L,max}$. These data were obtained for pressures ranging from 1 – 5 atm for H_2/air mixtures at equivalence ratios of 0.4, 0.6, 0.8 and 1.0. Inspection of the stretch response curves for these mixtures revealed that the 0.8 and 1.0 equivalence ratio mixtures had positive Markstein lengths. Since scaling law given by Eq. (4.6) were derived for negative Markstein length fuels, these data were omitted in Figure 88. Generally speaking it seems that data collapses reasonably well except for the one point corresponding to $\phi = 0.4$ at 5 atm.

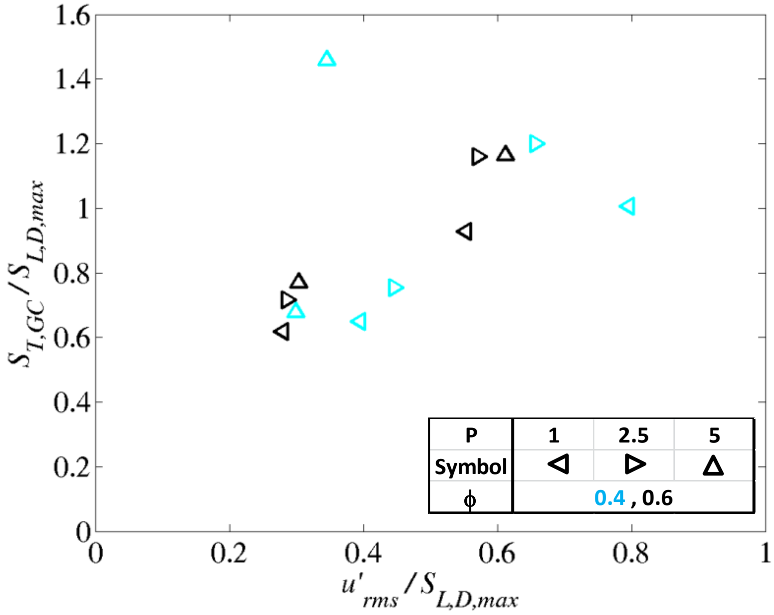

Figure 88: $S_{T,GC}$ as a function of u'_{rms} normalized by $S_{L,\max}$ for the data reported in Ref. [52].

Figure 89, which plots the complete spherical bomb database together shows that the $S_{L,max}$ normalization does a reasonably good job of collapsing the data. As noted with the Nakahara data in Figure 87, the data collapse is particularly good at low $u'_{rms}/S_{L,D,\max}$.

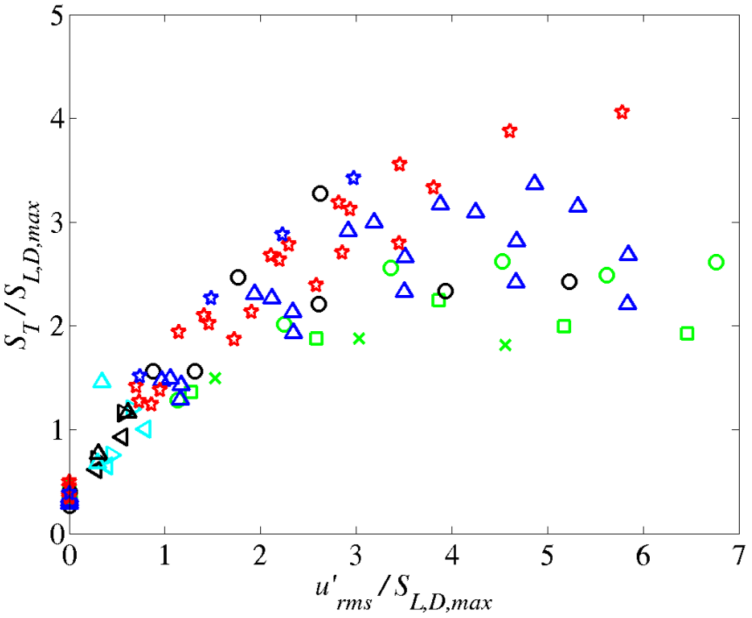

Figure 89: $S_{T,GC}$ as a function of u'_{rms} normalized by $S_{L,\max}$ for the spherical bomb database. Legend has been carried over from the individual datasets.

4.4.4 Low swirl burner database

Figure 90 plots the results of normalizing the low swirl burner $S_{T,LD}$ database by $S_{L,max}$ and the normalized data does not appear to collapse particularly well. Recall that this data is acquired at atmospheric pressure, so the observed scatter cannot be attributed to the variations in pressure. The potential reasons for the scatter will be investigated in the following sections.

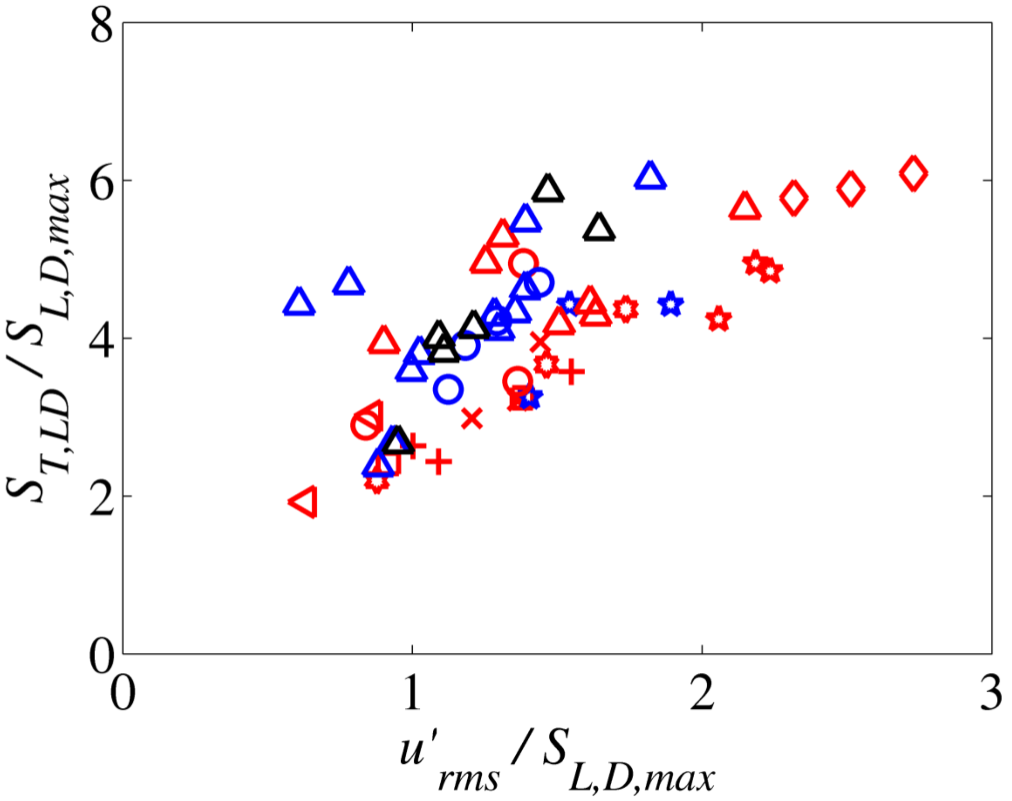

Figure 90: $S_{T,GC}$ as a function of u'_{rms} normalized by $S_{L,\max}$ based on the displacement speed definition for the low swirl burner database. (See Table 6 for legend).

4.5 Incorporation of non-quasi-steady effects

The above results show that the $S_{L,max}$ concept provides some interesting prospects for collapsing a range of H_2/CO data, but does not work well in collapsing data taken across different pressures. Furthermore, the scaling law is only moderately effective when applied to the data extracted from the literature. Potential reasons for the limitations of the scaling are given below.

First, note that the $S_{T,GC}$ data reported here by virtue of Eq. (1.7) necessarily average over potentially significant variations in local flame speeds whereas the scaling

As a result, adjustments to suitably average over a spatially developing flow field and flame brush are required. Nonetheless, the very good collapse of the large data set obtained in this work provides strong evidence for the basic validity of the scaling argument shown in Eq.(4.6). Note that this argument will need revisiting for $l_M > 0$ flames, where the attracting point argument discussed above requires modification.

Second, it is important to note that $S_{L,max}$ is itself not a fundamental property of the mixture; rather, it depends on a variety of different factors.. For example, the burning velocity of highly stretched flames is a function of the manner in which the flame is stretched, i.e., by tangential flow straining or curvature, as well as the stretch profile through the flame (manifested by, for example, moderate sensitivities of $S_{L,max}$ or κ_{ext} to the opposed flow nozzle separation distance or velocity profile) [30]. Note that our calculations derive $S_{L,max}$ from a tangentially stretched flame, while the actual flame leading points are curved. Results of computations of expanding cylindrical flame and tubular flame for lean H_2/air mixtures by Amato *et al.* [107] is presented in Figure 91. These calculations indicate that $S_{L,max}$ varies by about 20-40%, depending the manner in which the flame stretch is applied.

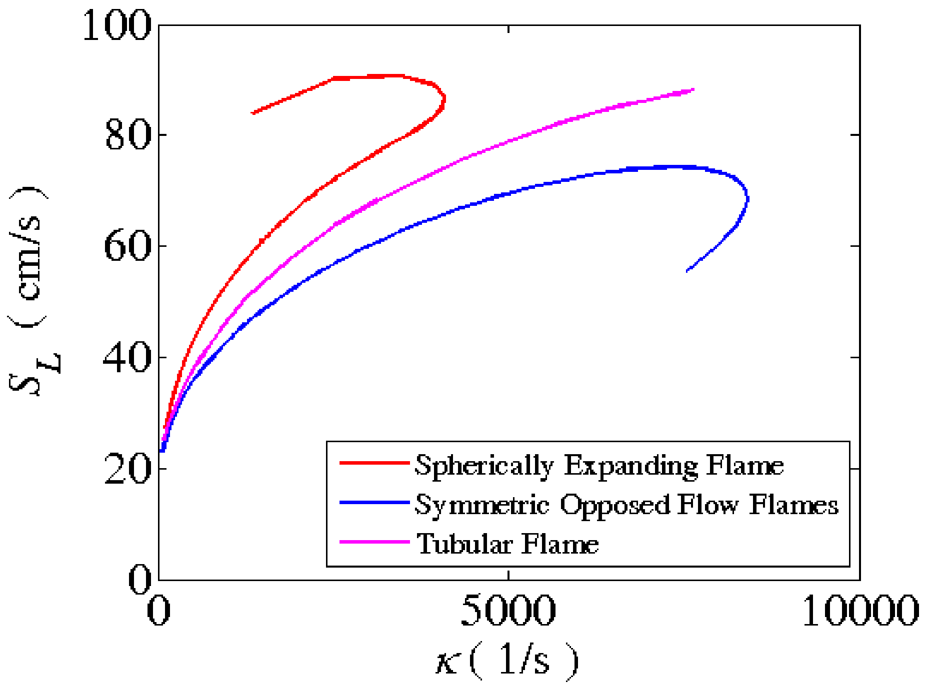

Figure 91: Comparison of stretch sensitivities of a ϕ = 0.37, H_2/air mixture at STP calculated using a spherically expanding flame geometry, the symmetric opposed jets flame and the tubular flame geometry. S_L is based on the H_2 consumption rate given by Eq.(4.1). Figure adapted from Ref.[107].

Paralleling the discussing in Sec. 3.1.1, the choice of the kinetic mechanism also influences the computed stretch response of the mixtures. It is reasonable to expect that when the calculations are carried out at conditions that are outside the range at which the mechanism have been optimized for, uncertainties are introduced into the values of $S_{L,max}$ and l_M. It is difficult to make an assessment of the influence the mechanisms have on the high stretch response rate of some of these mixtures due to the convergence issues in the calculations.

As discussed in Sec. 4.2.2, and shown in Figure 67, very different $S_{L,max}$ values are obtained when using consumption and displacement based burning velocities [7].

Finally, $S_{L,max}$ is itself a frequency dependent quantity [31]; the steady-state values used here are only appropriate if the internal structure of the leading point is quasi-steady.

We focus on the non-quasi-steady chemical processes for the rest of this discussion, as the calculations presented next suggest that this is the largest effect.

To investigate this influence, the chemical time scale associated with the critically stretched flamelet is calculated from:

$$\tau_{S_{L,\max}} = \frac{\delta_F \big|_{S_{L,\max}}}{S_{L,\max}} \tag{4.12}$$

where $\delta_F \big|_{S_{L,\max}}$ is the flame thickness corresponding to $S_{L,max}$:

$$\delta_F = \frac{T_b - T_u}{\left(dT/dx \right)_{\max}} \tag{4.13}$$

For the calculations presented, the laminar flame speeds are based on the heat release consumption speed definition.

The variation in the chemical time scale across H_2/CO mixtures and pressures is shown in Figure 92 for the constant $S_{L,0}$ mixtures investigated in the Georgia Tech database. The point corresponding to 0% H_2 is the pure CH_4/air case that was used in the constant $S_{L,0}$ studies with the 20 mm burner.

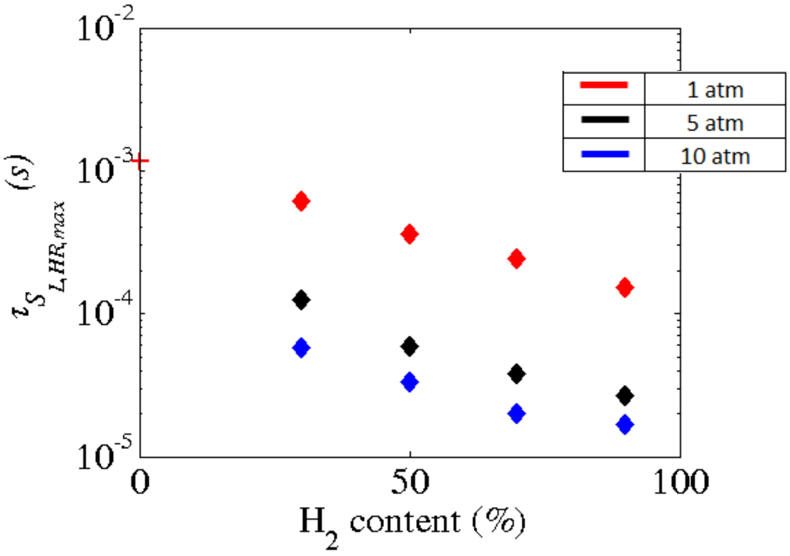

Figure 92: Variation in $\tau_{S_{L,HR,\max}}$ as a function of H_2 content for the different mixtures and conditions investigated. 0% H_2 corresponds to the pure CH_4 mixture.

Within the H_2/CO mixtures, $\tau_{S_{L,HR,\max}}$ increases by about a factor of 4 as the H_2 content is increased from 30% to 90% at 1 atm. The difference between the CH_4 case and the 90/10 H_2/CO mixture is about a factor of 7.7. In addition, for a fixed H_2 content of 30%, there is a factor of 5 and 11 reduction in $\tau_{S_{L,HR,\max}}$ for a pressure increase from 1 to 5 and 10 atm, respectively. This result shows that pressure variations and changes from H_2/CO to CH_4 leads to the largest chemical time variations.

These effects can be incorporated into Eq. (4.6) by replacing $S_{L,max}$ with $S_{L,\max}(\omega)$, which is the frequency dependent $S_{L,max}$. The resulting expression can then be divided by the steady-state $S_{L,max}$ to give:

$$\frac{S_T}{S_{L,\max}} = \frac{S_{L,\max}(\omega)}{S_{L,\max}} + \frac{\langle u'_{rms} \rangle_{LP}}{S_{L,\max}} \tag{4.14}$$

The degree of non-quasi-steadiness can be determined using a Damköhler number defined as, $Da = \tau_{S_{L,\max}} / \tau_{flow}$, where $\tau_{S_{L,\max}}$ is a chemical time scale associated with the highly stretched flamelets and τ_{flow} is a characteristic fluid mechanic time scale. The chemical time scale, $\tau_{S_{L,\max}}$, is given by $\tau_{S_{L,\max}} = \delta_F \big|_{S_{L,\max}} / S_{L,\max}$ where $\delta_F \big|_{S_{L,\max}}$ is the flame thickness at $S_{L,\max}$ calculated using $\delta_F = (T_b - T_u) / (dT/dx)_{\max}$. We would then expect that $S_{L,\max}(\omega) / S_{L,\max} \to 1$ as $\tau_{S_{L,\max}} / \tau_{flow} \to 0$.

4.5.1 Bunsen database

This analysis is applied to the data acquired in this study. Figure 93 and Figure 94 plot $S_{T,GC} / S_{L,HR,\max}$ as a function of $\tau_{S_{L,HR,\max}} / \tau_{flow}$, at two representative fixed turbulence intensity conditions, $u'_{rms} / S_{L,HR,\max}$ of 3.5 and 6.5 for the 12 mm diameter burner. In Figure 93, τ_{flow} is defined as a bulk flow time scale $\tau_B = D / U_0$ and as a Taylor time scale $\tau_\lambda = l_\lambda / u'_{rms}$ in Figure 94. The Taylor scale, l_λ, is scaled as [37]:

$$l_\lambda = l_{\text{int}} \sqrt{10}\, \text{Re}_t^{-1/2} \tag{4.15}$$

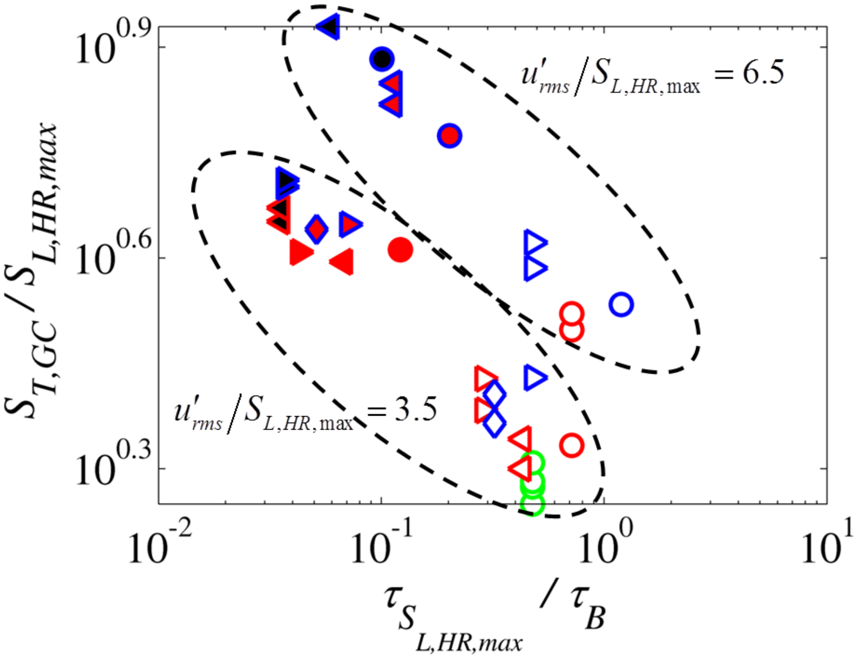

Figure 93: Dependence of $S_{T,GC}/S_{L,HR,\max}$ upon $\tau_{S_{L,HR,\max}}/\tau_{flow}$ at fixed turbulence intensities, $u'_{rms}/S_{L,HR,\max}$ = 3.5 and 6.5 for the 12mm diameter burner where τ_{flow} is scaled as $D/U_0 = \tau_B$.

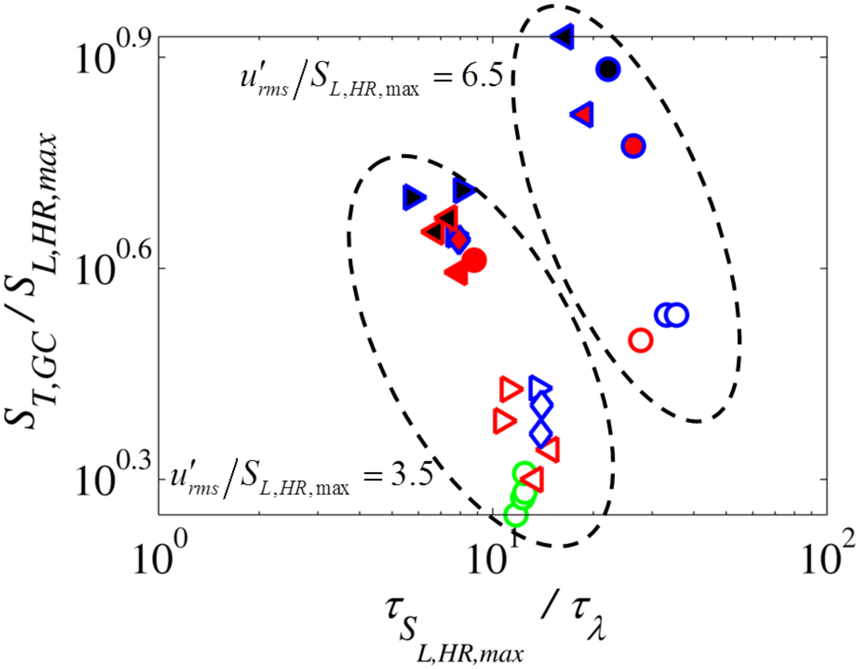

Figure 94: Dependence of $S_{T,GC}/S_{L,HR,\max}$ upon $\tau_{S_{L,HR,\max}}/\tau_{flow}$ at fixed turbulence intensities, $u'_{rms}/S_{L,HR,\max}$ = 3.5 and 6.5 for the 12mm diameter burner where τ_{flow} is scaled as $l_\lambda/u'_{rms} = \tau_\lambda$.

Note from Figure 93 the clear correlation between the normalized turbulent flame speed and time scale ratio across the entire range of pressure and fuel compositions. Slower chemistry is associated with lower values of the normalized turbulent flame speed, as would be expected, since the effective $s_{L,\max}$ value of the non-quasi-steady flame is lower than its quasi-steady value.

Figure 94 plots these same data using the Taylor flow time-scale. In contrast to the bulk flow time scaling shown in Figure 93, τ_λ does have a pressure sensitivity through the Reynolds number. Note from Figure 94 that the range of normalized chemical time scales has decreased compared to in Figure 93. This can be attributed to the fact that although the chemical time scale decreases with pressure as $\tau_{s_{L,\max}} \sim p^{-1}$ as shown in Figure 92 the Taylor time-scale decreases with pressure as $\tau_\lambda \sim p^{-1/2}$. Also note that $\tau_{s_{L,HR,\max}} / \tau_{flow}$ is greater than 1 suggesting that the leading point is non-quasi-steady with respect to the Taylor time-scale.

Similar analyses were performed for the 20 mm data and the results are shown in Figure 95 and Figure 96. The same trends seen in Figure 93 and Figure 94 are also seen here, namely, the correlation between the turbulent flame speed and the time scale ratio across the range of mixtures and conditions. Also as before, the range in the normalized time-scale is decreased when the Taylor time-scale is utilized, and the leading point appears non-quasi-steady with respect to the Taylor time-scale.

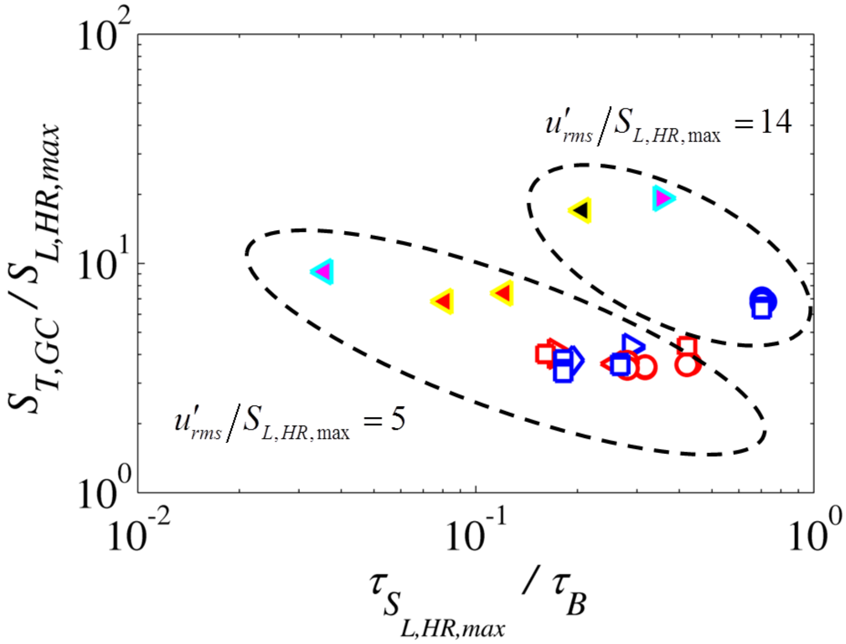

Figure 95: Dependence of $S_{T,GC}/S_{L,HR,\max}$ upon $\tau_{S_{L,HR,\max}}/\tau_{flow}$ at fixed turbulence intensities, $u'_{rms}/S_{L,HR,\max}$ = 5 and 14 for the 20 mm diameter burner where τ_{flow} is scaled as D/U_0 .

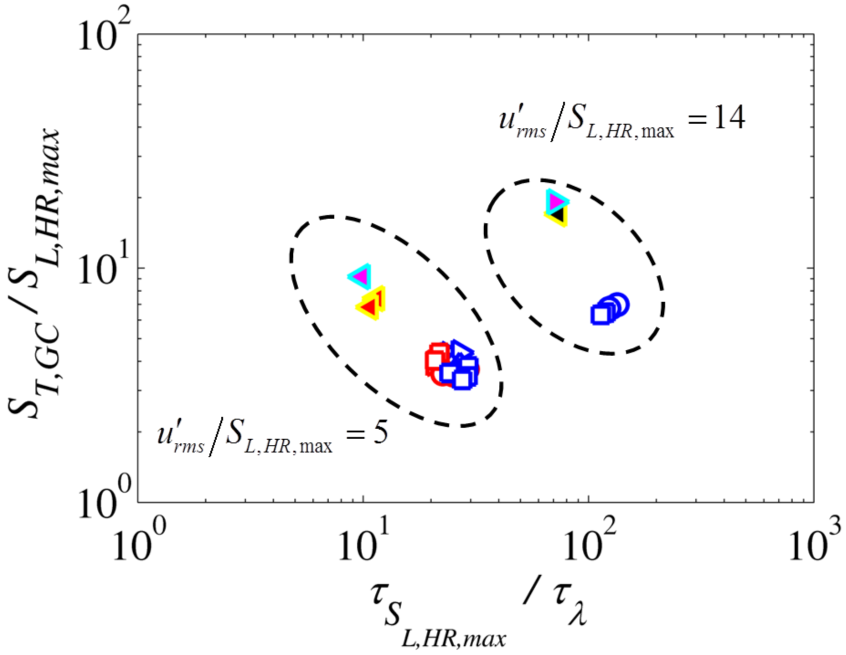

Figure 96: Dependence of $S_{T,GC}/S_{L,HR,\max}$ upon $\tau_{S_{L,HR,\max}}/\tau_{flow}$ at fixed turbulence intensities, $u'_{rms}/S_{L,HR,\max}$ = 5 and 14 for the 20 mm diameter burner where τ_{flow} is scaled as l_λ/u'_{rms} .

Similar analysis was employed to investigate the PSI database. Figure 97 plots $S_{T,GC}/S_{L,HR,\max}$ as a function of $\tau_{S_{L,HR,\max}}/\tau_{flow}$, where $\tau_{flow} = D/U_0$, for fixed turbulence intensities, $u'_{rms}/S_{L,HR,\max}$, of 2.5, 4.5, 6.5, and each color denotes a different constant $u'_{rms}/S_{L,HR,\max}$ grouping.

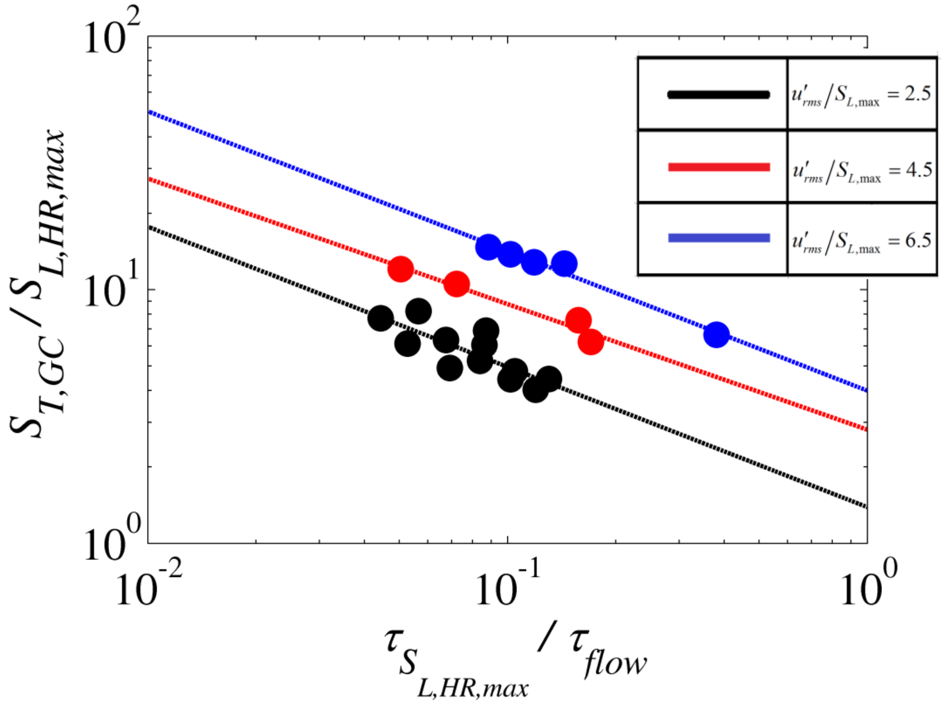

Figure 97: Dependence of $S_{T,GC}/S_{L,HR,\max}$ upon $\tau_{S_{L,HR,\max}}/\tau_{flow}$ at fixed turbulence intensities, $u'_{rms}/S_{L,HR,\max}$, of 2.5,4.5 and 6.5 for the PSI database.

The correlation between turbulent flame speed and critically stretched chemical time scale ratio that we noted with our data in Figure 93 to Figure 96 is also observed here across the range of pressure and fuel compositions that have been investigated in this database.

For comparative purposes, consumption speed data at the same constant $u'_{rms}/S_{L,HR,\max}$ as those in Figure 97 were extracted from the Georgia Tech 20 mm data presented in Figure 83. This data is also adjusted to account for the fact that our turbulent consumption speeds are calculated using an average flame area based on $\langle c \rangle = 0.5$, while the PSI data uses an average flame area based on $\langle c \rangle = 0.05$. This adjustment factor was obtained by calculating the ratio of flame areas associated with these two progress variables from our 20 mm burner data, examples of which are given in Appendix C.

Figure 98 plots the $S_{T,GC}/S_{L,0}$ as a function of $u'_{rms}/S_{L,0}$ from the two databases corresponding to $u'_{rms}/S_{L,HR,\max}$ = 2.5, 4.5 and 6.5. As before, the different constant $u'_{rms}/S_{L,HR,\max}$ groupings are differentiated by color and the two databases are distinguished by filled symbols (PSI) and the unfilled symbols (Georgia Tech).

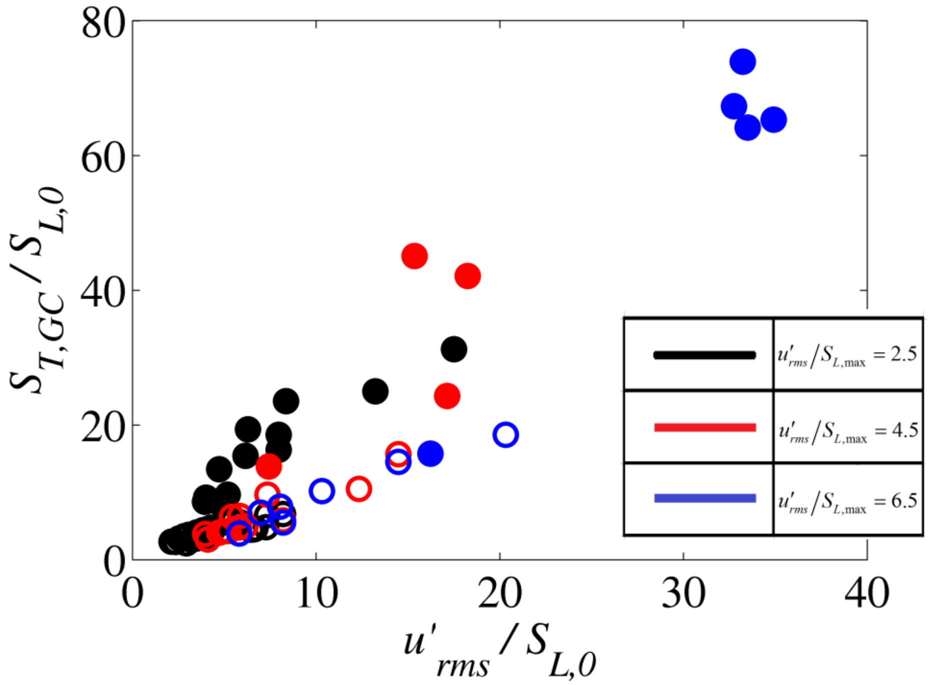

Figure 98: Plots of $S_{T,GC}/S_{L,0}$ as a function of $u'_{rms}/S_{L,0}$ at constant $u'_{rms}/S_{L,HR,\max}$ = 2.5, 4.5 and 6.5 for the Georgia Tech (unfilled symbols) and PSI database (filled symbols).

From Figure 98, there do not seem to be any overarching trends between the two data sets. However, when the data is re-plotted using the normalized critically stretched chemical time scale, as shown in Figure 99, somewhat consistent quantitative trends between the two data sets emerge, which is encouraging to see. We do not expect the data to correlate identically because of differences in the experimental configuration (pilot flame stabilized versus recirculation zone stabilized) and flame area calculation (ideal cone versus ellipsoid of revolution).

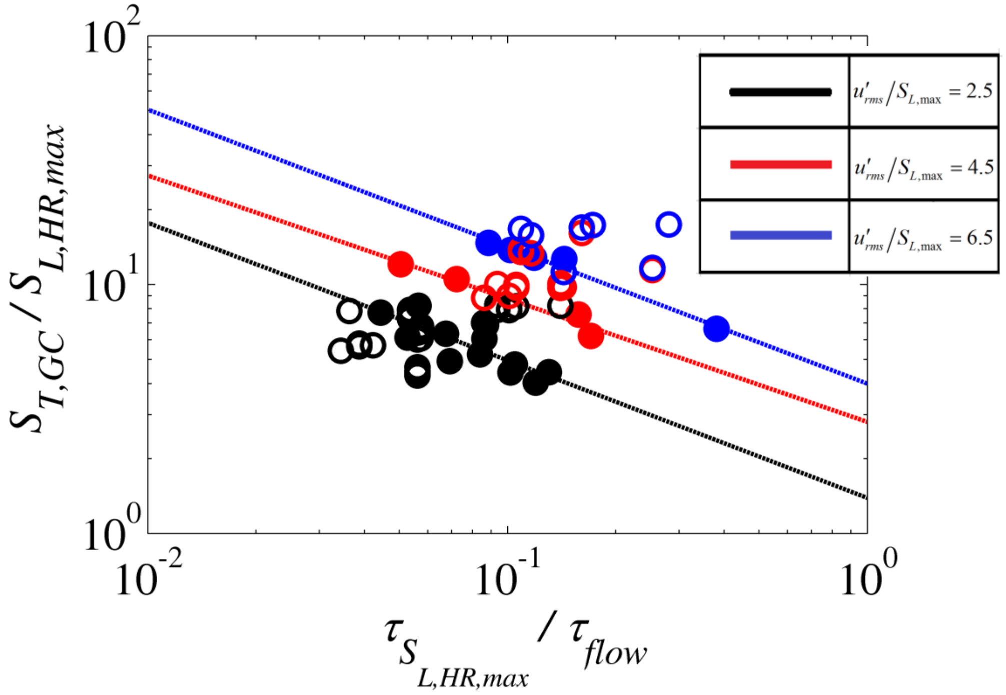

Figure 99: Dependence of $S_{T,GC}/S_{L,HR,\max}$ upon $\tau_{S_{L,HR,\max}}/\tau_{flow}$ at fixed turbulence intensities, $u'_{rms}/S_{L,HR,\max}$, of 2.5,4.5 and 6.5 for both the PSI database (filled symbols) and the Georgia Tech 20 mm burner data (unfilled symbols).

4.5.2 Spherical bomb database

We perform a similar time scale analysis with the spherical bomb data sets. In Figure 100, we plot $S_T/S_{L,D,\max}$ as a function of $\tau_{S_{L,D,\max}}/\tau_{flow}$, at two representative fixed turbulence intensity conditions, $u'_{rms}/S_{L,D,\max}$ of 2.5 and 5.0. For this analysis, τ_{flow} is defined as l_{int}/u'_{rms}. The $u'_{rms}/S_{L,D,\max}$ values of 2.5 and 5.0 were selected because those were the regions in Figure 89 where the scatter in the $S_{L,max}$ normalized data was the largest. As a result, these data groupings only contain atmospheric pressure cases because the high pressure data from the Kitagawa data set was confined to the low $u'_{rms}/S_{L,D,\max}$ regions in Figure 89 where the data collapsed quite well.

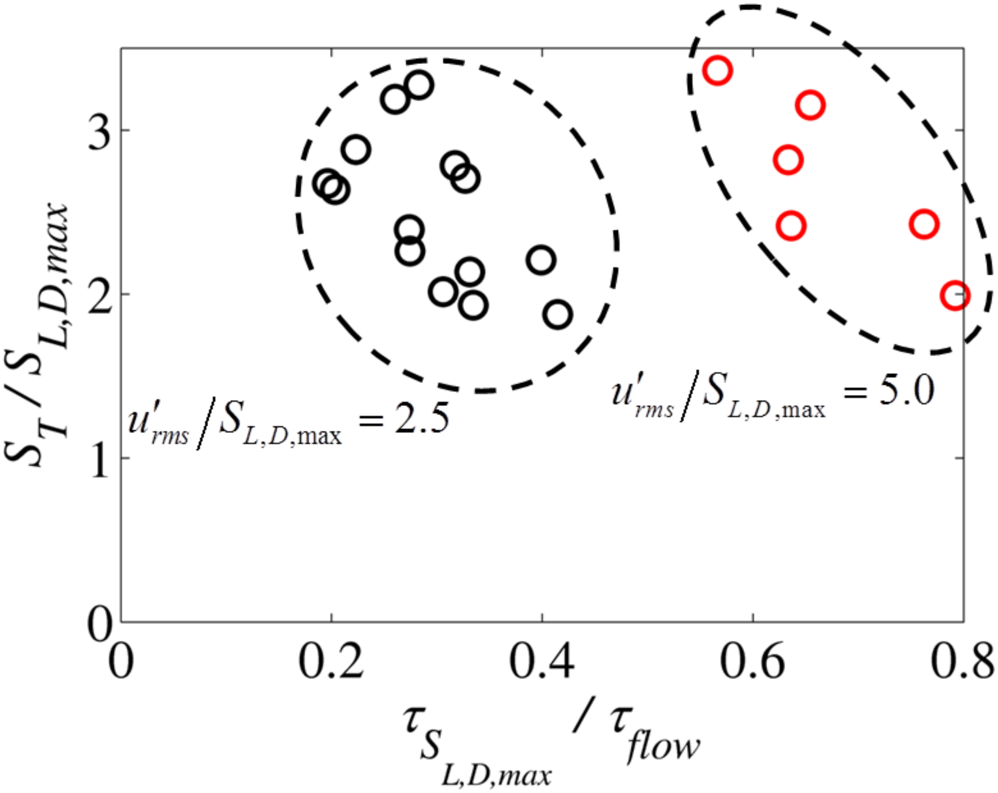

Figure 100: Dependence of $S_T/S_{L,D,\max}$ upon $\tau_{S_{L,D,\max}}/\tau_{flow}$ at fixed turbulence intensities, $u'_{rms}/S_{L,D,\max}$, of 2.5 and 5 for the spherical bomb data set.

From Figure 100, note the decreasing trend of $S_T/S_{L,D,\max}$ with the normalized leading point chemical time scale, which is consistent with the trends observed with the Bunsen data sets. As before, lower values of the normalized turbulent flame speed can be associated with slower chemistry, as would be expected, since the effective $S_{L,D,\max}$ value of the non-quasi-steady flame is lower than its quasi-steady value.

In addition, since the normalized leading point chemical is uniformly less than 1, this suggests that the leading point is quasi-steady with respect to the large turbulent scales.

4.5.3 Low swirl burner database

The time scale analysis with the low swirl burner data set is presented here. In Figure 101, two representative $u'_{rms}/S_{L,\max}$ values are selected, and $S_{T,LD}/S_{L,\max}$ is plotted as a function of $\tau_{S_{L,D,\max}}/\tau_{flow}$. For this figure, τ_{flow} is defined as R_i/u'_{rms}, where R_i is the outer radius of the LSB as shown in Figure 58.

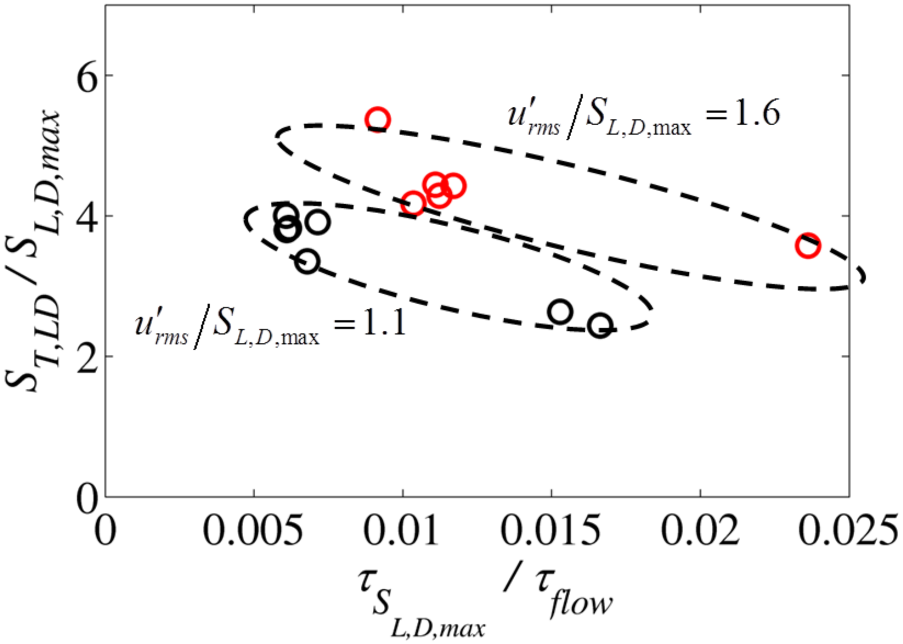

Figure 101: Dependence of $S_{T,LD}/S_{L,\max}$ upon $\tau_{S_{L,D,\max}}/\tau_{flow}$ at fixed turbulence intensities, $u'_{rms}/S_{L,D,\max}$, of 1.1 and 1.6 for the low swirl burner data set.

In Figure 101, we see the previously observed decreasing trend in $S_{T,LD}/S_{L,\max}$ with the normalized leading point chemical time scale. Furthermore, the normalized leading point chemical time scale is less than 1suggesting that the leading point is quasi-steady with respect to the large turbulent scales.

4.6 Remarks

In this chapter, it has been shown that a broad range of fuel composition and pressure data can be correlated with the maximum laminar flame speed, $S_{L,max}$, and a chemical time scale ratio scaling. In other words, the data can be correlated with an expression of the form:

$$\frac{S_T}{S_{L,\max}} = f\left(\frac{u'_{rms}}{S_{L,\max}}, \frac{\tau_{S_{L,\max}}}{\tau_{flow}}\right) \tag{4.16}$$

In particular, it was suggested that pressure effects influence the turbulent burning velocity by altering how well the flame's internal chemistry can track the time varying stretch rate at the leading point. If this assertion is true, then it clearly indicates the strong coupling effects of stretch and pressure. In particular, a key feature of this argument is that, in flames where $S_{L,\max}/S_{L,0} >> 1$, then non-quasi-steady effects can significantly alter the burning velocity of the leading point. This argument also suggests then, that non-quasi-steady effects should have much less effect on mixtures with weak stretch sensitivity, where $S_{L,\max}/S_{L,0} \sim 1$.

Returning to the Georgia Tech data, it must also be emphasized that the data, when normalized by $S_{L,max}$, showed a clear correlation with pressure. Thus, any parameter that also correlates with pressure will also do a reasonable job of scaling the pressure effects. In particular, the Reynolds number linearly increases with pressure. As a result, these pressure effects could also be correlated with Reynolds number. In addition, the Taylor and Kolmogorov length scales also have a Reynolds number, and therefore a pressure sensitivity as shown in Eq. (4.17)

$$\frac{l_{\text{int}}}{\eta} \sim \mathrm{Re}_t^{-3/4} \tag{4.17}$$

where η is the Kolmogorov length scale. Thus, these pressure effects could also be scaled using a length scale ratio. To illustrate, Figure 102 and Figure 103 plot $S_{T,GC}/S_{L,HR,\max}$ as a function of the turbulent Reynolds number and the normalized Taylor micro-scale respectively, at two constant $u'_{rms}/S_{L,HR,\max}$ values.

In Figure 102 $S_{T,GC}/S_{L,HR,\max}$ increases with the turbulent Reynolds number, which is consistent with findings in the literature [108, 109]. This has been traditionally attributed to the fact that larger turbulent Reynolds numbers suggest the presence of a wider range of turbulent length scales in the flow which can generate a wider range of wrinkles on the turbulent flame front. This results in an augmentation of the flame area, resulting in larger turbulent flame speeds.

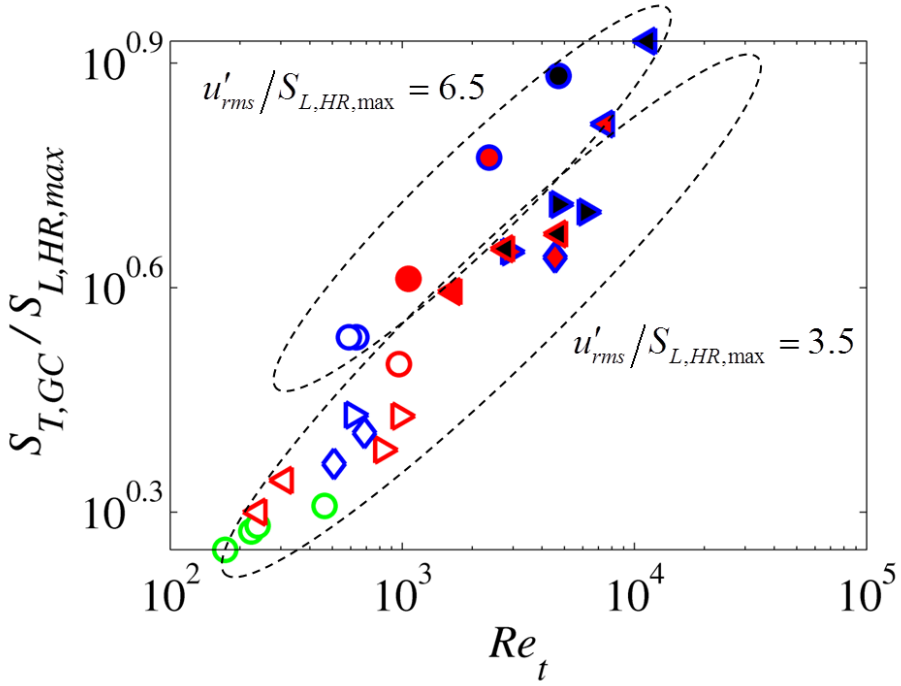

Figure 102: $S_{T,GC}/S_{L,HR,\max}$ as a function of the turbulent Reynolds number at constant $u'_{rms}/S_{L,HR,\max}$ values of 3.5 and 6.5 for the 12 mm diameter dataset for the Georgia Tech database.

In Figure 103 $S_{T,GC}/S_{L,HR,\max}$ decreases with the normalized Taylor scale. This trend is essentially a Reynolds number scaling similar to that in Figure 102, since the Taylor scale has a turbulent Reynolds dependency given by Eq. (4.15). Larger turbulent Reynolds numbers suggest smaller Taylor scales which leads to larger $S_{T,GC}/S_{L,HR,\max}$.

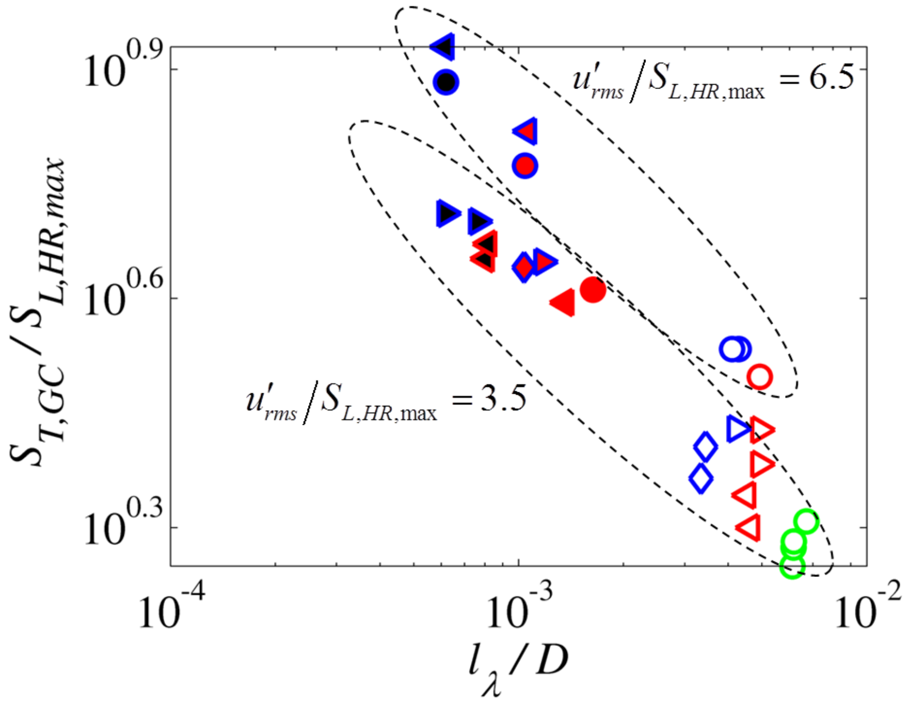

Figure 103: $S_{T,GC}/S_{L,HR,\max}$ as a function of the normalized Taylor scale at constant $u'_{rms}/S_{L,HR,\max}$ values of 3.5 and 6.5 for the 12 mm diameter dataset for the Georgia Tech database.

These results indicate that additional data is needed to differentiate between chemical time and Reynolds number effects. One avenue for future work is to explore a broadened set of experimental conditions that will enable differentiation between time scale, length scale, and Reynolds number effects on the turbulent burning velocity.

Chapter 5
Characteristics of the Turbulent Flame Brush

5.1 Introduction

In this chapter the influence of fuel composition and pressure on the turbulent flame brush thickness is analyzed. The turbulent flame brush has been the subject of a review article [36], where it was proposed that the flame brush thickness, similar to the turbulent flame speed, is an important global parameter of the turbulent flame that can be used to assess combustion codes. In addition, since the flame brush represents the heat release distribution normal to the turbulent flame, it has important implications for the design of combustion systems.

Although the review paper compiles a large set of flame brush thickness data, there are limited data that systematically explore the influence of fuel composition and pressure. This chapter seeks to address this deficiency by analyzing the characteristics of the turbulent flame brush for the range of mixtures and conditions at which the turbulent consumption speeds were measured.

First, the methodology employed to calculate the flame brush thickness is fully described. The sensitivities of the flame brush thickness to different parameters, such as turbulence intensity, fuel composition (H_2/CO ratio and equivalence ratios), and pressure are then presented. The flame brush thickness data obtained in this work is then compared to models for the flame brush thickness presented in Chapter 1. The chapter concludes with a discussion of the self-similar structure of the turbulent flame brush and the definition dependent nature of the flame brush thickness.

5.2 Calculation of the turbulent flame brush

The starting point of the flame brush thickness calculation is the Abel deconvoluted image, which were generated for the turbulent consumption speed calculation, as discussed in Chapter 3. In addition, since the Abel deconvoluted image is symmetric, only one half of the image is considered in the calculation.

Step 1: The flame image is separated into two sections as shown in Figure 104; section A where the flame brush is oriented roughly parallel to the flow and section B where the flame brush exhibits more curvature. The point at which the image is split is the height above the burner at which the centerline intensity is 25% of the maximum intensity.

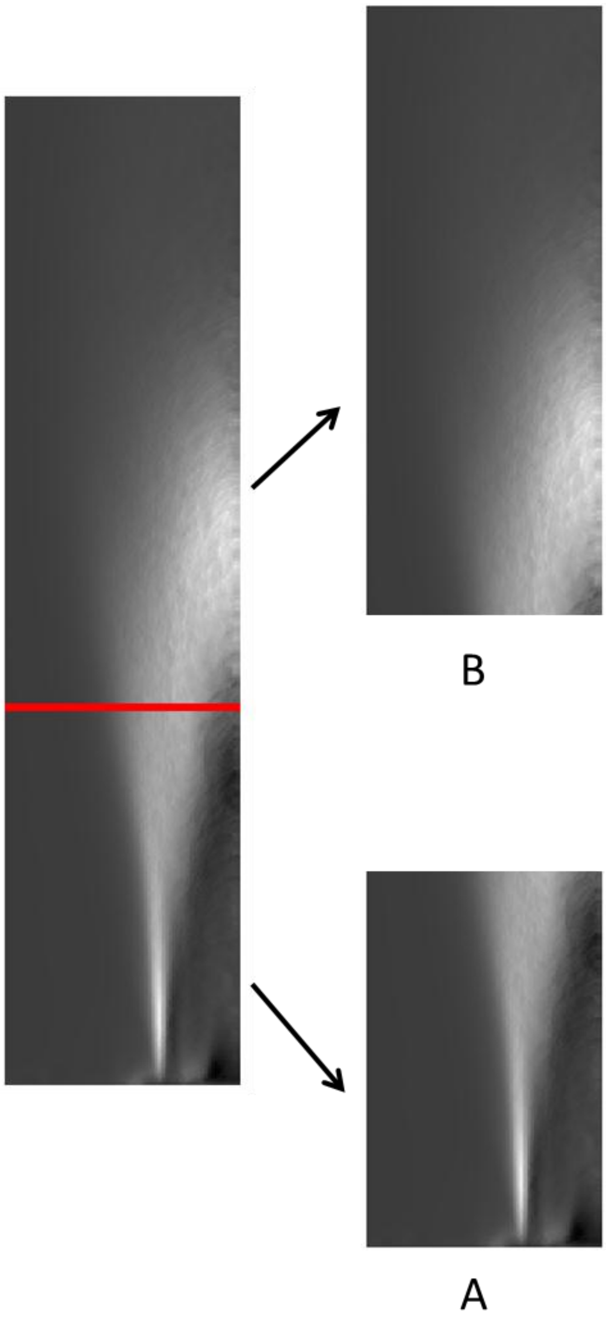

Figure 104: Illustrative image showing the two segments of the Abel transformed image that are considered for the first estimate for the <*c*> = 0.5 contour.

Step 2: An initial estimate for the <*c*>=0.5 contour is then made by employing different search patterns in segment A and segment B of the image shown in Figure 104

In segment A, the intensity variation at each row is examined and the local <*c*> = 0.5 contour is defined as the location of maximum intensity. In segment B, the intensity variation along a radius originating from the corner of the image is examined. Example radii are shown in Figure 105.

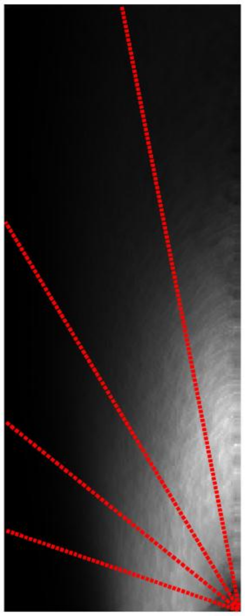

Figure 105: Example paths along which intensity profiles are extracted in segment B in Figure 104.

From both search paths, the intensity profile is fit with a Gaussian profile, and the location of the <*c*> = 0.5 contour is found from the maxima of the fitted intensity profile.

<u>Step 3:</u> The first estimate for the <*c*>=0.5 contour is then fitted with an equation of the form:

$$y = \frac{a}{\left(x^2 - b^2\right)^4} - \frac{a}{\left(R_p^2 - b^2\right)^4} \tag{5.1}$$

or

$$y = \frac{a}{\left(x^2 - b^2\right)^2} - \frac{a}{\left(R_p^2 - b^2\right)^2} \tag{5.2}$$

where R_p is the distance of the burner edge from the centerline in pixels.

Step 4: The next iteration to find the $<c>$ = 0.5 contour is performed. In this step, the intensity variations along normals to the curve given by Eq. (5.1) or (5.2) are examined. Similar to Step 2, the intensity variation along the normal is fit with a Gaussian profile and the local <c> = 0.5 location is found from the maxima of the profile. Step 3 is then repeated for the new estimate of the <c> = 0.5 contour.

Step 5: As in Step 4, the intensity profiles along the normals to the new <c> = 0.5 contour, represented by Eq.(5.1) or Eq. (5.2), are extracted.

Before proceeding to extract the local average progress variable locations, it is important to recall that the flame brush thickness is controlled by two processes; flame front wrinkling and flame flapping. The focus of this work is on the influence of flame wrinkling on the turbulent flame brush. However, in the Bunsen geometry, with downstream distance, there is increasing interaction between the flames that are on diametrically opposite sides. In order to eliminate this aspect in the flame brush thickness calculation, the flame brush thickness is only determined up to a certain height above the burner exit, above which, it is assumed there is significant interaction. This threshold height is determined fitting the intensity variation along each normal with a Gaussian profile of the form given by Eq. (5.3), and a few representative cases are provided in Figure 106.

$$I\left(x;\mu,\sigma^{2}\right)=\frac{1}{\sigma\sqrt{2\pi}}\exp\left[-\frac{1}{2}\left(\frac{x-\mu}{\sigma}\right)^{2}\right] \tag{5.3}$$

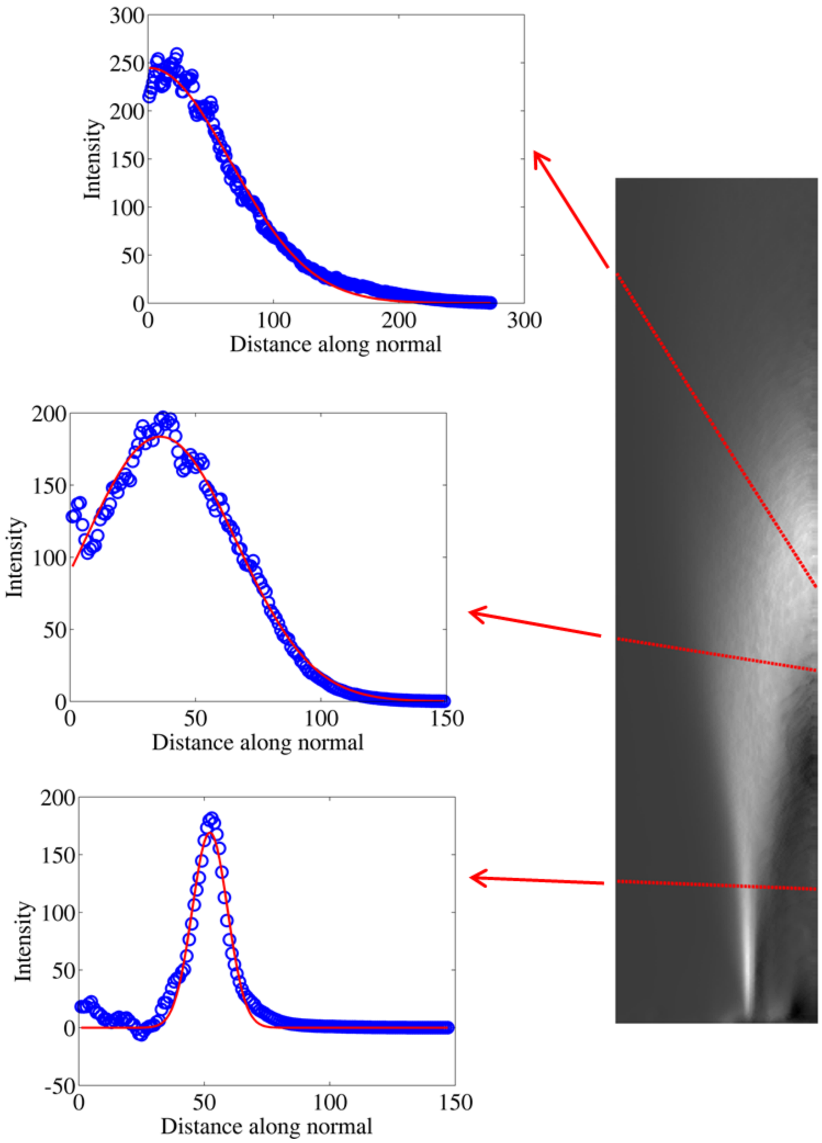

Figure 106: Intensity profiles along with the Gaussian fits along normals at different locations in the flame brush.

The intensity profiles along the normals are quite different depending on their location along the turbulent flame brush. Near the top of the flame, the intensity starts off near its maximum before tailing off. This makes the determination of the lower average progress variable contours (<*c*> < 0.5) quite problematic. Near the base of the flame, the intensity profile follows a Gaussian profile. As a result, a threshold criteria, defined by Eq. (5.4) is implemented

$$\Lambda = \frac{\left|\overline{I_i} - \overline{I_f}\right|}{\mathrm{I}_{\max}} \tag{5.4}$$

where $\overline{I_i}$ and $\overline{I_f}$ are defined as the average intensity of the first three and last three points along the normal respectively. For this analysis, if Λ at a point along the <*c*> = 0.5 contour is more than 0.3, that location is not considered in the flame brush thickness calculation. Changing the value of this threshold did not alter the observed trends or the conclusions made in this work.

For the normals that met the threshold criteria, the locations of each progress variable, $x_{<c>}$, along the normal were then determined by solving Eq. (5.5):

$$\langle c \rangle = \frac{1}{2}\left[1 + erf\left(\frac{x_{\langle c \rangle} - \mu}{\sigma\sqrt{2}}\right)\right] \tag{5.5}$$

In Eq.(5.5), μ and σ are the mean and standard deviation of the Gaussian fit to the intensity profile and *erf* is the error function. A derivation of Eq. (5.5) is given in Appendix B.

The local flame brush thicknesses are calculated using the following three definitions:

1. The distance between the <*c*> = 0.2 and 0.8 contours.
2. The distance between the <*c*> = 0.3 and 0.7 contours.

3. Utilizing Eq.(1.27).

5.3 Flame brush thickness sensitivities

The sensitivities of the flame brush thickness to the turbulence intensity, pressure, and fuel composition are presented in this section. Data from the two sets of experiments conducted for the $S_{T,GC}$ measurements are considered. These data will consist of the constant $S_{L,0}$ studies performed with the 12 mm diameter burner and the equivalence ratio sweep studies performed using the 20 mm diameter burner. Flame brush thicknesses are plotted as a function of the flame coordinate, s, which is defined as the distance from the burner exit along the $\langle c \rangle = 0.5$ contour. In addition, the flame brush thickness is defined as the distance between the $\langle c \rangle = 0.3$ and 0.7 contours in the direction along the normal to the $\langle c \rangle = 0 .5$ contour. Dependence of the observed trends on the definition is discussed in a later section.

5.3.1 Effect of turbulence intensity

In this section, the influence of turbulence intensity on the flame brush thickness for the constant $S_{L,0}$ data obtained at 50 m/s using the 12 mm diameter burner is analyzed. Since $S_{L,0}$ is constant across all the mixtures, this section is essentially looking at the influence of changing u'_{rms}. Furthermore, since U_0 is also constant across these mixtures, $u'_{rms}/S_{L,0}$ and u'_{rms}/U_0 are equivalent.

Figure 107 plots the flame brush thickness as a function of the flame coordinate for various $u'_{rms}/S_{L,0}$ for the 50/50 and 70/30 H_2/CO ratios at 1 atm. Also plotted are one-sided error bars that reflect the effect of image resolution on the flame brush thickness. Since a minimum of two pixels are required to resolve the flame brush thickness, the flame brush thickness that is calculated represents an upper bound. In reality, there may be intensity variations on the sub-pixel scale which will not be resolved.

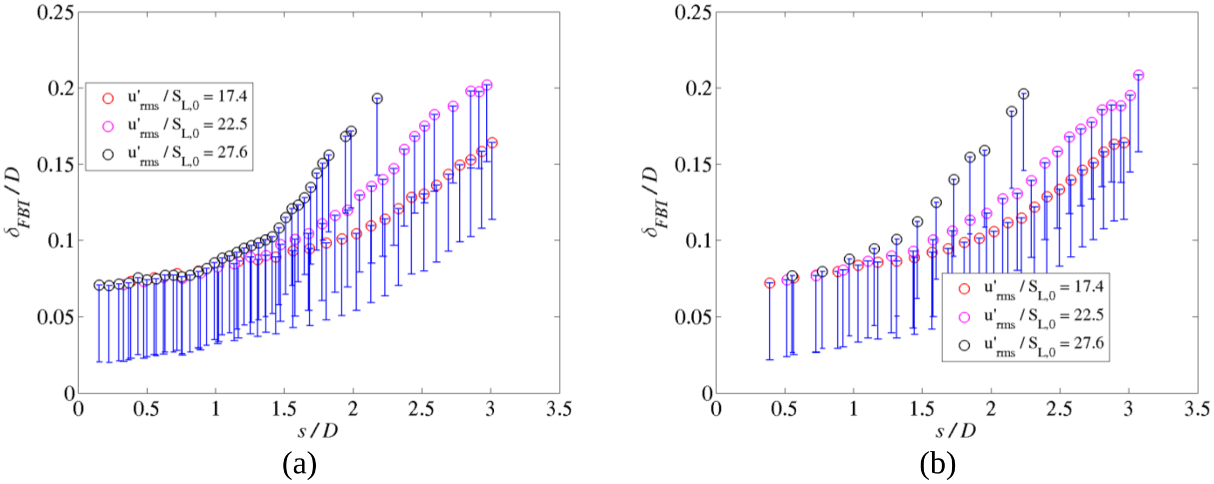

(a) (b)

Figure 107: Variation of flame brush thickness as a function of the flame coordinate for (a) the ϕ = 0.55, 50/50 H_2/CO mixture and (b) ϕ = 0.51, 70/30 H_2/CO mixture both at 1 atm. Measurements obtained for the 12 mm diameter burner at 50 m/s.

Figure 108 plots the flame brush thickness as a function of the flame coordinate for various $u'_{rms}/S_{L,0}$ for 30/70 and 70/30 H_2/CO ratios at 10 atm. These data were obtained at a mean flow velocity of 50 m/s using the 12 mm diameter burner.

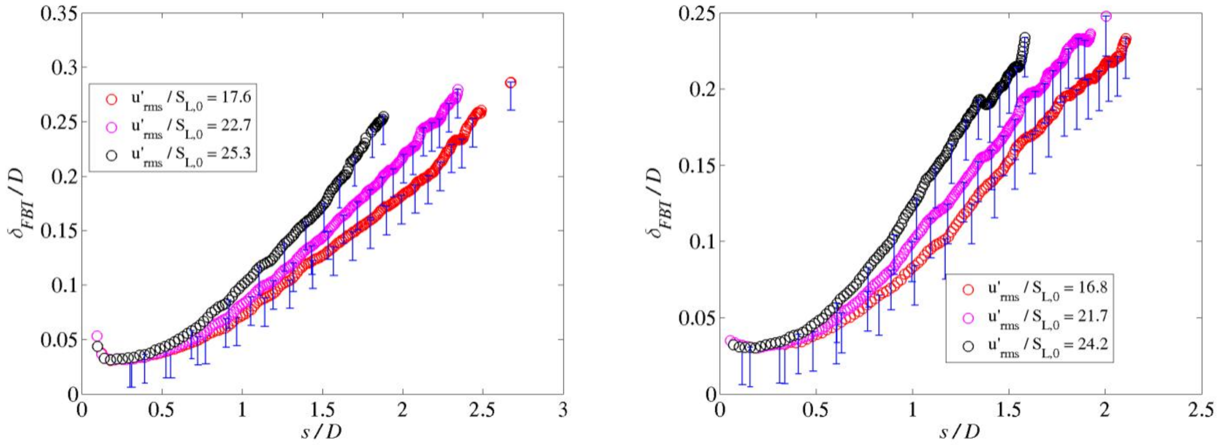

(a) (b)

Figure 108: Variation of flame brush thickness as a function of the flame coordinate for (a) a ϕ = 0.84, 30/70 H_2/CO mixture and (b) a ϕ = 0.70, 70/30 H_2/CO mixture, both at 10 atm. Measurements obtained for the 12 mm diameter burner at 50 m/s.

A few observations can be made from Figure 107 and Figure 108. First, note that at each $u'_{rms}/S_{L,0}$, the flame brush thickness grows continuously in the downstream direction from the burner exit, which is consistent with the notion that the flame brush thickness is controlled by turbulent diffusion. As a group of fluid particles that coincide with the flame convect downstream, they are dispersed due to turbulent diffusion [36].

Second, for a given mixture and pressure, the flame brush thickness is initially ($s/D < 0.5$) independent of the turbulence intensity. At larger s/D, the flame brush thickness is observed to increase with the turbulence intensity. In the near field, which is region near the burner exit, the flame motion and wrinkling is restricted by the anchoring boundary condition, which results in an unchanging flame brush thickness. In addition, studies of non-reacting mixing layers have shown that the transverse profiles of the axial fluctuations, $\overline{u'^2}$, and radial fluctuations, $\overline{v'^2}$, at various downstream locations collapse when normalized by U_s^2, where U_S is the difference between the mean jet and ambient velocities [37]. Since U_s^2 does not change in the downstream direction, then $\overline{u'^2}$ must also remain constant in order to maintain constant $\overline{u'^2}/U_s^2$. As a result, for a fixed mean flow velocity, the flames are exposed to essentially the same turbulence levels, resulting in little change in the flame brush thickness.

Further downstream, the flame front is residing in the potential core region of the jet and is influenced more by the turbulence levels in the jet [35]. As a result, higher jet turbulence intensities, result in greater flame brush thickness.

5.3.2 Effect of fuel composition

Constant $S_{L,0}$ studies

In this subsection, the influence of varying the H_2/CO ratio while keep the mixture $S_{L,0}$ constant is investigated. These data were obtained at a mean flow velocity of 50 m/s using the 12 mm diameter burner. As with the previous study, since $S_{L,0}$ and U_0 is constant across all the mixtures presented in this section, constant $u'_{rms}/S_{L,0}$ is equivalence to constant u'_{rms} and u'_{rms}/U_0.

Figure 109 plots the turbulent flame brush thickness as a function of the flame coordinate for various H_2/CO mixtures at $u'_{rms}/S_{L,0}$ of 17.40 and 27.60 at 1 atm.

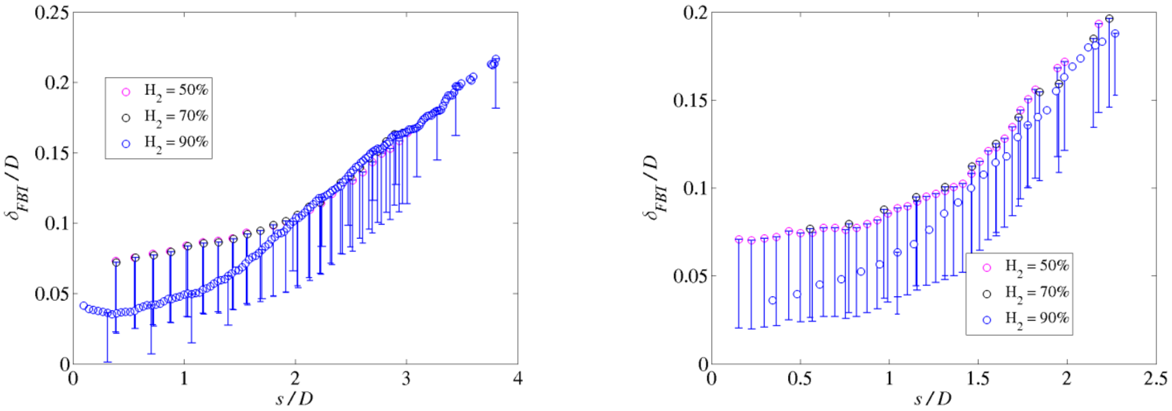

(a) (b)

Figure 109: Variation of flame brush thickness as a function of the flame coordinate for various H_2/CO ratios whose mixture $S_{L,0}$ has been held fixed. Measurements shown are obtained with the 12 mm diameter burner at (a) $u'_{rms}/S_{L,0}$ = 17.4 and (b) $u'_{rms}/S_{L,0}$ = 27.6 for a mean flow velocity of 50 m/s and pressure of 1 atm.

In Figure 109, the flame brush thickness initially ($s/D < 2$) has a dependence on the fuel composition, with the 30/70 and 50/50 H_2/CO mixtures having thicker flame brushes than the 90/10 mixture. Beyond this region, the curves merge and the flame brush thickness becomes independent of the fuel composition. The observed trend in the initial region can be attributed to the image resolution for the 90/10 H_2/CO case being roughly double that for the 30/70 and 50/50 cases. As a result, the lower resolution for the 30/70 and 50/50 cases is insufficient to resolve the flame brush thickness in the region $s/D < 1$, which is reflected by the 90/10 H_2/CO data residing within the error bars of the 30/70 and 50/50 H_2/CO data.

Similarly, Figure 110 plots the turbulent flame brush thickness as a function of the flame coordinate for various H_2/CO mixtures at $u'_{rms}/S_{L,0}$ of 17.40 and 27.60 at 10 atm. Although not a strong dependence, the flame brush thickness grows slightly with H_2

content for constant $S_{L,0}$. Although there is a dependence on fuel composition at 10 atm that is not present at 1 atm, the dependence is still fairly weak.

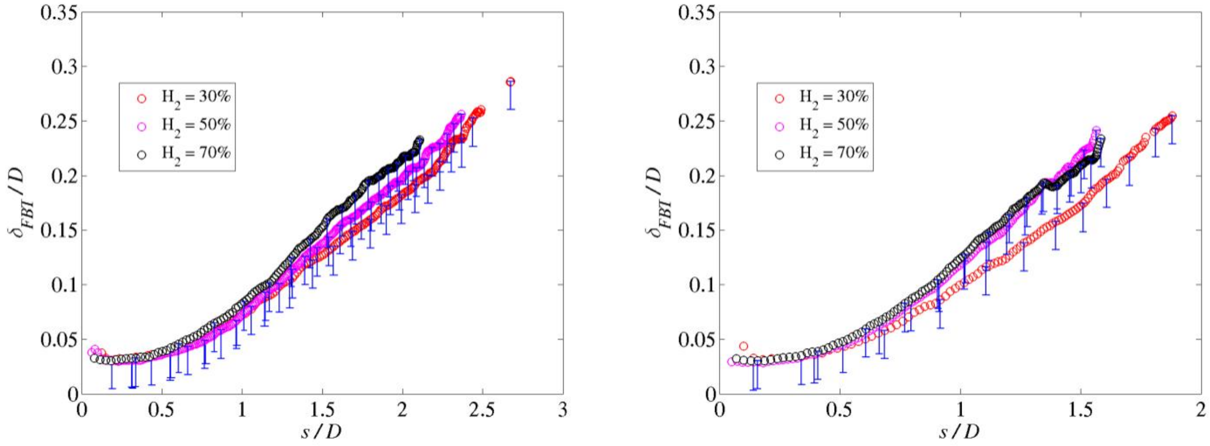

(a) (b)

Figure 110: Variation of flame brush thickness as a function of the flame coordinate for various H_2/CO ratios whose mixture $S_{L,0}$ has been held fixed. Measurements shown are obtained with the 12 mm diameter burner at (a) $u'_{rms}/S_{L,0}$ = 17.40 and (b) $u'_{rms}/S_{L,0}$ = 25 for a mean flow velocity of 50 m/s and pressure of 10 atm.

In general, it is reasonable to conclude that fuel composition has negligible influence on the flame brush thickness. These trends are in agreement with the traditional models that predict that the flame brush thickness is governed by large-scale turbulent diffusion only.

Equivalence ratio sweeps

In this subsection, the data obtained from experiments where the H_2/CO ratio is held fixed while the equivalence ratio is varied, is analyzed. The data presented were obtained using the 20 mm diameter burner.

Figure 111 plots the spatial variation of the turbulent flame brush thickness for a 30/70 H_2/CO mixture at equivalence ratios of 0.55 and 0.61 at $u'_{rms}/S_{L,0}$ of 21 at 5 atm.

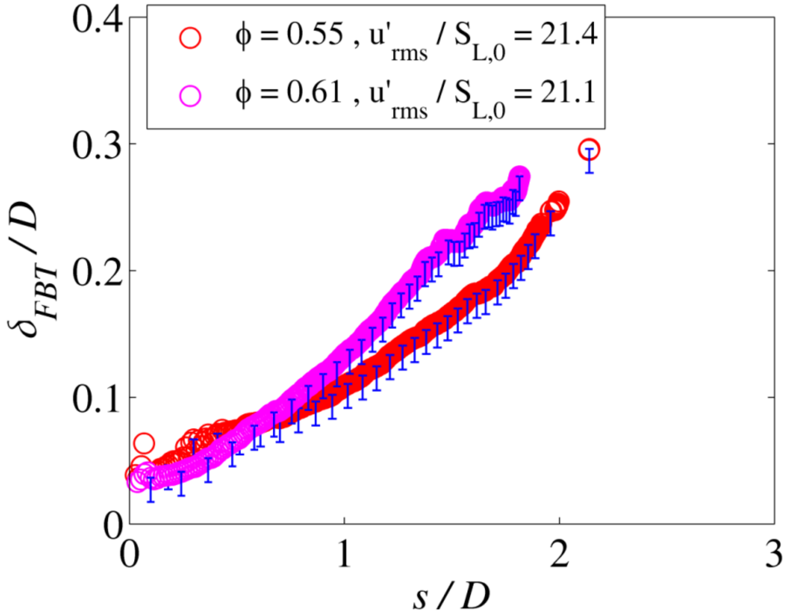

Figure 111: Variation of flame brush thickness as a function of the flame coordinate for a H_2/CO ratio of 30/70 at equivalence ratios of 0.55 and 0.61 at fixed $u'_{rms}/S_{L,0}$ = 21. Measurements obtained at a mean flow velocity of 25 m/s and pressure of 5 atm using the 20 mm diameter burner.

From Figure 111, the flame brush thickness is invariant with the distance downstream until about *s*/*D* = 1, beyond which, the richer mixture displays a larger flame brush thickness. This can be explained by the fact that the $S_{L,0}$ is higher at $\phi = 0.61$ than at $\phi = 0.55$, and so a higher u'_{rms} is required to maintain a constant $u'_{rms}/S_{L,0}$.

To remove the effect of varying u'_{rms}, Figure 112 plots the flame brush thickness as a function of the flame coordinate for the same mixtures as in Figure 111, but at constant u'_{rms}/U_0 instead of constant $u'_{rms}/S_{L,0}$. However, since the data were obtained at constant U_0, the data in Figure 112(a) and Figure 112(b) are essentially at constant u'_{rms}.

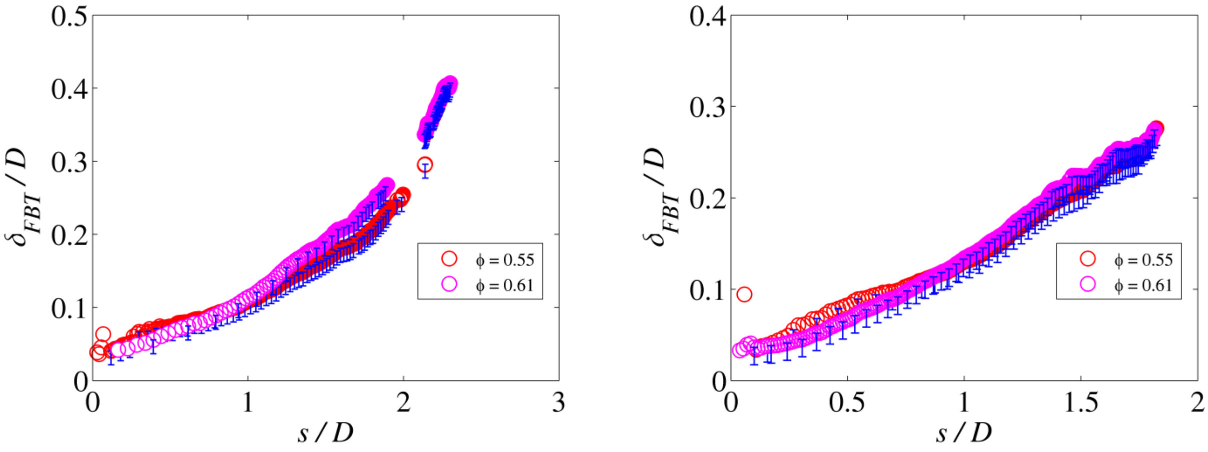

(a) (b)

Figure 112: Variation of flame brush thickness as a function of the flame coordinate for a H_2/CO ratio of 30/70 at equivalence ratios of 0.55 and 0.61 at (a) u'_{rms}/U_0 = 0.135 and (b) u'_{rms}/U_0 =0.178. Measurements obtained at a mean flow velocity of 25 m/s and pressure of 5 atm using the 20 mm diameter burner.

Figure 112 shows that at $u'_{rms}/U_0 = 0.135$ the ϕ = 0.61 case has a slightly larger flame brush thickness at higher *s*/*D* compared to the ϕ = 0.55 case. However, at the higher u'_{rms}/U_0, the differences between stoichiometry disappears. This suggests fuel composition effects are present at lower turbulence intensities, but are washed out by turbulence diffusion effects at higher turbulence intensities. It would be interesting to further investigate this effect by going to lower u'_{rms}/U_0 to see if the difference in flame brush thicknesses between equivalence ratios becomes more prevalent. Also note that when the effect of fuel composition is present, the richer mixture possesses the thicker flame brush. This is in contrast to trends observed in the turbulent flame speed, where more stretch sensitive (leaner) mixtures possess higher flame speeds.

Figure 113 plots the flame brush thickness as a function of the flame coordinate for equivalence ratios of 0.45 and 0.50 for a 50/50 H_2/CO mixture at 5 atm at constant u'_{rms}/U_0 of 0.135 and 0.178. Similar to Figure 112, at the lower u'_{rms}/U_0, the mixture with the richer equivalence ratio has a slightly thicker turbulent flame brush. However, influence of stoichiometry disappears at the higher u'_{rms}/U_0.

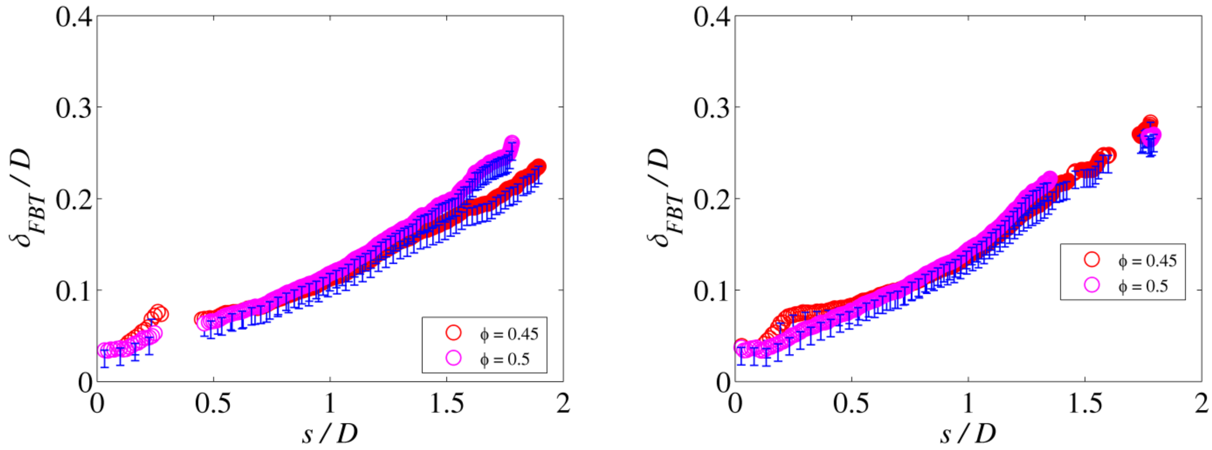

(a) (b)

Figure 113: Variation of flame brush thickness as a function of the flame coordinate for a H_2/CO ratio of 50/50 at equivalence ratios of 0.45 and 0.50 at (a) u'_{rms}/U_0 = 0.135 and (b) u'_{rms}/U_0 =0.178. Measurements obtained at a mean flow velocity of 25 m/s and pressure of 5 atm using the 20 mm diameter burner.

5.3.3 Effect of pressure

Pressure effect at constant $S_{L,0}$

In this section the influence of pressure on the flame brush thickness is analyzed for the experiments where the mixture $S_{L,0}$ is held constant across the pressures. These data were acquired with the 12 mm diameter burner at a mean flow velocity of 50 m/s. Since $S_{L,0}$ and U_0 is constant across all the mixtures presented in this section, then constant $u'_{rms}/S_{L,0}$ also means constant u'_{rms} and u'_{rms}/U_0 .

Figure 114 plots the turbulent flame brush thickness as a function of the flame coordinate for a 50/50 H_2/CO mixture at $u'_{rms}/S_{L,0}$ of 17.50 and 27.60 at 1 and 10 atm.

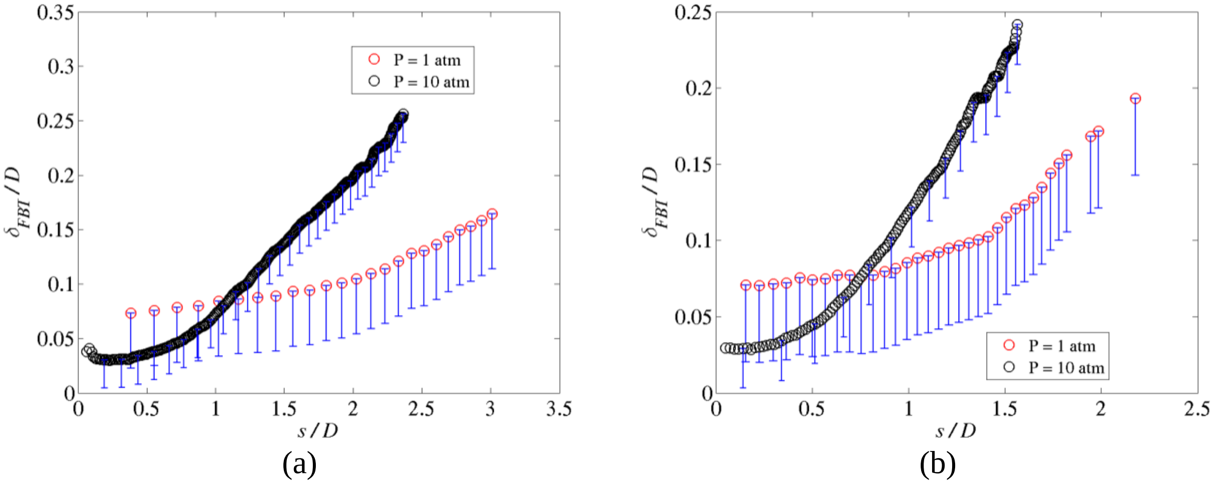

(a) (b)

Figure 114: Variation of flame brush thickness as a function of the flame coordinate for a H_2/CO ratio of 50/50 at 1 and 10 atm at (a) $u'_{rms}/S_{L,0}$ = 17.4 and (b) $u'_{rms}/S_{L,0}$ = 27.6. Measurements obtained at a mean flow velocity of 50 m/s using the 12 mm diameter burner.

Figure 115 plots the turbulent flame brush thickness as a function of the flame coordinate for a 70/30 H_2/CO mixture at $u'_{rms}/S_{L,0}$ of 17.50 and 27.6 at 1 and 10 atm.

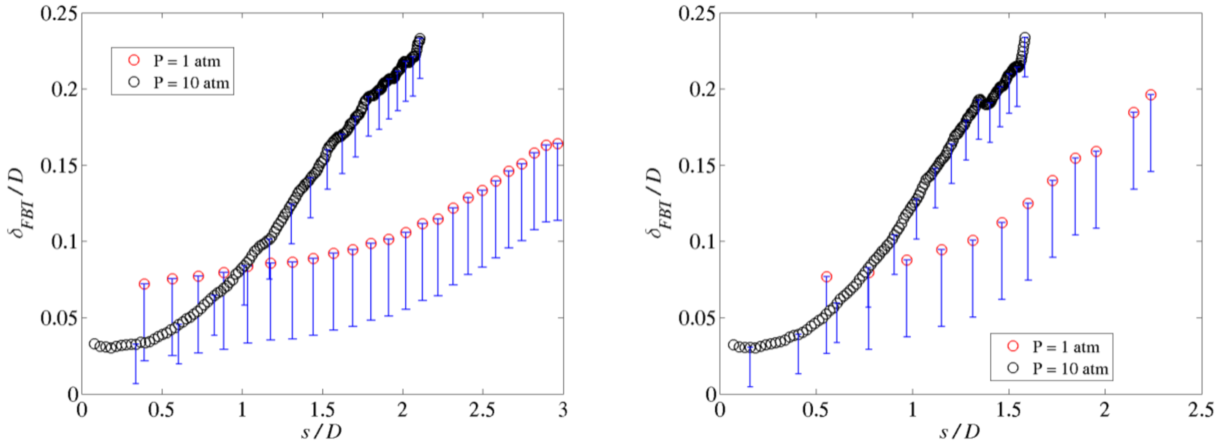

(a) (b)

Figure 115: Variation of flame brush thickness as a function of the flame coordinate for a H_2/CO ratio of 70/30 at 1 and 10 atm at (a) $u'_{rms}/S_{L,0}$ = 17.4 and (b) $u'_{rms}/S_{L,0}$ = 27.6. Measurements obtained at a mean flow velocity of 50 m/s using the 12 mm diameter burner.

Figure 114 and Figure 115 show that initially, in the region $s/D < 1$, the flame brush thickness is larger at 1 atm than at 10 atm. Beyond this region, the flame brush thickness is significantly augmented by pressure, at fixed $u'_{rms}/S_{L,0}$. As before, the observation from the initial region can be attributed to the lower imaging resolution of the 1 atm cases compared to the 10 atm cases, which is reflected in the error bars. Presumably, in reality the flame brush thickness at 1 atm is consistently lower than that at 10 atm, before merging at low *s*/*D*.

To further investigate this pressure effect, Figure 116 and Figure 117 plot the ratio of the flame brush thickness at 10 atm to the flame brush thickness at 1 atm for the 50/50 and 70/30 H_2/CO mixtures respectively. The ratio is calculated only in the region where the flame brush thickness at 10 atm is greater than at 1 atm.

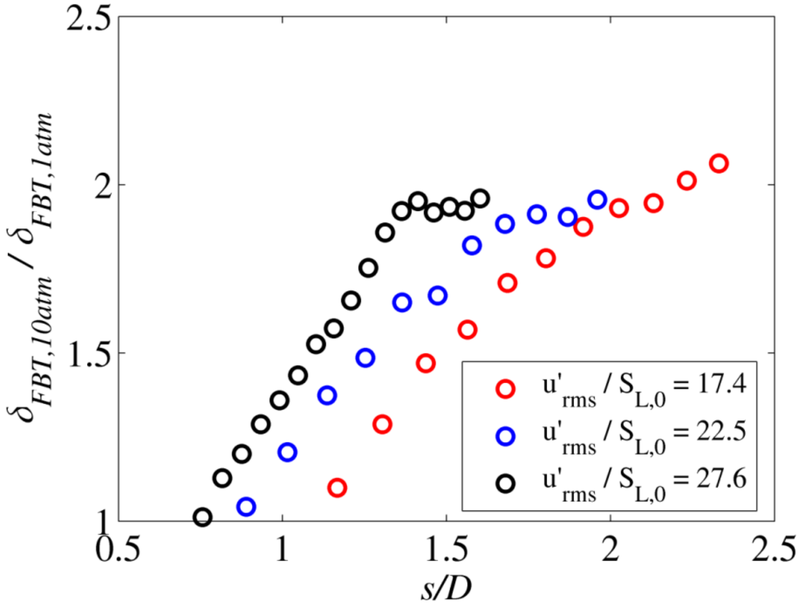

Figure 116: Ratio of the flame brush thickness at 10 atm to the flame brush thickness at 1 atm as a function of the flame coordinate for the 50/50 H_2/CO mixture.

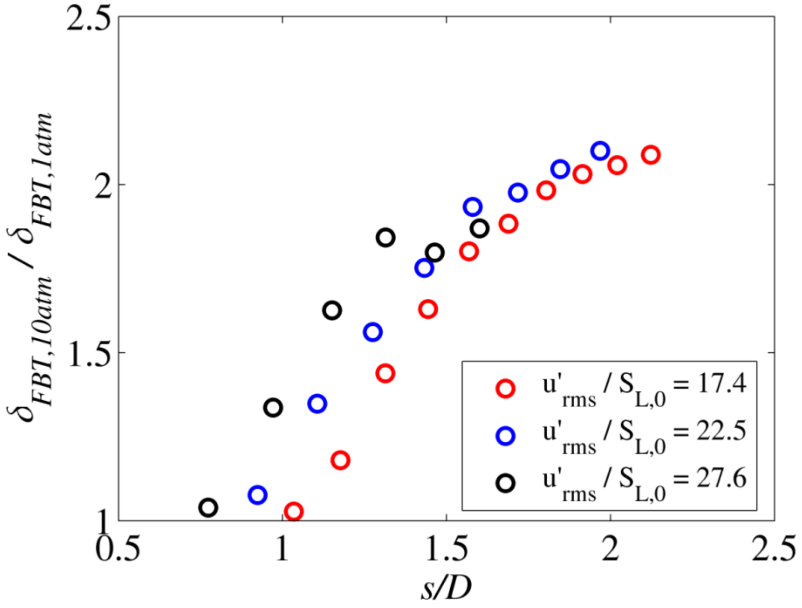

Figure 117: Ratio of the flame brush thickness at 10 atm to the flame brush thickness at 1 atm as a function of the flame coordinate surface for the 70/30 H_2/CO mixture.

Some observations can be made from Figure 116 and Figure 117. First, the ratio of flame brush thickness grows roughly linearly with the distance along the flame coordinate before saturating. The cause of this saturation is unclear, but the location where the saturation starts corresponds to the location where a change in the slope of the 1 atm data in Figure 114 and Figure 115 is seen. Second, the ratio of flame brush thicknesses increases with $u'_{rms}/S_{L,0}$ suggesting that the turbulence has a stronger augmenting effect on the flame brush thickness at higher pressures

In Figure 118, the same ratio of flame brush thicknesses is compared between the 50/50 and 70/30 H_2/CO mixtures at $u'_{rms}/S_{L,0} = 17.4$ and $u'_{rms}/S_{L,0} = 27.6$ while $S_{L,0}$ is held constant across the mixtures.

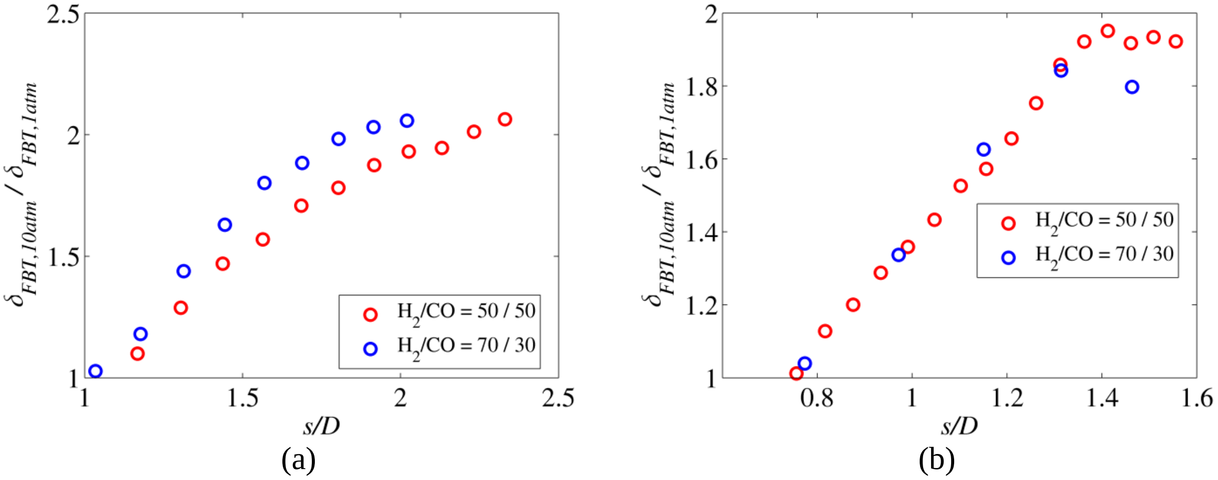

(a) (b)

Figure 118: Effect of fuel composition on the ratio of the flame brush thickness at 10 atm to the flame brush thickness at 1 atm at (a) $u'_{rms}/S_{L,0} = 17.4$ and (b) $u'_{rms}/S_{L,0} = 27.6$.

Note that the ratio in flame brush thicknesses is higher for the 70/30 H_2/CO mixtures at the lower turbulence intensity. However, when the turbulence intensity level is increased the ratio in flame brush thickness is independent of the mixture composition.

This suggests that there may be a coupling between the fuel composition and pressure effects in the form of Darrieus-Landau and thermo-diffusive instabilities that is influencing the brush thickness. However, as was pointed out earlier, it would be instructive in the future to take data at lower values of u'_{rms}/U_0 to see if the fuel composition effect becomes more prevalent.

The mechanism by which pressure augments the flame brush thickness is uncertain at this point. The turbulence characteristics in the mixing layer and fully developed region of the jet do not have a Reynolds number dependence through which the pressure can exert an influence [37]. As a result, this is an issue that will need to be investigated in more detail in the future.

Pressure effect at non-constant $S_{L,0}$

Having looked at the influence of pressure when $S_{L,0}$ is held constant, this section analyzes the influence of pressure when $S_{L,0}$ varied across pressure. The data analyzed in this section were obtained with the 20 mm diameter burner.

Figure 119 plots the flame brush thickness as a function of the flame coordinate for a 30/70 H_2/CO mixture with roughly similar equivalence ratios at pressures of 5 and 10 atm.

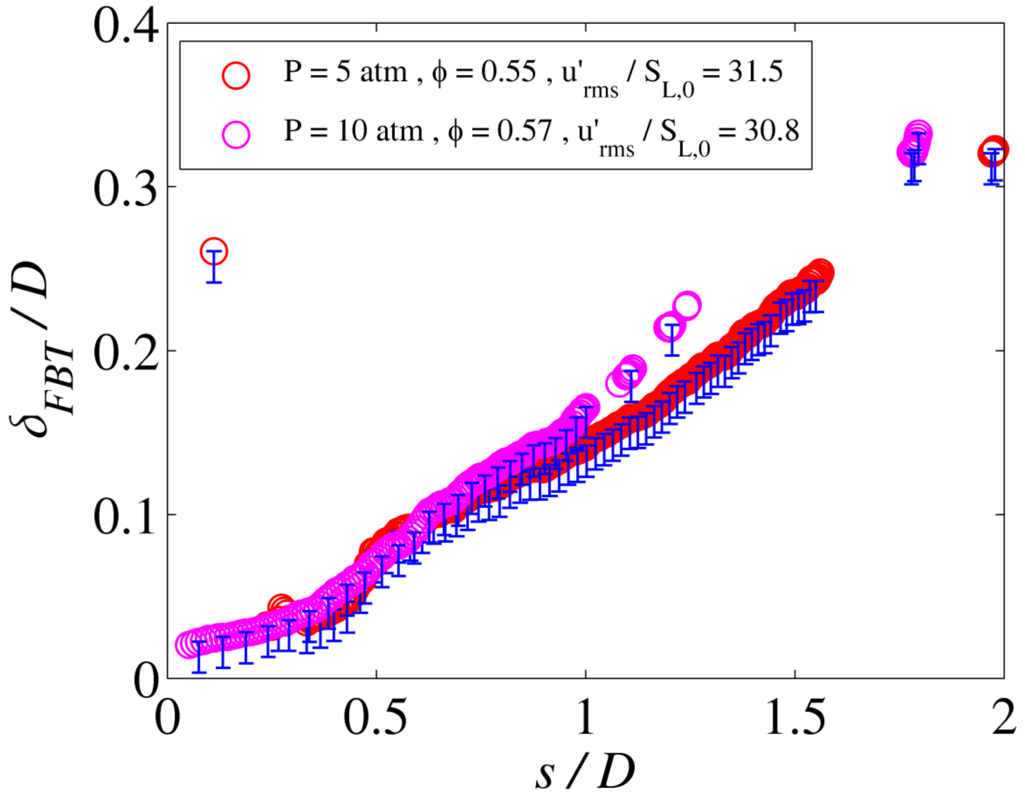

Figure 119: Variation of flame brush thickness as a function of the flame coordinate for the 30/70 H_2/CO mixture for ϕ = 0.55 and 0.57 at 5 and 10 atm respectively at $u'_{rms}/S_{L,0} = 30$. Measurements obtained at a mean flow velocity of 25 m/s using the 20 mm diameter burner.

From Figure 119 is appears that pressure has a slight augmenting effect on the flame brush thickness at constant $u'_{rms}/S_{L,0}$ when the mixture $S_{L,0}$ is varying across pressures. Since $S_{L,0}$ at ϕ = 0.57 at 10 atm ($S_{L,0}$ = 12.7 cm/s) is lower than $S_{L,0}$ at ϕ = 0.55 and 5 atm ($S_{L,0}$ = 15.8 cm/s), a higher u'_{rms} is needed to maintain constant $u'_{rms}/S_{L,0}$ for the ϕ = 0.57 case at 10 atm, which augments the flame brush thickness.

As before, to remove the influence of varying u'_{rms} across pressures, Figure 120 plots the flame brush thickness as a function of the flame coordinate for the same mixtures at constant u'_{rms}/U_0 . Consistent with the findings in at constant $S_{L,0}$, pressure has an augmenting influence on the flame brush thickness at constant u'_{rms}/U_0 even when $S_{L,0}$ is not held constant.

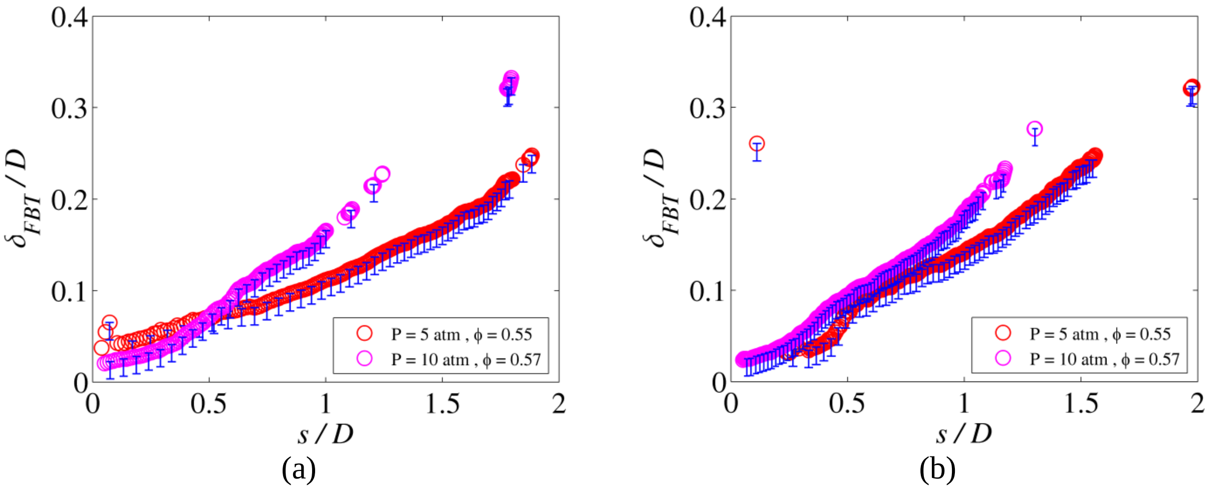

Figure 120: Variation of flame brush thickness as a function of the flame coordinate for the 30/70 H_2/CO mixture for ϕ = 0.55 and 0.57 at pressure 5 atm for (a) u'_{rms}/U_0 = 0.156 and (b) u'_{rms}/U_0 = 0.199. Measurements obtained at a mean flow velocity of 25 m/s using the 20 mm diameter burner.

Similar analysis for a 70/30 H_2/CO mixture at a constant equivalence ratio and $u'_{rms}/S_{L,0}$ at pressures of 10 and 20 atm shows that pressure augments the flame brush thickness.

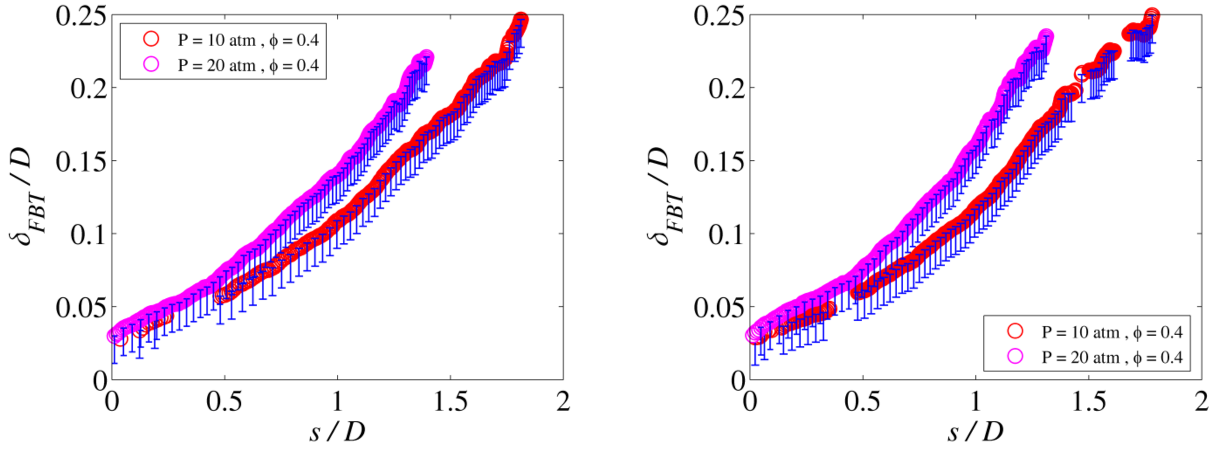

(a) (b)

Figure 121: Variation of flame brush thickness as a function of the flame coordinate for a 70/30 H_2/CO mixture for ϕ = 0.40 at 10 and 20 atm at (a) u'_{rms}/U_0 = 0.135 and (a) u'_{rms}/U_0 = 0.156. Measurements obtained using the 20 mm diameter burner.

5.4 Summary of trends

It is instructive at this junction to summarize the main trends from the data presented in the earlier sections.

First, the turbulence intensity is shown to affect the flame brush thickness differently depending on the region of the flow field in which the flame resides. In the initial region just above the burner, the flame resides in the mixing layer between the jet potential core and the quiescent ambient. In this region, the turbulent fluctuations possess a self-similar characteristic when normalized by the square of the velocity difference between the mean jet velocity and the mean ambient velocity. In this region, the velocity difference is unchanging, and so the turbulent fluctuations also remain roughly constant, which may explain why the flame brush thickness is independent of the centerline turbulence intensity.

Further downstream, once the shear layers merge, the flame brush thickness is controlled more by the jet turbulence, and higher levels of jet turbulence, result in a thicker flame brush.

Second, the flame brush thickness is independent of the fuel composition at constant u'_{rms}/U_0. This observation corroborates findings reported in the literature [36], but for a wide range of H_2/CO mixtures over a broad range of pressures and turbulence intensities. This observation is explaining by attributing the turbulent flame characteristics to large-scale turbulent diffusion processes, which are independent of the instantaneous flame characteristics. However, the flame brush thickness is also observed to increase with mixture equivalence ratio for a fixed H_2/CO ratio. This effect is more apparent at the lower turbulence intensity, while at the higher turbulence intensities the dependency on equivalence ratio disappears, presumably due to turbulent diffusion.

Finally, the pressure is seen to augment the turbulent flame brush thickness for a given H_2/CO mixture at constant u'_{rms}/U_0. This is a significant finding because the dependence of the flame brush thickness on pressure has not been previously reported. However, the mechanism by which this augmentation occurs is not apparent, since the turbulence characteristics in the jet shear layer and the fully developed region do not carry a Reynolds number dependence.

5.5 Comparisons to theoretical predictions

In this section comparisons between the data presented in this chapter and the predictions from the model given by Eq. (1.25) will be made. To recall, Eq. (1.25) is derived by assuming that at large turbulence intensities, $u'_{rms}/S_{L,0} >> 1$, the flame elements are convected along by the turbulent flow as a passive scalar. The equation represents the dispersion between the fluid particles that coincide with the flame elements.

In the work by Goix *et al.*[59], the flame brush thickness data is shown to collapse when parameterized by the Lagrangian length scale, l_L Lagrangian time scale, τ_L, and the flame development time t_F, as represented by Eq. (5.6), which is a validation of treating the flame as a passive scalar in a turbulent flow field.

$$\frac{\delta_{FBT}}{l_L} = f\left(\frac{t_F}{\tau_L}\right) \tag{5.6}$$

The primary difficulty in this analysis is the estimation of the Lagrangian time scale. However, in Ref.[59], τ_L is estimated as l_{int}/u'_{rms} , l_L is calculated as $l_L = U_0\tau_L$ and the flame development time is calculated as $t_F = y/U_0$, where y is the axial distance from the burner to the average flame. Note that the distance is considered along the axial coordinate and not the flame coordinate.

Figure 122 and Figure 123, plot the data obtained using the 12 mm diameter burner at 1 and 10 atm respectively.

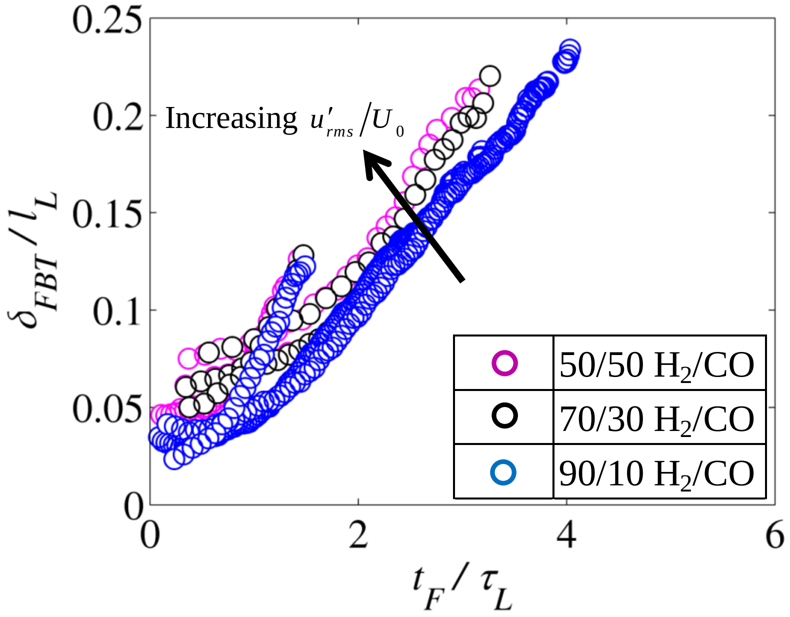

Figure 122: Flame brush thickness data obtained at 1 atm using the 12 mm diameter burner parameterized by Eq. (5.6).

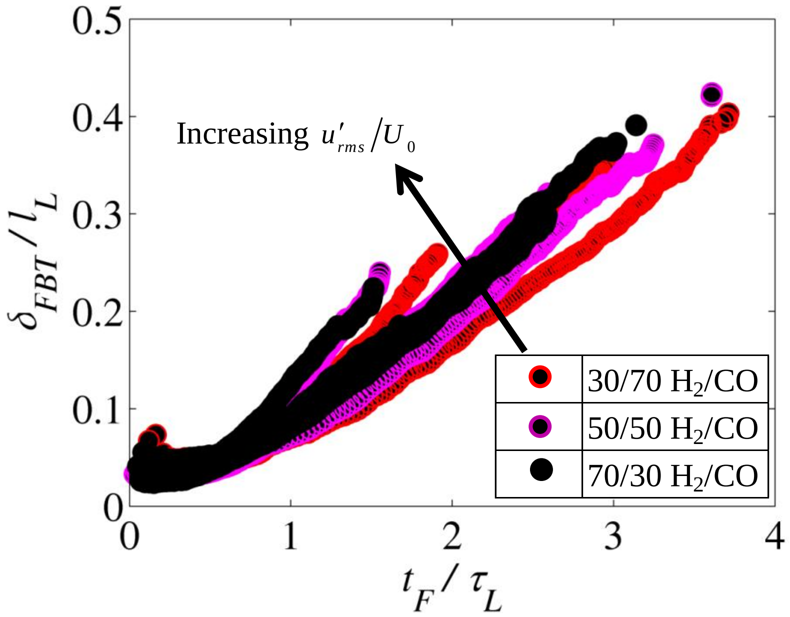

Figure 123: Flame brush thickness data obtained at 1 atm using the 12 mm diameter burner parameterized by Eq. (5.6).

Figure 122 and Figure 123 show that Eq. (5.6) does a reasonable job of collapsing the flame brush thickness data. In particular, the scaling collapses the data into groups of constant u'_{rms}/U_0. However, the scaling does not collapse across u'_{rms}/U_0. This is in contrast to the results presented in Ref.[59], where they showed that the parameterization given by Eq. (5.6), collapses the data across all turbulence intensities. However, the absolute range of normalized turbulence intensities considered (u'_{rms}/U_0 ~ 3.5-5%) was significantly smaller than the range explored here (13-20%).

Figure 124, which plots the 1 and 10 atm data together, shows that the parameterization provided by Eq. (5.6) is unable to collapse the data across the pressures.

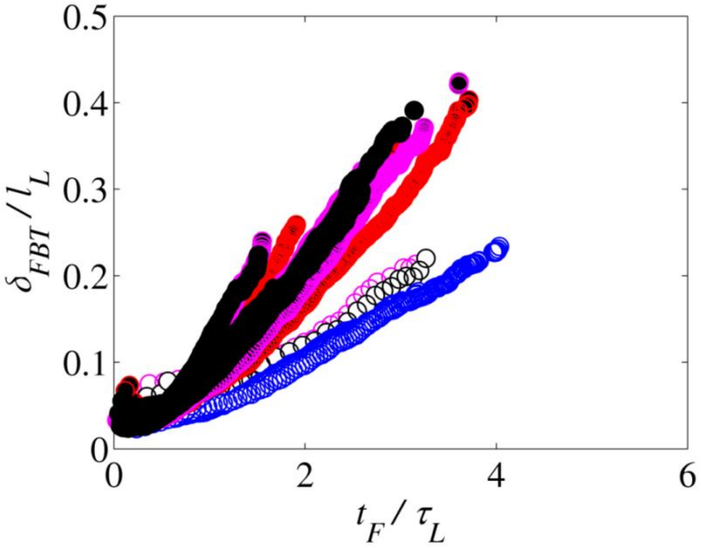

Figure 124: Flame brush thickness data obtained at 1 and 10 atm using the 12 mm diameter burner parameterized by Eq. (5.6). Unfilled symbols correspond to 1 atm while filled symbols correspond to 10 atm.

To analyze the parameterization given by Eq. (5.6) further, Figure 125 and Figure 126 plot comparisons between the model for the flame brush thickness, given by Eq. (1.25), and the actual data.

In Figure 125, comparisons are given for the 50/50 and 90/10 H_2/CO mixtures obtained at 1 atm while Figure 126, provides comparisons for the 30/70 and 70/30 H_2/CO mixtures at 10 atm.

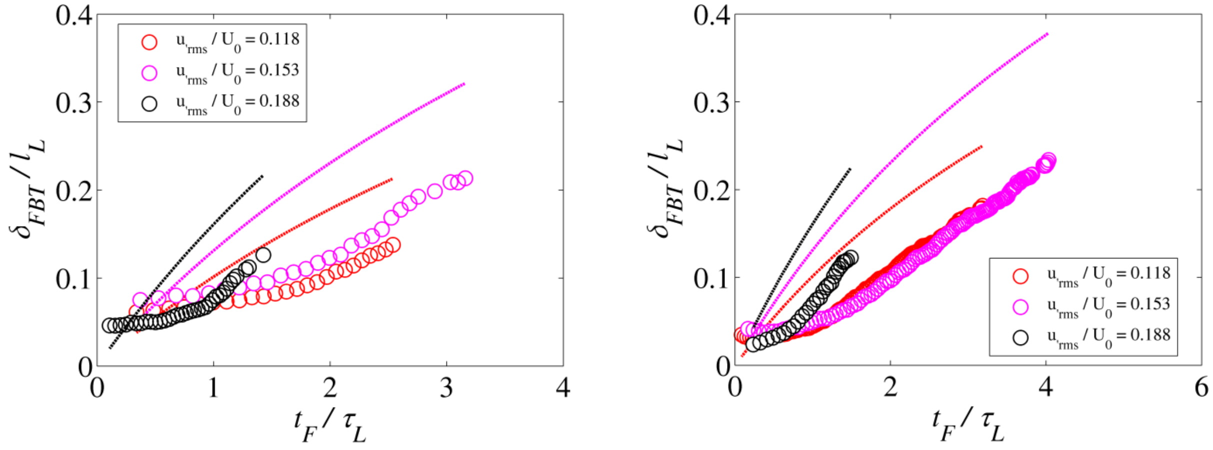

(a) (b)

Figure 125: Comparison between the actual normalized flame brush data (circles) and model (line) given by Eq. (1.25) for (a) 50/50 and (b) 90/10 H_2/CO mixtures at 1 atm and constant $S_{L,0}$ obtained using the 12 mm diameter burner.

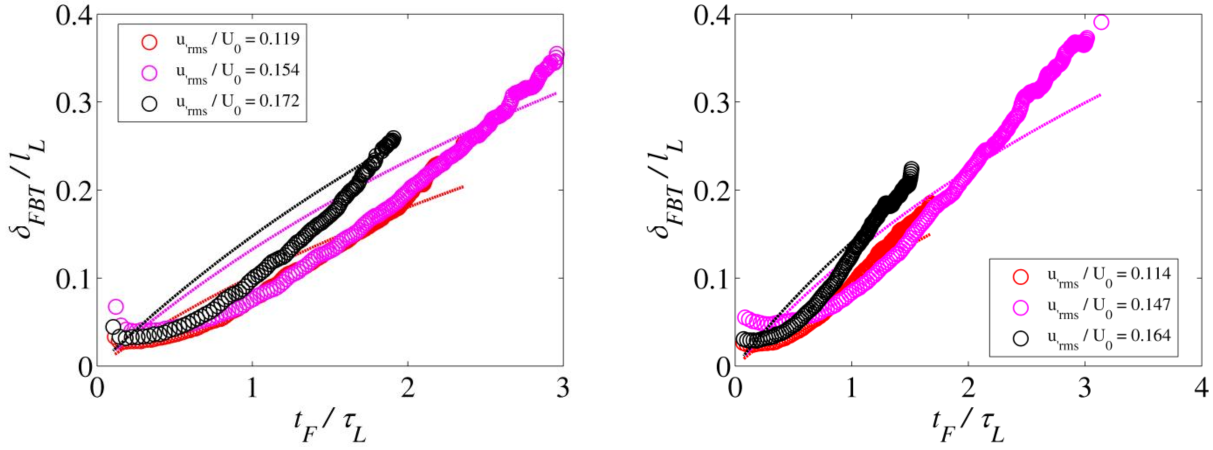

(a) (b)

Figure 126: Comparison between the actual normalized flame brush data (circles) and model (line) given by Eq. (1.25) for (a) 30/70 and (b) 70/30 H_2/CO mixtures at 10 atm and constant $S_{L,0}$ obtained using the 12 mm diameter burner.

Before commenting on the comparisons between the data and the model, it is worthwhile to revisit the expressions for Eq. (1.25) in the limit of small and large t_F / τ_L , given by Eq. (1.26). In the limit of small t_F / τ_L , the flame brush thickness is predicted to vary linearly with the flame development time, while at large t_F / τ_L , the flame brush thickness varies as the square root of the development time.

Due to the limitations in the image resolution, it is unclear whether the flame brush thickness near the flame base, where $t_F / \tau_L << 1$, varies linearly with the flame development time. Further downstream, the flame brush thickness growth rate is predicted to saturate and vary as the square root of the flame development time, which is not observed with the data. However, the square root dependence has been reported previously in Ref. [36, 59], for rod-stabilized V-shaped flames geometry.

The absence of the saturation in the data may be attributed to the geometry of the flame brush. In the rod-stabilized flames, the two sides of the flames do not merge with increasing downstream distance, while in the Bunsen flame they do merge. As a result, since the flame brush thickness calculation is this work seeks to minimize the effects of flame interaction, the region considered may not proceed far enough downstream for the thickness to start saturating. In fact this saturation may not ever occur due to the interaction downstream..

It is also interesting to note that although the model generally over-predicts the data, the model over-predicts the 1 atm data by a greater margin than it does the 10 atm data.

These results show that although there is some success in collapsing the data taken at constant u'_{rms}/U_0 with the parameterization given by Eq. (5.6), scaling is unable to collapse the data across u'_{rms}/U_0 and pressure. Furthermore, the model for the flame brush thickness predicts a saturation in the flame brush thickness which is not observed in the data, and the model also consistently over-predicts the data.

5.6 Self-similar structure of the turbulent flame brush

It is worthwhile to make a few points regarding the self-similar structure of the turbulent flame brush. As discussed in the introduction to this chapter, Lipatnikov and Chomiak [36] found that the average progress variable profile through the flame followed a self-similar profile when the distance through the flame brush was normalized by the local flame brush thickness.

Figure 127 plots the variation of the average progress variable through the turbulent flame brush for a subset of the 12 mm diameter burner dataset. The normalized distance through the turbulent flame brush is defined in Eq. (1.23), and the flame brush thickness is defined as the distance between the $\langle c \rangle = 0.3$ and 0.7 contours. In order to distinguish between data that may lie on top of each other, each data point is given a ‘random jitter’ in the *x* and *y* directions, explaining the ‘cloud’ of points at each location. In addition, the error function profile given by Eq. (5.7) is also plotted, where μ and σ in Eq. (5.5) are equated to $x_{\langle c \rangle = 0.5}$ and δ_{FBT}, which is defined similarly to the data.

$$\langle c \rangle = \frac{1}{2}\left[1 + erf\left(\frac{x_{\langle c \rangle} - x_{\langle c \rangle = 0.5}}{\delta_{FBT}\sqrt{2}}\right)\right] \tag{5.7}$$

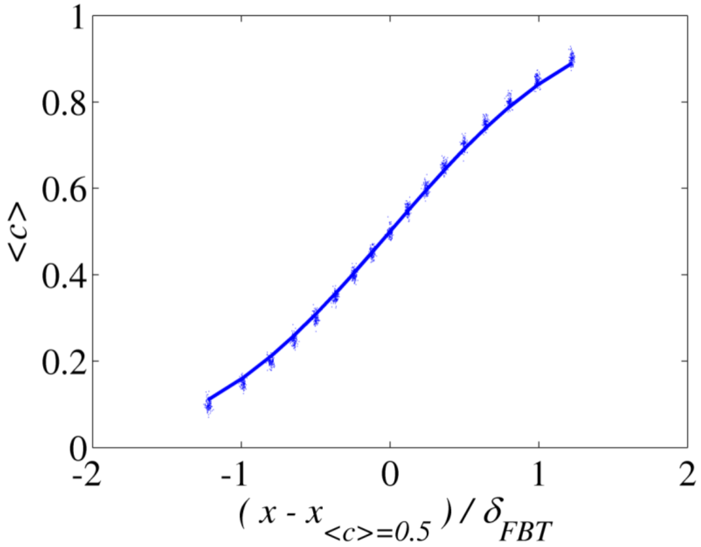

Figure 127: Progress variable variation as a function of the normalized distance through the flame brush for a sample of data from the 12 mm diameter burner data set. The flame brush thickness is defined as the distance between the <c> = 0.3 and 0.7 surfaces.

As expected, the progress variable distribution through the flame follows an error function distribution, since the locations of each progress variable contour is calculated using Eq. (5.5).

In addition, properties of the standard normal distribution can be utilized to show why the data is represented almost exactly by Eq.(5.7). Starting from the definition that the average progress variable value denotes the cdf of the flame position:

$$< c >= P\left(-\infty < x < x_{<c>}\right) \tag{5.8}$$

Eq.(5.5) can then be used to write the following expressions to determine the location of the respective progress variable surfaces

$$
\begin{aligned}
0.3 &= \frac{1}{2}\left[1 + erf\left(\frac{x_{\langle c\rangle=0.3} - \mu}{\sigma\sqrt{2}}\right)\right] \\
0.7 &= \frac{1}{2}\left[1 + erf\left(\frac{x_{\langle c\rangle=0.7} - \mu}{\sigma\sqrt{2}}\right)\right]
\end{aligned}
\tag{5.9}
$$

To determine the number of standard deviations the contours are from the mean location, $x = \mu + n\sigma$ is substituted into Eq. (5.9) to obtain:

$$
\begin{aligned}
0.3 &= \frac{1}{2}\left[1 + erf\left(\frac{n_{\langle c\rangle=0.3}}{\sqrt{2}}\right)\right] \\
0.7 &= \frac{1}{2}\left[1 + erf\left(\frac{n_{\langle c\rangle=0.7}}{\sqrt{2}}\right)\right]
\end{aligned}
\tag{5.10}
$$

Since the Gaussian profile is symmetric about the mean, the 0.3 and 0.7 contours lie equal number of standard deviations away from the mean, only one of the standard deviations in Eq.(5.10) needs to be solved for. Using tabulated values for the error function, the <c> = 0.3 contour is calculated to lie 0.52 standard deviations from the mean. As a result, the flame brush thickness when calculated as the distance between the 0.3 and 0.7 progress variable contours corresponds to almost one standard deviation, σ, leading to an almost exact fit of the data when a fit of the form given in Eq. (5.7) is used.

So although Lipatnikov and Chomiak state that the self-similar nature of the progress variable profile is a significant finding [36], the same finding here is really a consequence of the fact that our intensity profiles are being fit using a Gaussian profile. But the conclusions derived in Ref.[36] can be reinterpreted to state that the normalized scalar (temperature, mass fraction, etc.) variations normal to the flame brush closely follow a Gaussian profile.

5.7 Definition dependence of the turbulent flame brush

In the previous sections, the flame brush thickness was defined as the distance between the <c> = 0.3 and 0.7 contours. In this section, the trends observed when the flame brush thickness is calculated using other means given in Sec. 5.2 is briefly discussed.

Figure 128 plots the flame brush thickness defined by the three different definitions for a ϕ = 0.70, 70/30 H_2/CO mixture at $u'_{rms}/S_{L,0}$ = 25.3 and 10 atm.

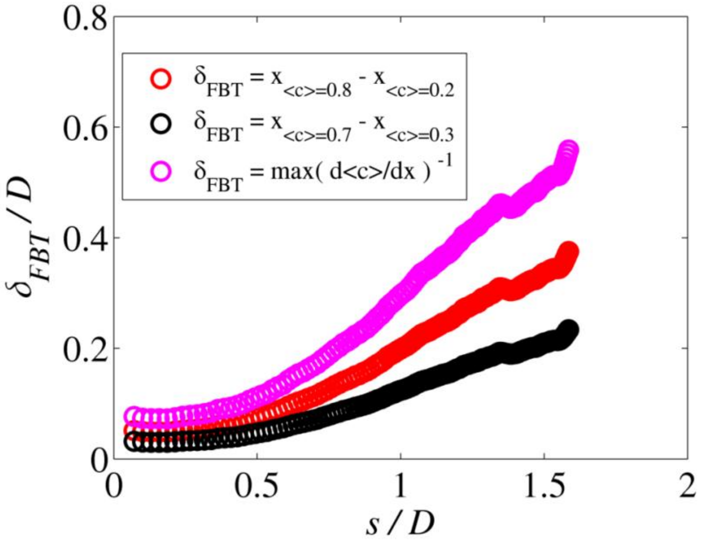

Figure 128:Dependence of flame brush thickness definition for a ϕ = 0.70, 70/30 H_2/CO mixture at $u'_{rms}/S_{L,0}$ = 25.3 at 10 atm. Data acquired using the 12 mm burner at 50 m/s mean flow velocity.

Although different definitions produce different quantitative results as would be expected, qualitatively the trends remain unchanged. In particular, the flame brush thickness defined using Eq. (1.27) produces the largest flame brush thicknesses, while the definition based on the distance between the 0.3 and 0.7 contours produces the smallest.

To investigate this point a little further, Figure 129 plots the influence of pressure on the flame brush thickness for the constant $S_{L,0}$ studies (presented in Sec. 5.3.3) for the three different definitions shown in Figure 128. It is evident that the choice of progress variables does not alter the final conclusion that the pressure has an augmenting influence on the flame brush thickness.

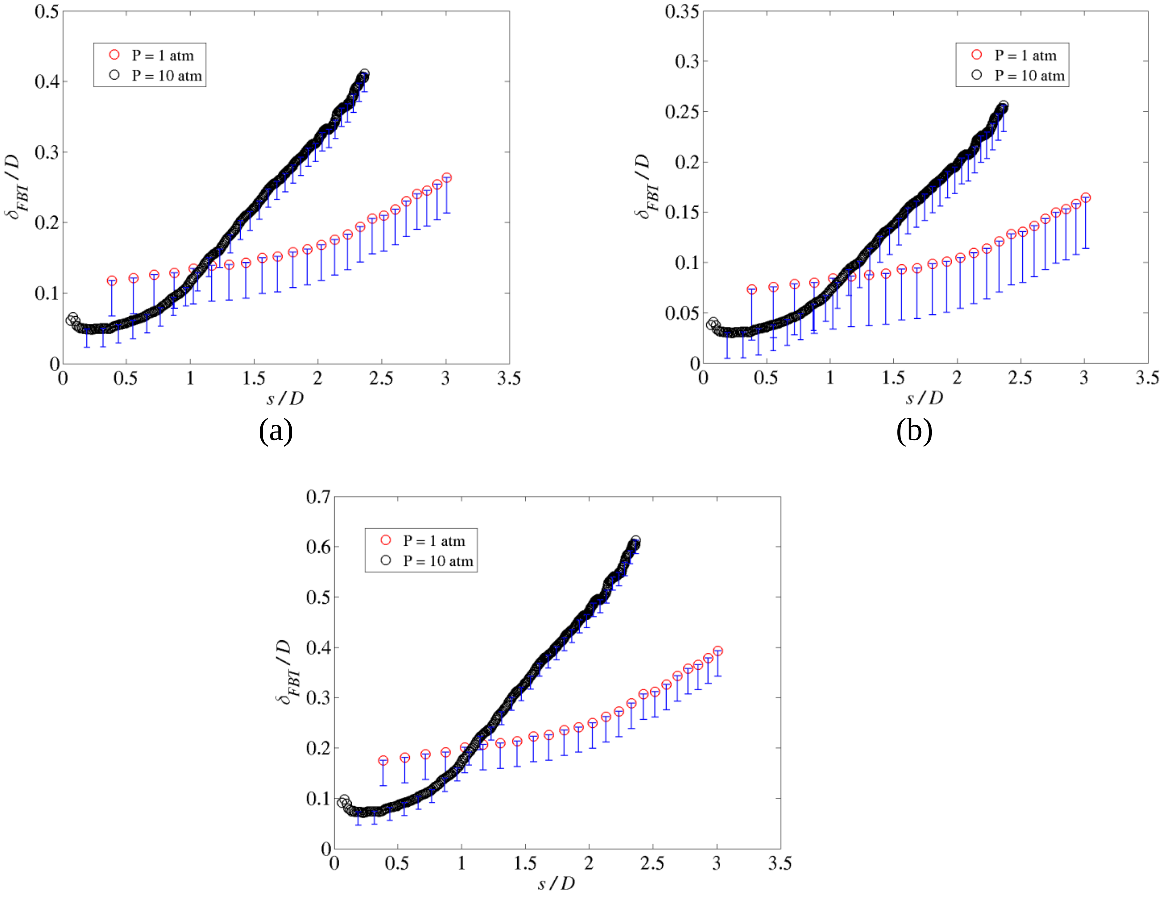

(a) (b)

(c)

Figure 129: Influence of pressure on the flame brush thickness when $S_{L,0}$ is held constant for a 50/50 H_2/CO mixture at $u'_{rms}/S_{L,0} = 17.5$, when δ_{FBT} is defined as (a) the distance between the <*c*> = 0.2 and 0.8 contours, (b) the distance between the <*c*> = 0.3 and 0.7 contours, and (c) Eq. (1.27).

In addition, Figure 130 plots the ratio of the flame brush thickness at 10 atm to the flame brush thickness at 1 atm for the three different definitions for the 50/50 H2/CO mixture. Note how all the data the ratio is identical regardless of the definition that is utilized. This can be explained by analyzing the characteristics of the Gaussian curve used to fit the intensity profiles along a normal at a point in the flame brush. At a given location *s*/*D* in the flame brushes at the two different pressures, the Gaussian profiles are characterized by different means and standard deviations. If the flame brush thickness is defined as the distance between any two progress variable contours, $<c>_1$ and $<c>_2$, then Eq. (5.11) can be utilized to determine the physical location, *x*, of the progress variable:

$$\begin{aligned} \langle c \rangle_1 &= \frac{1}{2}\left[1 + erf\left(\frac{x_1 - \mu}{\sigma\sqrt{2}}\right)\right] \\ \langle c \rangle_2 &= \frac{1}{2}\left[1 + erf\left(\frac{x_2 - \mu_2}{\sigma\sqrt{2}}\right)\right] \end{aligned} \tag{5.11}$$

Equation (5.11) can then be re-arranged to obtain:

$$\begin{aligned} erf\left(\frac{x_1 - \mu}{\sigma\sqrt{2}}\right) &= 2\langle c \rangle_1 - 1 \\ erf\left(\frac{x_2 - \mu}{\sigma\sqrt{2}}\right) &= 2\langle c \rangle_2 - 1 \end{aligned} \tag{5.12}$$

Since the error function is centered on $<c> = 0.5$, then using the symmetry properties of the error function, $\left|< c >_1 - 0.5\right| = \left|< c >_2 - 0.5\right|$, the following expressions can be written for the physical locations of the $<c>_1$ and $<c>_2$ contours:

$$\frac{x_1 - \mu}{\sigma\sqrt{2}} = \alpha_1$$
$$\frac{x_2 - \mu}{\sigma\sqrt{2}} = -\alpha_1 \tag{5.13}$$

where α is the argument of the error function that yields a value of $2\langle c \rangle - 1$ in Eq. (5.12). The flame brush thickness can then be calculated as:

$$\delta_{FBT} = x_1 - x_2 = 2\sigma\sqrt{2}\alpha_1 \tag{5.14}$$

From Eq. (5.14), it is evident that at a given location, *s*/*D*, in the flame brush, the ratio of δ_{FBT} between two different pressures simplifies to just the ratio of the standard deviations of the two Gaussian fits to the intensity along the normal. The ratio is independent of the progress variables used to define the flame brush thickness.

Similarly, when the flame brush thickness is defined using Eq.(1.27), $\left(d\langle c \rangle / dx\right)_{\max}$ occurs at the mean, $x = \mu$. Since $d\langle c \rangle / dx$ is equal to the original Gaussian fit given by Eq. (5.3), then substituting μ for x in Eq. (5.3), the following expression is obtained for the flame brush thickness:

$$\left(\frac{d\langle c \rangle}{dx}\right)_{\max}^{-1} = \sigma\sqrt{2\pi} \tag{5.15}$$

Once again, the ratio of the flame brush thickness simplifies to the ratio of the standard deviations, in the exact same way as when the flame brush thickness is defined as the distance between two progress variables.

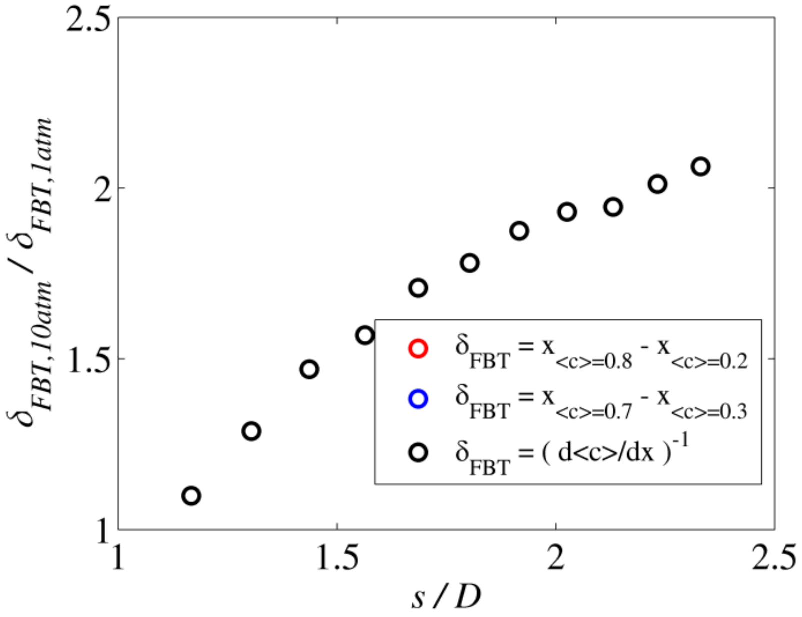

Figure 130: Dependence of the flame brush thickness ratio on the definition of the flame brush thickness.

Finally, it is also of interest to determine how the average progress variable distributions through the flames differ based on the different definitions for δ_{FBT}. Figure 131 plots the variation of the average progress variable as a function of the normalized distance through the flame brush, defined by Eq.(1.23), for a subset of the 12 mm diameter burner dataset. In addition, Eq. (5.5) is also plotted where μ and σ are defined as $x_{<c>=0.5}$ and δ_{FBT}. In Figure 131, we define δ_{FBT} to be the distance between the <c> = 0.2 and 0.8 contours.

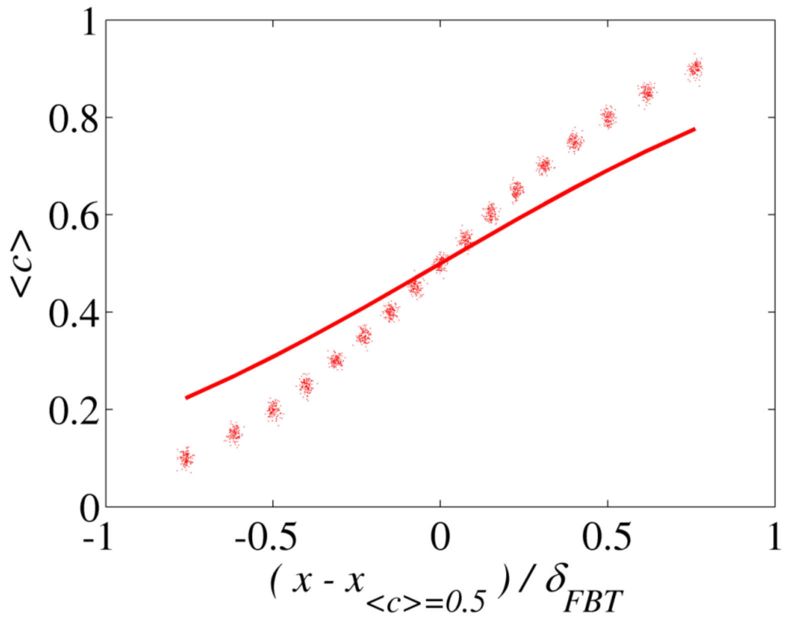

Figure 131: Progress variable variation as a function of the normalized distance through the flame brush for a sample of data from the 12 mm diameter burner data set. The flame brush thickness is defined as the distance between the <c> = 0.2 and 0.8 surfaces.

The data follows an error function profile, as is expected, but the error function profile computed using Eq. (5.7) does not match the data as well as in Figure 127. This can be explained by extending the previous arguments to show that the locations of the <c> = 0.2 and 0.8 contours are not one σ apart.

Figure 132 plots the variation of the average progress variable as a function of the normalized distance through the flame brush for a subset of the 12 mm diameter burner dataset. In addition, Eq. (5.5) is also plotted where μ and σ are defined as $x_{<c>=0.5}$and δ_{FBT}. In Figure 132, δ_{FBT} is defined using Eq.(1.27). As before, the discrepancy between the fit and data can be explained using an argument similar to that used to explain Figure 131.

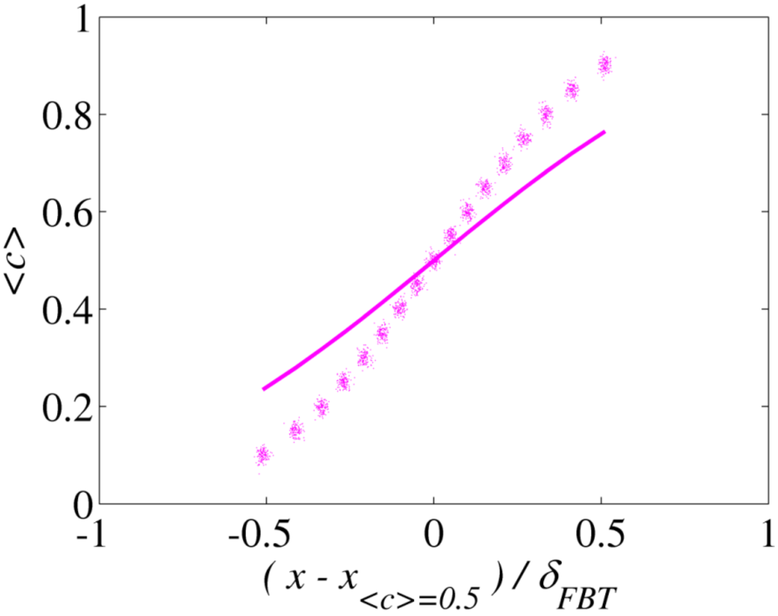

Figure 132: Progress variable variation as a function of the normalized distance through the flame brush for a sample of data from the 12 mm diameter burner data set. The flame brush thickness is defined using Eq. (1.27).

Chapter 6
Conclusions and Recommendations for Future Work

This chapter summarizes the principle findings of this work and discusses recommendations for future work.

6.1 Contributions

6.1.1 Flame speed database

This work has produced an extensive database of turbulent consumption speed measurements that span a wide range of H_2/CO ratios, turbulence intensities, mean flow velocities and pressures. Our data corroborates findings by other workers who have demonstrated that fuel mixtures with the same $S_{L,0}$ and exposed to the same turbulence intensity, u'_{rms}, can have appreciably different turbulent flame speeds by virtue of the mixture composition.

The key contribution of this work is to reproduce this finding for a wide range of H_2/CO mixtures at large normalized turbulence intensities and elevated pressures. It has been speculated that at high normalized turbulence intensities, these fuel effects, which are essentially molecular diffusion effects, would be washed out by turbulent diffusion. However, this work has shown the persistence of these fuel effects at $u'_{rms}/S_{L,0}$ up to 45.

Furthermore, we also show that these fuel effects persist at elevated pressures up to 10 atm.

The data obtained in this work has also demonstrated that pressure has an augmenting influence on the turbulent flame speed when $S_{L,0}$ is held constant across the pressures. More specifically, factor of five and ten increase in pressure resulted in factors of 2.2 and 2.4 increase in $S_{T,GC}$. These findings are in contrast to previous high pressure $S_{T,GC}$ measurements of $S_{T,GC}$ by Kobayashi *et al.* [48] and Daniele *et al.* [50], who showed that the turbulent consumption speed was independent of the pressure.

6.1.2 Leading points modeling

The influence of fuel composition variation on the turbulent flame speed has been traditionally attributed to the stretch sensitivity of the reactant mixtures. Our data is consistent with this observation since $S_{T,GC}$ is shown to increase with the absolute value of the Markstein length for these negative Markstein length mixtures. However, the Markstein length characterizes small strain behavior. Detailed stretch response calculations performed in this work have shown that coupled composition and pressure effects can affect low and high strain differently. For instance, for a fixed H_2/CO ratio at constant $S_{L,0}$ across the pressures, the absolute value of the Markstein length decreases proportionally with pressure, while the extinction strain rate increases proportionally with pressure. These two effects essentially cancel out to leave the maximum stretched laminar flame speed, $S_{L,max}$ relatively constant across pressure. So it becomes important to consider these coupled effects carefully when modeling the turbulent flame propagation.

To incorporate mixture stretch sensitivity effects into a model for the turbulent consumption speed, the leading points framework is adopted. Leading points are defined as the necessarily positively curved points on the turbulent flame front that propagate out furthest into the reactants. The dynamics of these leadings points is hypothesized to control the overall propagation of the turbulent flame. Using a model problem of a flat flame propagating into a spatially varying mean flow in an iso-density field, the flame is shown to undergo a brief transient before settling into a steady-state configuration where it propagates into the reactants at a speed equal to the propagation speed of the leading points. For the same set of assumptions, the steady-state speed of the leading point is shown to equal the maximum stretched laminar flame speed, $S_{L,max}$. A simple expression for the turbulent flame speed that closely resembles Damköhler’s classical scaling for the turbulent flame speed is then derived. In the derived scaling, $S_{L,max}$ emerges as a normalizing parameter.

When the $S_{T,GC}$ data obtained in this work is normalized by $S_{L,max}$, the data collapses very well for all the fuel mixtures, but not across pressures. To determine the wider applicability of this scaling model, the normalization is also applied to numerous data sets from the literature, but the scaling is not as effective in collapsing the data.

The cause of the scatter in the $S_{L,max}$ normalized data is attributed to non-quasi-steady effects. There are two important non-quasi-steady effects which influence this scaling, one related to the geometry of the turbulent flame brush, and the other related to the internal flame structure.

Since calculations show that the largest variations in the leading point chemical time occur when the pressure is varied, the scatter is attributed to non-quasi-steady effects related to the internal flame structure. In other words, factors of five and ten increases in pressure result in decreases in the leading point chemical time scale by similar factors. As a result, $S_{T,GC}$ is anticipated to increase with pressure since the leading point burning velocity tends towards the steady-state value. Indeed, $S_{T,GC} / S_{L,\max}$ is shown to increase as the normalized leading point chemical time decreases at constant $u'_{rms} / S_{L,\max}$.

Similar analysis with the data extracted from the literature yield similar results, suggesting that a two-parameter model of the form given in Eq. (4.16) is a promising approach to model turbulent flame propagation.

Although the concept of leading points has been around for several decades, the key contribution of this work has been to demonstrate that the leading point burning velocity can be equated to $S_{L,max}$ in the quasi-steady limit. In addition, the successful implementation of the resulting model to scale various turbulent flame speed data is another key contribution.

6.1.3 Flame brush thickness characteristics

The final part of this work focused on characterizing the influence of fuel composition and pressure on the turbulent flame brush. To our knowledge, there are no studies to date that have performed a systematic investigation of the dependence of the flame brush on fuel composition and pressure.

Some of the trends observed were consistent with the observations from the literature. For all the conditions explored, the turbulent flame brush thickness grew with downstream distance along the $<c> = 0.5$ contour, s. This is in accordance with the theories of turbulent diffusion that predict that flame brush thickness increases with larger flame development times.

Near the flame base, the flame brush thickness did not vary with jet turbulence intensity, while further downstream larger jet turbulence intensities resulted in thicker flame brushes. In the near field, the flame resides in the jet shear layer, where the turbulence fluctuations have a self-similar profile when normalized by the square of the velocity difference between the jet velocity and the ambient. Since the velocity difference is unchanging due to the presence of the potential core, the fluctuations in the shear layer are also constant, resulting in no change in the flame brush thickness. Further downstream, the flame resides in the jet potential core where it is more responsive to the inlet jet turbulence.

The flame brush thickness is also shown to be independent of the fuel composition, over a broad range of fuel mixtures, turbulence intensities and pressure, which corroborates findings reported in the literature. However, the flame brush thickness is found to increase when the equivalence ratio is increased (in the lean regime) for a fixed fuel composition. This sensitivity is present at the lower turbulence intensities, but gets washed out at higher turbulence intensities. It is interesting to note that the flame brush thickness increases with the equivalence ratio, which is in contrast to what is observed with turbulent flame speeds.

A key contribution of this work has been to demonstrate the effect of pressure on the flame brush thickness. First, when u'_{rms}/U_0 is held fixed, pressure augments the flame brush thickness. In addition, the ratio of the flame brush thickness at 10 atm to the flame brush thickness at 1 atm increases as u'_{rms}/U_0 increases, suggesting that the pressure augments the flame brush thickness to a greater degree at higher turbulence intensities. Furthermore, at the lower turbulence intensity, the same flame brush thickness ratio was larger for the 70% H_2 mixture compared to the 50% H_2 mixture when the mixture $S_{L,0}$ was held constant. However, this fuel composition dependency disappears at the higher turbulence intensity. These observations suggest that the pressure couples with the turbulence intensity and fuel composition in the form of Darrieus-Landau and/or thermo-diffusive instabilities. When the mixture $S_{L,0}$ is not held constant, higher pressures also augment the flame brush thickness when u'_{rms}/U_0 is held constant. The mechanism by which pressure affects the flame brush thickness is uncertain at this point. One possibility was a dependence of the turbulence characteristics in the jet shear layer or fully developed region on a Reynolds number, but studies of non-reacting mixing layers and jets suggest the absence of a Reynolds number effect. As a result, more detailed investigations are required to resolve this question.

Traditional scalings for the flame brush thickness based on the Lagrangian length and time scales and the flame development time collapse the flame brush thickness data at constant u'_{rms}/U_0 and pressures reasonably well. However the scalings are unable to collapse the data across u'_{rms}/U_0 and pressures.

Finally, the progress variable distributions through the flame brush are shown to follow error function profiles suggested by Lipatnikov and Chomiak in Ref.[36] when the distance through the flame brush is represented using Eq.(1.23). However, this is demonstrated to be a consequence of fitting the intensity profiles with Gaussian profiles. In addition, this error function profile is captured best with an analytical expression of the form given by Eq. (5.7) when δ_{FBT} is defined as the distance between the $<c>$ = 0.3 and 0.7 contours. But the important conclusion is that the intensity profiles can be represented very well by Gaussian profiles, from which the self-similarity is a natural consequence.

6.2 Recommendations for future work

In this work the leading points frameworks is shown to offer a promising approach to develop reduced order models for the turbulent flame speed. A scaling for the turbulent flame speed using a simple steady-state model problem is derived, which shows that the leading point propagates at $S_{L,max}$. However, this model needs to be experimentally validated by investigating the leading point characteristics of real flames. Simultaneous planar laser induced fluorescence of the OH radical, OH-PLIF and, particle image velocimetry, PIV, measurements will enable the determination of leading point curvatures and tangential strain rates. The strain rates obtained experimentally can then be compared with those obtained from stretch-sensitivity calculations such as the ones presented in Chapter 4. An associated question to answer from these studies is how the

2D strain rates and curvatures compare to the actual 3D values. This would be aided greatly by comparing against LES or DNS simulations of similar configurations.

The $S_{L,max}$ normalized turbulent flame speed data is also seen to increase as the leading point chemical time scale decreased. This is attributed to the leading point burning velocity becoming quasi-steady with increasing pressure. However, since the leading point chemical time scale also decreases with pressure, it is reasonable to expect any parameter that also correlates with pressure will also do a reasonable job of scaling the pressure effects, such as the Reynolds number, which increases linearly with pressure. This appears to be the case when the turbulent flame speed is shown to correlate well with the Reynolds number. These results indicate that additional data is needed to differentiate between chemical time and Reynolds number effects. A broadened set of experimental conditions that will enable differentiation between time scale, length scale, and Reynolds number effects on the turbulent burning velocity, will be of great value. One possible way to differentiate these effects is to vary the preheat temperature, since the Reynolds number will decrease with temperature while the leading point chemical time scale increases with temperature, as shown in Figure 133.

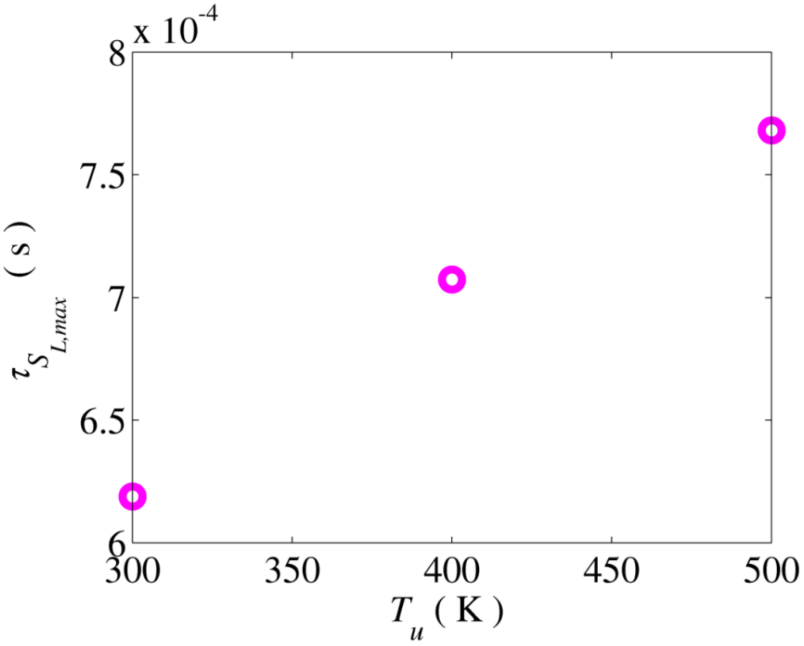

Figure 133: Influence of reactant temperature, T_u, on the leading point chemical time scale for a 30/70 H_2/CO mixture whose equivalence ratio is adjusted at each T_u to maintain a constant $S_{L,0}$ or 34 cm/s. Calculations done for mixture at 1 atm.

In Chapter 3, the possibility of the progress variable fields obtained from chemiluminescence measurements to be biased by the fuel composition was discussed. The results from detailed calculations showed that over a range of strain rates, the chemiluminescence and heat release rate were linearly related, suggesting that if the strain rates experienced by the flame lay in this range, then there would be no bias. However, to explore this issue in more detail, the stretch rate pdfs conditioned on the location within the turbulent flame brush as a function of the fuel composition are required. These would be an important set of measurements since data of this kind are lacking in the literature.

An interesting extension of this work would be to compare the dependence of the spatial variation of the average progress variable on the flame imaging technique for different mixtures. This will have important implications when comparing data sets of measurements, such as the turbulent flame speed, obtained by different techniques.

The mixtures investigated in this work are negative Markstein length fuel/air mixtures. Similar studies to ones conducted in this work can be performed to explore fuel effects for positive Markstein length fuel mixtures. This is motivated by the desire to use syngas fuels derived from other feedstocks, such as process and refinery gas, which have significant quantities of propane. Furthermore, the leading points model developed in this work was essentially for negative Markstein length fuel/air mixtures, and it would be of interest to see whether similar ideas can be utilized to model flame propagation in these mixtures.

Studies to investigate the influence of CO_2 and H_2O dilution on the flame propagation would also be of interest, in order to understand flame propagation in oxy-fuel combustion systems and in systems where significant exhaust gas recirculation (EGR) is present.

The final part of this thesis focused on investigating the sensitivities of the flame brush thickness. A key unanswered question from this study is the mechanism by which pressure augments the flame brush thickness. Some light on this issue could be shed by detailed measurements of the turbulence characteristics in the shear layer at different pressures. Furthermore, visualizations of the flame front at pressure may also be helpful, since the flame brush may not just be a function of the turbulence field, but also the topology of the instantaneous flame front.

Finally, the mixture equivalence ratio was also shown to have an influence on the flame brush thickness. In particular, at lower turbulence intensities, the turbulent flame brush thickness is augmented by larger equivalence ratios. However, this sensitivity disappears at higher turbulence intensities. Since the data reported in this work were at relatively large u'_{rms}/U_0 (14-18%), it would be of interest to take data at lower u'_{rms}/U_0 to investigate if there is a region over which fuel composition effects are important.

Appendix A
Error Analysis

In this appendix the details of the error analysis for the turbulent flame speed measurements are presented. To recall, the turbulent flame speed is calculated using Eq.(A.1):

$$S_{T,GC} = \frac{\dot{m}_R}{\rho_R A_{<c>}} \tag{A.1}$$

The sources of uncertainty in the calculation are the uncertainties in the measurement of the reactant flow rates and the calculation of the flame area. The uncertainty in $S_{T,GC}$, $\sigma_{S_{T,GC}}$ can be calculated using the standard formula [110]:

$$\sigma_{S_{T,GC}} = \sqrt{\left(\frac{\partial S_{T,GC}}{\partial \dot{m}_R}\sigma_{\dot{m}_R}\right)^2 + \left(\frac{\partial S_{T,GC}}{\partial A_{<c>}}\sigma_{A_{<c>}}\right)^2} \tag{A.2}$$

where $\sigma_{\dot{m}_R}$ and $\sigma_{A_{<c>}}$ are the uncertainties in reactant mass flow rate and flame area. The appropriate derivatives in Eq. (A.2) can be calculated by differentiating Eq. (A.1):

$$\begin{aligned} \frac{\partial S_{T,GC}}{\partial \dot{m}_R} &= \frac{1}{\rho_R A_{<c>}} \\ \frac{\partial S_{T,GC}}{\partial A_{<c>}} &= -\frac{\dot{m}_R}{\rho_R A_{<c>}^2} \end{aligned} \tag{A.4}$$

Equation (A.4) can then be substituted into Eq. (A.2)to obtain:

$$\sigma_{S_{T,GC}} = \sqrt{\left(\frac{\sigma_{\dot{m}_R}}{\rho_R A_{<c>}}\right)^2 + \left(\frac{\dot{m}_R}{\rho_R A_{<c>}^2}\sigma_{A_{<c>}}\right)^2} \tag{A.5}$$

The fractional uncertainty in $S_{T,GC}$ can then be shown to be:

$$\frac{\sigma_{S_{T,GC}}}{S_{T,GC}} = \sqrt{\left(\frac{\sigma_{\dot{m}_R}}{\dot{m}_R}\right)^2 + \left(\frac{\sigma_{A_{<c>}}}{A_{<c>}}\right)^2} \tag{A.6}$$

Each term in Eq. (A.6) is calculated individually in the following sections. First, the uncertainty in the reactant mass flow rate is calculated. The reactant mass flow rate is comprised of the air mass flow rate and the fuel mass flow rates, which are treated separately in the uncertainty analysis since the air mass flow rate is metered using a subcritical orifice assembly, while the fuel flow rates were metered with critical orifice assembly.

$$\dot{m}_R = \dot{m}_{air} + \dot{m}_{fuel} \tag{A.7}$$

Since the reactant flow rate is made up of summing the air and fuel flow rates, the absolute uncertainties are also summed:

$$\sigma_{\dot{m}_R} = \sigma_{\dot{m}_{air}} + \sigma_{\dot{m}_{fuel}} \tag{A.8}$$

A.1 Uncertainty in the air flow rate

Starting from the equation for one-dimensional mass flow rate given by:

$$\dot{m}_{air} = \rho U \left(\frac{\pi}{4} D^2\right) \tag{A.9}$$

The Bernoulli equation can then be substituted for the velocity in Eq. (A.9) to obtain Eq. (A.10). C_d and e_c , which are the discharge coefficient and the gas expansion coefficient respectively, are obtained from the calibration of the orifice plate and assumed to be constant. β is the ratio of the pipe diameter and the orifice plate bore diameter.

$$\dot{m}_{air} = \rho\left(C_d e_c \sqrt{\frac{1}{1-\beta^4}} \sqrt{\frac{2dP}{\rho}} \right)\left(\frac{\pi}{4} D^2 \right) \tag{A.10}$$

Using the ideal gas law, and lumping everything except for the pressure, temperature and differential pressure into a constant, Eq. (A.10) can be written as:

$$\dot{m}_{air} = \left(C_d e_c \sqrt{\frac{1}{1-\beta^4}} \sqrt{2\frac{pM}{RT} dp} \right)\left(\frac{\pi}{4} D^2 \right) = C\sqrt{\frac{p}{T} dp} = \dot{m}_{air}\left(dp, p, T \right) \tag{A.11}$$

The total uncertainty in the air mass flow measurement is calculated using the standard formula given in Eq. (A.12)

$$\sigma_{\dot{m}_{air}} = \sqrt{\left(\frac{\partial \dot{m}_{air}}{\partial \left(dp \right)} \sigma_{dp} \right)^2 + \left(\frac{\partial \dot{m}_{air}}{\partial p} \sigma_p \right)^2 + \left(\frac{\partial \dot{m}_{air}}{\partial T} \sigma_T \right)^2} \tag{A.12}$$

The appropriate derivatives required for Eq. (A.12) are calculated from differentiating Eq. (A.11):

$$\begin{aligned} \frac{\partial \dot{m}_{air}}{\partial \left(dp \right)} &= \frac{1}{2} C \sqrt{\frac{p}{Tdp}} \\ \frac{\partial \dot{m}_{air}}{\partial p} &= \frac{1}{2} C \sqrt{\frac{dp}{pT}} \\ \frac{\partial \dot{m}_{air}}{\partial T} &= -\frac{1}{2} C \sqrt{\frac{p}{T^3} dp} \end{aligned} \tag{A.13}$$

Substituting Eq. (A.13)into Eq.(A.12) , the uncertainty in the air mass flow rate can be calculated as:

$$\sigma_{\dot{m}_{air}} = \frac{1}{2} C \sqrt{\left(\sqrt{\frac{p}{Tdp}} \sigma_{dp} \right)^2 + \left(\sqrt{\frac{dp}{pT}} \sigma_p \right)^2 + \left(\sqrt{\frac{p}{T^3} dp \sigma_T} \right)^2} \tag{A.14}$$

The fractional uncertainty in the air mass flow rate can then be calculated to be:

$$\frac{\sigma_{\dot{m}_{air}}}{\dot{m}_{air}} = \frac{1}{2}\sqrt{\left(\frac{\sigma_{dP}}{dP}\right)^2 + \left(\frac{\sigma_p}{p}\right)^2 + \left(\frac{\sigma_T}{T}\right)^2} \tag{A.15}$$

Table 7 provides the uncertainties in the differential pressure, static pressure and temperature measurements.

Table 7: Fractional uncertainties from measurement devices for subcritical flow metering facility.

Quantity measured	Transducer	Fractional uncertainty (%)
Static pressure	Omega PX409	0.08
Differential pressure	Omega PX 771A	0.15
Temperature	Omega K-type thermocouple	0.75

The fractional uncertainties from Table 7 can be combined to give a fractional uncertainty of 0.38% in the air flow rate.

A.2 Uncertainty in the fuel flow rate

The mass flow rate at choked conditions is calculated using Eq. (A.16),

$$\dot{m}_{fuel} = A^* p_0 \sqrt{\frac{\gamma}{RT_0}} \left(\frac{\gamma + 1}{2}\right)^{\frac{\gamma+1}{2(\gamma-1)}} \tag{A.16}$$

Recognizing that the mass flow is only dependent on the upstream pressure and temperature when the flow is choked, Eq. (A.16) can be simplified to obtain:

$$\dot{m}_{fuel} = Cp_0\sqrt{\frac{1}{T_0}} = \dot{m}_{fuel}\left(p_0, T_0\right) \tag{A.17}$$

The uncertainty in the fuel flow rate is then calculated as:

$$\sigma_{\dot{m}_{fuel}} = \sqrt{\left(\frac{\partial \dot{m}_{fuel}}{\partial p_0}\sigma_{p_0}\right)^2 + \left(\frac{\partial \dot{m}_{fuel}}{\partial T_0}\sigma_{T_0}\right)^2} \tag{A.18}$$

where the derivatives in Eq. (A.18) are obtained by differentiating Eq. (A.17):

$$\frac{\partial \dot{m}_{fuel}}{\partial p_0} = C\sqrt{\frac{1}{T_0}}$$
$$\frac{\partial \dot{m}_{fuel}}{\partial T_0} = -\frac{1}{2}\frac{Cp_0}{T_0}\sqrt{\frac{1}{T_0}} \qquad \text{(A.19)}$$

Substituting Eq. (A.19) into Eq. (A.18), the uncertainty in the fuel flow rates can be calculated as:

$$\sigma_{\dot{m}_{fuel}} = C\sqrt{\left(\sqrt{\frac{1}{T_0}}\sigma_{p_0}\right)^2 + \left(\frac{1}{2}\frac{p_0}{T_0}\sqrt{\frac{1}{T_0}}\sigma_{T_0}\right)^2} \qquad \text{(A.20)}$$

The fractional uncertainty in the fuel flow rate measurement is then calculated as:

$$\frac{\sigma_{\dot{m}_{fuel}}}{\dot{m}_{fuel}} = \sqrt{\left(\frac{\sigma_{p_0}}{p_0}\right)^2 + \left(\frac{\sigma_{T_0}}{2T_0}\right)^2} \qquad \text{(A.21)}$$

Table 8 provides the uncertainties in the differential pressure, static pressure and temperature measurements

Table 8: Fractional uncertainties from measurement devices for critical flow metering facility.

Quantity measured	Transducer	Fractional uncertainty (%)
Static pressure	Omega PX409	0.08
Temperature	Omega K-type thermocouple	0.75

The fractional uncertainties from Table 8 can be combined to give a fractional uncertainty of about 0.38% in the fuel flow rates.

A.3 Uncertainty in the flame surface area

The surface area of the cone is calculated as:

$$A_{<c>} = \pi r s = \pi r\sqrt{h^2 + r^2} \qquad \text{(A.22)}$$

where s is the slant length of the cone. The uncertainty in the flame area can then be determined as follows:

$$\sigma_{A_{<c>}} = \frac{\partial A_{<c>}}{\partial h} \sigma_h \tag{A.23}$$

for which the required derivative of Eq. (A.22) is:

$$\frac{\partial A_{<c>}}{\partial h} = \frac{\pi r h}{\sqrt{h^2 + r^2}} \tag{A.24}$$

The uncertainty in the flame area is then calculated as:

$$\sigma_{A_{<c>}} = \frac{\pi r h}{\sqrt{h^2 + r^2}} \sigma_h \tag{A.25}$$

from which the fractional uncertainty in the flame area is determined as:

$$\frac{\sigma_{A_{<c>}}}{A_{<c>}} = \frac{h}{\left(h^2 + r^2\right)} \sigma_h \tag{A.26}$$

The uncertainty in the height, σ_h, is determined by the image resolution and varies from case to case. However, σ_h is typically around 0.075 mm for the images obtained in this work.

A.4 Total uncertainty

The uncertainties calculated in the previous sections can be combined using Eq. (A.6) to show that the uncertainty in the $S_{T,GC}$ measurement is about 0.40%.

Appendix B
Relating the Intensity to the Average Progress Variable

The Abel-transformed image is an intensity field that can be related to the progress variable field. This section describes how the progress variable field is extracted from the intensity field.

The normalized intensity profile along each normal, *I*, is fit with a Gaussian profile with mean μ and standard deviation σ:

$$I\left(x:\mu,\sigma\right)=\frac{1}{\sigma\sqrt{2\pi}}\exp\left[-\frac{1}{2}\left(\frac{x-\mu}{\sigma}\right)^2\right] \tag{B.1}$$

The progress variable is the cdf of the flame position, as shown in Eq. (B.2)

$$\left\langle c\right\rangle=P\left(-\infty<x<x_{\left\langle c\right\rangle}\right) \tag{B.2}$$

Applying Eq. (B.2) in Eq. (B.1), Eq. (B.3) is obtained:

$$\left\langle c\right\rangle=\frac{1}{\sigma\sqrt{2\pi}}\int_{-\infty}^{x_{<c>}}\exp\left[-\frac{1}{2}\left(\frac{x-\mu}{\sigma}\right)^2\right]dx \tag{B.3}$$

Using the following transformation

$$u=\frac{x-\mu}{\sigma\sqrt{2}} \tag{B.4}$$

Equation. (B.3) can be converted into:

$$\left\langle c\right\rangle=\frac{1}{\sqrt{\pi}}\int_{-\infty}^{u_{<c>}}\exp\left(-u^2\right)du \tag{B.5}$$

The integrand of Eq.(B.5) is symmetric about u = 0, and has the property that:

$$\frac{1}{\sqrt{\pi}} \int_{-\infty}^{\infty} \exp\left(u^2\right) du = 1 \tag{B.6}$$

which is just the normalization condition of a pdf. The symmetry of Eq. (B.6) can be utilized to write:

$$\frac{1}{\sqrt{\pi}} \int_{-\infty}^{0} \exp\left(u^2\right) du = \frac{1}{2} \tag{B.7}$$

Eq. (B.5) can then be rewritten as follows:

$$\left\langle c \right\rangle = \frac{1}{\sqrt{\pi}} \int_{-\infty}^{0} \exp\left(u^2\right) du + \frac{1}{\sqrt{\pi}} \int_{0}^{u_{<c>}} \exp\left(u^2\right) du \tag{B.8}$$

The first term in Eq. (B.8) can be replaced with the result from Eq. (B.7) to obtain:

$$\left\langle c \right\rangle = \frac{1}{2} + \frac{1}{\sqrt{\pi}} \int_{0}^{u_{<c>}} \exp\left(u^2\right) du \tag{B.9}$$

Recalling that the error function is defined as:

$$erf\left(x\right) = \frac{2}{\sqrt{\pi}} \int_{0}^{x} \exp\left(-t^2\right) dt \tag{B.10}$$

Substituting Eq. (B.10) into Eq.(B.9), and using the transformation in Eq. (B.4) to obtain:

$$\left\langle c \right\rangle = \frac{1}{2}\left[1 + erf\left(\frac{x_{\langle c \rangle} - \mu}{\sigma\sqrt{2}}\right)\right] \tag{B.11}$$

The locations, $x_{<c>}$, for each progress variable <c> can then be determined from Eq. (B.11) using a root finding algorithm.

Appendix C

$S_{T,GC}$ Conversion Factors

In this appendix the conversion factors required to convert the $S_{T,GC}$ values based on the $\langle c \rangle = 0.5$ contour to $S_{T,GC}$ based on any other contour is provided.

The data is grouped according to the two studies that were performed. The first set of studies, termed the "constant $S_{L,0}$ studies" is where the mixture equivalence ratio was adjusted for each H_2/CO ratio to maintain constant $S_{L,0}$ of 34 cm/s. $S_{L,0}$ was held constant at this value across the pressures as well. These data presented in this appendix were acquired using the 12 mm diameter burner.

In the second of experiments, termed "equivalence ratio sweep studies", the H_2/CO ratio was held fixed while the equivalence ratio was varied. These data presented in this appendix were acquired using the 20 mm diameter burner.

C.1 Constant $S_{L,0}$ studies

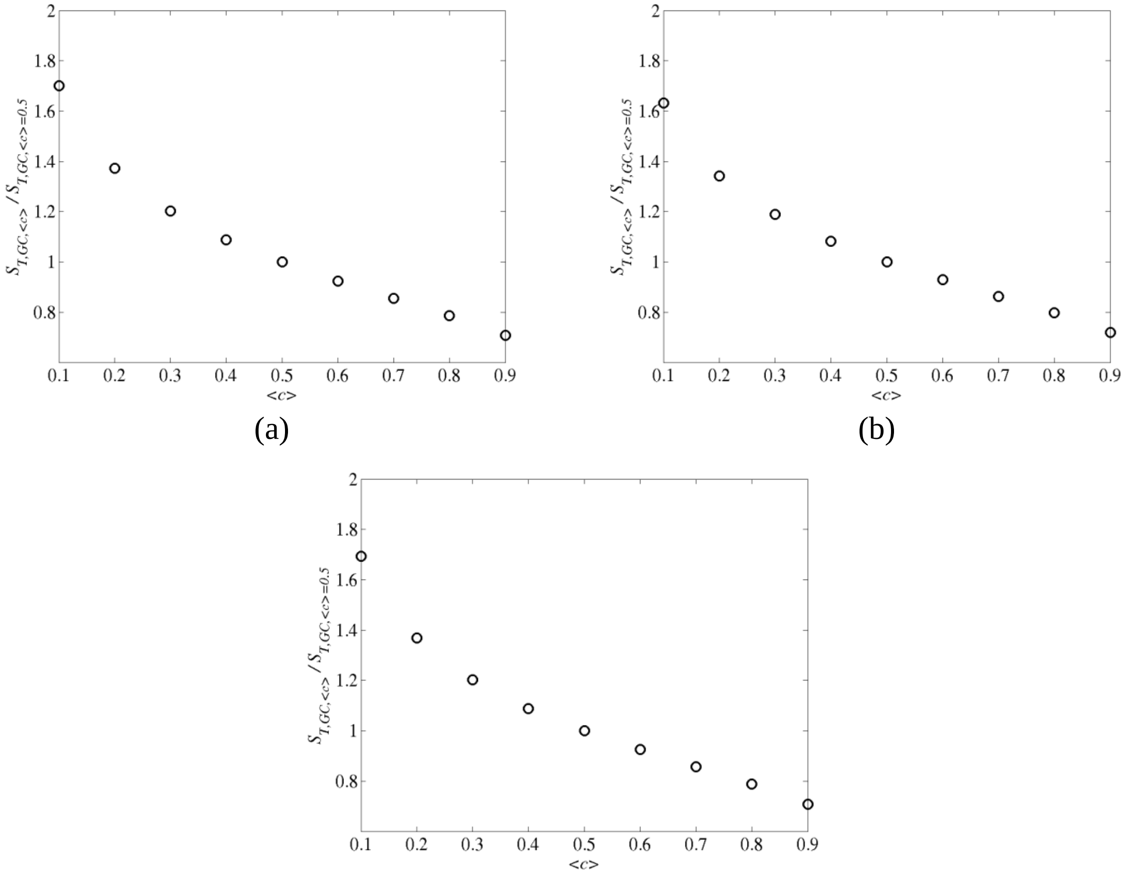

(a) (b)

(c)

Figure 134:$S_{T,GC,<c>}$ / $S_{T,GC,<c>=0.5}$ as a function of average progress variable for the 50/50 H_2/CO mixture at 1 atm, mean flow velocity of 50 m/s and $u'_{rms}/S_{L,0}$ of (a) 17.4 (b) 22.5 (c) 27.6.

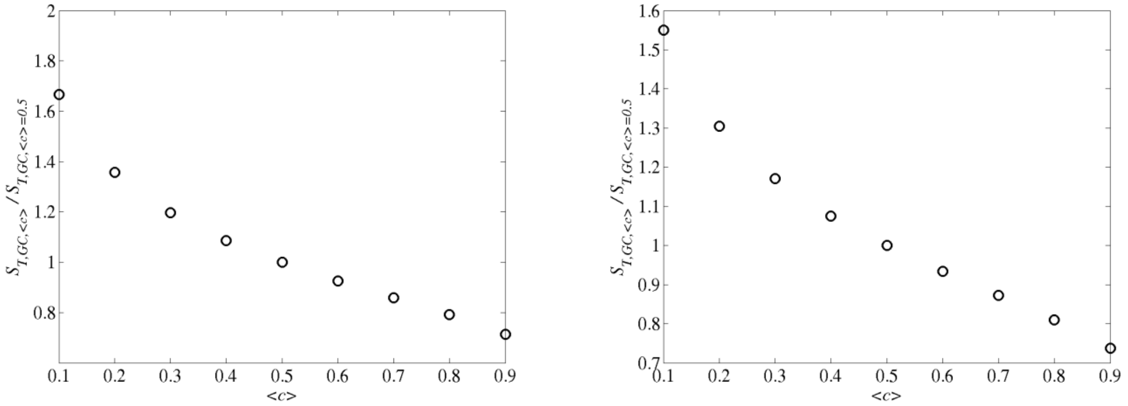

(a) (b)

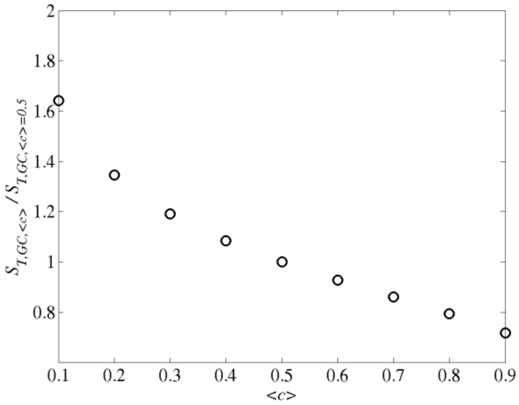

(c)

Figure 135: $S_{T,GC,<c>}$ / $S_{T,GC,<c>= 0.5}$ as a function of average progress variable for the 70/30 H_2/CO mixture at 1 atm, mean flow velocity of 50 m/s and $u'_{rms}/S_{L,0}$ of (a) 17.4 (b) 22.5 (c) 27.6.

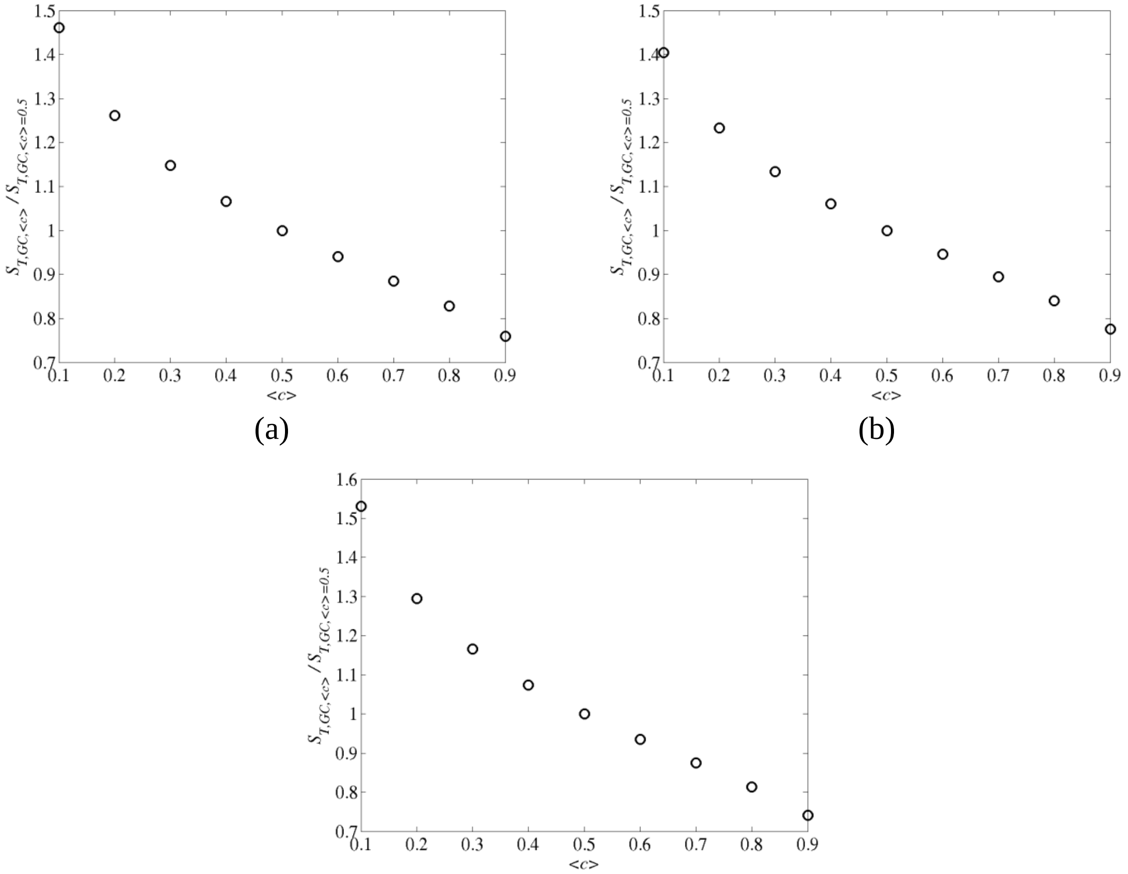

(a) (b)

(c)

Figure 136: $S_{T,GC,<c>}$ / $S_{T,GC,<c>=0.5}$ as a function of average progress variable for the 90/10 H_2/CO mixture at 1 atm, mean flow velocity of 50 m/s and $u'_{rms}/S_{L,0}$ of (a) 17.4 (b) 22.5 (c) 27.6.

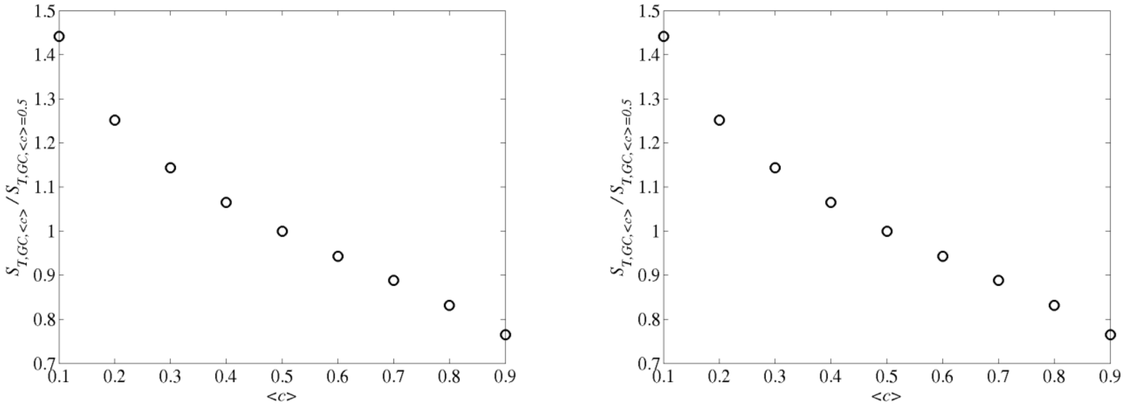

(a) (b)

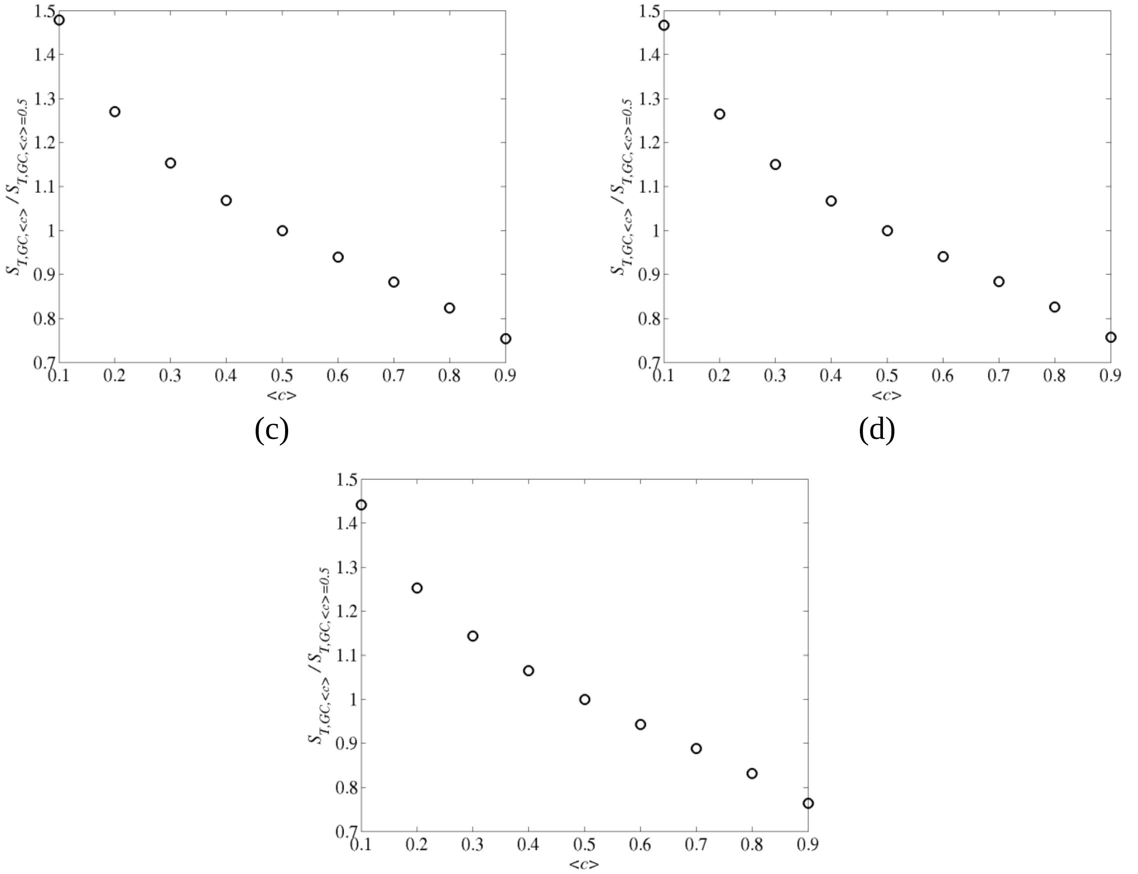

(c) (d)

(e)

Figure C-1: $S_{T,GC,<c>}$ / $S_{T,GC,<c>=0.5}$ as a function of average progress variable for the 30/70 H_2/CO mixture at 5 atm, mean flow velocity of 50 m/s and $u'_{rms}/S_{L,0}$ of (a) 17.4 (b) 20.0 (c) 22.5 (d) 25.1 (e) 27.6.

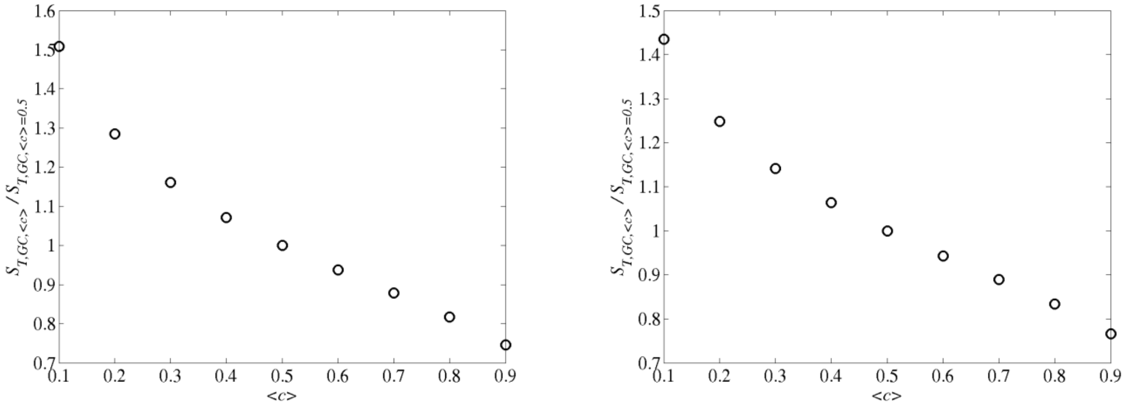

(a) (b)

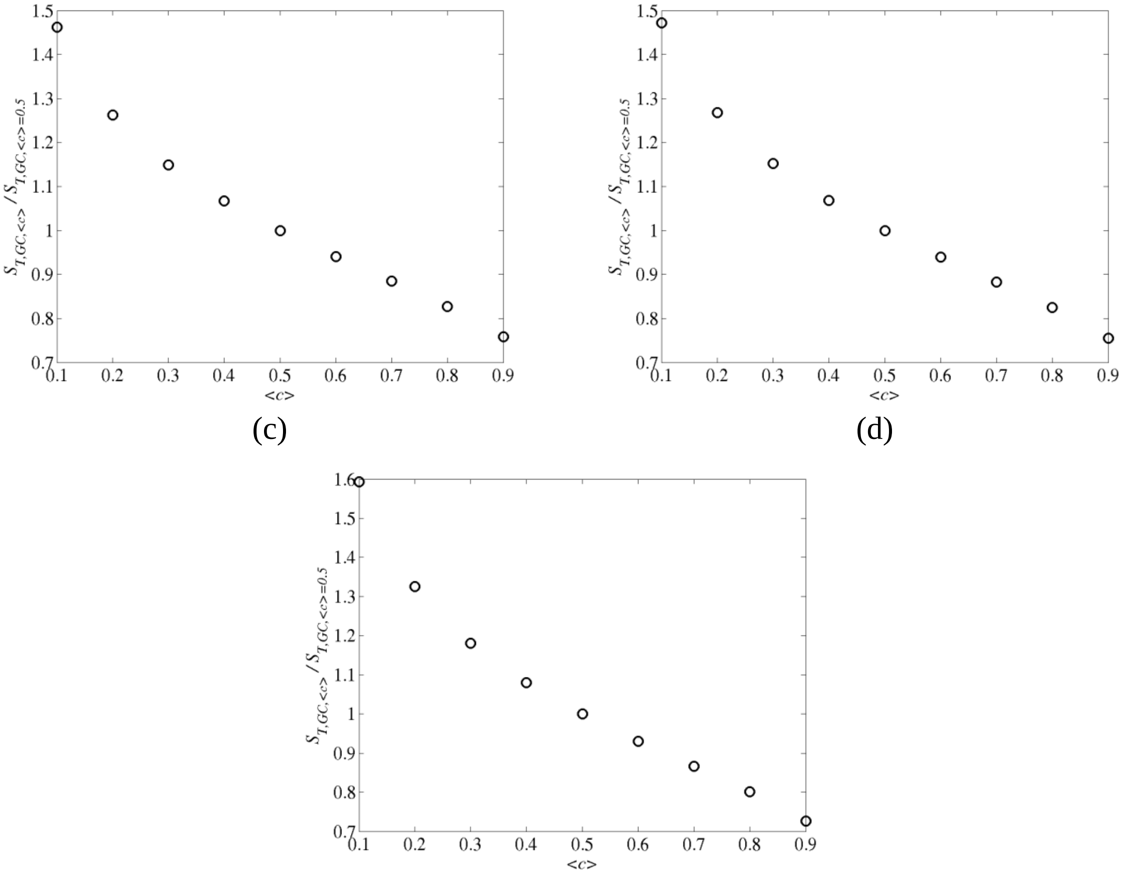

(c) (d)

(e)

Figure 137: $S_{T,GC,<c>}$ / $S_{T,GC,<c>= 0.5}$ as a function of average progress variable for the 50/50 H_2/CO mixture at 5 atm, mean flow velocity of 50 m/s and $u'_{rms}/S_{L,0}$ of (a) 17.4 (b) 20.0 (c) 22.5 (d) 25.1 (e) 27.6.

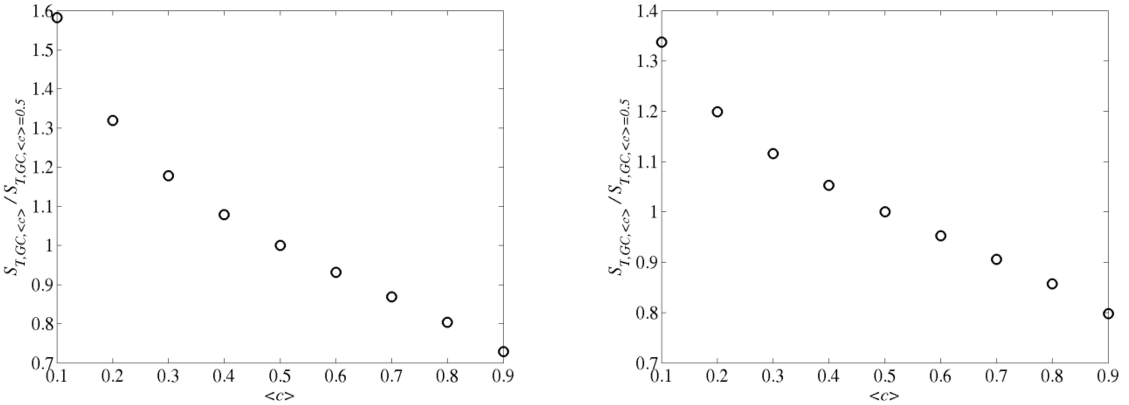

(a) (b)

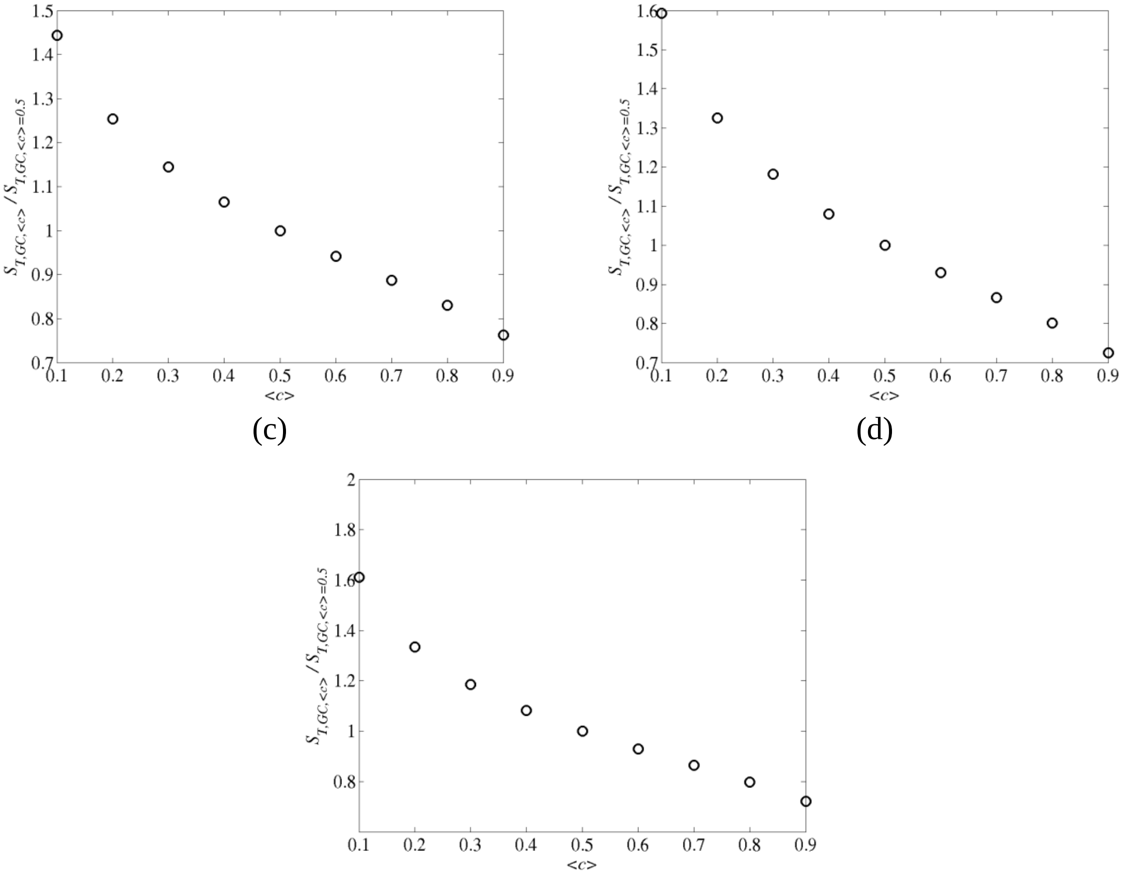

(c)

(d)

(e)

Figure 138: $S_{T,GC,<c>}$ / $S_{T,GC,<c>=0.5}$ as a function of average progress variable for the 70/30 H_2/CO mixture at 5 atm, mean flow velocity of 50 m/s and $u'_{rms}/S_{L,0}$ of (a) 17.4 (b) 20.0 (c) 22.5 (d) 25.1 (e) 27.6.

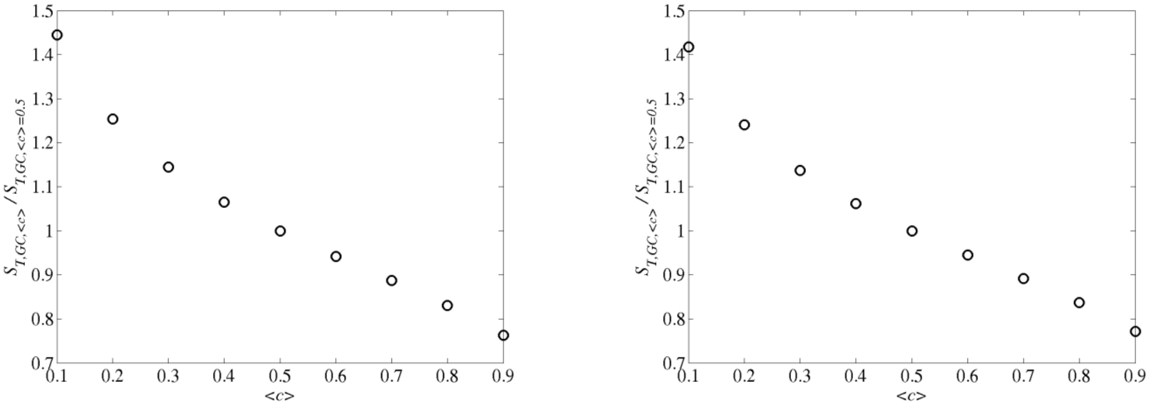

(a)

(b)

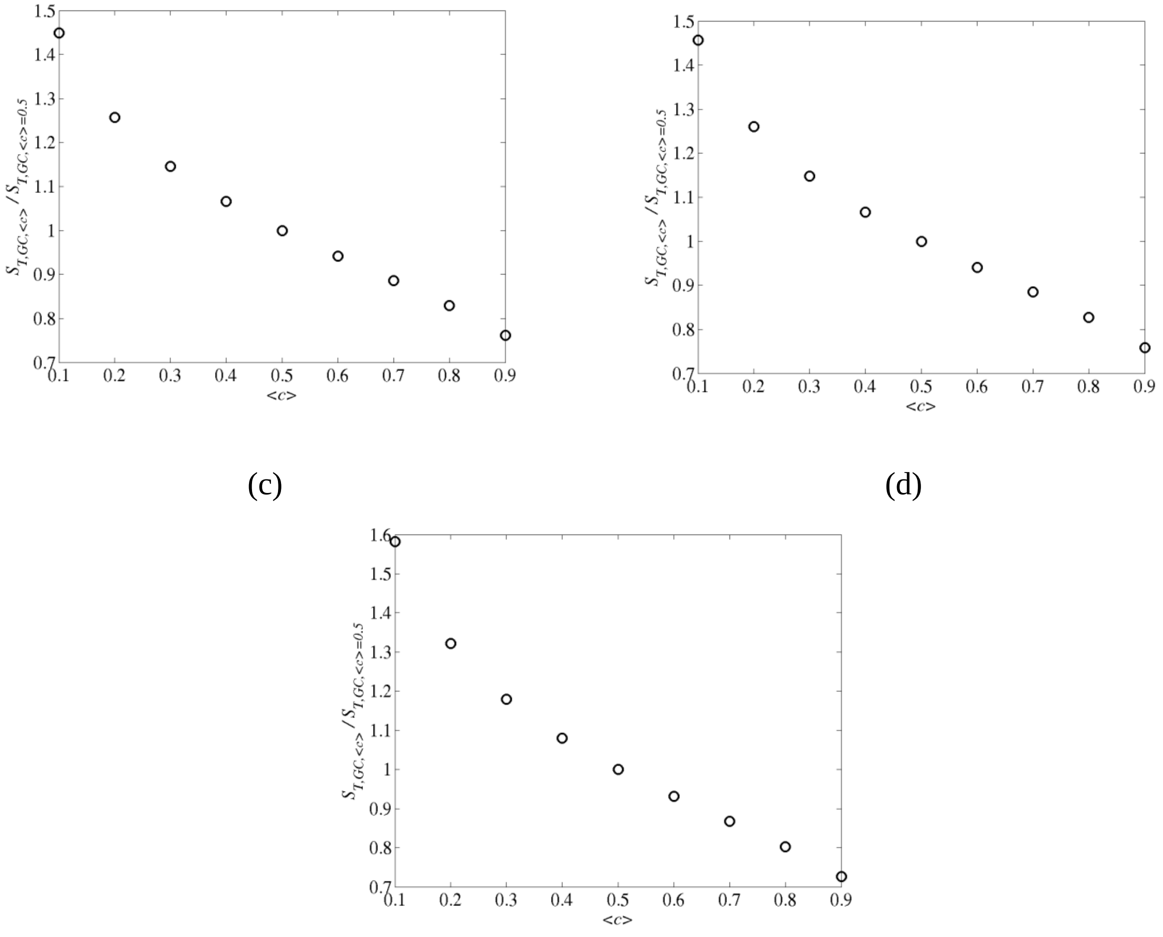

(c) (d)

(e)

Figure 139: $S_{T,GC,<c>}$ / $S_{T,GC,<c>=0.5}$ as a function of average progress variable for the 90/10 H_2/CO mixture at 5 atm, mean flow velocity of 50 m/s and $u'_{rms}/S_{L,0}$ of (a) 17.4 (b) 20.0 (c) 22.5 (d) 25.1 (e) 27.6.

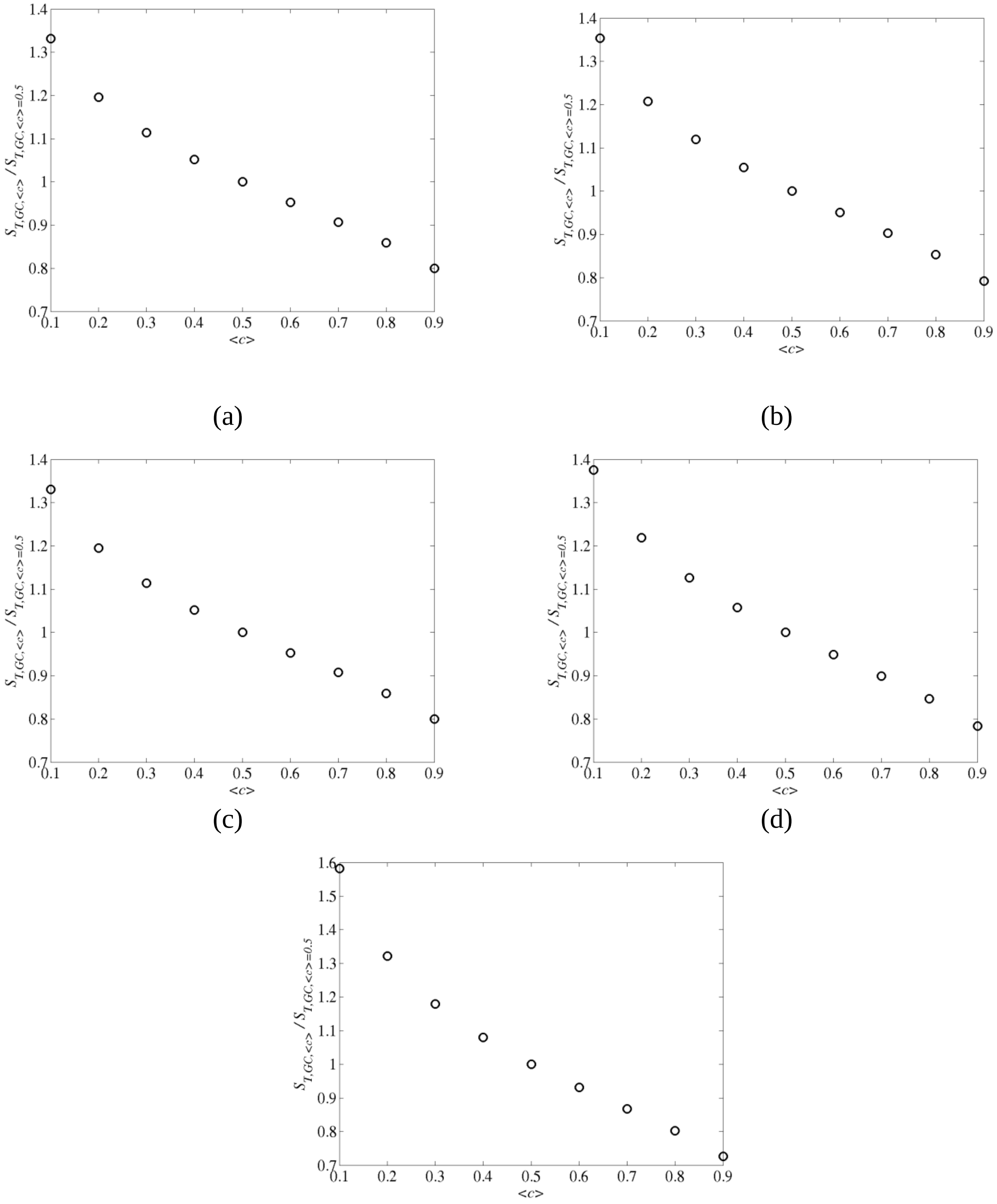

(a) (b)

(c) (d)

(e)

Figure 140: $S_{T,GC,<c>}$ / $S_{T,GC,<c>=0.5}$ as a function of average progress variable for the 30/70 H_2/CO mixture at 10 atm, mean flow velocity of 50 m/s and $u'_{rms} \big/ S_{L,0}$ of (a) 17.6 (b) 20.2 (c) 22.8 (d) 25.4 (e) 27.6.

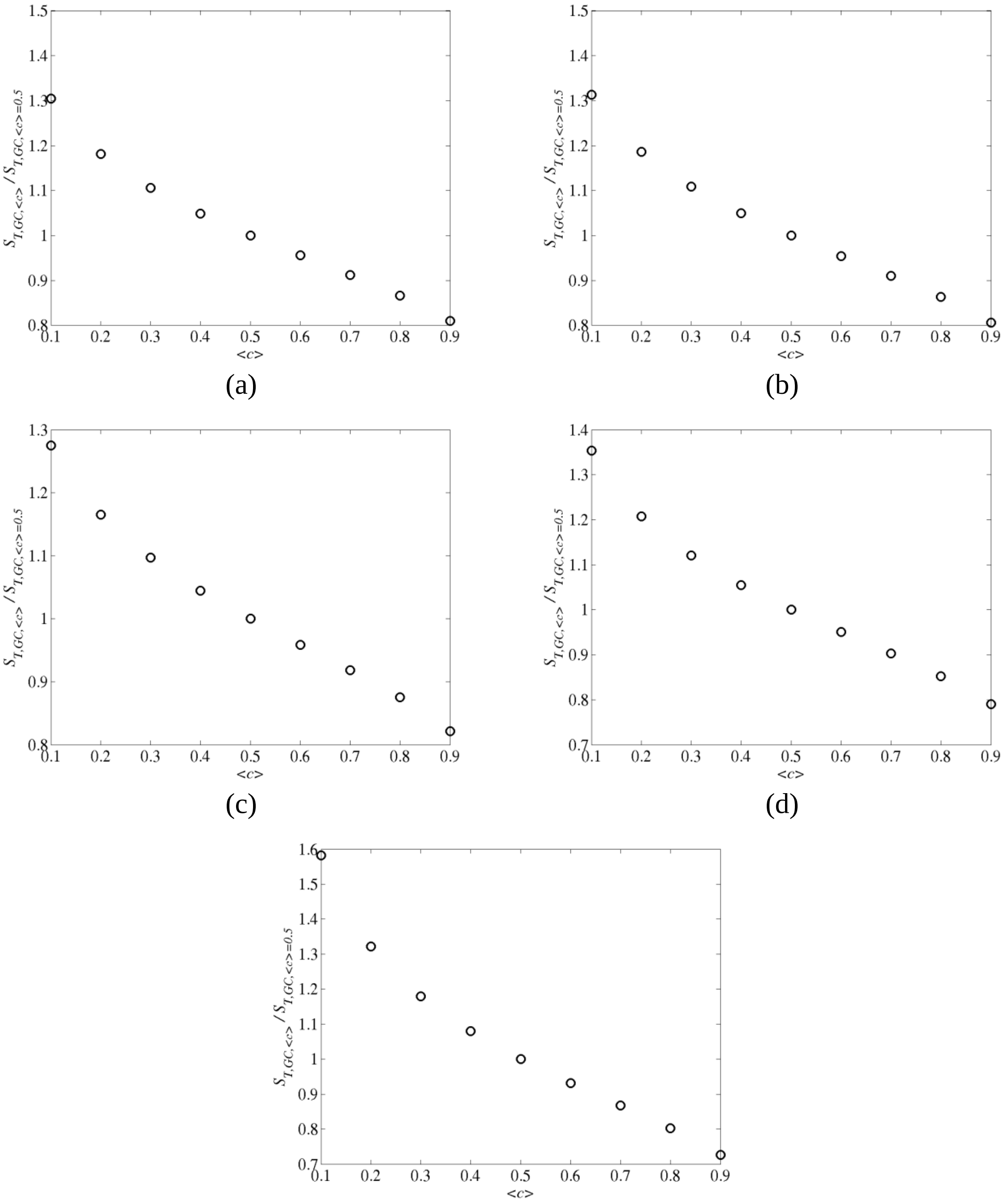

Figure 141: $S_{T,GC,<c>}$ / $S_{T,GC,<c>= 0.5}$ as a function of average progress variable for the 50/50 H_2/CO mixture at 10 atm, mean flow velocity of 50 m/s and $u'_{rms}/S_{L,0}$ of (a) 17.6 (b) 20.2 (c) 22.8 (d) 25.4 (e) 27.6.

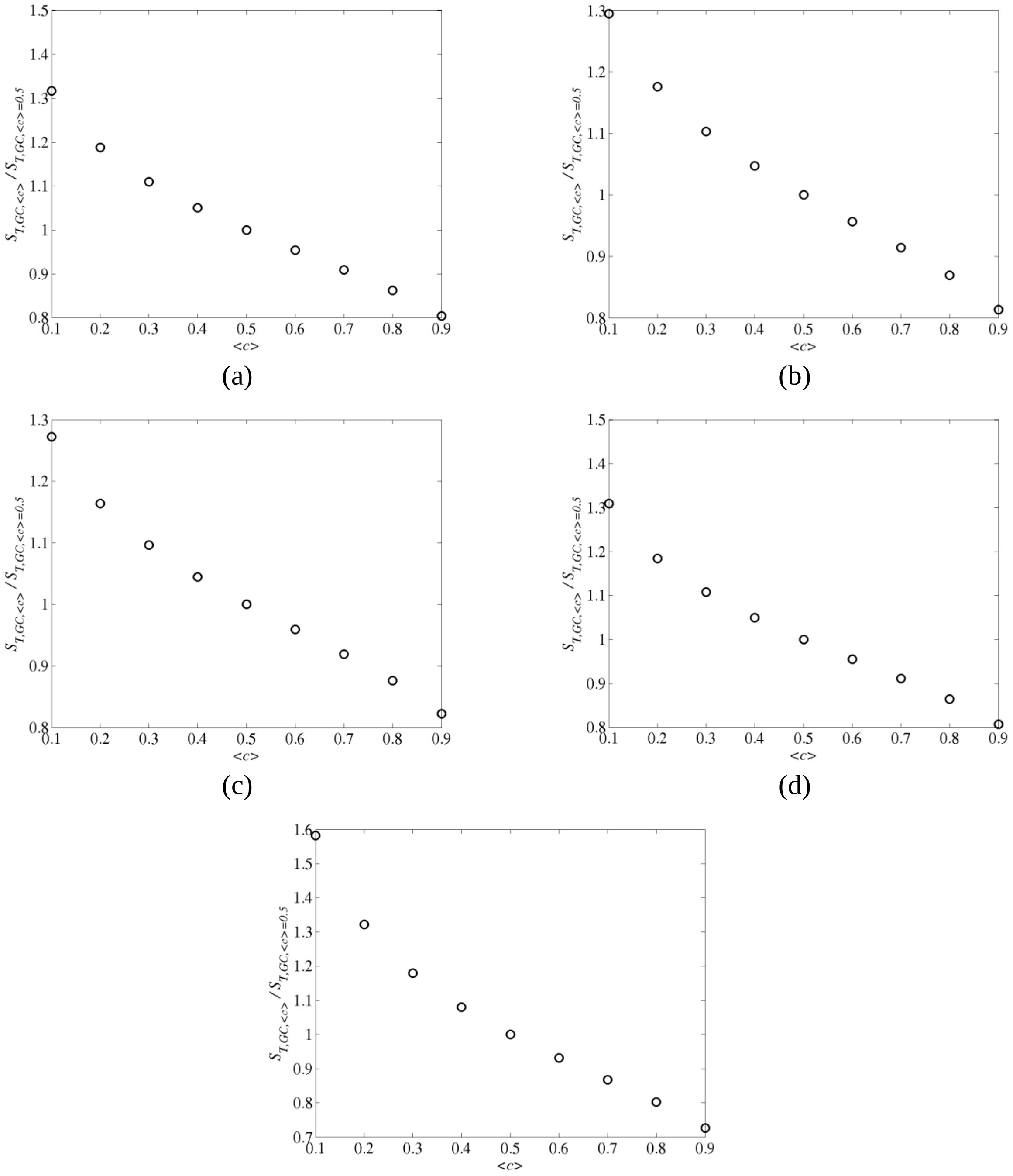

(a) (b) (c) (d) (e)

Figure 142: $S_{T,GC,<c>}$ / $S_{T,GC,<c>= 0.5}$ as a function of average progress variable for the 70/30 H_2/CO mixture at 10 atm, mean flow velocity of 50 m/s and $u'_{rms}\big/S_{L,0}$ of (a) 17.6 (b) 20.2 (c) 22.8 (d) 25.4 (e) 27.6.

C.2 Equivalence ratio sweep studies

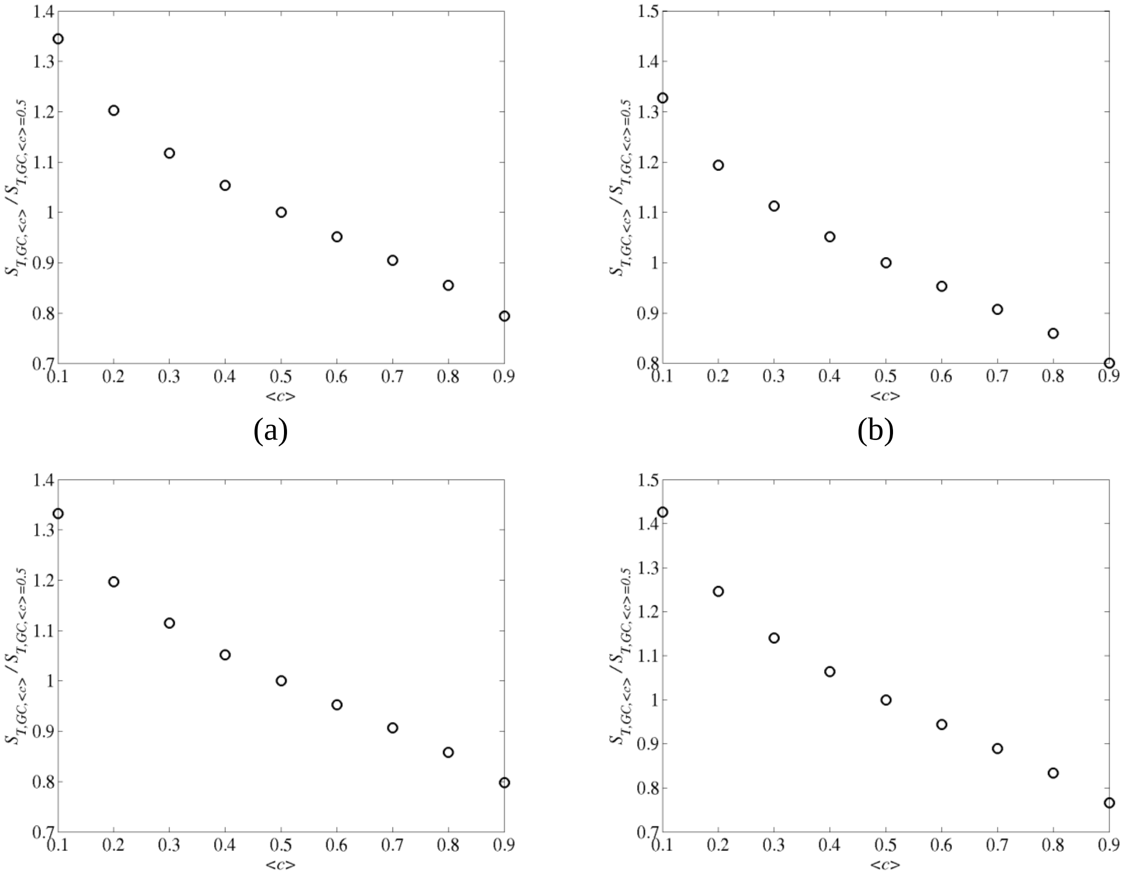

(a) (b)

(c) (d)

Figure 143: $S_{T,GC,<c>}$ / $S_{T,GC,<c>=0.5}$ as a function of average progress variable for a ϕ = 0.55 30/70 H_2/CO mixture at 5 atm, mean flow velocity of 25 m/s and $u'_{rms}/S_{L,0}$ of (a) 21.4 (b) 24.8 (c) 28.2 (d) 31.6.

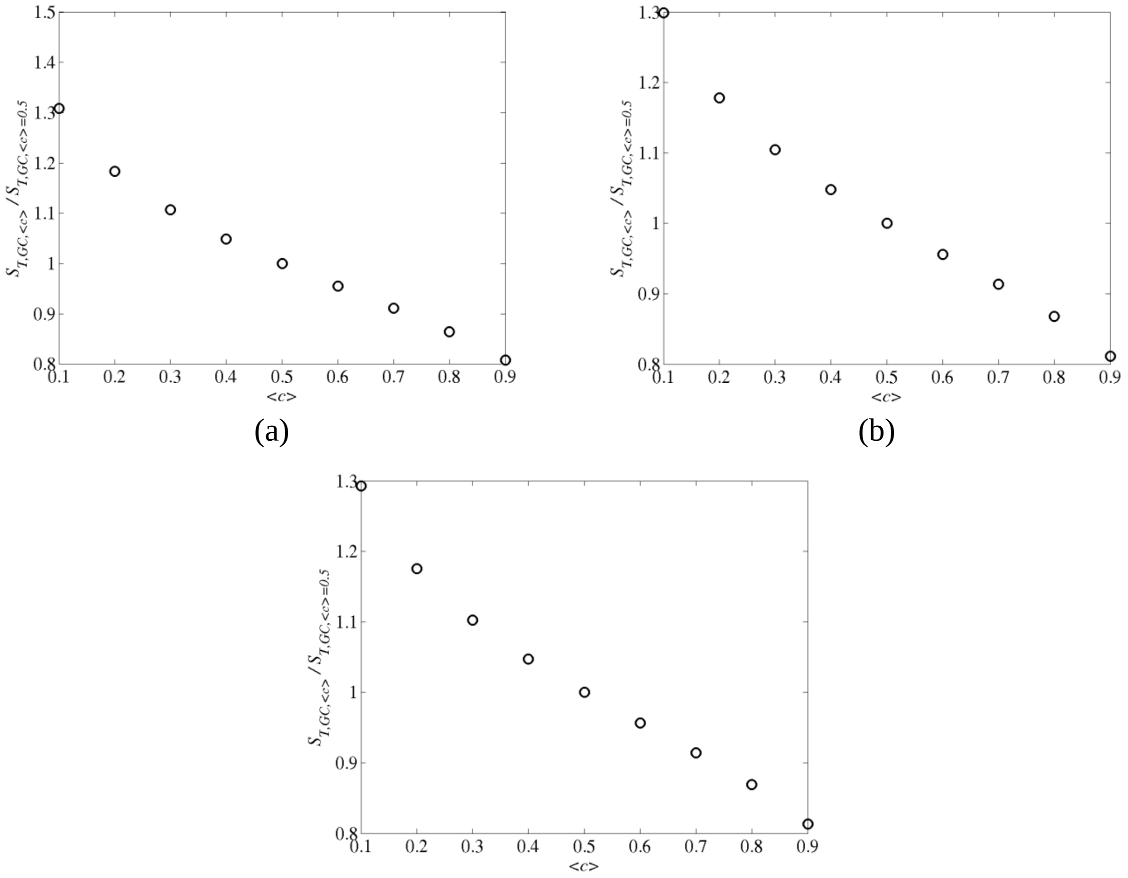

(a) (b)

(c)

Figure 144: $S_{T,GC,<c>}$ / $S_{T,GC,<c>= 0.5}$ as a function of average progress variable for a ϕ = 0.61 30/70 H_2/CO mixture at 5 atm, mean flow velocity of 25 m/s and $u'_{rms}/S_{L,0}$ of (a) 16.1 (b) 18.7 (c) 21.2.

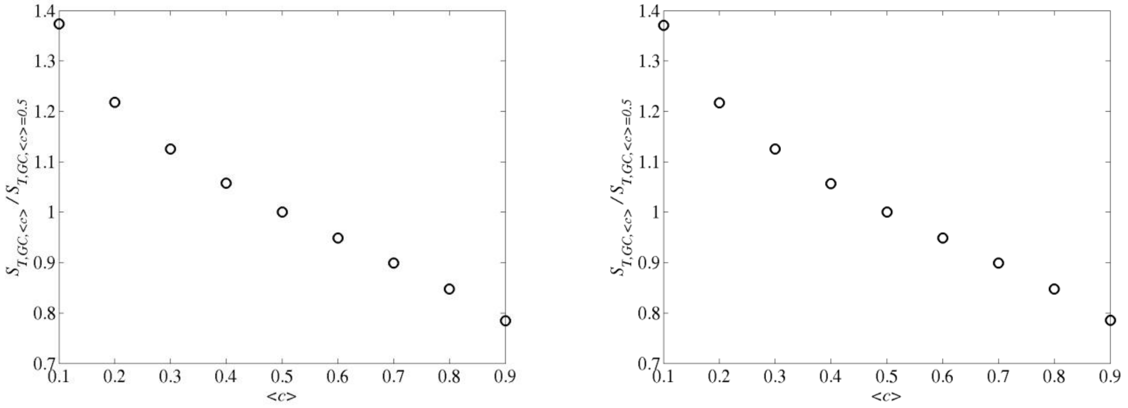

(a) (b)

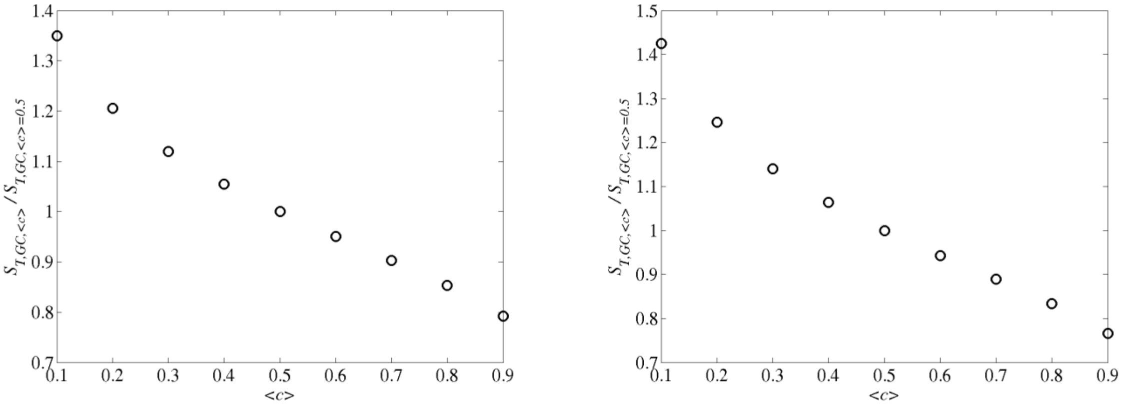

(c) (d)

Figure 145: $S_{T,GC,<c>}$ / $S_{T,GC,<c>= 0.5}$ as a function of average progress variable for a ϕ = 0.45 50/50 H_2/CO mixture at 5 atm, mean flow velocity of 25 m/s and $u'_{rms}/S_{L,0}$ of (a) 39.1 (b) 45.2 (c) 51.3 (d) 57.5.

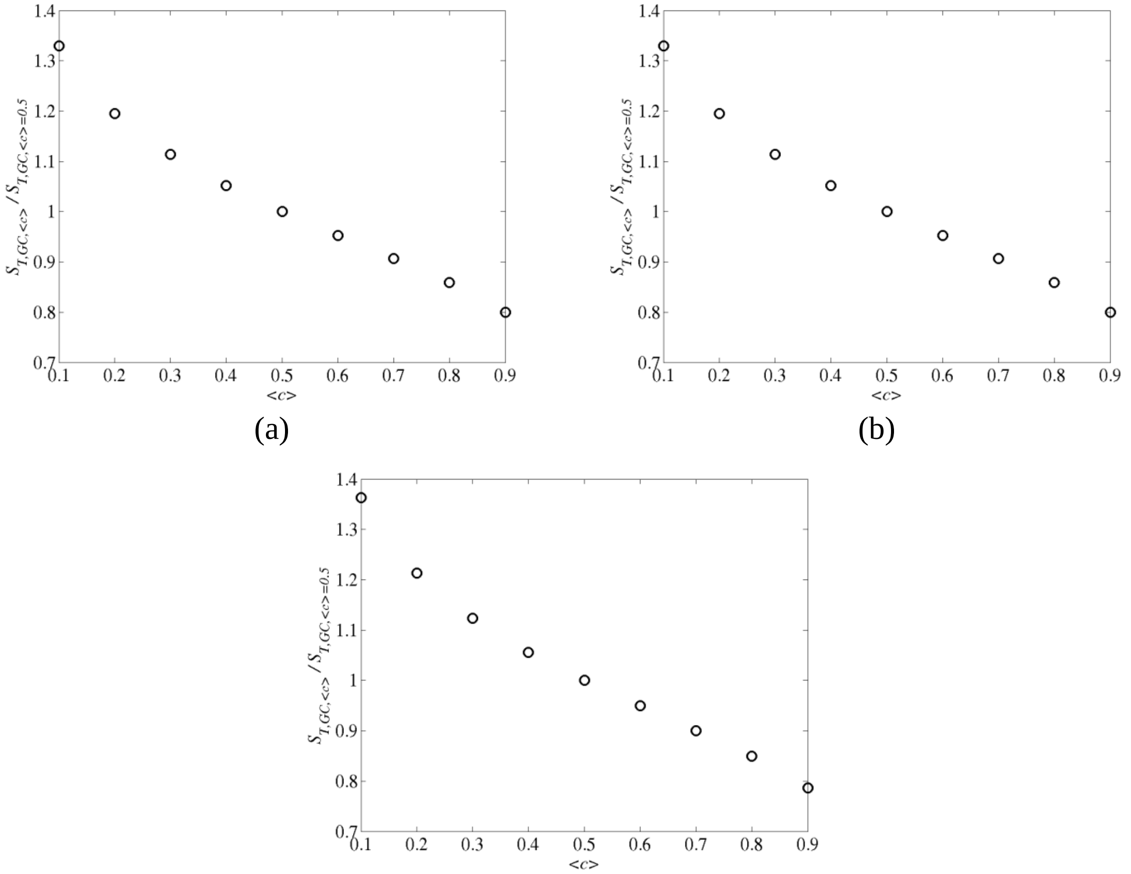

(a) (b)

(c)

Figure 146: $S_{T,GC,<c>}$ / $S_{T,GC,<c>= 0.5}$ as a function of average progress variable for a ϕ = 0.50 50/50 H_2/CO mixture at 5 atm, mean flow velocity of 25 m/s and $u'_{rms}/S_{L,0}$ of (a) 25.1 (b) 29.0 (c) 32.9.

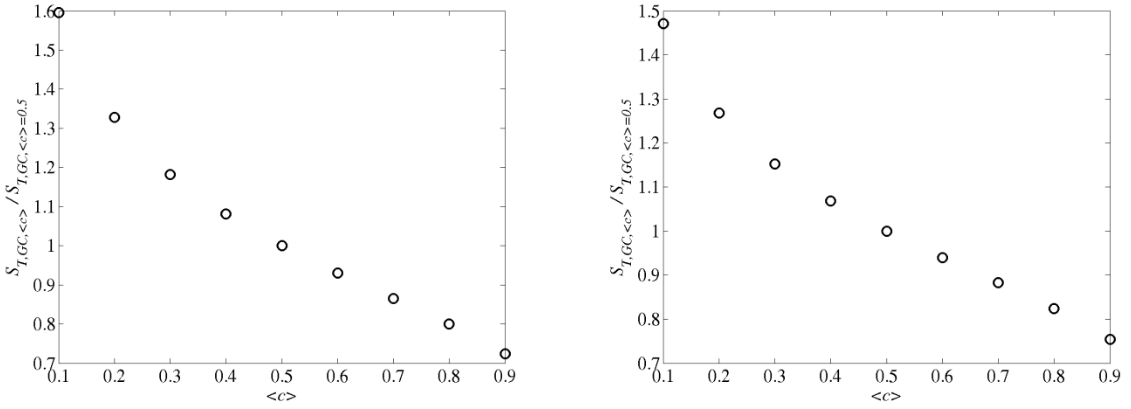

(a) (b)

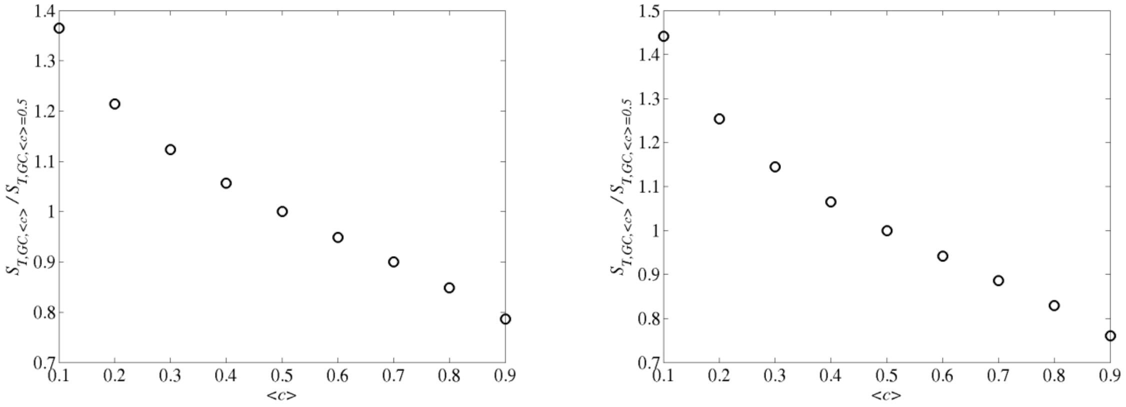

(c) (d)

Figure 147: $S_{T,GC,<c>}$ / $S_{T,GC,<c>=0.5}$ as a function of average progress variable for a $\phi = 0.57$ 30/70 H_2/CO mixture at 10 atm, mean flow velocity of 25 m/s and $u'_{rms} \Big/ S_{L,0}$ of (a) 26.6 (b) 30.8 (c) 35.0 (d) 39.2.

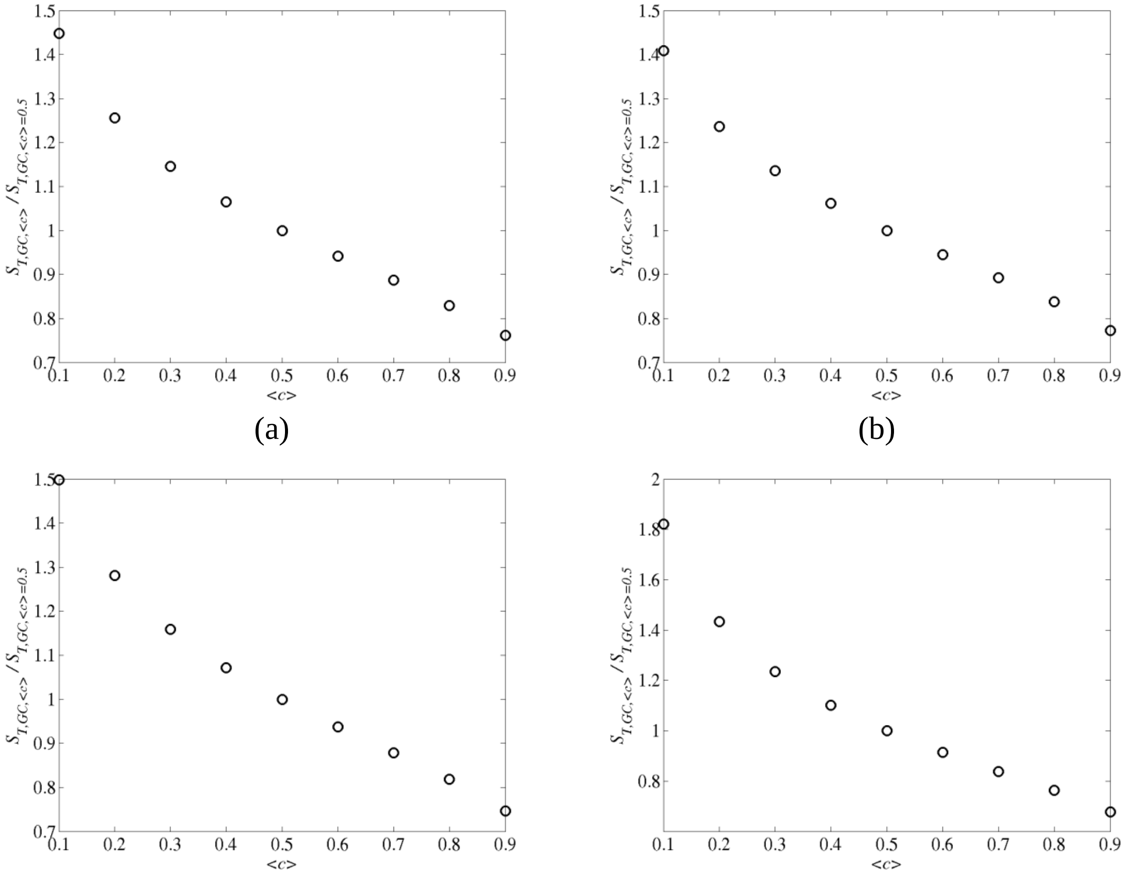

(a) (b)

(c) (d)

Figure 148: $S_{T,GC,<c>}$ / $S_{T,GC,<c>= 0.5}$ as a function of average progress variable for a ϕ = 0.40 50/50 H_2/CO mixture at 10 atm, mean flow velocity of 25 m/s and $u'_{rms}/S_{L,0}$ of (a) 183 (b) 240 (c) 269 (d) 297.

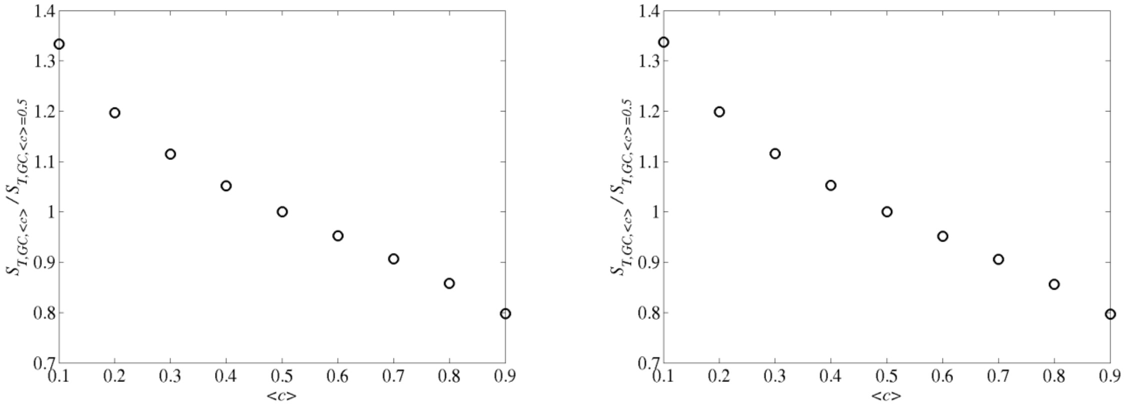

(a) (b)

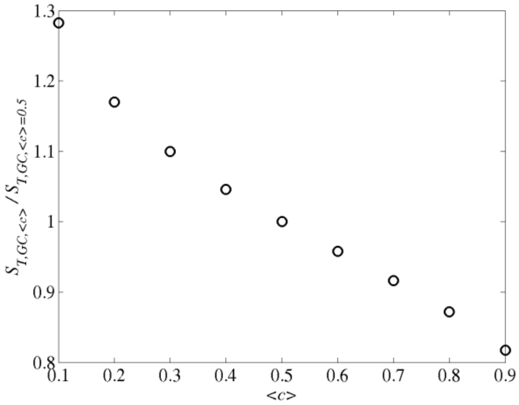

(c)

Figure 149: $S_{T,GC,<c>}$ / $S_{T,GC,<c>= 0.5}$ as a function of average progress variable for a ϕ = 0.40 70/30 H_2/CO mixture at 10 atm, mean flow velocity of 25 m/s and $u'_{rms} \big/ S_{L,0}$ of (a) 240 (b) 277 (c) 315.

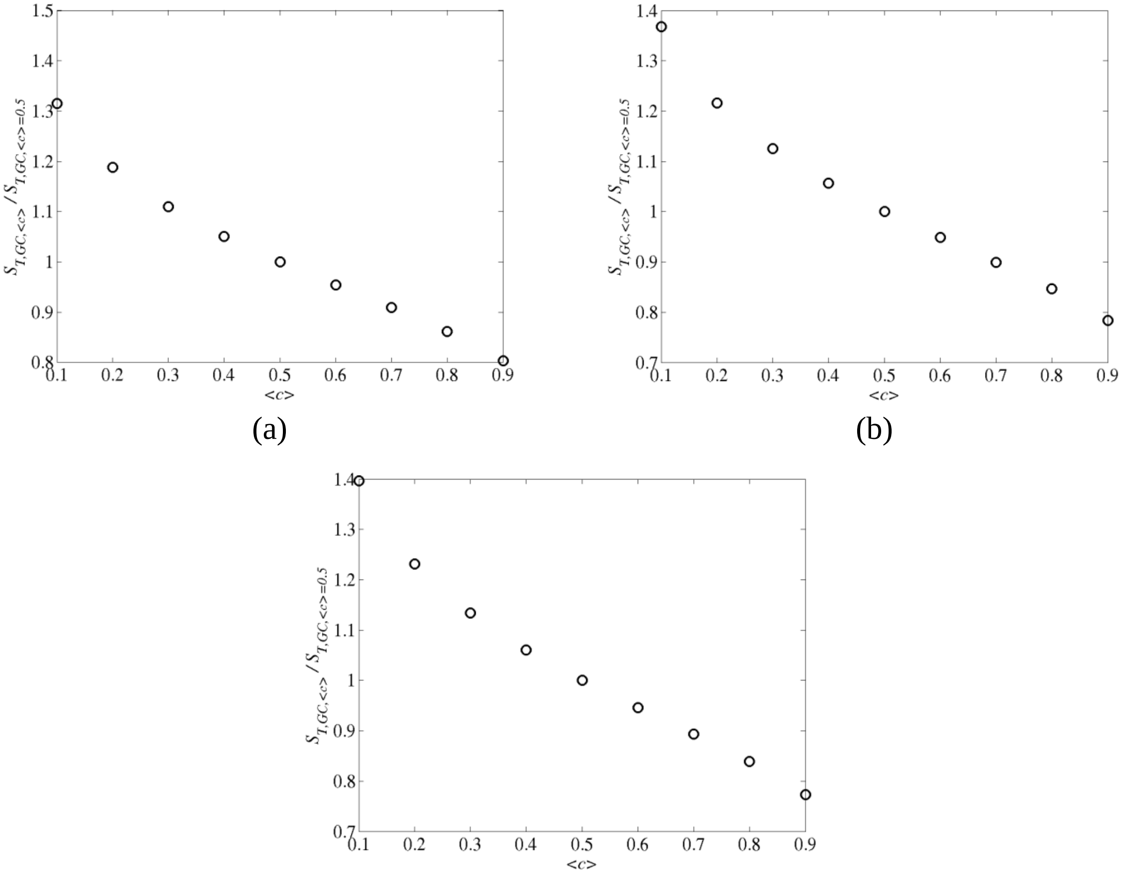

(a) (b)

(c)

Figure 150:: $S_{T,GC,<c>}$ / $S_{T,GC,<c>= 0.5}$ as a function of average progress variable for a ϕ = 0.50 50/50 H_2/CO mixture at 20 atm, mean flow velocity of 15 m/s and $u'_{rms} / S_{L,0}$ of (a) 46.0 (b) 53.3 (c) 60.5.

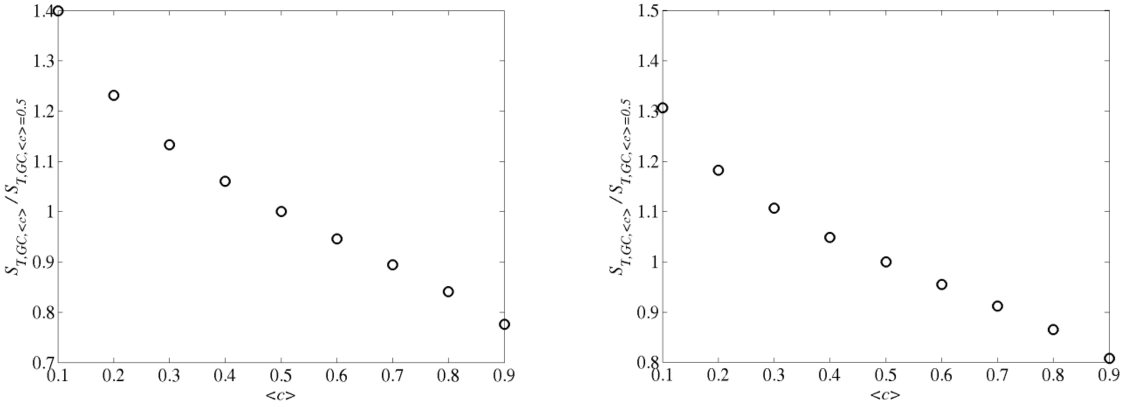

(a) (b)

Figure 151: $S_{T,GC,<c>}$ / $S_{T,GC,<c>=0.5}$ as a function of average progress variable for a ϕ = 0.32 70/30 H_2/CO mixture at 20 atm, mean flow velocity of 15 m/s and $u'_{rms}\big/S_{L,0}$ of (a) 1496 (b) 1731.

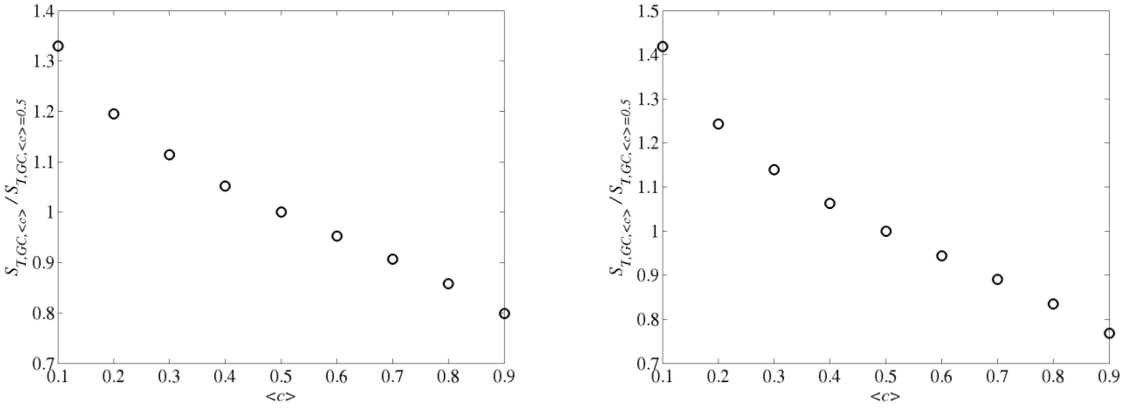

(a) (b)

Figure 152:: $S_{T,GC,<c>}$ / $S_{T,GC,<c>=0.5}$ as a function of average progress variable for a ϕ = 0.40 70/30 H_2/CO mixture at 20 atm, mean flow velocity of 15 m/s and $u'_{rms}\big/S_{L,0}$ of (a) 323 (b) 374.

References

1. C. K. Law, Combustion Physics, Cambridge University Press, New York, 2006, p.^pp.

2. S. Chih-Jen; C. K. Law, Combustion Science & Technology 180 (6) (2008) 1097-1116

3. G. A. Richards; K. H. Casleton, in: Synthesis Gas Combustion: Fundamentals and Applications, T. C. Lieuwen; V. Yang; R. A. Yetter, (Eds.) CRC Press: 2009; p 403.

4. T. Lieuwen; V. McDonell; E. Petersen; D. Santavicca, Journal of Engineering for Gas Turbines and Power 130 (2008) 011506-1 - 011506-10

5. T. C. Lieuwen, Yang, V., Progress in Astronautics and Aeronautics (2005)

6. L. Figura; J. G. Lee; B. D. Quay; D. A. Santavicca, ASME Conference Proceedings 2007 (47918) (2007) 181-187

7. T. Poinsot; D. Veynante, Theoretical and Numerical Combustion, RT Edwards, Inc., Philadelphia, 2005, p.^pp.

8. N. Peters, Proceedings of the Combustion Institute 21 (1) (1988) 1231-1250

9. N. Peters, Turbulent Combustion, Cambridge University Press, Cambridge, 2000, p.^pp.

10. R. Borghi, Recent advances in the aerospace sciences(A 85-47304 23-31). New York, Plenum Press, 1985 (1985) 117-138

11. N. Peters, Journal of Fluid Mechanics 384 (1999) 107-132

12. J. F. Driscoll, Progress in Energy and Combustion Science 34 (1) (2008) 91-134

13. S. R. Turns, An Introduction to Combustion, McGraw-Hill, New York, 1996, p.^pp.

14. R. K. Cheng, in: Synthesis Gas Combustion: Fundamentals and Applications, T. C. Lieuwen; V. Yang; R. A. Yetter, (Eds.) CRC Press: 2009; p 403.

15. S. Hemchandra; T. Lieuwen, Combustion and Flame 157 (5) (2010) 955-965

16. F. Gouldin; R. K. Cheng International Workshop on Premixed Turbulent Flames. http://eetd.lbl.gov/aet/combustion/workshop/workshop.html

17. G. Damköhler, Zeitschrift Electrochem 46 (1940) 601-626

18. K. Bray, Proceedings of the Royal Society of London. Series A, Mathematical and Physical Sciences 431 (1882) (1990) 315-335

19. T. C. Lieuwen, Unsteady Combustor Physics, Cambridge University Press, 2012, p.^pp.

20. R. S. C. Margolis; K. Bray; L. Kostiuk; B. Rogg, Combustion Science and Technology 95 (1-6) (1993) 261-276

21. I. Shepherd; R. Cheng, Combustion and Flame 127 (3) (2001) 2066-2075

22. C. Law; C. Sung, Progress in Energy and Combustion Science 26 (4-6) (2000) 459-505

23. F. A. Williams, Combustion Theory, Benjamin/Cummings Publishing Company, Menlo Park, 1985, p.^pp.

24. S. H. Chung; C. K. Law, Combustion and Flame 55 (1) (1984) 123-125

25. M. Matalon, Combustion Science and Technology 31 (3) (1983) 169-181

26. M. Matalon; B. J. Matkowsky, Journal of Fluid Mechanics Digital Archive 124 (-1) (1982) 239-259

27. W. Peiyong; S. Hu; J. A. Wehrmeyer; R. W. Pitz, in: *42nd AIAA Aerospace Sciences Meeting and Exhibit*, AIAA: AIAA-2004-148, Rena, NV, 2004.

28. R. J. Kee; J. A. Miller; G. H. Evans; G. Dixon-Lewis, Proceedings of the Combustion Institute 22 (1) (1989) 1479-1494

29. J. Y. Ren; W. Qin; F. N. Egolfopoulos; T. T. Tsotsis, Combustion and Flame 124 (4) (2001) 717-720

30. F. N. Egolfopoulos, Proceedings of the Combustion Institute 25 (1) (1994) 1375-1381

31. H. G. Im; J. H. Chen, Proceedings of the Combustion Institute 28 (2) (2000) 1833-1840

32. C. Rutland; A. Trouvé, Combustion and Flame 94 (1) (1993) 41-57

33. J. B. Bell; R. K. Cheng; M. S. Day; I. G. Shepherd, Proceedings of the Combustion Institute 31 (1) (2007) 1309-1317

34. M. Nakahara; H. Kido, AIAA Journal 46 (7) (2008) 1569-1575

35. M. S. Wu; S. Kwon; J. F. Driscoll; G. M. Faeth, Combustion Science and Technology 73 (1) (1990) 327-350

36. A. Lipatnikov; J. Chomiak, Progress in Energy and Combustion Science 28 (1) (2002) 1-74

37. S. Pope, Turbulent flows, Cambridge Univ Press, New York, 2000, p.^pp.

38. J. Hinze, Turbulence, 1975, p.^pp.

39. M. Namazian; L. Talbot; F. Robben, Symposium (International) on Combustion 20 (1) (1985) 411-419

40. A. Boukhalfa; I. Gökalp, Combustion and Flame 73 (1) (1988) 75-87

41. F. C. Gouldin; P. C. Miles, Combustion and Flame 100 (1–2) (1995) 202-210

42. S. K. Thumuluru. Effect of harmonic forcing on turbulent flame properties. PhD, Georgia Institute of Technology, 2010.

43. A. Lipatnikov; J. Chomiak, Progress in Energy and Combustion Science 31 (1) (2005) 1-73

44. S. Filatyev; J. Driscoll; C. Carter; J. Donbar, Combustion and Flame 141 (1-2) (2005) 1-21

45. D. R. Ballal; A. H. Lefebvre, Acta Astronautica 1 (3-4) (1974) 471-483

46. D. Ballal; A. Lefebvre, Proceedings of the Royal Society of London. A. Mathematical and Physical Sciences 344 (1637) (1975) 217-234

47. V. R. Kuznetsov; V. A. Sabel'nikov, in: Turbulence and Combustion, V. R. Kuznetsov; V. A. Sabel'nikov; P. A. Libby, (Eds.) Hemisphere Publishing Corporation: Moscow, 1986; p 362.

48. H. Kobayashi; T. Tamura; K. Maruta; T. Niioka; F. A. Williams, Proceedings of the Combustion Institute 26 (1) (1996) 389-396

49. M. Baum; T. Poinsot; D. Haworth; N. Darabiha, Journal of Fluid Mechanics 281 (1994) 1-32

50. S. Daniele; P. Jansohn; J. Mantzaras; K. Boulouchos, Proceedings of the Combustion Institute 33 (2) (2011) 2937-2944

51. V. P. Karpov; E. S. Severin, Combustion, Explosion, and Shock Waves 18 (6) (1982) 643-644

52. T. Kitagawa; T. Nakahara; K. Maruyama; K. Kado; A. Hayakawa; S. Kobayashi, International Journal of Hydrogen Energy 33 (20) (2008) 5842-5849

53. H. Kido; M. Nakahara; J. Hashimoto; D. Barat, JSME International Journal Series B Fluids and Thermal Engineering 45 (2) (2002) 355-362

54. Ö. Gülder; G. Smallwood; R. Wong; D. Snelling; R. Smith; B. Deschamps; J. Sautet, Combustion and Flame 120 (4) (2000) 407-416

55. A. S. Betev; V. P. Karpov; A. N. Lipatnikov; Z. P. Vardosanidze, Archivum Combustionis 15 (1995) 187-216

56. H. Kobayashi; Y. Kawabata; K. Maruta, Symposium (International) on Combustion 27 (1) (1998) 941-948

57. D. Bradley, Proceedings of the Combustion Institute 24 (1) (1992) 247-262

58. F. Dinkelacker; B. Manickam; S. P. R. Muppala, Combustion and Flame 158 (9) (2011) 1742-1749

59. P. Goix; P. Paranthoen; M. Trinite, Combustion and Flame 81 (3-4) (1990) 229-241

60. H. Kobayashi; K. Seyama; H. Hagiwara; Y. Ogami, Proceedings of the Combustion Institute 30 (1) (2005) 827-834

61. H. Kobayashi; Y. Kawabata; K. Maruta, Proceedings of the Combustion Institute 27 (1998) 941–948

62. H. Kobayashi, Experimental Thermal and Fluid Science 26 (2-4) (2002) 375-387

63. B. Videto; D. Santavicca, Combustion Science and Technology 76 (1) (1991) 159-164

64. B. Bédat; R. K. Cheng, Combustion and Flame 100 (3) (1995) 485-494

65. A. Marshall; P. Venkateswaran; D. Noble; J. Seitzman; T. Lieuwen, Experiments in Fluids 51 (3) (2011) 611-620

66. L. Prandtl, (1932)

67. G. Taylor, ZAMM-Journal of Applied Mathematics and Mechanics/Zeitschrift für Angewandte Mathematik und Mechanik 15 (1-2) (1935) 91-96

68. G. Comte-Bellot; S. Corrsin, Journal of Fluid Mechanics Digital Archive 25 (04) (1966) 657-682 doi:10.1017/S0022112066000338.

69. R. J. Kee; J. F. Grcar; M. Smooke; J. Miller, Sandia National Laboratories Report SAND85-8240, Sandia National Laboratories, Livermore (1983)

70. S. G. Davis; A. V. Joshi; H. Wang; F. Egolfopoulos, Proceedings of the Combustion Institute 30 (1) (2005) 1283-1292

71. G. P. Smith; D. M. Golden; M. Frenklach; N. W. Moriarty; B. Eiteneer; M. Goldenberg; C. T. Bowman; R. K. Hanson; S. Song; W. C. Gardiner Jr; V. V. Lissianski; Z. Qin GRI-Mech 3.0. http://www.me.berkeley.edu/gri_mech/

72. J. Li; Z. Zhao; A. Kazakov; M. Chaos; F. L. Dryer; J. J. Scire, International Journal of Chemical Kinetics 39 (3) (2007) 109-136

73. G. J. Smallwood; Ö. L. Gülder; D. R. Snelling; B. M. Deschamps; I. Gökalp, Combustion and Flame 101 (4) (1995) 461-470

74. P. Griebel; P. Siewert; P. Jansohn, Proceedings of the Combustion Institute 31 (2) (2007) 3083-3090

75. J. M. Seitzman; A. Üngüt; P. H. Paul; R. K. Hanson, Proceedings of the Combustion Institute 23 (1) (1991) 637-644

76. R. K. Hanson, Proceedings of the Combustion Institute 21 (1) (1988) 1677-1680

77. F. Halter; C. Chauveau; I. Gökalp; D. Veynante, Combustion and Flame 156 (3) (2009) 657-664

78. C. Dasch, Applied Optics 31 (8) (1992) 1146–1152

79. E. Cintosun; G. J. Smallwood; O. L. Gulder, AIAA Journal 45 (11) (2007) 2785

80. N. Peters; H. Wenzel; F. A. Williams, Proceedings of the Combustion Institute 28 (1) (2000) 235-243.

81. R. Aldredge; F. Williams, Journal of Fluid Mechanics 228 (2006) 487-511

82. A. N. Lipatnikov; J. Chomiak, Progress in Energy and Combustion Science 36 (1) (2010) 1-102

83. H. Kido; M. Nakahara; K. Nakashima; J. Hashimoto, Proceedings of the Combustion Institute 29 (2) (2002) 1855-1861

84. D. Bradley; M. Lawes; M. S. Mansour, Combustion and Flame 158 (1) (2011) 123-138

85. D. Bradley; M. Lawes; K. Liu; M. S. Mansour, Proceedings of the Combustion Institute 34 (1) (2013) 1519-1526

86. M. Fairweather; M. P. Ormsby; C. G. W. Sheppard; R. Woolley, Combustion and Flame 156 (4) (2009) 780-790

87. R. K. Cheng; D. Littlejohn; P. A. Strakey; T. Sidwell, Proceedings of the Combustion Institute 32 (2) (2009) 3001-3009

88. D. Littlejohn; R. K. Cheng; D. R. Noble; T. Lieuwen, Journal of Engineering for Gas Turbines and Power 132 (1) (2010) 011502-1-011502-8

89. R. K. Cheng; D. Littlejohn, Journal of Engineering for Gas Turbines and Power 130 (3) (2008) 031503

90. D. Littlejohn; R. K. Cheng, Proceedings of the Combustion Institute 31 (2) (2007) 3155-3162

91. M. Lauer; T. Sattelmayer, Journal of Engineering for Gas Turbines and Power 132 (6) (2010) 061502-8

92. V. N. Nori. Modeling and analysis of chemiluminescence sensing for syngas, methane and Jet-A combustion. PhD, Georgia Institute of Technology, 2008.

93. M. Day; S. Tachibana; J. Bell; M. Lijewski; V. Beckner; R. K. Cheng, Combustion and Flame 159 (1) (2012) 275-290

94. G. Dixon-Lewis, Symposium (International) on Combustion 23 (1) (1991) 305-324

95. R. J. Kee; M. E. Coltrin; P. Glarborg, Chemically reacting flow: theory and practice, Wiley-Interscience, 2003, p.^pp.

96. C. K. Wu; C. K. Law, Proceedings of the Combustion Institute 20 (1) (1985) 1941-1949

97. J. B. Chen; H. G. Im, Proceedings of the Combustion Institute 28 (1) (2000) 211-218

98. K. N. C. Bray; R. S. Cant, Proceedings: Mathematical and Physical Sciences (1991) 217-240

99. S. H. El Tahry; C. Rutland; J. Ferziger, Combustion and Flame 83 (1-2) (1991) 155-173

100. A. Lipatnikov; J. Chomiak, Proceedings of the Combustion Institute 30 (1) (2005) 843-850

101. P. J. Goix; I. G. Shepherd, Combustion Science and Technology 91 (4) (1993) 191 - 206

102. D. Haworth; T. Poinsot, Journal of Fluid Mechanics 244 (1992) 405-436

103. V. P. Karpov; A. N. Lipatnikov; V. L. Zimont, in: Advances in Combustion Science: In honor of Ya. B. Zel'dovich, W. A. Sirignano; A. G. Merzhanov; L. De Luca, (Eds.) AIAA: Reston, VA, 1997; Vol. 173, pp 235-250.

104. J. M. Duclos; D. Veynante; T. Poinsot, Combustion and Flame 95 (1–2) (1993) 101-117

105. D. H. Shin. Premixed Flame Kinematics in a Harmonically Oscillating Velocity Field. PhD, Georgia Institute of Techology, 2012.

106. P. Venkateswaran; A. Marshall; D. H. Shin; D. Noble; J. Seitzman; T. Lieuwen, Combustion and Flame 158 (8) (2011) 1602-1614

107. A. Amato; M. S. Day; R. K. Cheng; J. Bell; T. Lieuwen, in: *Central States Section Spring Technical Meeting*, Dayton, Ohio, 2012.

108. C.-C. Liu; S. S. Shy; M.-W. Peng; C.-W. Chiu; Y.-C. Dong, Combustion and Flame 159 (8) (2012) 2608-2619

109. C.-W. Chiu; Y.-C. Dong; S. S. Shy, International Journal of Hydrogen Energy 37 (14) (2012) 10935-10946

110. T. G. Beckwith; R. D. Marangoni; J. H. Lienhard, Mechanical measurements, Pearson Prentice Hall, 2007, p.^pp.